Imperial College London

Characterisation and prediction of failure in injection-moulded short-fibre composites from coupons to components

by

Yuki Fujita

Department of Mechanical Engineering, Imperial College London,
South Kensington Campus, London SW7 2AZ, United Kingdom

This thesis is submitted for the degree of
Doctor of Philosophy of Imperial College London

April 2024

Abstract

Injection-moulded (IM) short-glass fibre reinforced thermoplastics (SFRPs) have drawn large interest from automotive industry for cost and weight reduction. The injection-moulding process creates a core-shell micro-structure with complex fibre orientation, leading to anisotropic and heterogeneous properties and failure modes, which complicates the design of IM-SFRP components. When designing such components, it is necessary to predict when and where failure will occur. However, existing failure criteria for SFRPs underestimate the failure load, because they consider failure initiation only and neglect the material's toughness. The objective of this work was to develop a Finite-Element (FE) based methodology to accurately predict the performance of polyamide 6.6 based IM-SFRPs, by accounting for the material's progressive failure.

The initiation and propagation fracture toughnesses (Full R-curves) were characterised from Compact Tension tests with the combined effect of fibre orientation, moisture and temperature. FE simulations have demonstrated the need to consider both initiation and propagation toughnesses to predict the response of notched coupons.

State-of-the-art structural FE simulations, coupled with fibre orientation fields, were conducted using IM-SFRP automotive (sub)components. The conventional methodology using failure initiation criterion underestimated the maximum load by 20%. By introducing the experimentally-measured toughnesses, this methodology showed excellent agreement (within 3% error) with the tests under all conditions, highlighting the importance of accounting for the material's toughness to predict the ultimate failure of IM-SFRPs.

Damage initiation and propagation in the (sub)components were predicted by the proposed FE simulations. Using fractographic analyses, the sequence of failure events in the (sub)components were inferred experimentally. These results presented good agreement, demonstrating that fractography has been successfully used to support the proposed models.

This research demonstrates that accounting for the material's toughness is required to accurately predict the ultimate failure of IM-SFRP components. The output of this research will contribute to design safer and more efficient damage-tolerant IM-SFRP components.

Declaration of originality

The work hereby presented is based on research carried out by the author at the Department of Mechanical Engineering and the Department of Aeronautics in Imperial College London, and it is all the author's own work except where otherwise acknowledged. No part of the present work has been submitted elsewhere for another degree or qualification.

Copyright declaration

The copyright of this thesis rests with the author. Unless otherwise indicated, its contents are licensed under a Creative Commons Attribution-NonCommercial 4.0 International Licence (CC BY-NC). Under this licence, you may copy and redistribute the material in any medium or format. You may also create and distribute modified versions of the work. This is on the condition that: you credit the author and do not use it, or any derivative works, for a commercial purpose. When reusing or sharing this work, ensure you make the licence terms clear to others by naming the licence and linking to the licence text. Where a work has been adapted, you should indicate that the work has been changed and describe those changes. Please seek permission from the copyright holder for uses of this work that are not included in this licence or permitted under UK Copyright Law.

Contents

Abstract 2

Contents 5

List of figures 10

List of tables 17

Acknowledgements 19

List of publications 20

Peer-reviewed journal publications 20

Refereed conference publications 20

Award 21

Acronyms and Abbreviations 22

Notation 23

Chapter 1 – Introduction 25

1.1 Background 25

1.2 Objectives 27

Chapter 2 - Literature review 29

2.1 Microstructure of IM-SFRPs 29

2.2 Characterisation at coupon scale 32

2.3 Fractography and fracture mechanisms 34

2.4 State-of-the-art models for IM-SFRP materials 34

2.4.1 Two-step pseudo-grain approach for short fibre composites 35

2.4.2 Elastic response of aligned short fibre composites 37

2.4.3 Digimat's elastic-plastic material model for the matrix 38

2.4.4 Failure criteria for injection-moulded short-fibre composites 39

2.4.5 Calibration of material properties using Digimat 39

2.5 Fibre orientation models in injection-moulding process simulation 40

2.5.1 Folger-Tucker model 41

2.5.2 Reduced Strain Closure model 42

2.5.3 Moldflow Rotational Diffusion model 43

2.6 Coupled process/structural simulations 43

2.7 Cohesive zone modelling ____ 44
2.8 Thesis outline ____ 45

Chapter 3 - Material properties of injection-moulded short glass fibre-reinforced polyamide 6.6 composites ____ 47
3.1 Introduction ____ 47
3.2. Experimental procedures ____ 48
3.2.1. Manufacturing of injection-moulded plates ____ 48
3.2.2. Characterisation of fibre orientation in the plate ____ 48
3.2.3. Tensile testing of dog-bone coupons ____ 49
3.2.4. Fractography ____ 50
3.2.5. Dynamic Mechanical Analysis ____ 50
3.2.6. Differential Scanning Calorimetry analysis ____ 50
3.3. Results ____ 51
3.3.1. Fibre orientation tensor in the plate ____ 51
3.3.2. Tensile mechanical properties for different fibre orientations ____ 52
3.3.3. Fractographic analysis after tensile testing of the dog-bone coupons ____ 54
3.3.4. Glass transition temperature of PA66-GF50 ____ 56
3.3.5. Crystallinity of PA66 materials ____ 56
3.4. Discussion ____ 57
3.4.1. Fibre orientation state in the plates ____ 57
3.4.2. Effect of fibre orientation on the mechanical properties of the coupons ____ 57
3.4.3. Crystallinity of PA66 materials ____ 57
3.4.4. Temperature-moisture equivalence in coupons ____ 58
3.5. Conclusions ____ 59

Chapter 4 - Calibration of elastic, elastic-plastic and failure models used in state-of-the-art simulation for IM-SFRPs ____ 60
4.1 Introduction ____ 60
4.2 Prediction of fibre orientation field in IM-SFRP plates by process simulation ____ 60
4.3 Experimental calibration and validation of elastic models for IM-SFRPs ____ 62
4.3.1 Stiffness prediction using Digimat's and analytical implementations ____ 62
4.3.2 Parametric studies of fibre and matrix properties for stiffness prediction ____ 63

4.4 Experimental calibration and validation of elastic-plastic and strength models for IM-SFRPs 67
4.4.1 Elastic-plastic model 67
4.4.2 Strength model (Tsai-Hill failure criterion) 67
4.4.3 FE simulations of dogbone coupon's tensile testing 69
4.5 Discussion 70
4.5.1 Prediction of the fibre orientation state in the IM-plates 70
4.5.2 Prediction of the coupon's stiffness 71
4.5.3 Prediction of the coupon's tensile strength 71
4.6 Conclusions 72

Chapter 5 - Initiation and propagation fracture toughness of IM-SFRPs under different environmental conditions 74
5.1 Introduction 74
5.2 Experimental details 75
5.2.1 Fracture toughness testing 75
5.2.2 Data reduction of fracture toughness tests 76
5.2.3 Fractography 78
5.3 Results 78
5.3.1 Fracture toughness 78
5.3.2 Fractography 82
5.4 Discussion 85
5.4.1 Methodology for measuring fracture toughness in SFRPs 85
5.4.2 Fibre orientation and environmental effects on the fracture toughness of SFRPs 87
5.4.3 Justification of bending fibre-failure morphologies under tensile loading 89
5.4.4 Novelty and implications 89
5.5 Conclusions 90

Chapter 6 - Predicting failure in injection-moulded short-fibre subcomponents under varied environmental conditions through fracture mechanics 92
6.1 Introduction 92
6.2 Coupon characterisation 93
6.3 Experimental methods for subcomponents 94
6.3.1 Manufacturing of IM-SFRP subcomponents 94

6.3.2 Static indentation test of IM-SFRP subcomponents _____ 95
6.3.3 Fractography _____ 96
6.4 Experimental results for subcomponents _____ 96
6.4.1 Overall response of PA66-GF50 subcomponents under static indentation _____ 96
6.4.2 Fracture surfaces of the subcomponents under different environmental conditions _____ 97
6.5 Virtual testing of the subcomponents _____ 101
6.5.1 Process simulation of the subcomponents _____ 101
6.5.2 Structural simulation of the subcomponents according to the state of the art ___ 102
6.5.3 FE modelling of the subcomponents using combined methodologies of coupled FEA and cohesive zone modelling _____ 104
6.6 FE Simulation results for the subcomponents _____ 106
6.6.1 Prediction of maximum failure load of PA66-GF50 subcomponents _____ 106
6.6.2 Prediction of the sequence of failure events and post-peak behaviour using cohesive zone modelling _____ 109
6.7. Discussion _____ 112
6.7.1 Damage mechanisms and sequence of failure events at 23°C-DAM conditions __ 112
6.7.2 Prediction of PA66-GF50 subcomponent failure using FE models _____ 113
6.7.3 Effect of temperature and moisture on the damage mechanisms and fracture morphology _____ 115
6.7.4 Temperature-moisture equivalence _____ 116
6.7.5 Novelty and implications _____ 117
6.8 Conclusions _____ 118

Chapter 7 - Predicting failure in injection-moulded short-fibre components through fracture mechanics _____ 121
7.1 Introduction _____ 121
7.2 Experiments _____ 122
7.2.1 Procedures _____ 122
7.2.2 Results _____ 125
7.3 Process simulations of PA66-GF50 components _____ 134
7.3.1 Procedures _____ 134
7.3.2 Results _____ 134
7.4 Coupled FE simulations of PA66-GF50 components _____ 137

7.4.1 Methodology 137
7.4.2 Results 140
7.5 Discussion 142
7.5.1 Prediction of PA66-GF50 component failure using coupled FEA combined with CZM 142
7.5.2 Damage mechanisms and sequence of failure events in components 143
7.6 Conclusions 146

Chapter 8 - Discussion 148
8.1 On the accuracy of failure prediction from coupons to components 148
8.2 On the sequence of failure events in IM-SFRP (sub)components 149
8.3 On the T-M equivalence 150
8.4 Novelty of this research 150
8.5 Potential impact of this research 151

Chapter 9 – Conclusions 153

Chapter 10 - Future work 155
10.1 Strain rate effects on the mechanical properties and the damage mechanisms of IM-SFRPs 155
10.2 Development of a toughness model for coupled FEA using CZM 156
10.3 Characterisation of the weldline in the components 157
Bibliography 159
Appendix A 168
A.1. FE model for compliance calibration (VTM-CC) 168
A.2. Data reduction of CT tests using FE-supported compliance calibration 169
Appendix B 170
B.1. Design criteria 170
B.2. Virtual CT tests with simulation of crack propagation using Cohesive Elements (VTM-CE) 170
B.3. Estimation of plastic zones using coupled simulations with plasticity models (VTM-CP) 171
Appendix C 173
Appendix D 175

List of figures

Fig. 1.1. Volume breakdown of the use of different materials in the global composites market [3]. 25
Fig. 1.2. Expectation of global injection moulded automotive parts market between 2022-2032. 26
Fig. 1.3. Examples of the application of IM-SFRPs in automotive. 26
Fig. 1.4. Testing pyramid of IM-SFRP coupons, subcomponents and components used in this thesis. 28

Fig. 2.1. Definition of (a) coordinate system and Eulerian angles of a fibre's direction (represented by its main axis), and (b) elliptical section in the 1-2 plane of a fibre with circular cross-section and diameter b 30
Fig. 2.2. Examples of the description of fibre orientation tensor: (a) unidirectional alignment along 1-axis, (b) perfectly random in 2D, and (c) perfectly random in 3D. 30
Fig. 2.3. Two-step homogenisation procedure for a composite with misaligned inclusions. Top: real RVE. Left: decomposition into an aggregate of pseudo-grains. Bottom: homogenisation of each pseudo-grain (first step). Right: homogenisation of the aggregate of homogenised pseudo-grains (second step). 36

Fig. 3.1. Photograph of an injection-moulded PA66-GF50 plate (2 mm thick). 48
Fig. 3.2. Definition of the machining angles of dog-bone coupons (relating the plate coordinate system xyz with the coupon coordinate system XYZ). 50
Fig. 3.3. (a) Cross-sectional optical micrograph across the A-A line in Fig. 3.1, with zoom-ins shown in (b) in the skin, and (c) in the core, and (d) in-plane diagonal components of the fibre orientation tensor in the injection-moulded PA66-GF50 plates. 51
Fig. 3.4. Representative load-displacement curves of PA66-GF50 dogbone coupons at different machining angles: (a) 23°C-DAM, (b) 23°C-RH50 and (c) 80°C-RH50. 52
Fig. 3.5. (a) The Young's modulus, (b) tensile strength, and (c) failure strain of PA66-GF50 as a function of machining angle under the five different environmental conditions. 52
Fig. 3.6. (a) The Young's modulus, (b) tensile strength, and (c) failure strain of PA66-GF50 as a function of fibre orientation components α_{YY} under the five different environmental conditions. 54
Fig. 3.7. Representative scanning electron micrographs of fracture surfaces of dog-bone coupons tested under 23°C-DAM: (a)-(c) at 0° direction, (d)-(f) at 45° direction and (g)-(i) at 90° direction for the overall area through the thickness, in the skin and in the core, respectively. 55
Fig. 3.8. Tan-Delta curves of PA66-GF50 under DAM and RH50 conditions. 56

Fig. 4.1. Predicted fibre orientation tensor along the x-direction in the plate (α_{XX}), using the MRD model: (a) plate overview, (b) cross-section at the centre of the plate along the x-direction

(along the A-A line indicated in Subfigure (a)). The colourbar shown represents α_{XX} consistently for both subfigures. 61
Fig. 4.2. Comparison of fibre orientation tensor α_{XX} obtained from the experiments (as reported in Section 3.3.1) and process simulations using three different fibre orientation models. 62
Fig. 4.3. Predicted Young's modulus of PA66-GF50 using Digimat's elastic model and Matlab implementation of Mori-Tanaka's mean-field homogenisation with orientation averaging as a function of fibre volume fraction at 0° and 90° directions under 23°C-DAM. 63
Fig. 4.4. The Young's modulus of PA66-GF50 as a function of fibre orientation tensor under the three different environmental conditions from the experiments and prediction using Digimat's elastic material model (i) varying the matrix modulus and (ii) varying the fibre aspect ratio: (a) 23°C-DAM, (b) 23°C-RH50, and (c) 80°C-RH50. 65
Fig. 4.5. Difference in the Young's modulus of PA66-GF50 between the experiments and outputs from Digimat's elastic model, using different fibre aspect-ratio inputs. These values are calculated as the average of the square root of the sum of the squared differences for all machining directions and environmental conditions. 66
Fig. 4.6. Difference in the Young's modulus of PA66-GF50 material between the experiments and outputs from Digimat's elastic model, using different matrix moduli inputs under (a) 23°C-DAM, (b) 23°C-RH50, and (c) 80°C-RH50. These values are calculated as the square root of the sum of the squared differences for all machining directions. 66
Fig. 4.7. Tensile strength of PA66-GF50 as a function of fibre orientation tensor under the three different environmental conditions from the experiments and prediction using Digimat's elastic-plastic material model in Digimat-MF. All datapoints from experiments have error bars representing one standard deviation (some error bars are sufficiently small to be hidden behind the corresponding datapoint). 68
Fig. 4.8. Mesh and boundary conditions used for the FE model of dogbone coupons. 69
Fig. 4.9. Stress-strain curves of dogbone coupons from the experiments (all the five curves are shown) and the coupled FEA: (a) 23°C-DAM for 0°, 45° and 90° directions, (b) 23°C-RH50 for 0° and 90° directions, and (c) 80°C-RH50 for 0° and 90° directions. 70

Fig. 5.1. Design of CT coupons: (a) details of the geometry (all dimensions in mm), and (b) definition of the machining angles (relating the plate coordinate system xyz with the coupon coordinate system XYZ). The two blue targets indicate the position to extract the opening displacement from DIC maps. 76
Fig. 5.2. Definition of the contour $\Gamma^0 = \{C_1, \dots, C_9\}$ in the CT coupons, used for the J-integral calculation. 78

Fig. 5.3. Representative load-displacement curves of PA66-GF50 CT coupons at different machining angles: (a) 23°C-DAM, (b) 23°C-RH50 and (c) 80°C-RH50, and (d) all four load-displacement curves at 0° and 90° for 23°C-DAM condition. 79
Fig. 5.4. Representative R-curves of PA66-GF50 CT coupons at distinct machining angles using the compliance calibration method: (a) 23°C-DAM, (b) 23°C-RH50 and (c) 80°C-RH50. 80
Fig. 5.5. Comparison of R-curves calculated using the compliance calibration and J-integral methods for 0° coupons: (a) 23°C-DAM, (b) 23°C-RH50 and (c) 80°C-RH50. Each cross at 0-mm crack propagation corresponds to the average initiation fracture toughness under each environmental condition, measured with the J-integral method. The dotted vertical lines identify the beginning of the plateaued toughness values (which were averaged to calculate the propagation fracture toughness under each environmental condition). 80
Fig. 5.6. Initiation and propagation fracture toughness of 0° coupons calculated using the compliance calibration and J-integral methods. Error bars represent one standard deviation. 81
Fig. 5.7. Propagation fracture toughness as a function of machining angle (a) and fibre orientation tensor (b) at different environmental conditions, calculated using the compliance calibration method. All datapoints have error bars representing one standard deviation. 82
Fig. 5.8. Photographs of crack plane in CT coupons (four replicates) machined at 0°, 45° and 90°, after compact tension testing at 23°C-DAM. 83
Fig. 5.9. Electron micrographs of the fracture surfaces of CT coupons (in skin, propagation site) after testing at 23°C-DAM conditions, for all machining angles (θ) tested: (a) 0°, (b) 20°, (c) 30°, (d) 45°, (e) 60°, (f) 90°. 84
Fig. 5.10. Scanning electron micrographs of fracture surfaces of the CT coupons (in skin, propagation site) after compact tension testing under different environmental conditions, for three several machining angles. 85
Fig. 5.11. Load-displacement curves of CT coupons comparing results from the experimental tests and FE simulations using bilinear and trilinear cohesive laws: (a) at 0° under 23°C-DAM, (b) at 90° under 23°C-DAM, (c) at 0° under 23°C-RH50, and (d) at 0° under 80°C-RH50. 87
Fig. 5.12. Schematic illustration of stress distributions leading to fibre-failure under bending: (a) in an aligned fibre embedded in PA66 matrix, (b) on a fibre fracture surface. 89

Fig. 6.1. Propagation fracture toughness of PA66-GF50 as a function of fibre orientation tensor, for five different environmental conditions. 94
Fig. 6.2. Geometry of the subcomponents, boundary conditions and testing set up (all dimensions in mm). 95
Fig. 6.3. load-displacement curves of PA66GF50 subcomponents at under five different environmental conditions. 96

Fig. 6.4. Crack initiation and propagation in PA66-GF50 subcomponent: (a) crack initiation location (photograph taken at the maximum load during the test), (b) schematic illustration of fracture plane $y-z$ from the front, and (c) schematic illustration of fracture plane $y-z$ from the backface. 97
Fig. 6.5. (A) Representative optical image of the fracture surface of a subcomponent tested at 23^{O}C-DAM, and (B) representative scanning electron micrographs of fracture surfaces of a subcomponent tested at 23°C-DAM, near the symmetry axis; Subfigures (a)-(e) correspond to the regions identified in Subfigure (A) with green circles. The yellow arrows represent the local direction of crack propagation, identified by the matrix morphologies (riverlines). 99
Fig. 6.6. Scanning electron micrographs of fracture surfaces of the subcomponents under different environmental conditions at the crack initiation site in skin region (region in Fig. 6.5 (a)). 100
Fig. 6.7. Scanning electron micrographs of fracture surfaces of the subcomponents under different environmental conditions in the core region along the symmetry axis (region in Fig. 6.5 (b)). 101
Fig. 6.8. Predicted fibre orientation tensor in the subcomponents: on the overall subcomponent surface, along the x (a), y (d) and z (g) directions; on the backface, along the x (b), y (e) and z (h) directions; local view of the fracture plane (indicated in Subfigure (b)), along the x (c), y (f) and z (i) directions. 102
Fig. 6.9. FE model of the subcomponents: (a) Global view of the subcomponent and the indenter, (b) Zoom-in of the mesh at the front edge, (c), Zoom-in of the mesh around the fracture plane at the front edge for coupled FEA only with solid elements, (d) Zoom-in of the mesh around the fracture plane at the front edge for coupled FEA with solid and cohesive elements, and (e) Mesh on the fracture plane (all dimensions in mm). 103
Fig. 6.10. Trilinear cohesive laws used for cohesive elements in skin and core at 23°C-DAM and 23°C-RH50. 106
Fig. 6.11. Load-displacement curves of the subcomponents from experimental tests and coupled FEA until maximum load using the state-of-the-art methodology (*FEA (Tsai-Hill)*) or bilinear cohesive laws (*FEA (CZM skin*) or *FEA (CZM skin-core)*). 108
Fig. 6.12. Load-displacement curves of the subcomponents from experimental tests and coupled FEA until the maximum load using bilinear (*FEA (CZM skin-core)*) and trilinear (*FEA (CZM trilinear)*) cohesive laws. 109
Fig. 6.13. Load-displacement curves of the subcomponents from experiments and coupled FEA including the post-peak behaviour, using different methodologies. 110
Fig. 6.14. Stiffness degradation and deletion of cohesive elements in the coupled FEA combined with CZM at 23°C-DAM: (a) *FEA (CZM skin)* and (b) *FEA (CZM skin-core)*. 111
Fig. 6.15. Stiffness degradation and deletion of cohesive elements in the coupled FEA combined with CZM at 23°C-RH50: (a) *FEA (CZM skin)* and (b) *FEA (CZM skin-core)*. 111

Fig. 6.16. Stiffness degradation and deletion of cohesive elements in the coupled FEA combined with CZM at 60°C-DAM: (a) *FEA (CZM skin)* and (b) *FEA (CZM skin-core)*. 111
Fig. 6.17. Schematic illustration of the sequence of failure identified from the micrographs and coupled FEA combined with CZM at 23°C DAM (yellow arrows: crack propagation by matrix failure/interfacial debonding (observed experimentally); red arrows: crack propagation by shear failure (observed experimentally); white arrows: estimated crack propagation direction; green circles: SEM observation points; dark-orange areas: damaged region). 113

Fig. 7.1. Overall 3D view of the geometry of the component (all dimensions in mm). 123
Fig. 7.2. Location of the injection point, weldline, and mould partition in the component: (a) global view, and (b) zoom-in of the injection point (all dimension in mm).....123
Fig. 7.3. Testing set-up for the components: (a) front view, (b) angled view, and (c) set-up for DIC measurements.....125
Fig. 7.4. Load-displacement curves of PA66-GF50 components. 126
Fig. 7.5. Observation of the two fracture locations in PA66-GF50 components (after failure): *Top-failure* component (left) and *Weld-failure* component (right). 127
Fig. 7.6. Contour of strains obtained from DIC measurements just before a component failed at the top (*Top-failure*): (a) strain along the x-direction, and (b) equivalent strain. 128
Fig. 7.7. Contour of strains obtained from DIC measurement just before a component failed at the weldline (*Weld-failure*): (a) strain along the x-direction, and (b) equivalent strain. 128
Fig. 7.8. Formation of a witness mark due to contact between the loading pin and the component. 130
Fig. 7.9. Load-displacement curves of PA66-GF50 components after correcting for the initial non-linearity (below 0.8 mm). 131
Fig. 7.10. Representative scanning electron micrographs of the fracture surfaces of a component with *Top-failure*: (A) global view; Subfigures (a)-(f) correspond to the regions identified in Subfigure (A). The yellow arrows represent the local direction of crack propagation, identified by matrix fracture morphologies (riverlines). 132
Fig. 7.11. Representative scanning electron micrographs of the fracture surfaces of components with *Weld-failure*. (A) and (B): global views from the two different components; Subfigures (a)-(h) correspond to the regions identified in Subfigure (A). The yellow arrows represent the local direction of crack propagation, identified by matrix fracture morphologies (riverlines).....133
Fig. 7.12. Predicted fibre orientation tensor in the component: (a) on the overall component surface, along the x-direction, (b) local view across the *Top-failure* fracture plane, and (c) local view across the *Weld-failure* fracture plane. 135

Fig. 7.13. Scanning electron micrographs of fracture surfaces at the mid-width of a component with *Top-failure* (same location as Fig. 7.10 (e)). The yellow dotted lines indicate the interface between apparent skin and core layers, with their proportions across the thickness indicated. 136
Fig. 7.14. Partitioning patterns for the fibre orientation states in the Top-failure fracture plane to be used in the coupled FE simulations. 136
Fig. 7.15. FE model of the components. 138
Fig. 7.16. Load-displacement curves of the components from experimental tests and coupled FEA with CZM until the maximum load: (a) *Top-failure*, and (b) *Weld-failure*. 141
Fig. 7.17. Stiffness degradation of the cohesive elements in the coupled FEA combined with CZM at 23°C-DAM: (a) *Top-failure* (*FEA (CZM 5:3:2)*) and (b) *Weld-failure* (*FEA (CZM PA66)*). 142
Fig. 7.18. Schematic illustration of the sequence of failure events, identified from the micrographs and coupled FEA combined with CZM for *Top-failure*. 145
Fig. 7.19. Schematic illustration of the sequence of failure events, identified from the micrographs and coupled FEA combined with CZM for *Weld-failure*. 145

Fig. A.1. Image of virtual testing model (a) used for Compliance Calibration (VTM-CC, described in Appendix A.1, where the relative Y- displacement between the yellow targets is used as dFE to calculate the compliance) and (b) with Cohesive Elements (VTM-CE, described in Appendix B.2). 169

Fig. B.1. Contours of plastic strain energy density (units: J/m^3) from the VTM-CP FE simulations (with 10 layers of elements in the through-the-thickness) at a 0-degree machining angle, under 23°C-DAM: (a) overview of coupon surface, (b)-(f) J-integral area for each element layer in the through-the-thickness direction. 172
Fig. B.2. Contours of plastic strain energy density (units: J/m^3) from the VTM-CP FE simulations (with 10 layers of elements in the through-the-thickness at 0-degree machining angle under 80°C-RH50: (a) overview of coupon surface, (b)-(f) J-integral area for each element layer in the through-the-thickness direction. 172

Fig. C.1. Position to extract the maximum crack opening displacement from DIC results, to calibrate the trilinear cohesive laws used in the FE simulations of the CT coupons. 174
Fig. C.2. Calibrated trilinear cohesive law used in the FE simulations of the CT coupons. 174

Fig. D.1. Load-displacement curves of the subcomponents from *FEA (CZM skin)* model using different numerical parameters: (a) stabilization, (b) number of CE layers and (c) CE thickness; the

maximum load from these predicted curves is shown for different values of (d) stabilization, (e) number of CE layers and (f) CE thickness. 176

List of tables

Table 2.1. Previous work characterising fracture toughness of IM-SFRPs. 32
Table 2.2. Parameters calibrated using reverse engineering option in Digimat. 40
Table 2.3. Details of each term used in the Folger-Tucker equation. 42

Table 3.1. Injection moulding parameters of the plates for coupon testing. 48
Table 3.2. Testing specifications for dog-bone tensile coupons 49
Table 3.3. Testing specifications for dynamic mechanical analysis. 50
Table 3.4. Analysis specifications for differential scanning calorimetry. 51
Table 3.5. Summary of the effect of fibre orientation and environmental conditions on the tensile mechanical properties of PA66-GF50. 53
Table 3.6. 2nd order fibre orientation component in the plate along the loading direction. 53
Table 3.7. Summary of the failure mechanisms of PA66-GF50 dog-bone coupons after tensile testing at 23°C-DAM. 56
Table 3.8. Crystallinity of PA66 with different fibre weight fractions. 56
Table 3.9. Difference in the measured mechanical properties of coupons within equivalent temperature/moisture pairs 58

Table 4.1. Properties of the fibre and matrix used for homogenisation. 63
Table 4.2. Nominal properties used in Digimat's elastic model for parametric studies of matrix moduli and fibre aspect ratios. 64
Table 4.3. Additional properties (to the ones presented in Table 4.2) of the fibre and matrix calibrated for Digimat's elastic-plastic model. 67
Table 4.4. Tensile strength differences between experimentally measured values and predictions using Digimat's elastic-plastic model for PA66-GF50 material. 68

Table 5.1. Testing specifications for CT coupons 76

Table 6.1. Injection moulding parameters for the subcomponents 95
Table 6.2. Testing specifications for PA66-GF50 subcomponents 95
Table 6.3. Averaged maximum load and the standard deviation in the load-displacement curves of subcomponents under five different environmental conditions. 97
Table 6.4. Input properties for bilinear cohesive law used for cohesive elements in skin ($\alpha_{xx} = 0.8$). 106
Table 6.5. Input properties for bilinear cohesive law used for cohesive elements in core ($\alpha_{xx} = 0.2$). 106

Table 6.6. Error of the maximum failure load predicted for the subcomponents by the different FEA methodologies for varied environmental conditions, compared to the average from experiments. 109

Table 7.1. Injection moulding parameters for the components 122
Table 7.2. Testing specification for PA66-GF50 components 125
Table 7.3. Averaged maximum load and their standard deviation of the components tested. 127
Table 7.4. Averaged stiffness calculated from the load-displacement curves of the components at displacements between 0.1-0.2 mm and 0.8-0.9 mm. 129
Table 7.5. Average fibre orientation tensors at the fracture plane in *Top-failure* components, for the two different partitioning patterns shown in Fig. 7.14 137
Table 7.6. Input properties for cohesive elements in *Top-failure* with different partition patterns. 139
Table 7.7. Input properties for cohesive elements in *Weld-failure*. 139
Table 7.8. Error of the maximum failure load predicted for the components by the different FEA methodologies, compared to the average from experiments. 141

Table C.1. Initiation and propagation fracture toughness of PA66-GF50 used in the FE simulations 173

Table D.1. Parameters used in the convergence studies for the FE simulations of subcomponents 175

Acknowledgements

To Soraia Pimenta and Emile S Greenhalgh, my supervisors, for sharing their time, their knowledge, brilliance, and their intensive support throughout my PhD. I feel that I have learnt so much during these past four years, thank you for everything.

To Prof. Bamber Blackman and Dr. Ajit Panesar, who supported me by sharing their expertise and experiences for a wide range of research fields.

To the staff in Mechanical Engineering Department and Aeronautics Department, Dr Ruth Brooker, Mr. Jon Cole, Mr. Gary Senior, Mr. Keith Wolstenholme and Joseph Megyessi, for the technical support and guidance provided during the project.

To my colleagues in meComposites Group, with whom I shared very good moments throughout this PhD project: Dr. Bo Yu, Dr. Mayank Patni, Dr. Dimitrios Bikos, Dr. Marco Alves, Ms. Hwei Linn Khoo, Mr. Xiwen Dai, Mr. Sam Patel, Mr. Wisely Yeung and Nicholas Wilger.

To the members of Asahi Kasei Corporation, Mr. Kazuya Noda, Mr. Osamu Fujii, Mr. Sadahiko Yamaguchi, Mr. Yoshihiro Ashida, Mr. Yuki Mori, Dr. Junichi Takahashi, Mr. Masakazu Kudo, Mr. Kazuya Yada, Mr. Satoshi Noda, Mr. Shunta Kimura and Ms. Aya Hosoi, for their financial and technical supports.

To my family, especially my wife, Nana Fujita, for their incredible supports, motivations and encouragements during this PhD journey. It would not have been possible for me to write this thesis if you were not always there with me.

List of publications

Parts of the work presented in this thesis have been disseminated through a number of written publications and oral communications; these are listed below, as of April 2024.

Peer-reviewed journal publications

[P1] Y. Fujita, S. Noda, J. Takahashi, E. S. Greenhalgh, S. Pimenta, "Initiation and propagation fracture toughness of injection-moulded short fibre composites under different environmental conditions", *Composite Science and Technology*, 233:109891, 2023.

[P2] Y. Fujita, S. Noda, J. Takahashi, E. S. Greenhalgh, S. Pimenta, "Predicting failure in injection-moulded short-fibre subcomponents under varied environmental conditions through fracture mechanics", *Composites Part B: Engineering*, 275:111343, 2024.

[P3] Y. Fujita, W. Yeung, S. Kimura, S. Noda, J. Takahashi, E. S. Greenhalgh, S. Pimenta, "Analysing and predicting progressive failure in injection-moulded short-fibre real components", *Composites Part B: Engineering* (manuscript submitted).

Refereed conference publications

[c1] Y. Fujita, S. Noda, J. Takahashi, E. S. Greenhalgh, S. Pimenta, "Analysing and predicting failure of injection-moulded short-fibre composite components", in *CompTest 2021*, *10th International Conference on Composite Testing and Model Identification* (Fully online conference), 18-20 June 2021 (oral presentation).

[c2] Y. Fujita, S. Noda, J. Takahashi, E. S. Greenhalgh, S. Pimenta, "Analysing and predicting failure of injection-moulded short-fibre composite components", in *ECCM 20*, *20th European Conference on Composite Materials* (Lausanne, Switzerland), 26-30 June 2022 (oral presentation).

[c3] Y. Fujita, S. Noda, J. Takahashi, E. S. Greenhalgh, S. Pimenta, "Failure prediction of injection-moulded short-fibre composites: characterisation and prediction from

coupons to components", in *ICCM 23*, *23rd International Conference on Composite Materials* (Belfast, Ireland), 30 July – 4 August 2023 (poster and oral presentation).

[c4] Y. Fujita, S. Noda, S. Kimura, J. Takahashi, E. S. Greenhalgh, S. Pimenta, "Failure prediction of injection-moulded short-fibre composites: characterisation and prediction from coupons to components", in *Composites2023* (Sicily, Italy), 12-14 September 2023 (oral presentation).

[c5] Y. Fujita, S. Noda, S. Kimura, J. Takahashi, E. S. Greenhalgh, S. Pimenta, "Failure prediction of injection-moulded short-fibre composites: characterisation and prediction from coupons to components", in *JCCM 15*, *15th Japanese Conference on Composite Materials* (Kyoto, Japan), 13-15 March 2024 (oral presentation).

[c6] Y. Fujita, S. Noda, S. Kimura, J. Takahashi, E. S. Greenhalgh, S. Pimenta, "Failure prediction of injection-moulded short-fibre composites: characterisation and prediction from coupons to components", in *ECCM 21*, *21st European Conference on Composite Materials* (Nantes, France), 2-5 July 2024 (oral presentation).

Award

[A1] "Best presentation award", Y. Fujita, S. Noda, S. Kimura, J. Takahashi, E. S. Greenhalgh, S. Pimenta, "Failure prediction of injection-moulded short-fibre composites: characterisation and prediction from coupons to components", in *JCCM 15*, *15th Japanese Conference on Composite Materials* (Kyoto, Japan), 13-15 March 2024 (oral presentation).

Acronyms and Abbreviations

CE	Cohesive Element
coupled FEA	coupled process/structural Finite Element Analysis
CT	Compact Tension
CZM	Cohesive Zone Modelling
DAM	Dry-As-Moulded
DMA	Dynamic Mechanical Analysis
DIC	Digital Image Correlation
DSC	Differential Scanning Calorimetry
FE	Finite Element
FEA	Finite Element Analysis
FOD	Fibre Orientation Distributions
GF	Glass Fibre
HD	HydroDynamic
IM	Injection-Moulded
IRD	Isotropic Rotary Diffusion
MPC	Multi-Point Constraint
MRD	Moldflow Rotational Diffusion
ORW	ORthotropic fitted closure approximation for a Wide range of interaction coefficient values
PA66	Polyamide 6.6
PA66-GF50	Short glass-fibre (fibre weight fraction: 50%) reinforced PA66
RH50	50% Relative Humidity
RSC	Reduced Strain Closure
RVE	Representative Volume Element
SEM	Scanning Electron Microscope
SEN	Single-Edge Notched
SENT	Single-Edge Notched Tension
SFRP	Short-glass Fibre Reinforced thermoPlastic
T-M	Temperature-Moisture
UD	UniDirectional
VTM	Virtual Test Model

Notation

Uppercase Roman Variables

A_r	Aspect ratio	Y	Transverse tensile strength of pseudo-grains
B_i	Scalar constant	$\mathbf{A}$	Second-order fibre orientation tensor
C_DIC	Experimental compliance of CT coupon	$\mathbf{A}^\mathrm{FT}$	Folger-Tucker's second-order fibre orientation tensor
C_FE	Compliance of CT coupon from FE simulation	$\mathbf{A}^\mathrm{HD}$	Hydrodynamic contributor
C_{ij}^UD	UD stiffness tensor	$\mathbf{A}^\mathrm{IRD}$	Isotropic rotary diffusion contributor
C_{ijkl}^3D	Fourth-order stiffness tensor	$\mathbf{A}^\mathrm{MRD}$	MRD's second-order fibre orientation tensor
C_I	Interaction coefficient	$\mathbf{A}^\mathrm{RSC}$	RSC's second-order fibre orientation tensor
E_f	Fibre Young's modulus	$\mathbf{C}, \mathbf{C}^\mathrm{3D}$	Composite stiffness tensor
E_m	Matrix Young's modulus	$\mathbf{C}^\mathrm{f}$	Fibre stiffness tensor
F	Failure index	$\mathbf{C}^\mathrm{m}$	Matrix stiffness tensor
F_critical	User-selected threshold of failure index	$\mathbf{C}^\mathrm{3D}$	Composite stiffness tensor
G	Fracture toughness (or strain energy release rate)	$\mathbf{C}_{i=\{1,\ldots,N\}}$	Stiffness tensor of pseudo-grain i
ΔH_f	Melting enthalpy of PA66	$\mathbf{D}$	Rate-of-deformation tensor
$\Delta H_\mathrm{f^0}$	Melting enthalpy of perfectly-crystalline PA66	$[\mathbf{D}]$	Elastic stiffness matrix
J	J-integral	$\mathbf{E}$	Eshelby tensor
P	Load	$\mathbf{L}$	Velocity gradient tensor
R_∞	Hardening modulus	L_{ij}	Velocity gradient tensor component
$R(p)$	Isotropic strain hardening function	$\mathbf{S}^\mathbf{m}$	Compliance tensor of the matrix
S	In-plane shear strength of pseudo-grains	$\mathbf{W}$	Vorticity tensor
T_g	Glass transition temperature	$\mathbb{A}$	Fourth-order fibre orientation tensor
V_f	Fibre volume fraction	$\mathbb{L}$	Fourth-order eigenvalues tensor of $\mathbf{A}$
X	Longitudinal tensile strength of pseudo-grains	$\mathbb{M}$	Fourth-order eigenvectors tensor of $\mathbf{A}$
X_c	Crystallinity of PA66		

Lowercase Roman variables

a_{ij}	Second-order orientation tensor
a_{ijkl}	Fourth order orientation tensor
Δa	Crack length
Δa_{eq}	Equivalent crack growth
d_{DIC}	DIC opening displacement of CT coupon
d_{FE}	Displacement of CT coupon from FE simulation
e_i	Eigenvectors of second-order orientation tensor
f_i	Failure index of each pseudo-grain
k	Linear hardening modulus
m	Hardening exponent
$\{n\}$	Outward normal to Γ^0
$\mathbf{p}$	Orientation vector of a fibre
p	Equivalent accumulated plastic strain
t	Thickness of coupon
u	DIC displacement
v_{f}	Fibre Poisson's ratio
v_{m}	Matrix Poisson's ratio
w_{f}	Fibre weight fraction
w_i	Weight of each pseudo-grain

Greek variables

$\dot{\gamma}$	Strain rate
δ_{ij}	Kronecker tensor
ε	Strain
ε_{ij}	Average strain in dilute composite
ε_{kl}^{*}	Fibre strain
$\dot{\boldsymbol{\varepsilon}}_{\mathrm{p}}$	Plastic strain rate tensor
ξ	Particle shape parameter
θ	Eulerian angle (with the 3rd axis) of a fibre's direction; machining direction of coupons
κ	Strain reduction factor
λ_i	Eigenvalue of second-order orientation tensor
σ	Stress
σ_{ij}	Stress tensor component
σ_{eq}	von Mises equivalent stress
σ_{Y}	Yield stress
φ	Eulerian angle (in the 1-2 plane) of a fibre's direction
Γ^0	Contour enclosing the crack
$\psi(\mathbf{p})$	Orientation distribution function

Chapter 1 – Introduction

1.1 Background

The market size for lightweight materials has been increasing globally, with revenue forecast of 225.3 billion dollars in 2024 [1]. Polymers and polymer-matrix composites are used as the main materials for lightweighting. The major application of those lightweight materials is in the automotive industries, with around 86% share in terms of revenue [1].

Injection-moulded (IM) short-glass fibre reinforced thermoplastics (SFRPs) [2] have superior manufacturability for complex lightweight geometries, with short production cycles over conventional materials. As IM-SFRP components are usually mass-produced, the volume of SFRPs occupies a high ratio in the industry: about 45% in the European composites market (Fig. 1.1) [3]. The global market of IM automotive parts is expected to increase from 56.4 billion dollars to 84.5 billion dollars between 2022 and 2032 (Fig. 1.2) [4]. As for lightweight materials in general, the main application of IM-SFRPs is in the automotive industries (Fig. 1.3). This demonstrates that IM-SFRPs is an important class of automotive materials, and therefore understanding and enhancing their performance has important benefits to the automotive field.

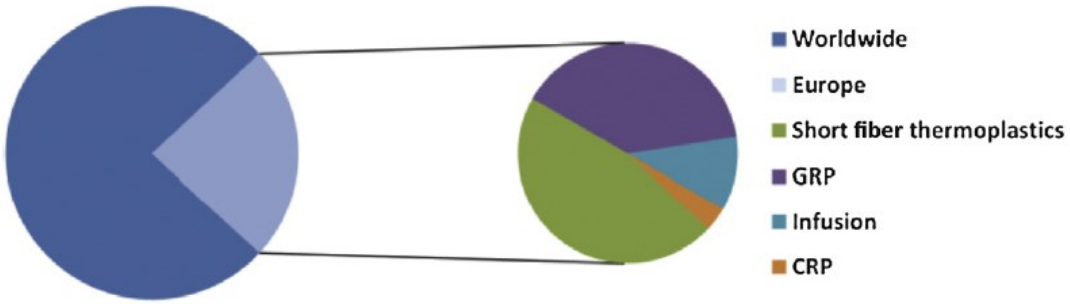


Fig. 1.1. Volume breakdown of the use of different materials in the global composites market [3].

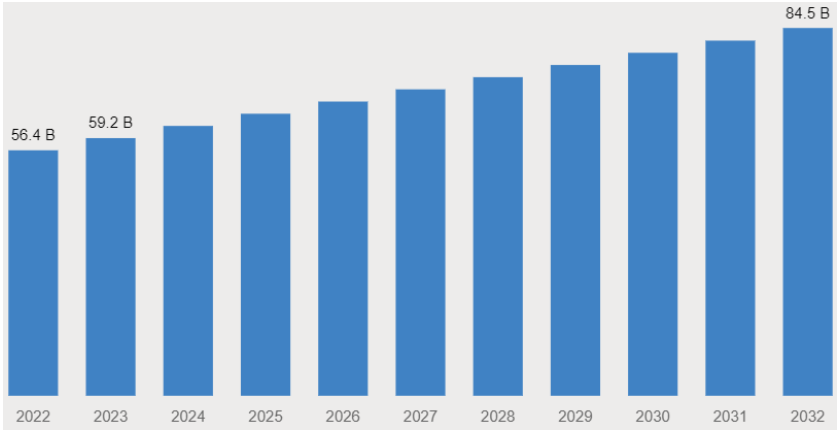


Fig. 1.2. Expectation of global injection moulded automotive parts market between 2022-2032 (in billion dollars) [4].

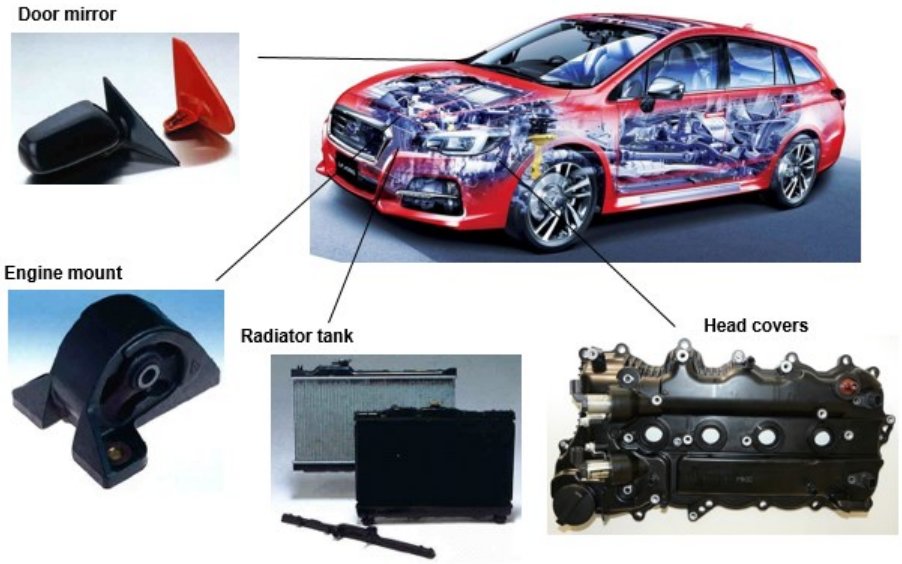


Fig. 1.3. Examples of the application of IM-SFRPs in automotive (provided by Asahi Kasei Corporation).

When designing IM-SFRP components using Finite Element (FE) simulations, it is necessary to predict their ultimate load-bearing capability and post-failure behaviour. Unfortunately, criteria to predict the maximum failure load of IM-SFRPs are not well established: the existing failure criteria for IM-SFRPs (e.g., based on Tsai-Hill criterion [5], as reviewed in Chapter 2) consider failure initiation only, and therefore often under-predict the ultimate failure load in components. This leads to overly conservative design, and hence excessively heavy and costly components in industry.

One of the most widely used IM-SFRP materials in the automotive field are polyamide 6.6 (PA66)-based composites, reinforced with short (200-400 µm long) glass fibres (GF). These PA66-

based materials can be used for a wide range of applications, not only for exterior parts, but also for the interior and around the engine. A short glass-fibre (fibre weight fraction: 50%; fibre volume fraction: 31%) reinforced PA66 ("PA66-GF50") is one of the main products from Asahi Kasei Corporation, which is an international supplier of these PA66-based IM-SFRP materials (with headquarters in Japan). The PA66-GF50 material is especially used for application where a high load is applied (e.g. in engine mounts). Therefore, it is important to understand the fracture behaviour of PA66-GF50, and reflect it in the design of components.

1.2 Objectives

This thesis reports on the development of an in-depth understanding and characterisation of the fracture behaviour of IM-SFRPs, and the development of a FE simulation methodology to predict failure of IM-SFRP materials based on experimentally measured material properties, from the coupon level to the component level as shown in Fig. 1.4. This required the following challenges to be addressed:

- To characterise the fracture toughness of a PA66-GF50 material at coupon level, under the combined effect of fibre orientation, service temperature and moisture content;
- To develop a new FE simulation methodology to predict failure of a (sub)component, considering the material's progressive failure, based on the fracture toughness experimentally measured at the coupon level;
- To validate the newly developed FE simulation methodology under different environmental conditions, to investigate the robustness of the methodology;
- To deduce the damage mechanisms of the IM- PA66-GF50 (sub)components using fractographic analysis, and contrast that analysis with the FE results to provide a more comprehensive understanding of the sequence of failure events.

Chapter 2 reviews the current state-of-the-art literature about the characterisations and FE simulation methodologies for IM-SFRPs. The structure of this thesis is then outlined at the end of Chapter 2 (in Section 2.8).

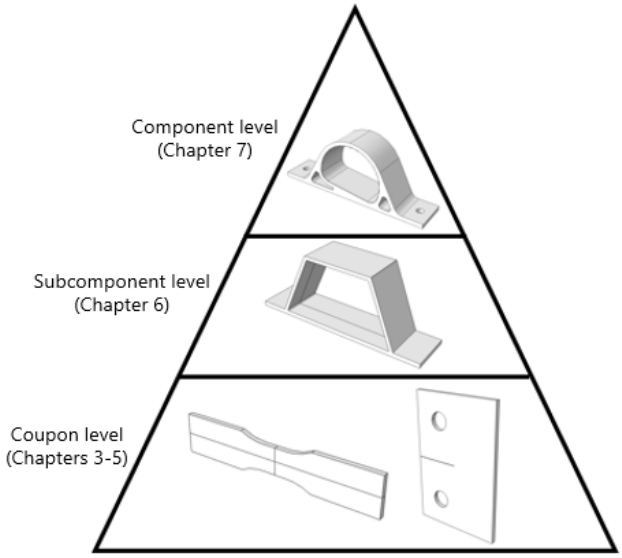


Fig. 1.4. Testing pyramid of IM-SFRP coupons, subcomponents and components used in this thesis.

Chapter 2 - Literature review

This Chapter reviews the current state-of-the-art literature about the experimental characterisation and FE simulation of IM-SFRPs. The background knowledge and techniques reviewed in this Chapter 2 are used in the subsequent Chapters.

Section 2.1 presents the microstructures of IM-SFRPs and the methods used to characterise it. Section 2.2 describes the characterisation of mechanical properties of composites at coupon level, including tensile tests using dogbone coupons and their application to IM-SFRPs, and fracture toughness tests using different test and data reduction methods. General background of fractography for the characterisation of damage mechanisms of IM-SFRPs is explained in Section 2.3. The state-of-the-art material models used for the coupled process/structural FE simulation of IM-SFRPs, considering their anisotropy and non-linearity, are detailed in Section 2.4. Fibre orientation models, which are available in commercial injection-moulding process simulation software, to predict the fibre orientation fields in IM-SFRPs are reviewed in Sections 2.5. Section 2.6 describes the methodology of the coupled process/structural FE simulations through the commercial software Digimat. The fundamentals of cohesive zone modelling are reviewed in Section 2.7, as they are used to consider the material's progressive failure in coupled process/structural FE simulations . Finally, the structure of this thesis is outlined in Section 2.8.

2.1 Microstructure of IM-SFRPs

The injection-moulding process of IM-SFRPs creates a core-shell structure in the composite with complex fibre orientation states: the fibres align along the flow direction near the mould surfaces (i.e. in the "shells"), and along the transverse direction or randomly in the "core" [6]. This anisotropy and heterogeneous microstructure complicates the mechanical characterisation and design of IM-SFRP materials and components.

The anisotropy of the microstructure of IM-SFRPs can be characterised by probabilistic fibre orientation distributions (FOD) in the 3D space. The spatial orientation of a fibre is defined using its orientation vector $\mathbf{p}$, with its Cartesian components on a generic {1,2,3} coordinate system defined as [7]

$$\begin{aligned} \mathbf{p}_1 &= \sin\theta\cos\varphi\,, \\ \mathbf{p}_2 &= \sin\theta\sin\varphi\,, \\ \mathbf{p}_3 &= \cos\theta\,, \end{aligned} \tag{2.1}$$

where θ and φ are the Eulerian angles, defined in Fig. 2.1. For a group of fibres, the components of the second-order orientation tensor proposed by Advani and Tucker [7], a_{ij}, are calculated as follows (where the angled brackets $\langle\chi\rangle$ represent the average of χ over all fibres):

$$\mathbf{A} = a_{ij} = \langle \mathbf{p}_i \mathbf{p}_j \rangle = \begin{bmatrix} \langle \sin^2\theta\cos^2\varphi \rangle & \langle \sin^2\theta\cos\varphi\sin\varphi \rangle & \langle \sin\theta\cos\theta\cos\varphi \rangle \\ \langle \sin^2\theta\cos\varphi\sin\varphi \rangle & \langle \sin^2\theta\sin^2\varphi \rangle & \langle \sin\theta\cos\theta\sin\varphi \rangle \\ \langle \sin\theta\cos\theta\cos\varphi \rangle & \langle \sin\theta\cos\theta\sin\varphi \rangle & \langle \cos^2\theta \rangle \end{bmatrix}. \tag{2.2}$$

The examples of the description of a_{ij} are shown in Fig. 2.2.

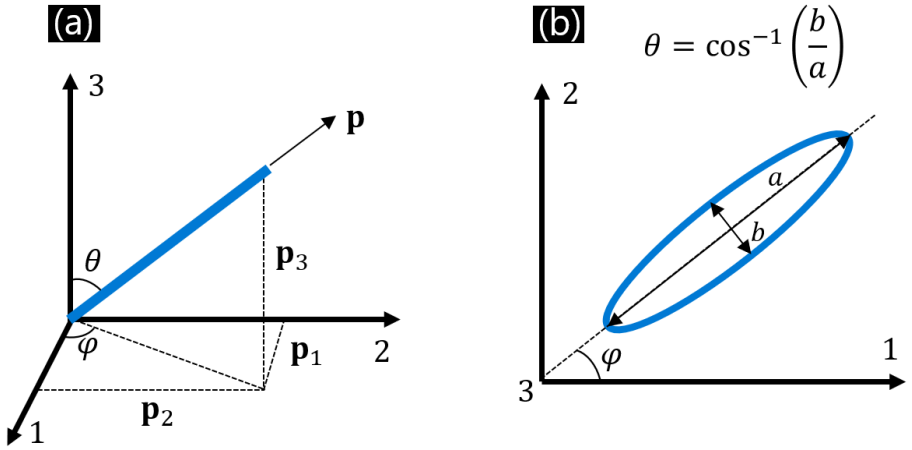
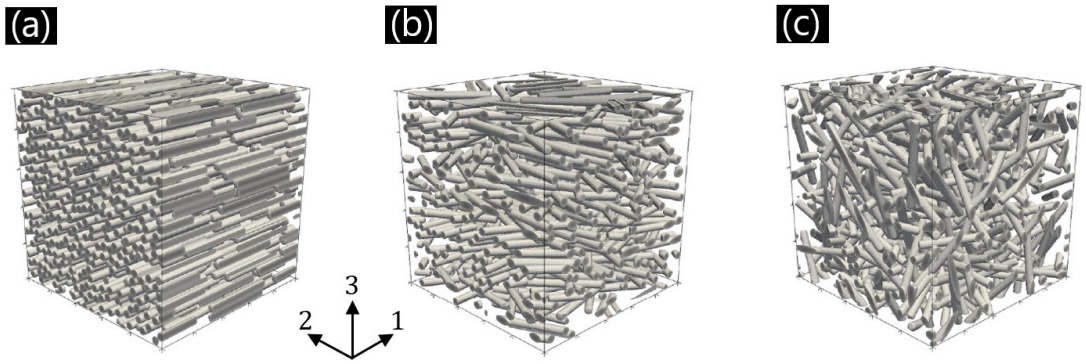


Fig. 2.1. Definition of (a) coordinate system and Eulerian angles of a fibre's direction (represented by its main axis), and (b) elliptical section in the 1-2 plane of a fibre with circular cross-section and diameter b [7].



$$a_{ij} = \begin{bmatrix} 1 & 0 & 0 \\ 0 & 0 & 0 \\ 0 & 0 & 0 \end{bmatrix} \qquad a_{ij} = \begin{bmatrix} 0.5 & 0 & 0 \\ 0 & 0.5 & 0 \\ 0 & 0 & 0 \end{bmatrix} \qquad a_{ij} = \begin{bmatrix} 0.33 & 0 & 0 \\ 0 & 0.33 & 0 \\ 0 & 0 & 0.33 \end{bmatrix}$$

Fig. 2.2. Examples of the description of fibre orientation tensor: (a) unidirectional alignment along 1-axis, (b) perfectly random in 2D, and (c) perfectly random in 3D [8].

Experimental measurement of the FOD is necessary for the characterisation of the composite microstructure. The method of ellipses [9], which uses optical images of a polished sample to reveal the elliptical cross sections of inclined fibres on the image plane, has been widely used previously. The angles θ and φ (in Fig. 2.1) are obtained from fitted ellipses to the fibre apparent section, to calculate a_{ij}. Though this method is unable to provide the 3D orientation unambiguously [10], it remains the most preferred method for FOD measurements in industry due to the advantages of simplicity and low cost.

The FOD plays a vital role on the local mechanical properties of the composite. Advani and Tucker [7] proposed to determine the components of the fourth-order stiffness tensor $< C_{ijkl}^{3D} >$ for any given fibre orientation state, expressed as

$$C_{ijkl}^{3D} = B_1 a_{ijkl} + B_2\left(a_{ij}\delta_{kl}\right) + B_3\left(a_{ik}\delta_{jl} + a_{il}\delta_{jk} + a_{jl}\delta_{ik} + a_{jk}\delta_{il}\right) + B_4\left(\delta_{ij}\delta_{kl} + B_5\left(\delta_{ik}\delta_{jl} + \delta_{il}\delta_{jk}\right)\right) \quad (2.3)$$

where a_{ijkl} is the fourth order fibre orientation tensor,

$$a_{ijkl} = \oint p_i p_j p_k p_l \, \mathrm{d}\psi(\mathbf{p}), \quad (2.4)$$

δ_{ij} is the Kronecker tensor, and B_i are scalar constants related to the components of the UD stiffness tensor C_{ij}^{UD}, expressed as

$$\begin{aligned} &B_1 = C_{11}^{\mathrm{UD}} + C_{22}^{\mathrm{UD}} - 2C_{12}^{\mathrm{UD}} - 4C_{66}^{\mathrm{UD}}, B_2 = C_{12}^{\mathrm{UD}} + C_{22}^{\mathrm{UD}}, \\ &B_3 = C_{66}^{\mathrm{UD}} + \frac{1}{2(C_{23}^{\mathrm{UD}} - C_{22}^{\mathrm{UD}})}, B_4 = C_{23}^{\mathrm{UD}}, B_5 = \frac{1}{2(C_{22}^{\mathrm{UD}} - C_{23}^{\mathrm{UD}})}. \end{aligned} \quad (2.5)$$

In this theory, it is assumed that the composite stiffness tensor is taken as the average of the UD composite stiffness tensor over all fibre directions, weighted by the orientation distribution function $\psi(\mathbf{p})$, with a unit vector $\mathbf{p}$. The fourth-order tensor can be estimated from the second-order tensor by applying the orthotropic closure approximation presented by Cintra and Tucker [11]. Chung and Kwon [12] improved the model for the use with a wide range of fibre-fibre interaction coefficients, which is called '*orthotropic fitted closure approximation for a wide range of interaction coefficient values* (ORW)'. This orthotropic closure gives the most accurate approximation when compared to experimental results [13]; therefore, this approximation is commonly used in the commercial software in IM-SFRP field.

2.2 Characterisation at coupon scale

The effect of fibre orientation on the tensile modulus and strength of IM-SFRPs has been characterised experimentally [14–17], by testing dog-bone shaped coupons machined from injection moulded plates at several angles with respect to the main flow (and preferential fibre-orientation) direction. The angle-dependent tensile strengths and elastic moduli decreased with increasing machining angle (and increasing angle between the loading direction and the preferential fibre orientation), due to the anisotropic fibre orientation.

Although the fracture toughness (or critical strain energy release rate) governs failure in structures with complex geometries, its characterisation for IM-SFRPs has been overlooked. There are only a few papers characterising the anisotropy of the fracture toughness of IM-SFRPs, and they are limited to testing under room temperature and dry conditions [18,19]. The measured initiation fracture toughness was highest for fracture across the main flow (and preferential fibre) direction, decreased with increasing machining angle, and reached a minimum for fracture along the main flow direction.

The fracture toughness of SFRPs has been characterised using several different methods as summarised in Table 2.1. In all cases, the fracture toughness measured corresponds to either an 'initiation', a 'peak-load', or an 'average' value; the full R-curve (which characterises the change in fracture toughness as a crack propagates) or its steady-state "propagation" value have never been measured for IM-SFRPs.

Table 2.1. Previous work characterising fracture toughness of IM-SFRPs.

Test methods	Obtained fracture toughness
Single-edge notch (SEN) three-point bending test [18,20,21]	Initiation
SEN impact test [22,23]	Average
Single edge notched tension (SENT) test [24]	Initiation
Charpy test [19,25–29]	Average
Compact Tension (CT) tests [19,30–33]	Initiation

The full R-curve has been characterised for continuous and discontinuous fibre-reinforced thermoset composites using compact tension (CT) tests [34–36]. In fibre-reinforced composites, the propagation fracture toughness is often considerably higher than that at initiation [34,35]; therefore, using only the initiation fracture toughness may lead to an under-estimation of the damage tolerance of the material and hence over-designed components. One of the simplest data reduction methods to calculate the full R-curve from CT tests is based on FE-supported

compliance calibration [34,35]; however, this method assumes that the material is linear-elastic. Alternatively, the J-integral method proposed by Becker et al. [37], which uses full-field measurements from Digital Image Correlation (DIC), is valid for nonlinear materials (as it is characteristic of IM-SFRPs), as long as the contour for the calculation of the J-integral fully encloses the nonlinear zone around the crack tip. Li et al. [38] proved that the J-integral can be characterised either with a line contour or an area contour around the crack tip.

Environmental conditions such as temperature and moisture content also influence the mechanical properties of many SFRPs, particularly with PA66 matrices. At the dog-bone coupon level, the tensile strength and elastic modulus decrease while the strain to failure increases with an increase in temperature and moisture content [14,15,39–42]. However, for the fracture toughness of SFRPs measured under quasi-static remote loading, environmental effects have been reported by only a few researchers [20,21,32], who concluded that a higher moisture level or temperature leads to higher fracture toughness (although they only focused on a single fibre-orientation state). The effect of environmental conditions (combined temperature and moisture) on the fracture toughness of SFRPs has also been reported under impact conditions [27–29,33], although no R-curve effects were reported.

The mechanical performance of IM-SFRPs is also influenced by weldlines, which are surfaces formed at the confluence of the molten composite during the moulding process. The presence of weldlines causes the deterioration of the mechanical properties of IM-SFRPs due to several reasons: (i) the fibre orientation becomes mostly parallel to the weldline, (ii) there is a lower fibre volume fraction locally, and there is presence of (iii) air voids, (iv) insufficient molecular interdiffusion, and (iv) poor bonding [43–47]. Baradi et al. [45,46] evaluated the void contents at the weldline; they concluded that the void formation is nearly unavoidable without using ventilation channels. Nevertheless, weldline effects can be minimised by optimising the injection-moulding parameters and the mould design, and consequently, moving weldlines to less-loaded regions of the component [48,49].

Another possible helpful tool to design IM-SFRP components is the concept of temperature-moisture (T-M) equivalence [50–52]. This assumes that, for example, an increase in temperature affects mechanical properties in a way equivalent to that of an increase in water content. This equivalence is because the glass transition temperature (T_g) of polymer-based materials shifts to a lower temperature when water is absorbed. The concept of T-M equivalence may reduce

the amount of material characterisation needed. Some researchers have verified the T-M equivalence for IM-thermoplastics and IM-SFRPs, for the elastic modulus and tensile strength [50–52]; however, the concept of T-M equivalence has not been investigated for the fracture toughness or for any aspects of the mechanical behaviour at the subcomponent/component level.

2.3 Fractography and fracture mechanisms

Fractography [53], which is the inspection and interpretation of fracture surfaces to deduce crack modes and growth directions, is a helpful technique to characterise composite materials. It has been used to identify the damage mechanisms governing failure of IM-SFRPs and their relationship with the material properties measured and the observed macroscopic behaviour of structures [20,32,53]. For instance, Ibanez-Gutierrez et al. [20] used fractography to identify a relationship between debonding of the matrix-fibre interface and the effect of moisture in the initiation fracture toughness of an IM-SFRP composite. However, the use of fractography for IM-SFRPs has been limited to the coupon level only [20,32]; no paper has applied fractography to identify the damage mechanisms of IM-SFRP components.

Properties and damage mechanisms of IM-SFRPs are significantly affected by environmental conditions (e.g., service temperature and moisture content), as demonstrated by the literature at a coupon level: their strength and elastic modulus decrease whilst the strain to failure and the fracture toughness increase with an increase in temperature and/or moisture content [14,15,20,21,32,39–42]. Therefore, this needs to be considered at component level as well.

Moreover, there is no literature on combining the characterisation of damage mechanisms with the prediction (e.g. using FE simulations) of sequence of failure events for IM-SFRPs at subcomponent/component level. Components are more challenging than coupons because they have more complex and non-uniform microstructure across the whole geometry, and typically combine different damage mechanisms in a complex sequence of failure events.

2.4 State-of-the-art models for IM-SFRP materials

This Section reviews predictive material models for discontinuous composites. These are micromechanical models that take the geometric and elastic properties of the fibres (Young's

modulus, E_{f}, Poisson's ratio, υ_{f}, and aspect ratio, A_{r}), the elastic (Young's modulus, E_{m}, and Poisson's ratio, υ_{m}) and elasto-plastic properties of the matrix, and the morphology of the composite (i.e. fibre volume fraction, V_{f}, and the FOD for IM-SFRPs). These models output the local homogenised (at the micromechanical fibre-matrix scale) properties of the composite, from the elastic to non-linear response and up to failure.

The Digimat software [5] includes native micromechanical models which are used as the state-of-the-art methodology for coupled process/structural simulations of IM-SFRP materials and applications (as detailed in Section 2.6); this uses the Mori-Tanaka micromechanical theory for homogenisation of fibres and matrix, followed by a pseudo-grains approach (described in Section 2.4.1). Although there are many other models in the literature (as reviewed by Tucker and Liang [54], Ghossein and Lévesque [55], Raju et al. [56] and Sertse et al. [57]), this thesis focuses on the material model available in Digimat for the following reasons:

(i) Its Mori-Tanaka foundation provides accurate predictions of the elastic response of SFRPs [54];
(ii) Digimat provides automatic mapping of fibre orientation fields predicted by process simulations onto an FE model (as detailed in Section 2.6);
(iii) All the analysis (including calibration of the material model using experimental data, coupling with process simulations, and submission of the FE simulation) can be done on a single GUI;
(iv) It is used for real applications in industrial settings (by companies such as Asahi Kasei, Solvay [58], Vibracoustic [59], Bosch [60], Volkswagen [61], TOYOTA [62], etc).

2.4.1 Two-step pseudo-grain approach for short fibre composites

IM-SFRPs have non-perfectly oriented fibres (i.e. they are not a lamina layer with perfectly aligned fibres) whose orientation can be characterised by FODs, and may also have a distribution of aspect ratios or even stiffness constants. Therefore, it is essential to have a material homogenisation model that can account for these distributions. The state-of-the-art model (implemented in Digimat) uses the pseudo-grain approach, which is based on a two-step homogenisation as shown in Fig. 2.3 [5,63].

Consider a general case where a matrix is reinforced with $i = \{1, \dots, N\}$ families of fibres, where each family i has the same stiffness constants, aspect ratio and orientation unit vector $\mathbf{p}$. Each family of fibres is aggregated in a "pseudo-grain", and the aggregate of pseudo-grains is analysed through a two-step homogenization procedure as follows:

- **First step**: Each pseudo-grain (defined as a bi-phase unidirectional composite consisting of a matrix reinforced with identical and aligned ellipsoidal fibres) is analysed through Mori-Tanaka mean-field homogenisation (as described in Sections 2.4.2-2.4.3), which outputs the (tangent) stiffness matrix $\mathbf{C}_{i=\{1,\dots,N\}}$ of each pseudo-grain.

- **Second step**: After the homogenisation in the first step, an representative volume element (RVE) with all pseudo-grains is treated as an aggregate, and this aggregate is homogenised over all grains, using weights depending on statistical fibre distributions, e.g. $\psi(\mathbf{p})$. This second homogenisation step calculates the overall (tangent) stiffness tensor of the whole using Voigt mean field homogenisation (i.e. assuming iso-strains).

Material models available in Digimat software are based on this two-step homogenisation using orientation averaging [7] and Mori-Tanaka/Voigt mean-field homogenisation [64]. Digimat's material model can be calibrated based on this homogenisation procedure using Digimat-MX [5], with the mechanical properties obtained by testing dog-bone coupons under several machining angles, thus accounting for the anisotropy (as detailed in Section 2.4.5).

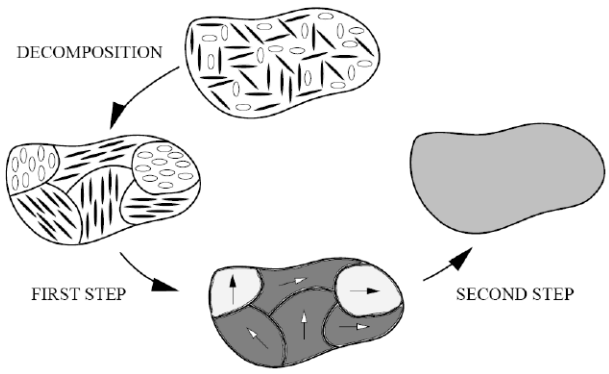


Fig. 2.3. Two-step homogenisation procedure for a composite with misaligned inclusions [5,63]. Top: real RVE. Left: decomposition into an aggregate of pseudo-grains. Bottom: homogenisation of each pseudo-grain (first step). Right: homogenisation of the aggregate of homogenised pseudo-grains (second step).

2.4.2 Elastic response of aligned short fibre composites

The first step in the elastic material model used in Digimat aims to predict the stiffness matrix of a discontinuous composite with all fibres aligned along the loading direction. This model is based on Mori-Tanaka's mean-field homogenisation, which is itself based on Eshelby's theory, as described next.

Eshelby solved for the elastic stress field in and around an ellipsoidal fibre in an infinite matrix [65], and predicts the stiffness matrix of a composite with ellipsoidal fibres at dilute concentrations. This model uses mean-field homogenisation, and assumes that the average strain in the dilute composite (ε_{ij}) is the same as the remotely applied strain; for ellipsoidal fibres, the fibre strain (ε^*_{kl}) is uniform. Consider that $\boldsymbol{C}^{\mathrm{f}}$ and $\boldsymbol{C}^{\mathrm{m}}$ are the stiffness tensor of the fibre and the matrix, and $\mathbf{S^m}$ is the compliance tensor of the matrix (note that the stiffness and compliance tensor depend on the Young's modulus, shear modulus and Poisson ratio [66]); the composite stiffness matrix $\mathbf{C}$ can be calculated as

$$\mathbf{C} = \mathbf{C^m} + V_{\mathrm{f}}\left(\mathbf{C^f} - \mathbf{C^m}\right)\mathbf{A}^{\mathrm{Eshelby}}, \tag{2.6}$$

where $\mathbf{A}^{\mathrm{Eshelby}}$ is the strain-concentration tensor based on Eshelby's theory, calculated as

$$\mathbf{A}^{\mathrm{Eshelby}} = \left[\mathbf{I} + \mathbf{E}\mathbf{S^m}\left(\mathbf{C^f} - \mathbf{C^m}\right)\right]^{-1}, \tag{2.7}$$

where $\mathbf{E}$ is the Eshelby tensor, which has been defined elsewhere [67]; for an isotropic fibre with ellipsoidal geometry, $\mathbf{E}$ depends only on the fibre aspect ratio and Poisson's ratio.

Mori and Tanaka originally proposed a mean-field homogenisation method for the stiffness matrix of non-dilute composites [64], which was then reformulated by Benveniste [68] in a simpler and clearer explanation. Mori-Tanaka's version of the strain-concentration tensor $\mathbf{A}^{\mathrm{MT}}$ is given as

$$\mathbf{A}^{\mathrm{MT}} = \mathbf{A}^{\mathrm{Eshelby}}\left[(1 - V_{\mathrm{f}})\mathbf{I} + V_{\mathrm{f}}\mathbf{A}^{\mathrm{Eshelby}}\right]^{-1} \tag{2.8}$$

The composite stiffness matrix can be calculated by replacing $\mathbf{A}^{\mathrm{Eshelby}}$ with $\mathbf{A}^{\mathrm{MT}}$. The Mori-Tanaka model is successful in predicting the effective elastic properties of two-phase composites with aligned fibres (i.e. of a pseudo-grain); it can be combined with orientation averaging (as explained in Section 2.1) to predict the elastic properties of a composite with a fibre orientation distribution (i.e. for an RVE of aggregated pseudo-grains) [54].

2.4.3 Digimat's elastic-plastic material model for the matrix

In Digimat, the non-linear response of IM-SFRPs is modelled applying the J_2-plasticity theory to the matrix [5], based on the von Mises equivalent stress (σ_{eq}), defined as

$$\sigma_{\mathrm{eq}} = \sqrt{3J_2} = \sqrt{\frac{(\sigma_{11} - \sigma_{22})^2 + (\sigma_{22} - \sigma_{33})^2 + (\sigma_{33} - \sigma_{11})^2 + 6(\sigma_{12}^2 + \sigma_{23}^2 + \sigma_{31}^2)}{2}}, \quad (2.9)$$

where σ_{ij} represents the components of the stress tensor of the matrix in a generic coordinate system. When σ_{eq} exceeds the matrix yield stress (σ_{Y}), the matrix response becomes nonlinear and plastic deformation appears, expressed as follows:

$$\sigma_{\mathrm{eq}} = \sigma_{\mathrm{Y}} + R(p), \quad (2.10)$$

where σ_{Y} is the initial yield stress; $R(p)$ is the isotropic strain hardening function; and p is the equivalent accumulated (over the entire loading period $\tau = [0, t]$) plastic strain, calculated as

$$p = \int_0^t \dot{p}(\tau)\mathrm{d}\tau, \quad (2.11)$$

which depends on the plastic strain rate tensor $\dot{\boldsymbol{\varepsilon}}_{\mathrm{p}}$ by

$$\dot{p} = \sqrt{\frac{2}{3}\dot{\boldsymbol{\varepsilon}}_{\mathrm{p}} : \dot{\boldsymbol{\varepsilon}}_{\mathrm{p}}}\,. \quad (2.12)$$

The isotropic strain hardening function can be modelled using a combination of exponential and linear laws as follows:

$$R(p) = kp + R_{\infty}[1 - \mathrm{e}^{-mp}], \quad (2.13)$$

where k is the linear hardening modulus, m is the hardening exponent, and R_{∞} is the hardening modulus, all of which are material parameters of the matrix which can be calibrated from experimental stress-strain curves of the SFRP (as explained in Section 2.4.5). Note that all four parameters for plasticity (k, m, R_{∞} and σ_{Y}) are applied for matrix level.

In this model, an applied external load is redistributed over the pseudo-grains, so that each pseudo-grain has a particular stress-strain response depending on its fibre orientation state. To compute the global stress-strain response from these pseudo-grains, the two-step homogenisation described in Section 2.4.1 is applied for this model as well, using Mori-Tanaka homogenisation to calculate the tangent stiffness matrix of each pseudo-grain (as described in Section 2.4.1), followed by Voigt's homogenization assuming iso-strain amongst all pseudo-grains.

2.4.4 Failure criteria for injection-moulded short-fibre composites

Failure criteria are used to predict the failure point of a material that is subjected to loads. One of the failure criteria available for IM-SFRPs is the Tsai-Hill 3D transversely-isotropic failure criterion [5], which is integrated into the Digimat software, defined as:

$$f_A = \sqrt{F_A(\sigma)} \tag{2.14}$$

$$F_A(\sigma) = \frac{\sigma_{11}^2}{X^2} - \frac{\sigma_{11}(\sigma_{22} + \sigma_{33})}{X^2} + \frac{\sigma_{22}^2 + \sigma_{33}^2}{Y^2} + \left(\frac{1}{X^2} - \frac{2}{Y^2}\right)\sigma_{22}\sigma_{33} + \frac{\sigma_{12}^2 + \sigma_{13}^2}{S^2} + \left(\frac{4}{Y^2} - \frac{1}{X^2}\right)\sigma_{23}^2, \tag{2.15}$$

where X is the longitudinal tensile strength, Y is the transverse tensile strength, and S is the in-plane shear strength of unidirectional pseudo-grains. These three parameters X, Y and S can be calibrated using the automatic "Reverse engineering" option in Digimat-MX, as described in Section 2.4.5. This criterion assumes the material to be isotropic in the 2-3 plane, and identical failure conditions for tension and compression (which is consistent with the plasticity model described in the previous subsection).

For each increment during the coupled FE simulations, the Digimat material model computes the failure index f_i (according to Tsai-Hill's criterion) separately for each individual unidirectional pseudo-grain (after the first step of the two-step homogenisation procedure mentioned in Section 2.4.1), at each integration point (where each integration point is assumed to have N pseudo-grains, with $i = \{1, \dots, N\}$); the weight of each pseudo-grain (w_i) is defined according to the local fibre orientation distribution $\psi(\mathbf{p})$ predicted by the process simulation [69]. The weighted average value of the failure criterion (*PGC*) is calculated as

$$F = \frac{\sum_{i=1}^{N} w_i f_i}{F_{\text{critical}}}, \tag{2.16}$$

where f_i is equal to the failure criterion computed for pseudo-grain i, and F_{critical} is a user-selected threshold (by default set at 0.95). The FE simulations output the field of F at each increment of the coupled FEA, and failure is assumed to occur when F reaches 1.

2.4.5 Calibration of material properties using Digimat

The parameters used for Digimat's material model can be calibrated based on the 2-steps homogenisation process described in Section 2.4.1. In this methodology, the properties are determined using the 'reverse engineering' option available in Digimat-MX [5]. This reverse

engineering calculates the parameters which minimise the sum of squared differences between the Digimat's computed elastic, plastic and failure properties and the experimental properties obtained by testing dog-bone coupons under several machining angles (e.g. 0, 45 and 90°), thus accounting for the anisotropy. The properties calibrated using the reverse engineering option are summarised in Table 2.2.

To consider the effect of fibre orientation in the calibration process, fibre orientation tensor components (i.e. α_{11}, α_{22}, α_{33}, α_{12}, α_{13}, α_{23}, defined in Fig. 2.1) are also required as inputs for the calibration of material models in Digimat-MX. Moreover, there are options to consider a RVE through either (i) a single-layer analysis with fibre orientation tensors homogenised through the thickness (i.e. aggregating the skin-core-skin microstructure which is typical of IM-SFRPs, as discussed in Section 2.1), or (ii) a multilayer analysis with the actual distribution of fibre orientation tensors (e.g. considering the skin-core-skin microstructure). To calibrate the properties in Digimat, a mechanical loading is applied to a RVE having the parameters summarised in Table 2.2, while accounting for the user-provided inputs defining the fibre orientation tensor; therefore, this process can capture the effect of machining angle in coupons and the anisotropy of mechanical properties in general.

Table 2.2. Parameters calibrated using reverse engineering option in Digimat.

	Properties
Elasticity	Fibre Young's modulus (E_{f})
	Fibre Poisson's ratio (υ_{f})
	Fibre aspect ratio (A_{r})
	Matrix Young's modulus (E_{m})
	Matrix Poisson's ratio (υ_{m})
Plasticity	Matrix yield stress (σ_{Y})
	Matrix linear hardening modulus (k)
	Matrix hardening modulus (R_{∞})
	Matrix hardening exponent (m)
Failure	Pseudo-grain longitudinal tensile strength (X)
	Pseudo-grain transverse tensile strength (Y)
	Pseudo-grain in-plane shear strength (S)

2.5 Fibre orientation models in injection-moulding process simulation

Moldflow software [69], which is a state-of-the-art injection moulding process simulation software, has three models to predict fibre orientation fields in IM-SFRPs. These three fibre orientation models are based on Jeffery's theory [70] for the motion of a single fibre in an infinite

Newtonian matrix, which calculates the rate of change of the 2nd order fibre orientation tensor $\dot{\mathbf{A}}$ (described in Section 2.1). These models are reviewed in this Section, and used in Chapter 4 to investigate their accuracy further and identify which will be used in the subsequent Chapters.

2.5.1 Folger-Tucker model

Jeffery's theory [70] considers the motion of a single fibre only. Therefore, Folger and Tucker [71] developed a fibre orientation model accounting for fibre-fibre interactions, by introducing an isotropic rotary diffusion term into the Jeffery's theory. This Folgar–Tucker equation involves two terms: (i) the Jeffery's hydrodynamic (HD) contributor ($\dot{\mathbf{A}}^{\mathrm{HD}}$), and (ii) the isotropic rotary diffusion (IRD) contributor ($\dot{\mathbf{A}}^{\mathrm{IRD}}$), expressed as

$$\dot{\mathbf{A}}^{\mathrm{FT}} = \dot{\mathbf{A}}^{\mathrm{HD}} + \dot{\mathbf{A}}^{\mathrm{IRD}}, \quad \text{where} \tag{2.17}$$

$$\dot{\mathbf{A}}^{\mathrm{HD}} = (\mathbf{W}\cdot\mathbf{A} - \mathbf{A}\cdot\mathbf{W}) + \xi(\mathbf{D}\cdot\mathbf{A} + \mathbf{A}\cdot\mathbf{D} - 2\mathbb{A}:\mathbf{D}) \quad \text{and} \tag{2.18}$$

$$\dot{\mathbf{A}}^{\mathrm{IRD}} = 2C_I\dot{\gamma}(\mathbf{I} - 3\mathbf{A}). \tag{2.19}$$

An explanation of each term is summarised in Table 2.3. This model is able to consider fibre-fibre interactions through the IRD term; however, it neglects the effect of fibre directions on the level of the fibre-fibre interactions (i.e. isotropic rotary diffusion). Although Folgar–Tucker model provided great progress in this field, some literature mentions that this model leads to inaccurate predictions due to a faster fibre orientation kinetics than experiments [72,73].

Table 2.3. Details of each term used in the Folger-Tucker equation.

Parameters	Equations
Velocity gradient tensor	$\mathbf{L} = \nabla\mathbf{v} = \mathbf{W} + \mathbf{D}$
Velocity gradient tensor components	$L_{ij} = \nabla_j v_i$
Vorticity tensor	$\mathbf{W} = \frac{1}{2}(\mathbf{L} - \mathbf{L}^T)$
Rate-of-deformation tensor	$\mathbf{D} = \frac{1}{2}(\mathbf{L} + \mathbf{L}^T)$
Strain rate	$\dot{\gamma} = (2\mathbf{D} : \mathbf{D})^{1/2}$
Particle shape parameter	$\xi = (A_r^2 - 1)/(A_r^2 + 1)$
Interaction coefficient	C_I
Fibre aspect ratio (material dependent)	A_r
4th-order closure approximation (Section 2.1)	$\mathbb{A} = f(\mathbf{A})$

2.5.2 Reduced Strain Closure model

To slow down the fibre kinetics in Folgar–Tucker model, Wang et al [73] introduced a strain reduction factor κ, thereby obtaining the reduced strain closure (RSC) model, expressed as

$$\dot{\mathbf{A}}^{\mathrm{RSC}} = \dot{\mathbf{A}}^{\mathrm{HD}} - 2\xi(1 - \kappa)(\mathbb{L} - \mathbb{M} : \mathbb{A}) : \mathbf{D} + \kappa\dot{A}^{\mathrm{IRD}}, \quad \text{where} \tag{2.20}$$

$$\mathbb{L} = \sum_{i=1}^{3} \lambda_i e_i e_i e_i e_i \quad \text{and} \tag{2.21}$$

$$\mathbb{M} = \sum_{i=1}^{3} e_i e_i e_i e_i. \tag{2.22}$$

where κ is the scholar RSC factor (a fitting parameter); $\mathbb{L}$ and $\mathbb{M}$ are 4th order tensors, where λ_i and e_i are eigenvalues and eigenvectors of the 2nd order orientation tensor $\mathbf{A}$, respectively. This RSC model is equal to Folger-Tucker model when $\kappa = 1.0$. The RSC model provides nearly the same fibre orientation states as the one from Folger-Tucker model in a variety of flows, but better predictions in kinetics.

2.5.3 Moldflow Rotational Diffusion model

More recently, Bakharev et al. [74] proposed the Moldflow Rotational Diffusion (MRD) model, which modifies the rotary contribution in Folger-Tucker's equation, expressed as

$$\dot{\mathbf{A}}^{\mathrm{MRD,total}} = \dot{\mathbf{A}}^{\mathrm{HD}} + \dot{\mathbf{A}}^{\mathrm{MRD}}, \qquad \text{where} \tag{2.23}$$

$$\dot{\mathbf{A}}^{\mathbf{MRD}} = 2C_{\mathrm{I}}\dot{\gamma}(\widehat{\mathbf{D}} - \mathrm{tr}(\widehat{\mathbf{D}})\mathbf{A}) \qquad \text{and} \qquad \widehat{\mathbf{D}} = \begin{bmatrix} D_1 & 0 & 0 \\ 0 & D_2 & 0 \\ 0 & 0 & D_3 \end{bmatrix}. \tag{2.24}$$

This MRD model considers anisotropic rotation of fibres; therefore, a fibre aligned across the preferential orientation has much stronger interaction with the rest of the fibres than those aligned along the preferential direction [72]. This model is equal to Folger-Tucker's model when $D_1 = D_2 = D_3 = 1.0$ (i.e. isotropic case). Previous literature comparing these fibre orientation models [72,74,75] concluded that the MRD model provided the best accuracy among these three models available in Moldflow software.

2.6 Coupled process/structural simulations

To design IM-SFRP components, the state of the art in industry uses a coupled process/structural Finite Element Analysis ("coupled FEA") to consider the effect of fibre orientation and material non-linearity [76], with the following steps [5,77]:

- An anisotropic and non-linear material model is calibrated with dog-bone tensile experimental data from IM-SFRP plates tested at relevant environmental conditions under several machining angles (e.g., using Digimat's elastic-plastic material model, based on orientation averaging [7], Mori-Tanaka/Voigt mean-field homogenisation [64], J_2-plasticity model [5], and the Tsai-Hill failure criterion [5], as described in Section 2.4),
- The injection-moulding processes are simulated to predict the fields of the local fibre orientation tensor in the components (e.g., using Moldflow software [69]),
- The obtained fibre orientation tensor is then mapped onto an FE model of the components, to be used to calculate the local material properties at each integration point (e.g., using Digimat-MAP [5]),

- Finally, this FE model, including the coupling with process simulation, is submitted through Digimat-RP [5] and solved by the Abaqus FE Implicit solver [78].

This methodology homogenises the fibres and the matrix into a continuum (as required for computational efficiency), but it considers the heterogeneous distribution of the local fibre orientation tensor at each point of the model (including the skin-core microstructure); it also considers material anisotropy (which is essential for correct stiffness predictions) and non-linearity (which is essential to capture the progressive loading behaviour of complex-shaped components). This coupled FEA has good agreement with experimental results in the initial stiffness and the subsequent non-linear behaviour, at both coupon and component levels [16,76,77,79,80].

However, when designing IM-SFRP components using FEA, it is also necessary to predict their ultimate load-bearing capability and post-failure behaviour. Unfortunately, the criteria to predict the maximum failure load are not well established. Existing failure criteria for IM-SFRPs (e.g., based on the Tsai-Hill criterion [5,16]), which consider failure initiation only and neglect the finite toughness of the material, often under-predict the failure load in components. This underprediction has been noticed in the simulation of automotive components in the industrial partner Asahi Kasei Corporation, and has also been reported by other companies in the automotive industry [81]. This leads to overly conservative design, and hence excessively heavy and costly components in industry; therefore, further research is required to predict failure of IM-SFRP components more accurately.

2.7 Cohesive zone modelling

As concluded in Section 2.6, the current state of the art methodology to simulation IM-SFRP components under-predicts the failure load in components. A key hypothesis of this thesis is that the accuracy of simulations can be improved by accounting for the finite fracture toughness of the material, in order to simulate its progressive failure.

Within FE simulations, Cohesive Zone Modelling (CZM) is a powerful tool to accurately simulate the fracture process by accounting for the fracture toughness of the material. A cohesive law governs the behaviour of the cohesive elements (CEs), accounting for the following stages: (i) the CEs initially behave linearly according to their stiffness; (ii) failure initiates at a critical stress, and the softening process starts; (iii) the CEs' stiffness degrades while dissipating

energy according to the input fracture toughness; (iv) full separation of the crack surfaces (and the optional CEs' deletion) when the stiffness is fully degraded and a critical relative displacement is reached. Different shapes of cohesive laws (e.g., bilinear or trilinear [82]) can be calibrated, using values for critical stress and fracture toughness that have been determined experimentally.

2.8 Thesis outline

This Chapter 2 reviewed the current state-of-the-art literature about the experimental characterisation and FE simulation methodologies for IM-SFRPs. To address the gaps between the state-of-the-art reviewed in Chapter 2 and the objectives of this PhD project described in Section 1.2, the structure of this thesis is outlined as follows:

- Chapter 3 focuses on the standard experimental characterisation of the mechanical properties of a PA66-GF50 material, performed at the coupon scale according to international standard or published methodologies. The effect of fibre orientation, moisture content and service temperature on tensile mechanical properties are characterised. The T-M equivalence at different fibre orientations at coupon-level testing is also discussed;
- Chapter 4 assesses the state-of-the-art predictive material models for the mechanical properties of IM-SFRPs, including elastic models, elastic-plastic models, and failure criteria, integrated in Digimat software. These integrated models are calibrated for the PA66-GF50 material, using the experimentally-measured properties obtained in Chapter 3, and the corresponding outputs are validated in their ability to reproduce the coupon test results;
- Chapter 5 details the novel characterisation of the initiation and propagation fracture toughness of the PA66-GF50 material, under the combined effect of fibre orientation, moisture level and temperature. This work is performed through tensile CT testing, using newly-designed coupons. Full R-curves are calculated using either an FE-based compliance calibration method, or the J-integral method based on full-field measurements from 3D-DIC;
- Chapter 6 proposes a new FE methodology to predict failure of PA66-GF50 (sub)components. This is the first attempt to account for the finite fracture toughness of the material in the FE simulations coupled with fibre orientation fields predicted by

an injection-moulding process simulation. This methodology is based on cohesive zone modelling calibrated with the experimentally-measured fracture toughness obtained in Chapter 5 (and the other mechanical properties characterised in Chapter 3). The results of this new proposed methodology are compared against the state-of-the-art method, which uses Tsai-Hill's failure initiation criterion but neglects damage propagation. Moreover, the concept of T-M equivalence is extended to the fracture toughness and to the subcomponent scale, and different environmental conditions are used to verify the robustness of the proposed FE methodology;

- Chapter 7 validates the FE methodology proposed in Chapter 6 using the real geometry of an automotive component, with the following objectives: (i) to characterise failure and how it is affected by the manufacturing process and variability, using a fractography, and (ii) to validate the new FE methodology to predict failure of IM-SFRPs, at the component level;
- Overall discussions are described in Chapter 8, where the key novelty and impacts of this work are also highlighted. Finally, the conclusions of this PhD thesis are summarised in Chapter 9, and some suggestions for further work are proposed in Chapter 10, with a focus on how to improve the potential impact of this work, including its application in industry.

Chapter 3 - Material properties of injection-moulded short glass fibre-reinforced polyamide 6.6 composites

3.1 Introduction

As described in Chapter 2, the injection-moulding process creates a core-shell microstructure in the composite with complex fibre orientation states [6], leading to anisotropic and heterogeneous mechanical properties and failure modes [14–17]. Moreover, environmental conditions such as temperature and moisture content also influence the mechanical properties of many IM-SFRPs, especially those with PA66 matrices [14,15,39–42]. Hence, it is essential to take these environmental effects into account in FE simulations when designing IM-SFRP components.

The concept of temperature-moisture (T-M) equivalence [50–52], reviewed in Section 2.3, has potential to reduce the amount of coupon characterisation needed. From existing literature, the T-M equivalence for modulus and the following non-linear behaviour (or failure strength) at the coupon level have been verified [50–52]. However, these previous works only focused on one fibre orientation state (i.e. transversely to flow direction), and the fibre orientation effect had not been considered in SFRP materials. Therefore, it is worth investigating as to whether the T-M equivalence is robustly applicable to all cases (i.e. different fibre orientations and environmental conditions).

This Chapter focuses on standard coupon tests of an IM-SFRP material – hereby referred to as 'PA66-GF50' – with the following objectives: (i) to characterise the effect of fibre orientation, moisture level and testing temperature on the mechanical properties of injection-moulded PA66-GF50, (ii) to validate the T-M equivalence at different fibre orientations at coupon-level testing, and (iii) to parameterise the constitutive properties required as inputs for the micromechanical models and Finite Element Analysis models in the subsequent Chapters. Section 3.2 describes the experimental procedures used to manufacture and test the injection-moulded PA66-GF50 coupons. The experimental results are analysed and discussed in Sections 3.3 and 3.4, respectively, and the main conclusions are conveyed in Section 3.5.

3.2. Experimental procedures

3.2.1. Manufacturing of injection-moulded plates

The material used in this work was a short glass-fibre (fibre weight fraction: 50%; fibre volume fraction: 31%) reinforced PA66 ("PA66-GF50") from Asahi Kasei Corporation (Leona^{TM}14G50, loaded with a carbon black additive). Plates (120 x 80 x 2 mm, as shown in Fig. 3.1) were prepared by injection moulding using a SE130D (SUMITOMO) machine, with the moulding conditions as described in Table 3.1. Directly following manufacture, the injection-moulded plates were stored in aluminium lined bags, to maintain them under dry-as-moulded (DAM) conditions. Note that only one coupon was obtained from each plate (at the centre) to avoid the effect of varying fibre orientations closer to the edges of the plate.

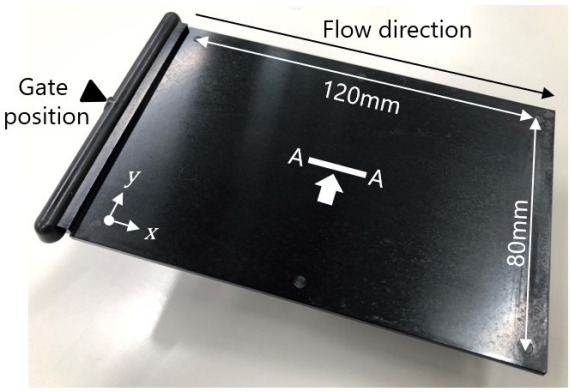


Fig. 3.1. Photograph of an injection-moulded PA66-GF50 plate (2 mm thick).
The line A-A indicates the plane over which fibre orientations were measured, as described in Section 3.2.2.

Table 3.1. Injection moulding parameters of the plates for coupon testing.

Cylinder temp. (°C)	Mould temp. (°C)	Injection time (s)	Holding pressure (MPa)	Cooling time (s)
290	80	0.3	80	15

3.2.2. Characterisation of fibre orientation in the plate

Cross-sections of the injection-moulded plates (across the A-A line in Fig. 3.1) were examined using optical microscopy. Fibre orientation distributions in the plates were characterised through the method of ellipses [9]. The local fibre orientation distribution was summarised into a second-order fibre orientation tensor, as proposed by Advani and Tucker [7],

$$\mathbf{A} = \begin{bmatrix} a_{xx} & a_{xy} & a_{xz} \\ a_{xy} & a_{yy} & a_{yz} \\ a_{xz} & a_{yz} & a_{zz} \end{bmatrix}. \tag{3.1}$$

3.2.3. Tensile testing of dog-bone coupons

The Young's modulus, tensile strength and failure strain of the PA66-GF50 IM-SFRP were characterised through tensile testing of dog-bone coupons with geometry according to the ISO standard 8256 (width: 10 mm) [83], and testing specifications shown in Table 3.2, using an optical strain gauge (gauge length: 10 mm) to measure strains. To characterise the effect of fibre orientation on material properties, the dog-bone coupons were machined at different angles with respect to the main flow direction (which is indicated in Fig. 3.1), as shown in Fig. 3.2.

To characterise the effect of moisture and temperature, some dog-bone coupons were conditioned (until saturation, corresponding to a weight increase by 1.2%) based on ISO1110 [83] for testing at 50% relative humidity (hereby referred to as 'RH50'), under five different temperatures (as detailed in Table 3.2). These environmental conditions were selected to be typical conditions for engine mounts in service (provided by the industrial partner, Asahi Kasei Corporation). The tests were performed in a thermal chamber with the following procedure: (i) each coupon in its sealed aluminium lined bag was exposed to the testing temperature in the chamber for 15 mins, (ii) the coupon was taken out from the aluminium bag and mounted in the machine, and (iii) the testing was started within 5 min of opening the aluminium bag. Note that the holding time (15 mins) was verified experimentally in preliminary work, which showed that the temperature-dependent properties of DAM coupons were converged with this holding time.

Table 3.2. Testing specifications for dog-bone tensile coupons.

Number of coupons	Nominal strain rate (s^{-1})	Environmental conditions	Machining angles (°)
Five per test condition	10^{-3}	23°C-DAM, 23°C-RH50, 60°C-DAM, 80°C-RH50, 120°C-DAM	0, 20, 30, 45, 60, 90

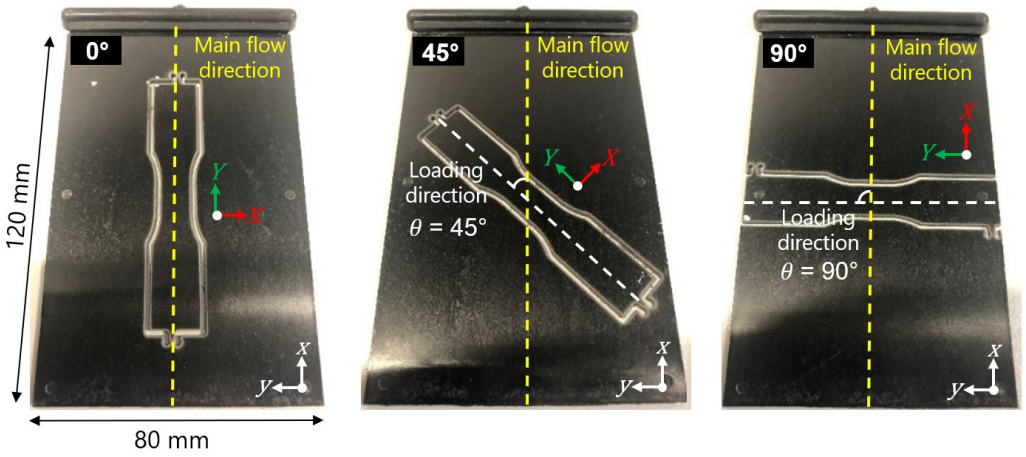


Fig. 3.2. Definition of the machining angles of dog-bone coupons (relating the plate coordinate system xyz with the coupon coordinate system XYZ).

3.2.4. Fractography

Following testing, fracture surfaces of selected dog-bone coupons were separated using a dry handsaw and mounted on stubs using carbon-black-loaded epoxy adhesive. These samples were sputter-coated with gold for 20 s, and examined using a Hitachi S-3700 scanning electron microscope (SEM), with an acceleration voltage of 12 kV.

3.2.5. Dynamic Mechanical Analysis

Dynamic mechanical analysis (DMA) was conducted using a RSA-G2 (TA Instruments) machine to investigate the effect of moisture on the glass transition temperature of the PA66-GF50 material. Rectangular coupons were machined from the injection-moulded plates along the main flow direction (0°) only, and some coupons were conditioned (until saturation, with the weight increase of 1.2%) based on ISO1110 [83] for testing at RH50. The testing specifications (which are based in work reported previously using injection-moulded PA66-GF30 [84], and modified for the available equipment) are summarised in Table 3.3.

Table 3.3. Testing specifications for dynamic mechanical analysis.

Number of coupons	Geometry (mm)	Test type	Temperature range (°C)	Frequency (Hz)	Strain (%)
Three per test condition	30 x 3 x 2	3-point bending	0 – 120	10	0.01

3.2.6. Differential Scanning Calorimetry analysis

Differential Scanning Calorimetry (DSC) analysis was carried out using Discovery (TA Instruments) to characterise the crystallinity of the PA66-GF50 material used in this work. The

analysis specifications are summarised in Table 3.4. To obtain a better characterisation of the effect of the fibres on the crystallinity of the material, four different fibre weight fractions were tested: $w_f = 0, 15, 35, 50\%$. The crystal weight fraction (or crystallinity, X_c) of PA66 was calculated using the following equations [85]:

$$X_c = \Delta H_f / \Delta H_{f^0} \tag{3.2}$$

where ΔH_f is the melting enthalpy of PA66 in the samples (obtained directly from the DSC test) and $\Delta H_{f^0} = 195$ J/g is the melting enthalpy of perfectly-crystalline PA66 [85].

Table 3.4. Analysis specifications for differential scanning calorimetry.

Sample amount (mg)	Temperature range (°C)	Holding time at 300 °C (min)	Cooling rate (°C/min)
5	R.T. - 300	5	10

3.3. Results

3.3.1. Fibre orientation tensor in the plate

An optical micrograph of the cross-section at the centre of the plate (across the A-A line in Fig. 3.1) is shown in Fig. 3.3 (a). The preferential fibre orientation was observed to have been along the flow direction in the skins, and transversely in the core, with 80% of the skin layers and 20% of the core layer through the thickness. The in-plane diagonal components of the fibre orientation tensor in the plates were measured through the method of ellipses, and plotted in Fig. 3.3 (b). The fibre orientation tensor averaged through the thickness of the plate is

$$\mathbf{A} = \begin{bmatrix} a_{xx} & a_{xy} & a_{xz} \\ a_{xy} & a_{yy} & a_{yz} \\ a_{xz} & a_{yz} & a_{zz} \end{bmatrix} = \begin{bmatrix} 0.72 & \sim 0 & \sim 0 \\ \sim 0 & 0.26 & \sim 0 \\ \sim 0 & \sim 0 & 0.02 \end{bmatrix}. \tag{3.3}$$

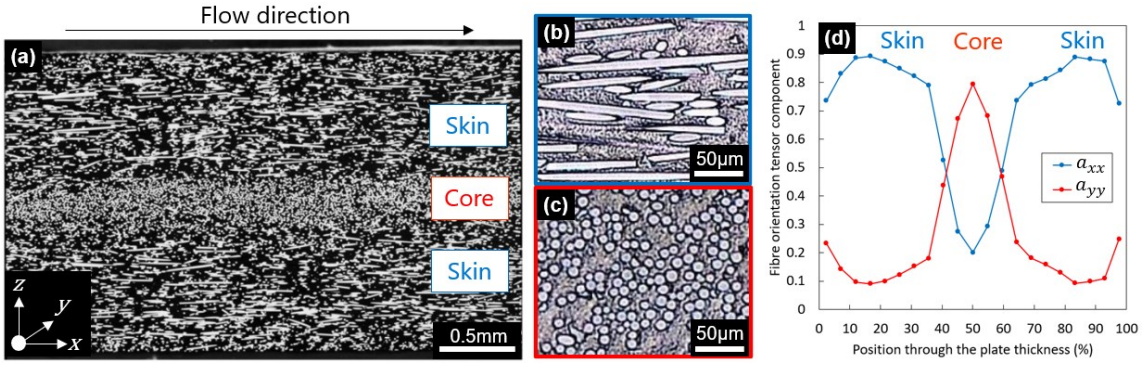


Fig. 3.3. (a) Cross-sectional optical micrograph across the A-A line in Fig. 3.1, with zoom-ins shown in (b) in the skin, and (c) in the core, and (d) in-plane diagonal components of the fibre orientation tensor in the injection-moulded PA66-GF50 plates.

3.3.2. Tensile mechanical properties for different fibre orientations

The stress-strain curves of PA66-GF50 at 0, 45 and 90° under different environmental conditions are shown in Fig. 3.4. The Young's modulus, tensile strength and failure strain of PA66-GF50 as a function of machining angle under the five different environmental conditions are plotted in Fig. 3.5. The qualitative effects of machining angles and environmental conditions on these properties are summarised in Table 3.5. These test results were repeatable (especially regarding the ultimate strength) within the five tests performed for each condition, apart from small levels of variability in the optical strains (which justifies the larger variability in Young's moduli than in tensile strengths).

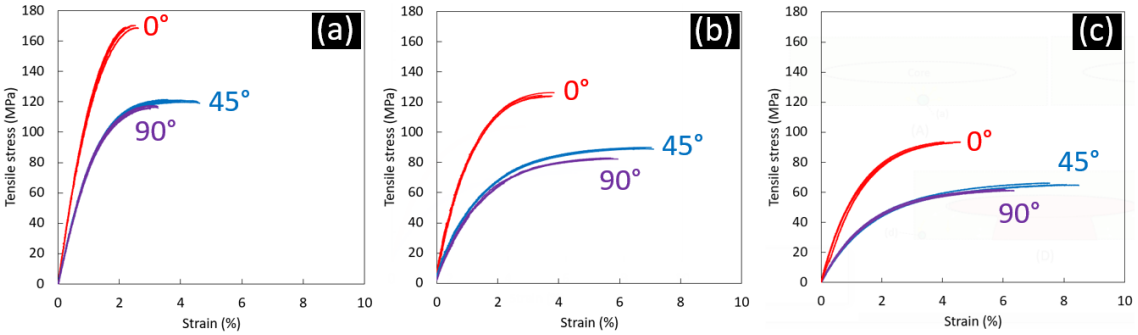


Fig. 3.4. Representative load-displacement curves of PA66-GF50 dogbone coupons at different machining angles: (a) 23°C-DAM, (b) 23°C-RH50 and (c) 80°C-RH50.

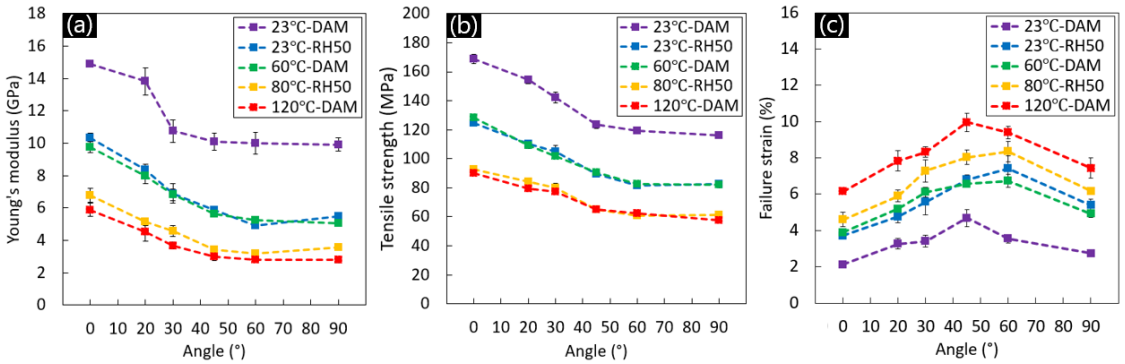


Fig. 3.5. (a) The Young's modulus, (b) tensile strength, and (c) failure strain of PA66-GF50 as a function of machining angle under the five different environmental conditions.
All datapoints have error bars representing one standard deviation (some error bars are sufficiently small to be obscured by the corresponding datapoint).

Table 3.5. Summary of the effect of fibre orientation and environmental conditions on the tensile mechanical properties of PA66-GF50.

	Effect of machining angles	Effect of environmental conditions
Young's modulus	● Highest at a 0° angle ● Progressively decreased with increasing machining angles ● The values at 90° decreased by 33-53% over 0°	● Decreased with increasing moisture content or temperature ● Agreement between 23°C-RH50 and 60°C-DAM ● Slightly stiffer under 80°C-RH50 than 120°C-DAM
Tensile strength	● Highest at a 0° angle ● Progressively decreased with increasing machining angles ● The values at 90° decreased by 31-36% over 0°	● Decreased with increasing moisture content or temperature ● Similar results obtained under 23°C-RH50 and 60°C-DAM, and also under 80°C-RH50 and 120°C-DAM
Failure strain	● Highest at 45° or 60°angle	● Increased with increasing moisture content or temperature ● Agreement between 23°C-RH50 and 60°C-DAM ● Higher under 120°C-DAM than 80°C-RH50

Since the fibres in the coupons were not all aligned in one direction, using the machining angle as the independent variable does not fully characterise the relationship between tensile mechanical properties and fibre orientation. Therefore, it was useful to calculate the fibre orientation component along the coupon loading direction, i.e. $\alpha_{YY}(\theta)$ defined in Fig. 3.2, by rotating the 2nd order fibre orientation tensor $\mathbf{A}$ (defined in Eq. (3.1) in Section 3.2.2) by the machining angle:

$$\mathbf{A}_{XYZ}(\theta) = \mathbf{T}(\theta) \cdot \mathbf{A}_{xyz} \cdot \mathbf{T}(\theta)^{\mathrm{T}}, \text{ where } \mathbf{T}(\theta) = \begin{bmatrix} \sin\theta & -\cos\theta & 0 \\ \cos\theta & \sin\theta & 0 \\ 0 & 0 & 1 \end{bmatrix}. \quad (3.4)$$

and the superscript $\mathbf{T}$ indicates matrix transposition. The result from this calculation is shown in Table 3.6. Finally, Fig. 3.5 are re-plotted as a function of these fibre orientation components α_{YY}, as shown in Fig. 3.6.

Table 3.6. 2nd order fibre orientation component in the plate along the loading direction.

Machining angle θ (°)	0	20	30	45	60	90
Fibre orientation component along the loading direction, α_{YY}	0.72	0.66	0.60	0.49	0.37	0.26

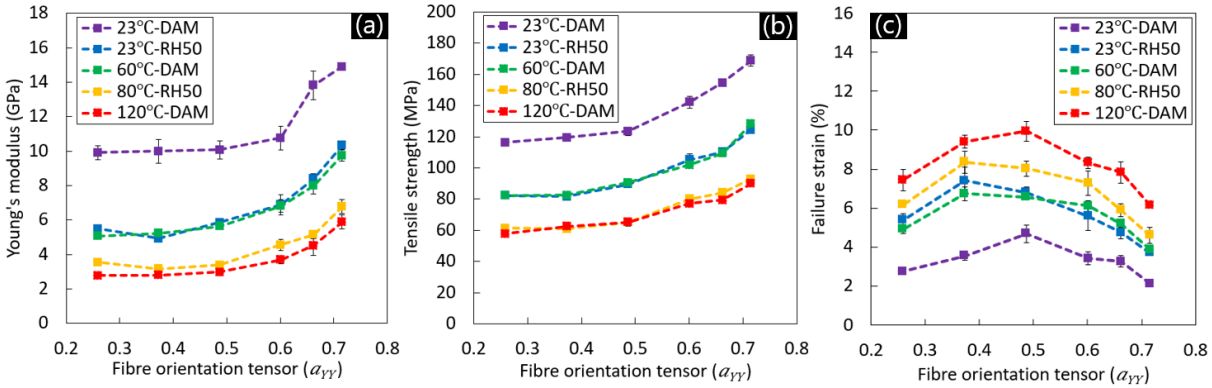


Fig. 3.6. (a) The Young's modulus, (b) tensile strength, and (c) failure strain of PA66-GF50 as a function of fibre orientation components α_{YY} under the five different environmental conditions.

3.3.3. Fractographic analysis after tensile testing of the dog-bone coupons

Representative scanning electron micrographs of fracture surfaces of PA66-GF50 dog-bone coupons tested under 23°C-DAM are shown in Fig. 3.7. In the 0° and 90° coupons, a typical T-fracture surface (with brittle PA66 matrix fracture and fibre pull-out, in the skins for 0° coupons and in the core for 90° coupons) and a L-fracture surface (with interfacial debonding, in the skins for 90° coupons and in the core for 0° coupons) were observed [53]. In the 45° coupons, aligned steps (indicative of shear failure) were present in both the skin and the core region. The details of the inferred failure mechanisms at each region are summarised in Table 3.7.

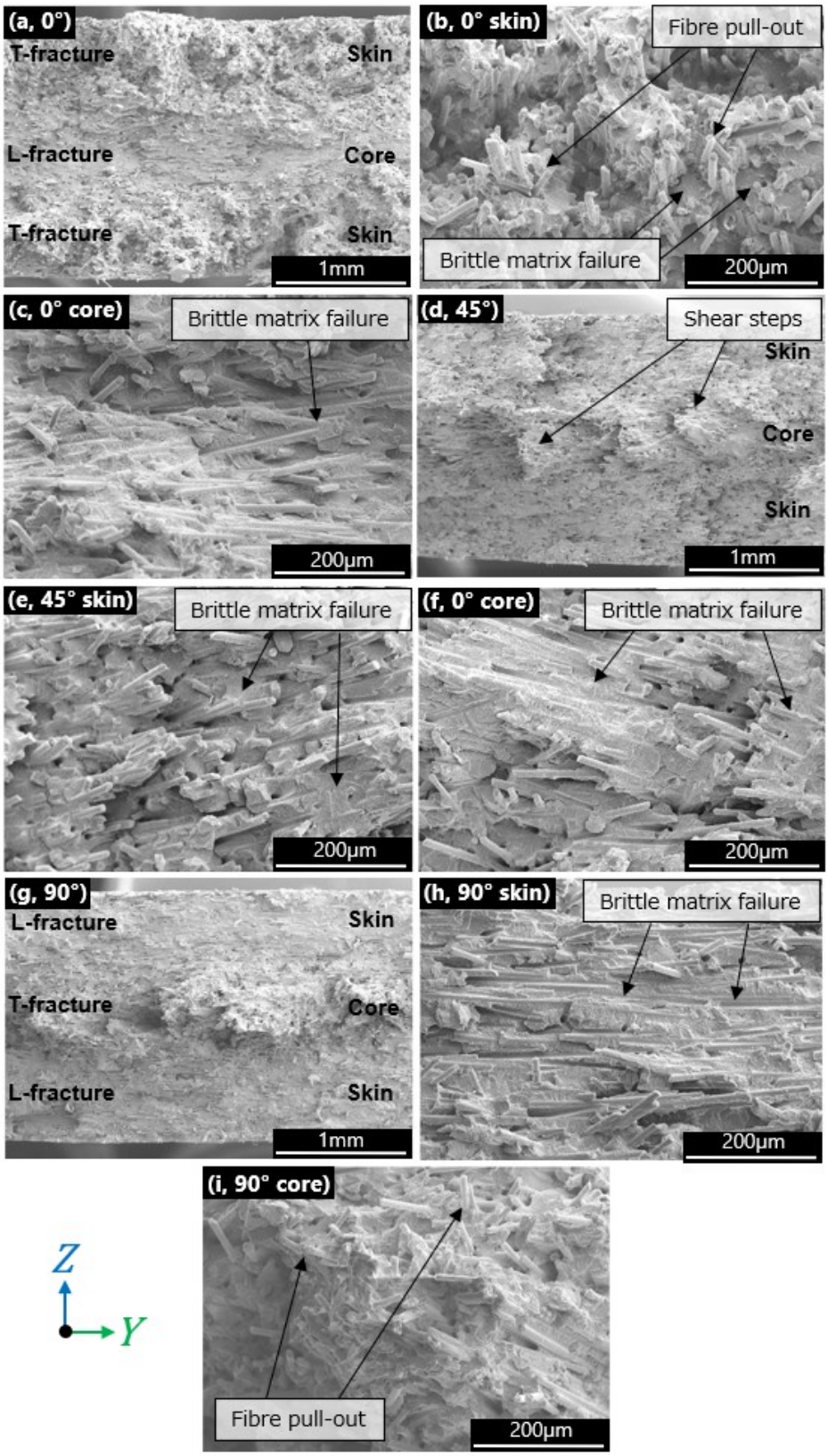


Fig. 3.7. Representative scanning electron micrographs of fracture surfaces of dog-bone coupons tested under 23°C-DAM: (a)-(c) at 0° direction, (d)-(f) at 45° direction and (g)-(i) at 90° direction for the overall area through the thickness, in the skin and in the core, respectively.

Table 3.7. Summary of the failure mechanisms of PA66-GF50 dog-bone coupons after tensile testing at 23°C-DAM.

	Skin	Core
0°	T-fracture surface	L-fracture surface
45°	Brittle matrix shear failure with shear steps	Brittle matrix shear failure with shear steps
90°	L-fracture surface	T-fracture surface

3.3.4. Glass transition temperature of PA66-GF50

The tan-Delta curves of PA66-GF50 under DAM and RH50 conditions are shown in Fig. 3.8. The curve shifted to lower temperatures due to moisture absorption: the glass transition temperatures (i.e. the temperatures at the maximum value tan-Delta [84]) are 63.5 $\pm$ 3.3 °C and 24.6 $\pm$ 2.8 °C under DAM and RH50 conditions, respectively. This represents a glass transition temperature shift of -38.9 °C with moisture absorption.

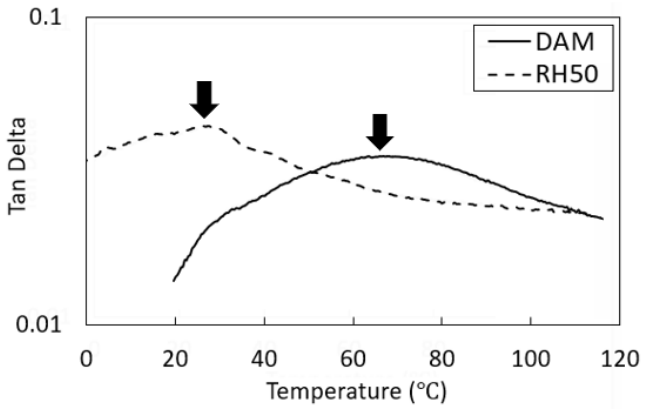


Fig. 3.8. Tan-Delta curves of PA66-GF50 under DAM and RH50 conditions. The arrows indicate the peak of the curves.

3.3.5. Crystallinity of PA66 materials

The crystallinity of PA66 matrix (X_c) obtained from DSC analysis was summarised in Table 3.8. It slightly increased with an increase in the glass fibre content.

Table 3.8. Crystallinity of PA66 with different fibre weight fractions.

w_f	0	15	35	50
X_c	35.2	35.8	38.4	44.2

3.4. Discussion

3.4.1. Fibre orientation state in the plates

Clear skin-core microstructures, with the fibres mostly aligned along the flow direction in the skin, and along the transverse direction in the core, were present in the plates. These microstructures are consistent with previous reports in thin plates [6,14,15].

3.4.2. Effect of fibre orientation on the mechanical properties of the coupons

Both the Young's modulus and the tensile strength were highest at θ = 0°, and progressively decreased with increasing machining angles under all environmental conditions; the values at 90° decreased by 33-53% over 0° for the Young's modulus, and decreased by 31-36% over 0° for the tensile strength. This fibre orientation effect on the tensile mechanical properties is consistent with the literature [14–17]. This is because IM-SFRPs show a matrix-dominated behaviour at large loading angles with respect to the preferential fibre orientation direction (i.e. between θ = 45° to 90°) than at small angles (i.e. between θ = 0° to 45°).

The highest failure strain was obtained between θ = 45° to 60° as shown in Fig. 3.5, corresponding to around $\alpha_{YY} = 0.4 - 0.5$ as shown in Fig. 3.6. A possible explanation is that a significant part of the remote strain for the intermediate-angle coupons (i.e. 45—60°) is due to re-orientation of the fibres. This creates a scissoring effect, because the skins-core microstructure is similar to a cross-ply laminate. For such cross-ply laminate, this scissoring effect is maximised for a loading angle of 45deg. However, IM-SFRPs have some level of distribution in the fibre orientation (as shown in Fig. 3.3), leading to a more complex behaviour in their damage processes (including shear deformation), and therefore the failure strain at 45° was almost equal to (or lower than) that at 60° in some cases (i.e. 80°C-RH50 in Fig. 3.5).

3.4.3. Crystallinity of PA66 materials

The crystallinity of the PA66 matrix (obtained from DSC analysis) increased progressively with an increase in the glass fibre content, up to 9% increase of crystallinity with the addition of 50% of glass fibres (i.e. from 35.2% to 44.2%). These values of crystallinity are very similar to those reported in the previous literature [85].

This increase in PA66 crystallinity with fibre content might lead to a small change of mechanical properties of the matrix in the IM-SFRP, compared to a neat IM-PA66. Nevertheless, the effect of the small change of the PA66 crystallinity on mechanical properties is expected to be small, based on the discussion in the previous literature investigating this effect using neat PA66 [86].

3.4.4. Temperature-moisture equivalence in coupons

The Young's modulus, tensile strength and failure strain of the coupons tested under 23°C-RH50 and 60°C-DAM (hereafter referred to as "Pair-A") had a good agreement (within the error bars) under all machining angles, as summarised in Table 3.9. The tan-Delta curves (Fig. 3.8) presented a glass transition temperature shift of -38.9 °C with moisture absorption from DAM to RH50 conditions (with a weight increase of 1.2%), which is consistent with previous reports [84,87,88]. Pair-A has a difference in testing temperature of 37°C, which roughly corresponds to the shift of the glass transition temperature measured due to the corresponding change in moisture conditions. This suggests that there is an equivalence between increasing the moisture level and increasing the testing temperature by the corresponding shift in DMA curves in this PA66-GF50 material, not only under a specific fibre orientation state as reported previously [52], but also under a wide range of machining angles in the coupon tests.

A similar trend was also found in the results of the coupons tested under 80°C-RH50 and 120°C-DAM ("Pair-B"), which also have a similar difference in the testing temperature of 40°C (just slightly above the shift in DMA curves). However, in Pair-B, a small mismatch was found in the results of Young's modulus and failure strain (slightly stiffer and more brittle behaviour observed under 80°C-RH50 conditions than under 120°C-DAM). A possible explanation is that water evaporated from the surface of the PA66-GF50 coupons during the tests under 80°C-RH50 conditions, meaning that the intended 80°C-RH50 might actually be a slightly drier condition. From weight measurements of coupons exposed to 80°C during 20 mins, it is estimated that the 80°C coupons were actually tested under RH48 rather than the intended RH50.

Table 3.9. Difference in the measured mechanical properties of coupons within equivalent temperature/moisture pairs.

	Young's modulus	Tensile strength	Failure strain
Pair-A (%)	5.0	1.6	7.5
Pair-B (%)	17.9	3.6	23.0

(*) calculated as the average of the six different machining angles

3.5. Conclusions

Characterisation of injection-moulded PA66-GF50 materials was conducted to quantify the effect of fibre orientation and environmental conditions on the mechanical properties at the coupon level. The main conclusions in this chapter are summarised as follows:

- The Young's modulus, tensile strength and failure strain of PA66-GF50 have been characterised under the combined effect of fibre orientation, moisture level, and temperature. A clear fibre orientation effect on these properties was seen under all environmental conditions. The PA66-GF50 material showed softer behaviour under hotter or wetter conditions.
- The results in this chapter provide the first analysis of temperature-moisture equivalence for injection-moulded SFRPs with the consideration of fibre orientation effects using more than one temperature-moisture pair (previous literature focused only on one fibre orientation state / machining angle). More details on the temperature-moisture equivalence for injection-moulded PA66-GF50 will be discussed in Chapter 6, at the subcomponent level.

The material properties characterised in this chapter are used in the subsequent Chapters 4-7, in Finite Element Analysis models.

Chapter 4 - Calibration of elastic, elastic-plastic and failure models used in state-of-the-art simulation for IM-SFRPs

4.1 Introduction

The state of the art in the simulation of IM-SFRP components uses coupled FEA with fibre orientation fields predicted by process simulations, and Digimat's elastic-plastic material model and Tsai-Hill criterion, as reviewed in Chapter 2. This methodology has been reported to predict the initial stiffness and the subsequent non-linear behaviour very well compared against experimental results, at both coupon and component levels [16,76,77,79,80]. To utilise these models, their parameters (described in Sections 2.4) need to be calibrated using experimental results from characterisation of coupons.

Chapter 4 focuses on the calibration and assessment of the state-of-the-art methodology to simulate IM-SFRPs [5] for the PA66-GF50 material characterised in Chapter 3, with the following objectives: (i) to verify the accuracy of fibre orientation models against the fibre orientation states observed experimentally in IM-plates, (ii) to study the sensitivity of this material model to micro-scale input properties, and (iii) to validate Digimat's calibrated elastic-plastic models and Tsai-Hill failure criterion, by verifying that they recover the experimental results used for the calibration at the coupon level. Section 4.2 presents the prediction of fibre orientation fields in the plate by the injection-moulding process simulation using three different fibre orientation models. Sections 4.3 and 4.4 then describe the details of the elastic and elastic-plastic models, and compares the output with the experimental results. The results are analysed and discussed in Sections 4.5, and the main conclusions are shown in Section 4.6.

4.2 Prediction of fibre orientation field in IM-SFRP plates by process simulation

In this section, the injection-moulding process of the PA66-GF50 IM-plates was simulated using Moldflow software [69] to predict the fibre orientation fields in the plates. The rheological and thermal properties of 'Leona 14G50 (Black): Asahi Kasei Corporation' were used in this process simulation (these properties had been characterised by the material manufacturer and

are available natively in the Moldflow software to all users). 3D meshes were created using the "Generate Mesh" function in Moldflow software, with 40 layers in the through-the-thickness direction. Three different fibre orientation models (Folger-Tucker [71], RSC [73] and MRD [72,74,75] models, reviewed in Section 2.5) using the default parameters were used, with the injection-moulding conditions representing the actual manufacturing of the plates (previously shown in Table 3.1).

Predicted fibre orientation tensor fields along the x-direction (α_{xx}) in the plate are shown in Fig. 4.1, and the values of α_{xx} along the A-A plane (normal to the y-direction at the centre of the plate) from the experiment and the simulations using three different fibre orientation models are compared in Fig. 4.2. The output of α_{xx} from these simulations was very similar to the one from the experiments, for all fibre orientation models used in this work; nevertheless, the Folger-Tucker and MRD models are slightly more accurate than the RSC model in capturing the transition between the skins and the core.

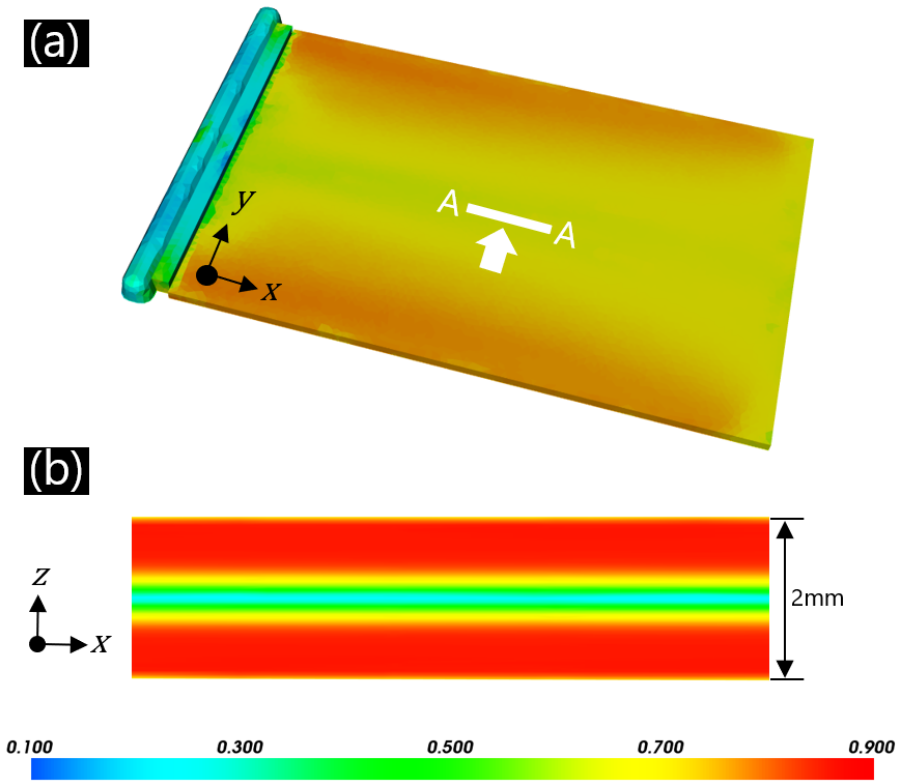


Fig. 4.1. Predicted fibre orientation tensor along the x-direction in the plate (a_{xx}), using the MRD model: (a) plate overview, (b) cross-section at the centre of the plate along the x-direction (along the A-A line indicated in Subfigure (a)).
The colourbar shown represents a_{xx} consistently for both subfigures.

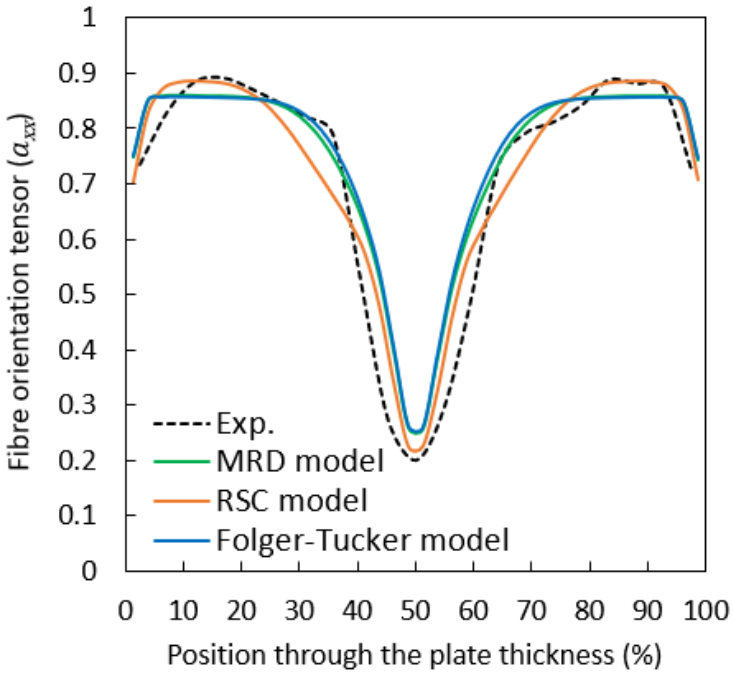


Fig. 4.2. Comparison of fibre orientation tensor α_{xx} obtained from the experiments (as reported in Section 3.3.1) and process simulations using three different fibre orientation models.

4.3 Experimental calibration and validation of elastic models for IM-SFRPs

In this section, Digimat's elastic model (based on Mori-Tanaka's mean-field homogenisation [64] with orientation averaging [7]) was calibrated to predict the Young's modulus of PA66-GF50 coupons, as measured experimentally in Chapter 3. Parametric studies on the effect of fibre and matrix micromechanical properties were also conducted, as these parameters are used in the model but were not characterised experimentally in Chapter 3.

4.3.1 Stiffness prediction using Digimat's and analytical implementations

The Young's modulus of unidirectional PA66-GF50 under 23°C-DAM was calculated using two different implementations of Mori-Tanaka's mean-field homogenisation [64]: (i) using a Matlab implemented code, and (ii) Digimat's elastic model [5]. These calculations were implemented for 0° and 90° directions of pseudo-grains (as shown in Section 2.4), and the constituent properties shown in Table 4.1. For the calculation using Digimat's elastic model, the calibrated model was loaded in Digimat-MF, and then a mechanical loading was applied to a RVE having those properties (as explained in Section 2.4).

Fig. 4.3 shows the predicted Young's moduli for the two directions as a function of fibre volume fraction. It was confirmed that Digimat's elastic model can be reproduced by implementing the Mori-Tanaka mean-field homogenisation with orientation averaging, for both 0° and 90° directions. Therefore, Digimat's elastic model is used in the subsequent Sections in this Chapter.

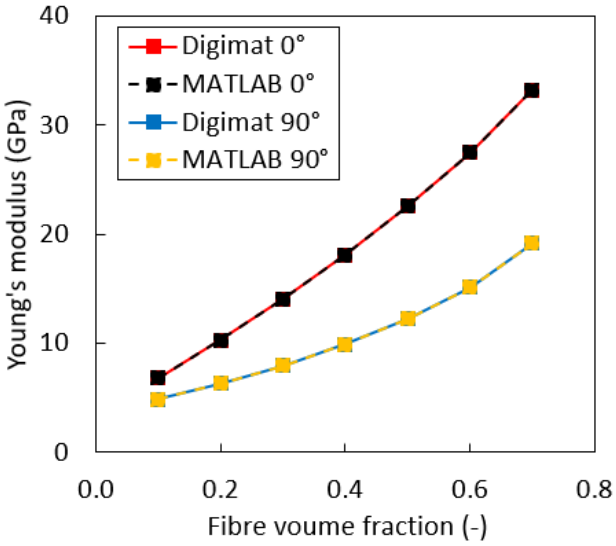


Fig. 4.3. Predicted Young's modulus of PA66-GF50 using Digimat's elastic model and Matlab implementation of Mori-Tanaka's mean-field homogenisation with orientation averaging as a function of fibre volume fraction at 0° and 90° directions under 23°C-DAM.

Table 4.1. Properties of the fibre and matrix used for homogenisation.

Environmental conditions	Fibre properties			Matrix properties	
	Young's modulus E_{f} (GPa)	Poisson's ratio υ_{f}	Aspect ratio A_{r} (-)	Young's modulus E_{m} (GPa)	Poisson's ratio υ_{m} (-)
23°C-DAM	72	0.22	20	3.6	0.35

4.3.2 Parametric studies of fibre and matrix properties for stiffness prediction

The effect of fibre orientation, matrix moduli, E_{m}, and fibre aspect ratio, A_{r}, on the predicted Young's modulus of PA66-GF50 was investigated using Digimat's elastic model under the three different environmental conditions mentioned in Table 4.2 (which are typically used for engine mounts in industry). The same procedure described in Section 4.3.1 was used for these calculations using the RVE available in Digimat-MF. These calculations were implemented for six different machining angles (using the actual overall fibre orientation tensor in the through-the-thickness direction (Fig. 3.3), and therefore can capture the effect of machining angle), using the

nominal inputs summarised in Table 4.2 (except when explicitly mentioned for the parametric studies on E_{m} and A_{r}). Note that these nominal values of E_{f} and υ_{f} were provided by the industrial partner (Asahi Kasei Corporation), and those of A_{r}, E_{m} and υ_{m} were calibrated automatically in Digimat-MX.

The predicted composite's Young's moduli, E_{YY}, are plotted as a function of α_{YY} (the fibre orientation component along the loading direction) and compared against the experimental results (previously presented in Section 3.3.2) in Fig. 4.4. The composite's Young's moduli increased with increasing α_{YY} and E_{m}, under all environmental conditions, as expected. For lower α_{YY} (e.g. 90° machining direction), the Young's modulus was very consistent regardless of the input fibre aspect ratio (A_{r}), while the effect of fibre aspect ratio on the composite's Young's modulus became larger for higher α_{YY} (e.g. 0° machining direction).

Table 4.2. Nominal properties used in Digimat's elastic model for parametric studies of matrix moduli and fibre aspect ratios.

	Environmental conditions	23°C-DAM	23°C-RH50	80°C-RH50
Fibre properties	Young's modulus E_{f} (GPa)	72	72	72
	Poisson's ratio υ_{f}	0.22	0.22	0.22
	Aspect ratio A_{r}	20	20	20
Matrix properties	Young's modulus E_{m} (GPa)	3.6	1.5	0.7
	Poisson's ratio υ_{m}	0.35	0.36	0.36

$^{(*)}E_f$ and υ_f were provided by Asahi Kasei Corporation.
$^{(*)}A_r$, E_m and υ_m were calibrated in Digimat-MX.

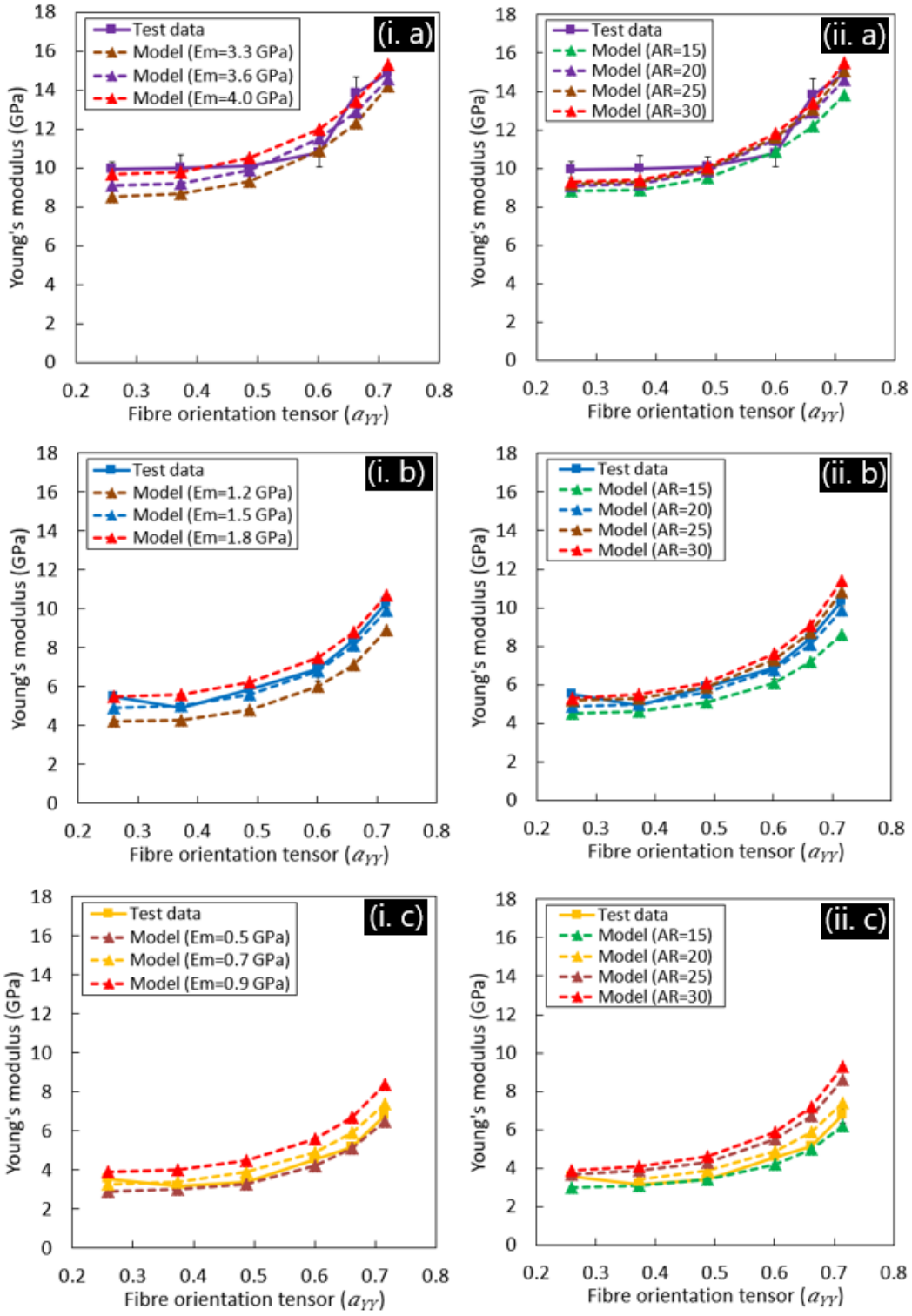


Fig. 4.4. The Young's modulus of PA66-GF50 as a function of fibre orientation tensor under the three different environmental conditions from the experiments and prediction using Digimat's elastic material model (i) varying the matrix modulus and (ii) varying the fibre aspect ratio: (a) 23°C-DAM, (b) 23°C-RH50, and (c) 80°C-RH50.
All datapoints from experiments have error bars representing one standard deviation (some error bars are sufficiently small to be hidden behind the corresponding datapoint).

The difference between the predicted E_{YY} (using varied A_{r} or E_{m}) and the experimentally measured values are summarised in Fig. 4.5 and Fig. 4.6, respectively. The predictions using the nominal inputs (calibrated in Digimat, shown in Table 4.2) presented the smallest averaged errors, compared to those using non-calibrated values of A_{r} and E_{m}, which justifies the use of the calibrated values.

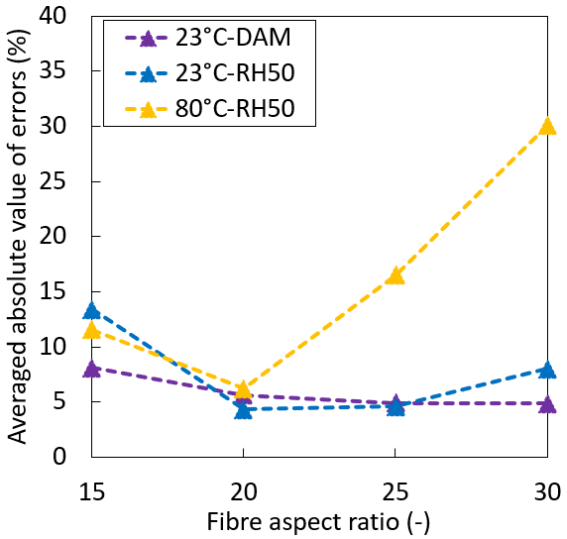


Fig. 4.5. Difference in the Young's modulus of PA66-GF50 between the experiments and outputs from Digimat's elastic model, using different fibre aspect-ratio inputs. These values are calculated as the average of the square root of the sum of the squared differences for all machining directions and environmental conditions.
(*)Calibrated aspect ratio in Digimat: A_r = 20.

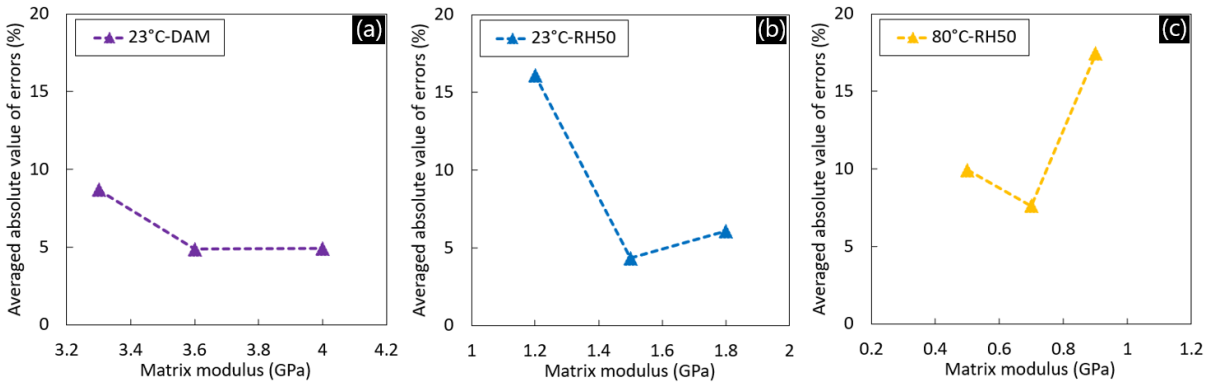


Fig. 4.6. Difference in the Young's modulus of PA66-GF50 material between the experiments and outputs from Digimat's elastic model, using different matrix moduli inputs under (a) 23°C-DAM, (b) 23°C-RH50, and (c) 80°C-RH50. These values are calculated as the square root of the sum of the squared differences for all machining directions.
(*)Calibrated matrix moduli in Digimat: E_m = 3.6, 1.5 and 0.7 GPa, respectively for 23°C-DAM, 23°C-RH50, and 80°C-RH50.

4.4 Experimental calibration and validation of elastic-plastic and strength models for IM-SFRPs

In this Section, the Digimat elastic-plastic material model and Tsai-Hill strength criterion [5] were calibrated using the PA66-GF50 stress versus strain curves experimentally characterised in Chapter 3. The calibrated models were then used to recover the tensile stress-strain behaviour and strength of PA66-GF50 coupons, and these predictions were then compared against the experimental results, to validate the calibration of these models and verify their suitability to PA66-GF50.

4.4.1 Elastic-plastic model

The tensile stress-strain behaviour of the PA66-GF50 material under the three different environmental conditions used in the previous Section was predicted using Digimat's elastic-plastic model [5]. The model was calibrated using the reverse engineering option in Digimat-MX described in Section 2.4 [5], with the tensile stress-strain curves obtained by testing dogbone coupons under several machining angles (previously shown in Fig. 3.4). The parameters calibrated for this model are summarised in Table 4.3.

Table 4.3. Additional properties (to the ones presented in Table 4.2) of the fibre and matrix calibrated for Digimat's elastic-plastic model.

	Environmental conditions	23°C-DAM	23°C-RH50	80°C-RH50
Matrix properties	Yield stress σ_Y (MPa)	16.8	15.6	5.2
	Linear hardening modulus k (MPa)	50.0	17.0	64.4
	Hardening modulus R_∞ (MPa)	74.7	38.1	43.1
	Hardening exponent m (-)	110.0	35.5	85.0

4.4.2 Strength model (Tsai-Hill failure criterion)

The Tsai-Hill 3D transversely-isotropic failure criterion integrated in Digimat was also calibrated using the reverse engineering option in Digimat-MX, by determining the parameters X (uniaxial tensile strength), Y (transverse tensile strength) and S (in-plane shear strength) of unidirectional pseudo-grains, as detailed in Section 2.4. The calibrated model was then loaded in Digimat-MF and, to calculate the tensile strength of PA66-GF50 material, a mechanical loading was applied to a RVE having the properties in the calibrated model. These calculations were

implemented for six different machining angles (using the actual overall fibre orientation tensor in the through-the-thickness direction (Fig. 3.3), as done in Section 4.3.1 and 4.3.2).

The obtained results are plotted as a function of α_{YY}, and compared with the experimental results as shown in Fig. 4.7. The tensile strength from the predictions increased with α_{YY} under all the environmental conditions, as expected. These predicted values showed good agreement with the experimental results, with a maximum difference of 4.5%, as summarised in Table 4.4.

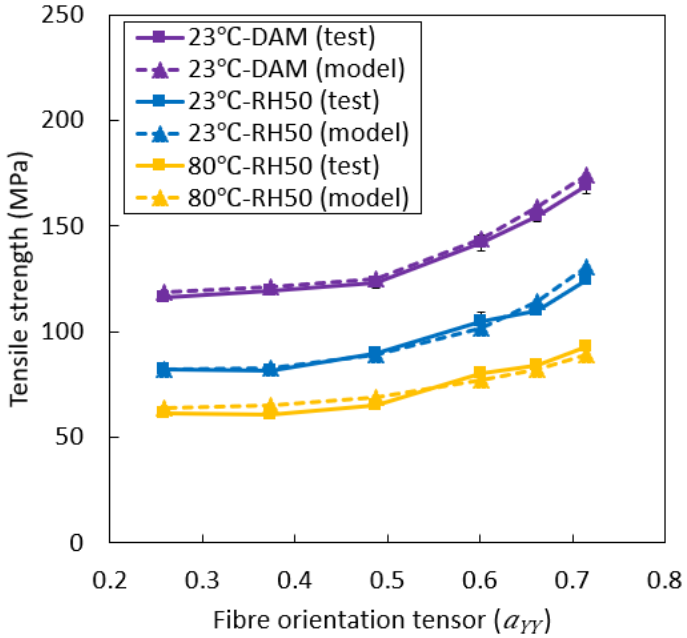


Fig. 4.7. Tensile strength of PA66-GF50 as a function of fibre orientation tensor under the three different environmental conditions from the experiments and prediction using Digimat's elastic-plastic material model in Digimat-MF. All datapoints from experiments have error bars representing one standard deviation (some error bars are sufficiently small to be hidden behind the corresponding datapoint).

Table 4.4. Tensile strength differences between experimentally measured values and predictions using Digimat's elastic-plastic model for PA66-GF50 material.

Environmental conditions	23°C-DAM	23°C-RH50	80°C-RH50
0° (α_{YY} = 0.72)	+ 3.1	+ 5.3	- 4.1
20° (α_{YY} = 0.66)	+ 2.8	+ 3.5	- 2.5
30° (α_{YY} = 0.60)	+ 1.2	- 3.0	- 3.8
45° (α_{YY} = 0.49)	+ 1.3	- 0.5	+ 5.8
60° (α_{YY} = 0.37)	+ 1.2	- 1.8	+ 6.7
90° (α_{YY} = 0.26)	+ 2.3	- 0.4	+ 4.3
<Averaged square root>	2.0	2.4	4.5

(*)The averaged values are calculated as the square root of each squared difference

4.4.3 FE simulations of dogbone coupon's tensile testing

To further validate the state-of-the-art coupled FEA procedure (described in Section 2.6), this Section reports the coupled FE simulation of dogbone coupon testing under quasi-static tension, for different machining angles under the three different environmental conditions (same as those used in the previous Section). This uses the calibrated material model previously described in this chapter, and the process simulation described in Section 4.2.

The mesh and the boundary conditions used in the FE model are shown in Fig. 4.8. The FE model has been entirely meshed with solid 8-node hexagonal elements (C3D8, approximately 0.5 mm wide, with 10 elements through the thickness). One end region was constrained to a main node (RP-1), with a prescribed displacement of 3 mm (allowing only movement along the Y-direction), and the other end region was fully constrained. The fibre orientation tensor fields of the plates predicted in Section 4.2 (Fig. 4.1, using the MRD model) were mapped onto the FE model of the dogbone coupon, and used to calculate the local material properties at each integration point, using Digimat-MAP [5]. Finally, this FE model, including the coupling with the process simulation, was submitted through Digimat-RP and solved by the Abaqus FE Implicit solver.

Fig. 4.9 (a) compares stress-strain curves of dogbone coupons from the experiments and coupled FEA (as well as the outputs from the calibrated Digimat's elastic-plastic model for 0°, 45° and 90° directions under 23°C-DAM condition). These coupled FEA and the model outputs showed good agreement with the initial stiffness and the subsequent non-linear behaviour of the test results. A similar trend was seen in the coupled FEA under 23°C-RH50 and 80°C-RH50 conditions for 0° and 90° directions, as shown in Fig. 4.9 (b) and (c). The points at failure load in the coupled FEA (when F reaches 1) also showed good agreement with the experimental results, within a 6% error in all cases.

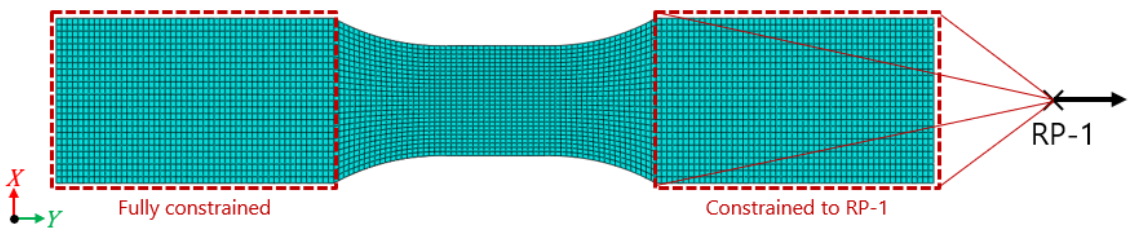


Fig. 4.8. Mesh and boundary conditions used for the FE model of dogbone coupons.

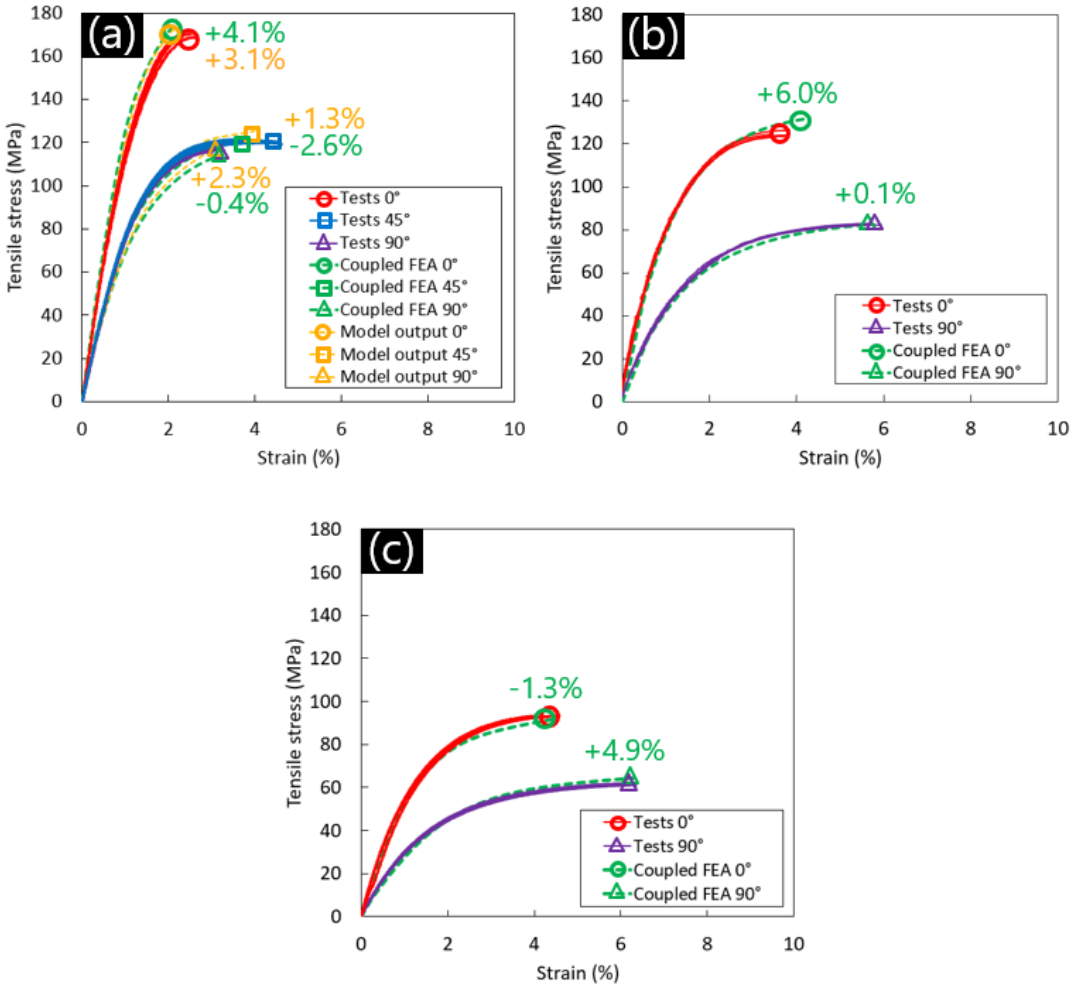


Fig. 4.9. Stress-strain curves of dogbone coupons from the experiments (all the five curves are shown) and the coupled FEA: (a) 23°C-DAM for 0°, 45° and 90° directions, (b) 23°C-RH50 for 0° and 90° directions, and (c) 80°C-RH50 for 0° and 90° directions.
Fig. 4.9 (a) also includes the output from the calibrated Digimat's elastic-plastic model.
The failure points in the experiments are determined to the average values of the five test results.

4.5 Discussion

4.5.1 Prediction of the fibre orientation state in the IM-plates

The fibre orientation state in the plates predicted by the process simulation (shown in Fig. 4.1) captured the experimental observations well, without a significant difference amongst the different fibre orientation models used. Previous literature comparing these fibre orientation models [72,74,75] concluded that the MRD model provided the best accuracy among these models (as described in Section 2.5). Therefore, the MRD model was used in the

subsequent chapters to predict the fibre orientation fields in the subcomponents (Chapter 6) and components (Chapter 7).

4.5.2 Prediction of the coupon's stiffness

The Young's moduli predicted using the nominal inputs (calibrated in Digimat-MX, shown in Fig. 4.4) by Digimat's elastic model captured the effect of fibre orientation on Young's modulus well, compared to experiments. Moreover, the predictions using the nominal inputs for E_{m} (under each environmental condition) showed the smallest errors compared to those using varied E_{m} (Fig. 4.6), indicating that the calibration of the elastic models considers the effect of E_{m} well. Note that the nominal inputs for E_{m} (calibrated in Digimat-MX) are slightly higher than the experimental results of neat PA66 matrix obtained in preliminary work at Asahi Kasei Corporation; however, for within the PA66-GF50 material, the effect of additives (i.e. carbon black), which might increase E_{m}, also needs to be taken into account, and the calibrated E_{m} reasonably considers this effect.

The fibre aspect ratio had different optimal values for the different environmental conditions, as shown in Fig. 4.5 (optimal $A_{\mathrm{r}} = 30$ under 23°C-DAM, and optimal $A_{\mathrm{r}} = 20$ under the other conditions); however, the value of A_{r} needs to be consistent regardless of the environmental conditions, as the conditioning process cannot change the fibre length in the composite. Preliminary experimental work in Asahi Kasei Corporation showed the average fibre aspect ratio in the PA66-GF50 plate was approximately 20-25 (200-250 μm in length, with a diameter of 10 μm); this also justifies the use of calibrated fibre aspect ratio ($A_{\mathrm{r}} = 20$) in the subsequent Chapters. Under 23°C-DAM, the predicted Young's modulus has only a minor dependency on A_{r} (only 0.8% difference between $A_{\mathrm{r}} = 30$ and $A_{\mathrm{r}} = 20$), because the matrix is relatively stiff and, consequently, the effect of the fibre-ends is minimal.

4.5.3 Prediction of the coupon's tensile strength

The tensile strength (Fig. 4.7) and the stress-strain behaviour of PA66-GF50 dogbone coupons (Fig. 4.9) were captured well using the calibrated Digimat's elastic-plastic models. The tensile strength obtained from the calibrated model showed good agreement with the test results, with a maximum error of 6.7% and averaged error of 4.5% (Table 4.4).

The Tsai-Hill criterion, which considers failure initiation only, predicted the failure of PA66-GF50 dogbone coupons well in the coupled FEA, within a 6% error compared to experimental results (Fig. 4.9). This result indicates that the Tsai-Hill initiation criterion is sufficient for simple coupons [63,77]. This is because the failure in dogbone coupons is fully controlled by failure initiation (and therefore any progressive failure would not influence the response): they experience uniform strains in the through-the-thickness direction, and the skins (which are the main load-carrying region of the coupons) have a lower failure strain than the core; therefore the remote stress for failure initiation coincides with final fracture. Similar results have been reported in previous work at the coupon level [63,77].

In addition, the output from Digimat's elastic-plastic model also showed good agreement with the curves from the coupled FEA and the tests (Fig. 4.9 (a)). These observations indicate that the calibration of the models and Tsai-Hill failure criterion was successful. Therefore, these models and failure criterion are utilised in the subsequent Chapters of this thesis. A good reliability of this state-of-the-art simulation framework is expected whenever the maximum load is controlled by failure initiation, as is the case for the dogbone coupons under tension; however, this framework is unable to consider failure propagation, which paves the way to the developments reported in Chapters 5-7.

4.6 Conclusions

The state-of-the-art methodology to simulate IM-SFRPs were calibrated for an injection-moulded PA66-GF50 material, using the experimental characterisation previously reported in Chapter 3. The predicted fibre orientation fields were compared against experiments, and the suitability of this methodology to the PA66-GF50 material was assessed by its ability to recover the elastic, plastic and strength response used in the calibration. The main conclusions in this chapter are summarised as follows:

- All three fibre orientation models tested were able to predict the skin-core microstructure of IM coupons with a simple geometry, with a good agreement with the local fibre orientation tensor distributions observed experimentally across the thickness of the coupons. The MRD model was selected to be used in the coupled FE simulations

in Chapters 5-7, since literature has been shown it to be the most accurate in a wider range of geometries.

- The results from Digimat's elastic model were exactly replicated by a Matlab implementation of the Mori-Tanaka mean-field homogenisation with orientation averaging. The Digimat's elastic model calibrated in Digimat-MX predicted the experimental results very well (within a 8% error for all individual environmental conditions and machining angles); therefore, the elastic properties determined in this chapter for these models will be used in the subsequent Chapters of this thesis.
- Coupled FEA of PA66-GF50 dogbone coupons using the calibrated Digimat's elastic-plastic models captured the stress-strain behaviour very well (within a 6% error of tensile stress at failure) under all different environmental conditions and machining angles, indicating that the calibration of Digimat's elastic-plastic models using experimental stress-strain curves was successful. These calibrations of Digimat's elastic-plastic models will, therefore, be used in the subsequent Chapters of this thesis.
- The Tsai-Hill failure criterion available in Digimat software captured the failure stress of PA66-GF50 dogbone coupons very well (within a 6% error for all individual environmental conditions and machining angles), indicating that the calibration of the Tsai-Hill failure criterion using experimental stress-strain curves was successful. Therefore, this failure criterion will be used in the subsequent Chapters of this thesis for the state-of-the-art prediction of failure of subcomponents (Chapter 6) and components (Chapter 7).

Chapter 5 - Initiation and propagation fracture toughness of IM-SFRPs under different environmental conditions

5.1 Introduction

The fracture toughness (or critical strain energy release rate) governs failure in structures with complex geometries; however, as described in Chapter 2, the experimental characterisation of IM-SFRPs is still rather limited. There are only a few papers characterising the anisotropy of the fracture toughness of IM-SFRPs, and they have been limited to testing under room temperature and dry conditions [18,19]. Moreover, the effect of temperature [32] and moisture [20,21] conditions on the fracture toughness of IM-SFRPs has been reported for one fibre orientation state only.

Using CT tests, the full R-curve (i.e. toughness versus crack length) has been characterised for continuous and discontinuous fibre-reinforced thermoset composites [34–36]. However, despite some literature [18–21,24,30–32] having characterising the tensile initiation fracture toughness of SFRPs, the propagation value of IM-SFRPs has yet to be characterised. Since the propagation fracture toughness is often considerably higher than that for initiation for continuous and discontinuous fibre-reinforced thermoset composites [34,35], using only the initiation fracture toughness may lead to an under-estimation of the damage tolerance of the material and hence to over-designed components.

This chapter focuses on two objectives for the characterisation of the fracture toughness of the PA66-GF50 material used throughout this thesis. Firstly, to characterise the combined effect of fibre orientation and environmental conditions (both temperature and moisture) on the tensile propagation fracture toughness of injection moulded PA66-based SFRPs (this is needed for the coupled FEA as described in Section 2.6). The second objective is to compare the outputs from two data reduction methods (FE-supported compliance calibration and DIC-based J-integral calculation) in terms of the initiation and propagation toughness. Section 5.2 details the experimental methods used to characterise the fracture toughness of the PA66-GF50 material including the data reduction methods. The novel results obtained with these experiments and data reduction methods are described and discussed in Section 5.3 and Section 5.4, respectively,

with the conclusions drawn in Section 5.5. As mentioned in Chapter 2, the term “fracture toughness” is used in the mechanics context, i.e. referring to the critical strain energy release rate (G_c, with units of energy per unit area).

5.2 Experimental details

5.2.1 Fracture toughness testing

There is no standard nor universally-accepted test method to characterise the propagation fracture toughness of SFRPs. Therefore, this work has adopted CT coupons [34], since they have been successfully used to characterise the full R-curves of continuous and discontinuous-fibre composites [35]. The CT coupon geometry was designed through FE simulations, as explained in Appendix B. The final coupon design is shown in Fig. 5.1, which was developed to fulfils the following criteria:

(i) feasibility to machine this geometry from the IM-plates shown in Fig. 3.1;
(ii) no undesirable failure modes (including buckling) predicted by the FE simulation of the CT test;
(iii) the plastic zones predicted by FE simulations were mostly confined to the crack tip and uniformly distributed along the through-the-thickness direction of the coupons;
(iv) post-processing the load-displacement curve predicted by the FE simulation (using cohesive zone modelling) through the compliance calibration method (explained in Appendix A) recovers the input fracture toughness (used in the cohesive elements).

The CT coupons were waterjet-machined from the centre of the injection-moulded PA66-GF50 plates (manufactured in Chapter 3) at several angles (θ) with respect to the main flow direction (as shown in Fig. 5.1). The pre-crack was cut using a V-shaped disk saw, and sharpened with a scalpel using a sawing motion. Some of these CT coupons were conditioned based on ISO1110 for testing under RH50 conditions. The testing specifications are shown in Table 5.1, and the procedures for high temperature testing have been explained in Section 3.2.3.

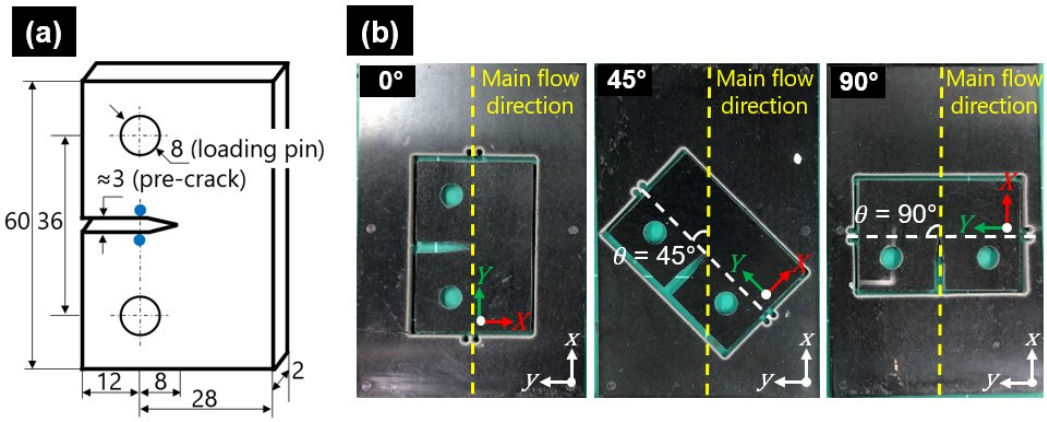


Fig. 5.1. Design of CT coupons: (a) details of the geometry (all dimensions in mm), and (b) definition of the machining angles (relating the plate coordinate system xyz with the coupon coordinate system XYZ). The two blue targets indicate the position to extract the opening displacement from DIC maps.

During the CT testing, the load (P) was applied through continuous quasi-static displacement control of the loading pins. Three-dimensional digital image correlation (3D-DIC) was used to obtain strain and displacement full-field maps on the coupons' surface during the tests. The opening displacement (d_{DIC}, used in the load-displacement curves shown in Section 5.3) was extracted from the DIC maps as the relative displacement between the two targets (distance: 5 mm) on the pre-crack faces that were colinear with the centre of the loading pins (as shown in Fig. 5.1).

Table 5.1. Testing specifications for CT coupons

Number of coupons	Displacement rate (mm/min)	Environmental conditions	Angles (°)
Four per test condition	0.5	23°C-DAM, 23°C-RH50, 80°C-RH50	0, 20, 30, 45, 60, 90

5.2.2 Data reduction of fracture toughness tests

5.2.2.1 FE-supported compliance calibration method

An FE-based compliance calibration method [35] was used to estimate the full R-curves of the PA66-GF50 material from two non-full-field test outputs: the opening displacement d_{DIC} and the corresponding applied load P. The FE models used for compliance calibration considered the orthotropy of elastic properties (Young's modulus, shear modulus and Poisson's

ratio) and how they were affected by machining angle, moisture level, and temperature (as described in Appendix A). These elastic properties were obtained from Digimat's elastic material model calibrated in Chapter 4.

5.2.2.2 DIC-based J-integral calculation method

The J-integral method used to calculate the R-curves from the experimental data required a line contour to be defined which fully enclosed the non-linear zone around the crack tip. This requirement was investigated using the coupled FEA, which considers the non-linear response of the PA66-GF50 material, using Digimat's elastic-plastic material model calibrated in Chapter 4. The plastic zones predicted by these coupled FEA (as detailed in Appendix C) suggested that the contour shown in yellow in Fig. 5.2 was suitable to evaluate the J-integral. Moreover, the experimentally-measured stress-strain curves revealed that the material remained linear-elastic below an applied strain of 0.4% (for all machining angles and environmental conditions used in this work). Therefore, from interpreting the DIC strain maps, it was concluded that the principal strain along the contour shown in Fig. 5.2 was consistently below the elastic threshold of 0.4% for all stages of the tests, further supporting this choice of J-integral contour.

The J-integral was calculated (using Matlab) from the expression for the line integral formulated by Catalanotti et al. [89], assuming that the crack lies in the X-axis:

$$J = \frac{1}{2}\int_{\Gamma^0} \{\sigma\}\{\varepsilon\}^{\mathrm{T}} n_X - 2\left\{\frac{\partial u}{\partial X}\right\}^{\mathrm{T}} [\sigma]\{n\}\,\mathrm{d}s, \tag{5.1}$$

where Γ^0 is the contour enclosing the crack (shown in Fig. 5.2), $\{n\} = \{n_X, n_Y\}$ is the outward normal to Γ^0, $\mathrm{d}s$ is the increment of arc length; the displacement ($\{u\} = \{u_X, u_Y\}$) and strain ($\{\varepsilon\} = \{\varepsilon_{XX}, \varepsilon_{YY}, \gamma_{XY}\}$) fields were provided by the DIC results, and the stresses $\{\sigma\} = \{\sigma_{XX}, \sigma_{YY}, \sigma_{XY}\}$ were computed as $\{\sigma\} = [\mathbf{D}]\{\varepsilon\}$, where $[\mathbf{D}]$ is the elastic stiffness matrix. The crack growth during the tests was monitored visually by measuring the length between the original position of the crack tip (origin of the coordinate system in Fig. 5.2) and the position of the crack tip (detected visually) at each time step in the DIC images.

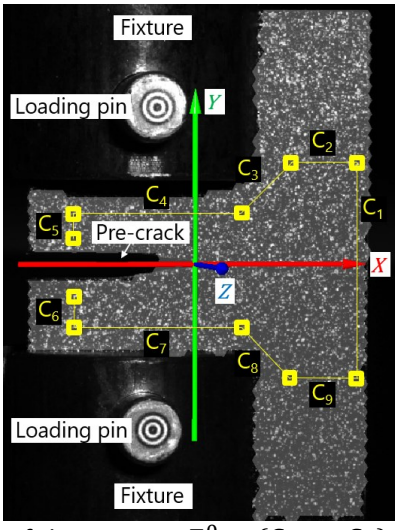


Fig. 5.2. Definition of the contour $\Gamma^0 = \{C_1, \dots, C_9\}$ in the CT coupons, used for the J-integral calculation.

5.2.3 Fractography

The fracture surfaces of the CT coupons were mounted on stubs using carbon-black-loaded epoxy adhesive. The damage mechanisms on the fracture surfaces were examined using a Hitachi S-3700 SEM with an acceleration voltage of 12 kV. The coupons were sputter coated with gold for 15s.

5.3 Results

5.3.1 Fracture toughness

Representative load-displacement curves of CT coupons tested at different machining angles and environmental conditions are shown in Fig. 5.3 (a)-(c). All coupons exhibited stable crack propagation (with a gradual decrease in the load after the peak). The peak load was the highest for the coupons machined at a 0° angle, and progressively decreased with increasing machining angles. For a given machine angle, the peak load decreased with an increase in moisture content or temperature. Fig. 5.3 (d) shows all four load-displacement curves at 0° and 90° for 23°C-DAM condition; it demonstrated that these tests were repeatable.

Fig. 5.4 shows representative and repeatable R-curves of tested CT coupons at different machining angles, for all environmental conditions, calculated using the compliance calibration method. For all cases tested, the initial part of the R-curves gives the impression that crack

initiation started when the strain energy release rate was zero, and that crack propagation occurred from the very beginning of the loading in all cases. However, this is a spurious result due to the use of linear-elastic FE models in the compliance calibration process. In the experiments, the compliance increased progressively even before crack initiation, due to the highly non-linear material response. The compliance calibration process incorrectly interpreted this increase in compliance as an increase in crack length. Therefore, the initial behaviour shown in the compliance-calibration R-curves is not strictly correct, as is shown following post-processing of the experimental data with the J-integral method instead (later in this Section).

Regardless of this problem affecting the initial part of the R-curves in Fig. 5.4, the energy release rate did reach a plateau for all cases; this plateau was taken as the propagation toughness for the compliance calibration method. This revealed a clear effect of the machining angle on the propagation toughness, which was a maximum at 0° and decreased with increasing machining angle. The propagation toughness increased with an increase in moisture content and in testing temperature.

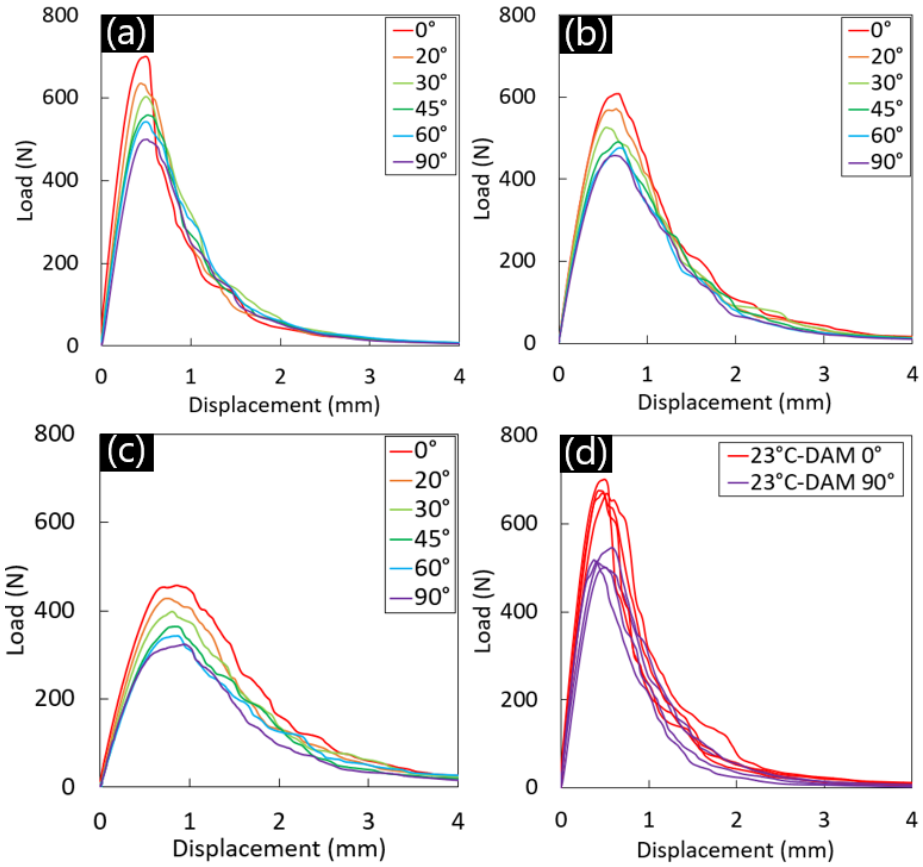


Fig. 5.3. Representative load-displacement curves of PA66-GF50 CT coupons at different machining angles: (a) 23°C-DAM, (b) 23°C-RH50 and (c) 80°C-RH50, and (d) all four load-displacement curves at 0° and 90° for 23°C-DAM condition.

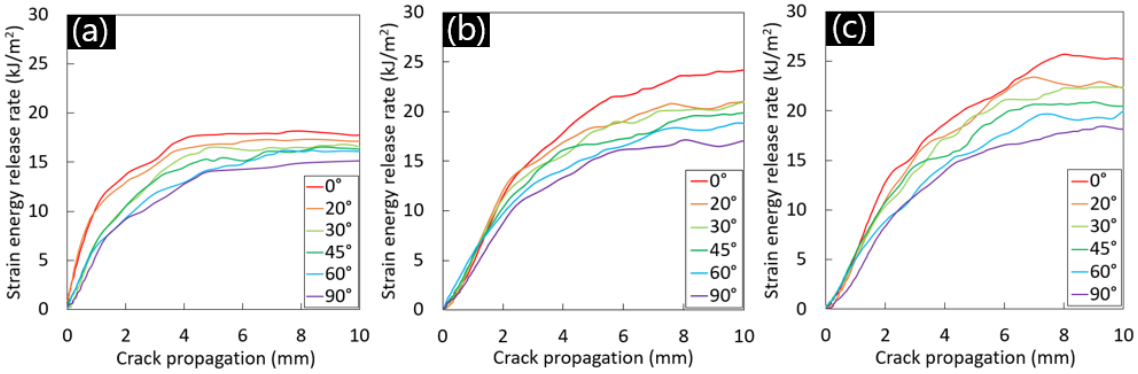


Fig. 5.4. Representative R-curves of PA66-GF50 CT coupons at distinct machining angles using the compliance calibration method: (a) 23°C-DAM, (b) 23°C-RH50 and (c) 80°C-RH50.

The R-curves obtained from the compliance calibration and those from the J-integral method (for the 0° machining angle, under all environmental conditions) are compared in Fig. 5.5. This result demonstrates that these R-curves were repeatable amongst nominally-identical coupons for all cases (although the R-curves calculated through the J-integral method were noisier). Since crack growth was monitored visually in the J-integral method, there was no spurious crack growth in the initial part of the R-curves, and it was possible to identify the initiation fracture toughness as the value of the J-integral when crack propagation was first detected in the DIC images. The propagation toughness was calculated by averaging the values of the J-integral in the plateaued region of the R-curves.

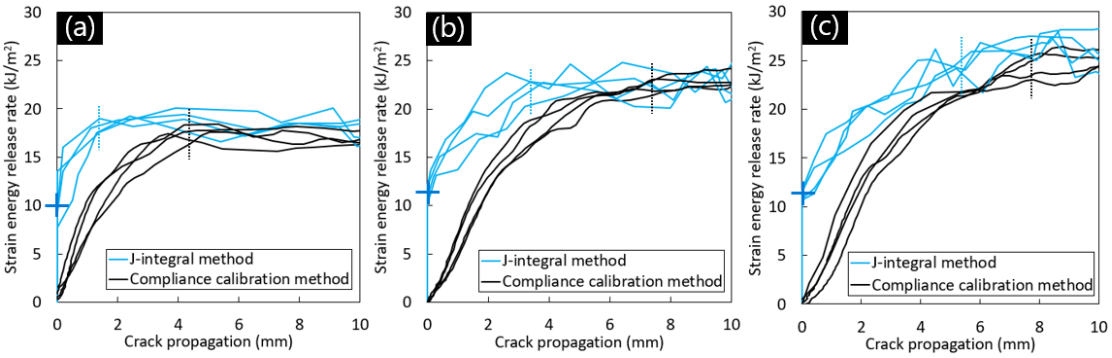


Fig. 5.5. Comparison of R-curves calculated using the compliance calibration and J-integral methods for 0° coupons: (a) 23°C-DAM, (b) 23°C-RH50 and (c) 80°C-RH50.
Each cross at 0-mm crack propagation corresponds to the average initiation fracture toughness under each environmental condition, measured with the J-integral method. The dotted vertical lines identify the beginning of the plateaued toughness values (which were averaged to calculate the propagation fracture toughness under each environmental condition).

Fig. 5.6 shows the initiation fracture toughness for the 0° coupons, where no significant effect of environmental conditions was found. It also compares the propagation toughnesses calculated with the compliance calibration against those from the J-integral method, which were almost equivalent under all environmental conditions (for the 0° coupons).

The propagation fracture toughness (calculated through the compliance calibration method) as a function of machining angle θ is shown in Fig. 5.7 (a). However, since the fibres in the coupons were not all aligned in one direction (due to the skin-core microstructure illustrated in Fig. 3.3 in Chapter 3), using the machining angle θ as the independent variable does not directly characterise the relationship between fracture toughness and fibre orientation. Therefore, the propagation fracture toughness as a function of homogenised fibre orientation component along the loading direction, $a_{YY}(\theta)$ (characterised in Section 3.3.2), were also presented in Fig. 5.7 (b): the fracture toughness increased with an increase in a_{YY}, moisture content and temperature. Previous research has proposed an exponential [90] or a bilinear (with a transition point at $a_{YY} = 0.6 - 0.9$) [18] fit for the relationship between energy dissipation and fibre orientation in short-fibre composites; however, no such trends were presented in Fig. 5.7.

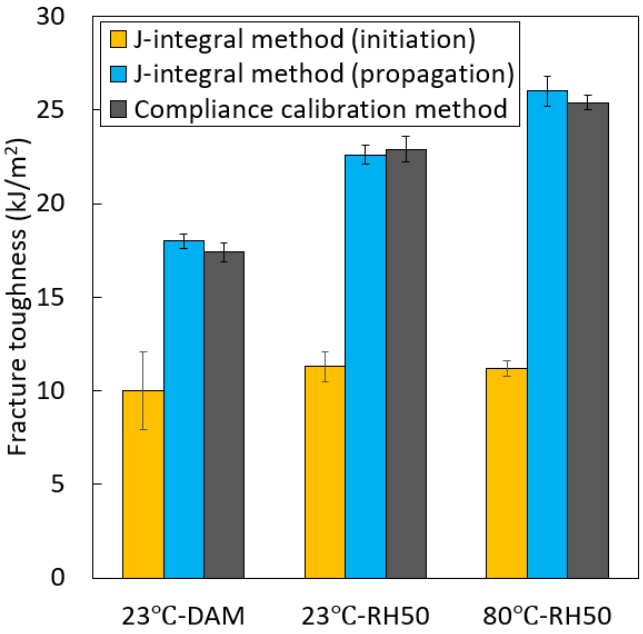


Fig. 5.6. Initiation and propagation fracture toughness of 0° coupons calculated using the compliance calibration and J-integral methods. Error bars represent one standard deviation.

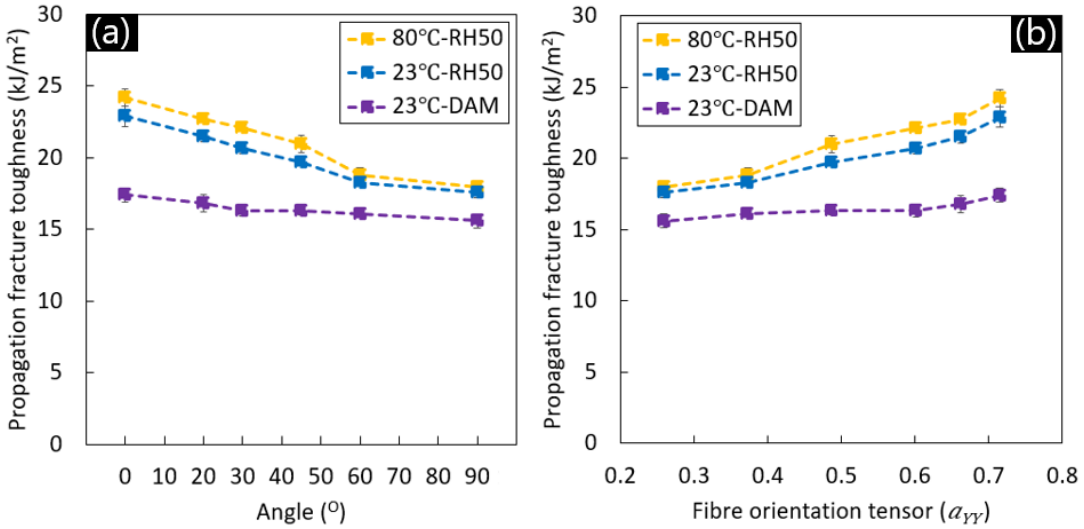


Fig. 5.7. Propagation fracture toughness as a function of machining angle (a) and fibre orientation tensor (b) at different environmental conditions, calculated using the compliance calibration method. All datapoints have error bars representing one standard deviation.

5.3.2 Fractography

Fig. 5.8 shows details of the CT coupons at the crack plane following testing at 23°C-DAM conditions. The macroscopic crack direction was slightly influenced by the machining angle and the local fibre orientation in the coupon. Relative to the pre-crack direction, crack propagation randomly deviated upwards or downwards in the 0° coupons, deviated upwards in 45° coupons (i.e. towards the main fibre direction), but no deviation in the 90° coupons. These crack propagation trends were consistently observed for all the environmental conditions.

Representative scanning electron micrographs of the fracture surfaces of CT coupons (in the skin region, crack propagation site) after the tests under 23°C-DAM conditions, for the different machining angles, are shown in Fig. 5.9. Large plastic deformation of the PA66 matrix with good interfacial adhesion was observed in all angles. It was also noted that failure of the skin region of the coupons was dominated by fibre tension in the 0° coupons (where the fibres were preferentially aligned across the crack faces), then shifting to matrix shear failure in the 45° coupons (where the fibres were preferentially aligned diagonally with respect to the crack faces), and to matrix transverse tension failure in the 90° coupons (where the fibres were preferentially aligned along the crack faces).

Representative scanning electron micrographs of the fracture surfaces of the 0°, 45° and 90° coupons (in the skin region, crack propagation site) tested under different environmental conditions are shown in Fig. 5.10. Both fibre-matrix interfacial debonding and permanent deformation of the PA66 matrix were more dominant at 23°C-RH50 and 80°C-RH50 conditions than at 23°C-DAM.

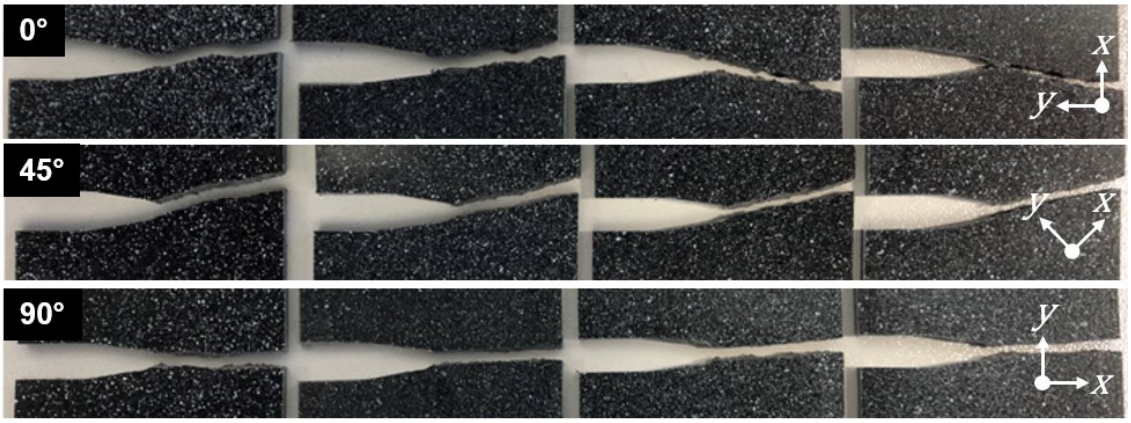


Fig. 5.8. Photographs of crack plane in CT coupons (four replicates) machined at 0°, 45° and 90°, after compact tension testing at 23°C-DAM.

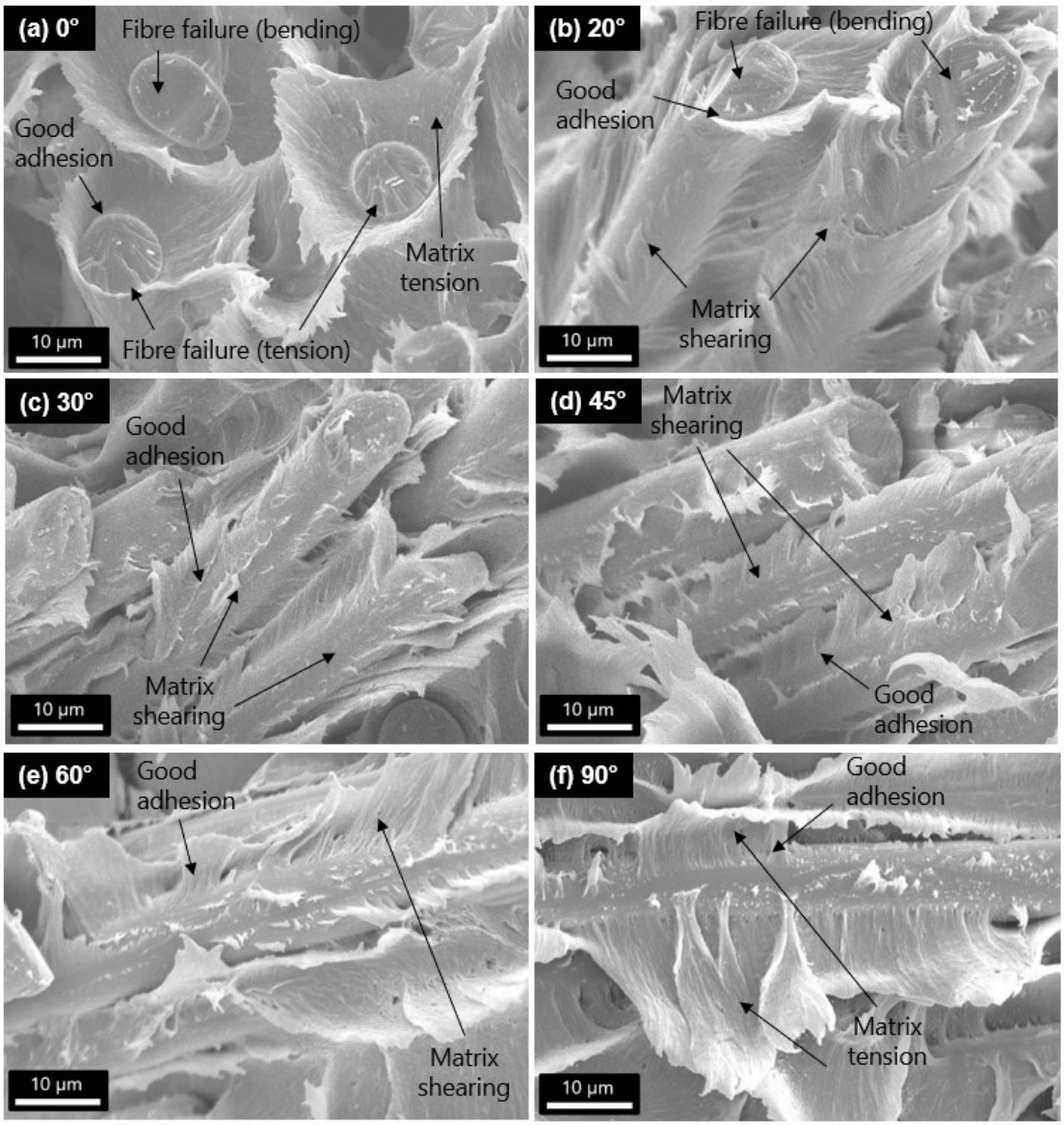


Fig. 5.9. Electron micrographs of the fracture surfaces of CT coupons (in skin, propagation site) after testing at 23°C-DAM conditions, for all machining angles (θ) tested: (a) 0°, (b) 20°, (c) 30°, (d) 45°, (e) 60°, (f) 90°.

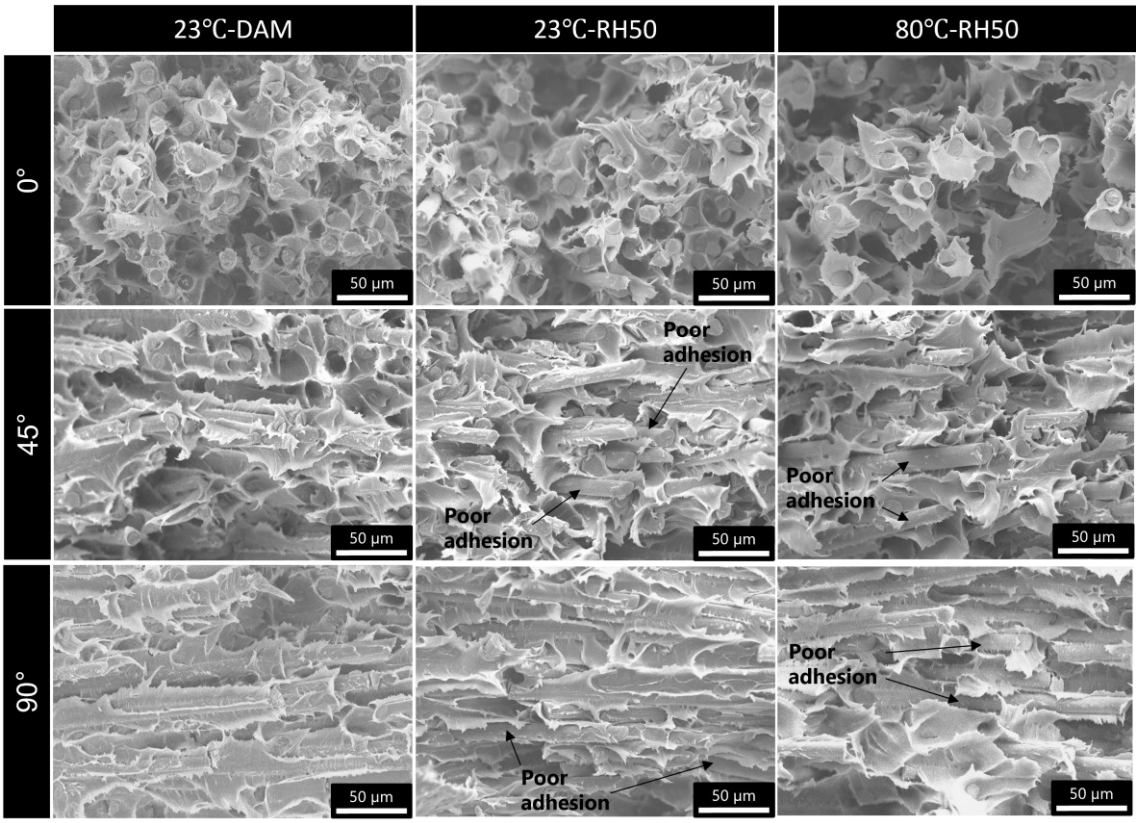


Fig. 5.10. Scanning electron micrographs of fracture surfaces of the CT coupons (in skin, propagation site) after compact tension testing under different environmental conditions, for three several machining angles.

5.4 Discussion

5.4.1 Methodology for measuring fracture toughness in SFRPs

This work proposes new methodologies to measure full R-curves, initiation and propagation values of the fracture toughness of injection-moulded PA66-GF50. Considerations for the coupon design and test protocols were defined in Section 5.2.1 (and further detailed in Appendix B), and the data reduction processes were described in Section 5.2.2.

The R-curves were calculated using both an FE-assisted compliance calibration method and a fully experimental J-integral method. The comparison between the results from these two methods (Fig. 5.5) demonstrated that, although the compliance calibration method could not characterise the initial part of R-curves accurately, both methods showed consistent values for the propagation toughness. Moreover, the J-integral method could also characterise the initiation toughness and a reliable shape of R-curves of IM-SFRPs (Fig. 5.5 and Fig. 5.6).

Regarding the relative usability of these methods, the compliance calibration method requires load-displacement curves and elastic FE models, while the J-integral method requires full-field DIC strain/displacement maps and a calculation algorithm. Therefore, future users are able to select one of these methods, depending on the equipment and expertise available, and also on the properties they are aiming to characterise.

To verify the representativeness of the fracture toughness measurements shown in Section 5.3.1, FE simulations of the CT tests were conducted using the experimentally-measured fracture toughness values as inputs for Cohesive Zone Modelling (CZM), as detailed in Appendix C. Fig. 5.11 compares the experimental load-displacement curves of the CT coupons with those predicted by the FE simulations, using three different cohesive laws: a bilinear law using either (i) the initiation toughness or (ii) the propagation toughness, and (iii) a trilinear law calibrated with the experimental R-curves from the J-integral method (and the crack-opening displacement at the transition to the propagation stage, as detailed in Appendix C). The results indicate that considering the initiation fracture toughness was sufficient to predict the maximum load in the CT coupons; however, considering the propagation fracture toughness is required to predict accurately the work of fracture of the coupons. These results agree with the previous literature using bilinear and trilinear laws for CT coupons of unidirectional carbon fibre reinforced epoxy composites [82]. This is likely the governing design criterion for energy absorption structures as used in, for example, automotive applications.

The fracture toughness measured from the CT tests in this work is assumed to be geometry independent, with the following reasoning:

- Size effect for the out-of-plane direction (e.g. a transition between plane stress and plane strain states, as observed in metals) can be ignored in fibre-reinforced composite materials, as plastic deformation of the matrix is constrained by the fibres. Moreover, the thickness of IM-plates affect their microstructure (and therefore the mechanical properties) [14]; it is not realistic to change the thickness of IM-plates to experimentally characterise its effect in isolation;
- Previous literature showed that fracture toughness measured from CT tests is size-independent, as far as the size of coupon is large enough [34]. In this work, the plastic zones in the CT coupons predicted by FE simulations were confined to the crack tip and uniformly distributed along the through-the-thickness direction (Figs. B.1 and B.2 in Appendix B); this indicates the size effect for in-plane directions can be ignored;

- Post-processed results through the compliance calibration method could recover the input fracture toughness (used in the cohesive elements).

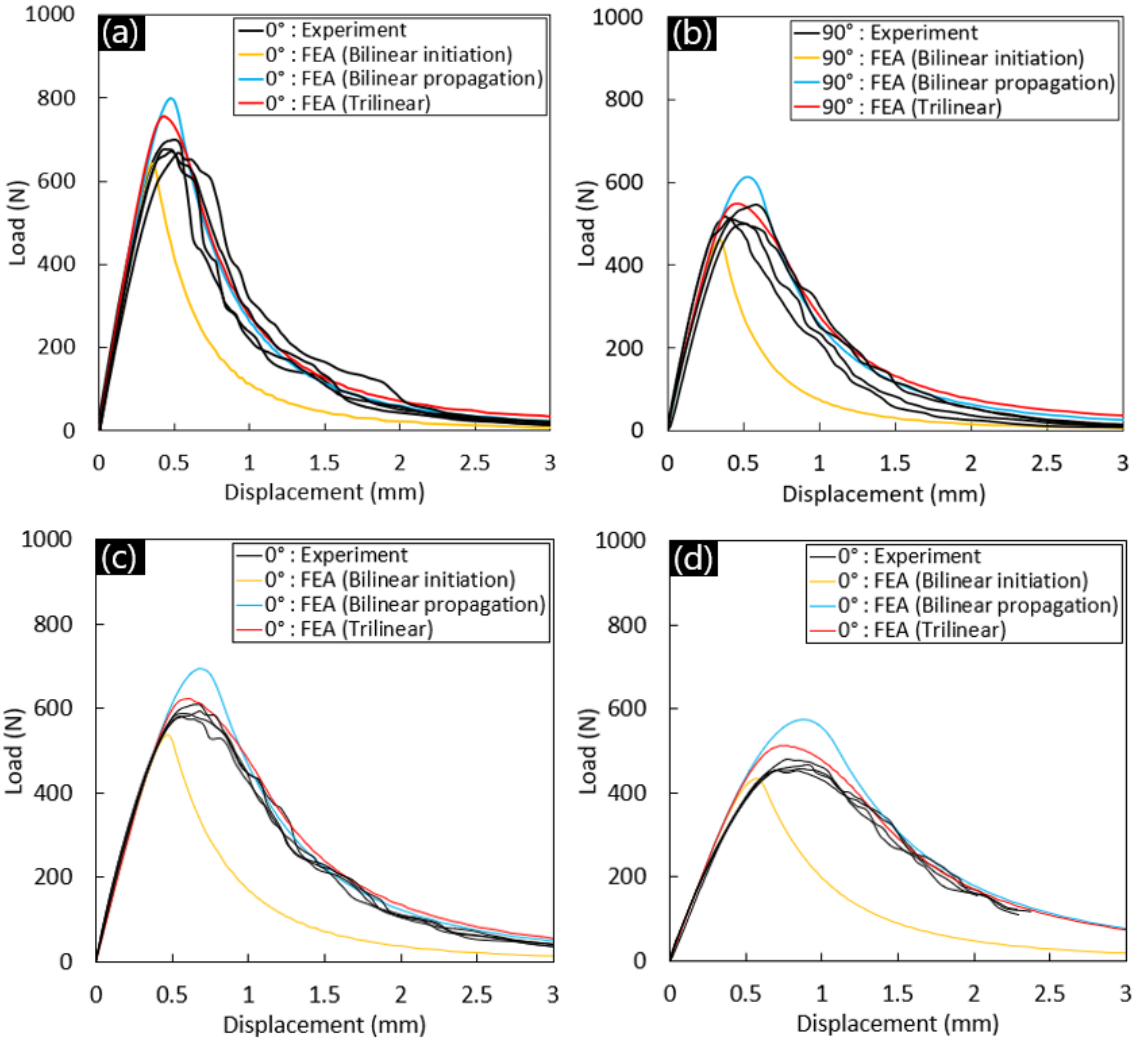


Fig. 5.11. Load-displacement curves of CT coupons comparing results from the experimental tests and FE simulations using bilinear and trilinear cohesive laws: (a) at 0° under 23°C-DAM, (b) at 90° under 23°C-DAM, (c) at 0° under 23°C-RH50, and (d) at 0° under 80°C-RH50.

5.4.2 Fibre orientation and environmental effects on the fracture toughness of SFRPs

Combining fracture toughness measurements (Fig. 5.7) and fractography of CT coupons tested under 23°C-DAM conditions (Fig. 5.9) revealed why the fracture toughness of PA66-GF50 varied with the fibre orientation (the load-aligned tensor component, a_{YY}, shown in Table 3.6). When the fibres were mostly aligned in the loading direction (i.e. in the 0° coupons, with a fibre orientation component $a_{YY} = 0.72$), the fracture toughness was a maximum and failure was fibre-dominated; this is attributed to extra energy having been dissipated by pull-out of the

fibres aligned at 0°, as each fibre failed individually in a different plane, which led to significant plastic deformation of the matrix around the fibre-breaks. When the fibres were mostly aligned across the loading direction (i.e. in the 90° coupons, with a fibre orientation component $a_{YY} = 0.26$), the fracture toughness was a minimum and the failure was matrix-dominated. In this instance the pull-out energy was minimised, and the main toughening mechanism was plastic deformation of the matrix [53,91].

The homogenisation (or averaging) of the fibre orientation tensor across the thickness of coupons and its use to characterise fracture toughness is only meaningful under two assumptions: (i) all points across the thickness of the coupons experience similar strain states, and (ii) the toughness can be approximated by mean field homogenisation of their values in the skins and core. Both assumptions are reasonable for the CT coupons used in this research, since they experience longitudinal strains which are fairly uniform across the thickness, and the fracture toughness should be well modelled by Voigt's rule of mixtures [18]. However, these average toughnesses will have to be de-homogenised (to capture the difference between skins and core) for more complex loading cases (e.g. bending), as will be discussed in the analysis of the subcomponents/components described in Chapter 6 and Chapter 7.

The fractographic results for the CT coupons tested under the different environmental conditions (Fig. 5.10) also illustrated why the fracture toughness increased with increasing moisture and temperature (as shown in Fig. 5.7). Plastic deformation of the PA66 matrix was much more significant under 23°C-RH50 and 80°C-RH50 conditions than under 23°C-DAM, thus dissipating more energy under wet conditions [21]. In addition, there was a slightly higher prevalence of interfacial debonding under 23°C-RH50 and 80°C-RH50 than under 23°C-DAM, which could have promoted more extensive pull-out (and, therefore, further energy dissipation) under wet conditions.

The polyamide matrix allows for hydrogen-bonding due to the heavily polar nature of the amide groups. The availability of these bonds mainly in the amorphous region promotes water absorption, which increases the PA66 molecular chain mobility, and therefore leads to softer and more ductile behaviour of the PA66 matrix [92–96]. This justifies, at a chemical level, both the increase in fracture toughness (Fig. 5.7) and the much more significant plastic deformation (Fig. 5.10) observed under 23°C-RH50 and 80°C-RH50 conditions, compared to the more brittle behaviour observed under 23°C-DAM conditions.

5.4.3 Justification of bending fibre-failure morphologies under tensile loading

Some fibre fractures shown in Fig. 5.9 were consistent with localised failure under flexure, which is often associated with compressive loading (especially for continuous-fibre composites with aligned fibres, where compressive failure occurs through fibre kinking [34]). However, a crack propagating in a CT coupon experiences a tensile rather than a compressive macroscopic stress state, so the presence of these flexural features needs to be explained.

A likely explanation is that the fibres exhibiting bending fracture surfaces were slightly misaligned with respect to the local crack opening direction, and therefore experienced bending during the pull-out process. This process is illustrated in the schematic in Fig. 5.12, and is related to the "snubbing effect" that has been widely observed in randomly-oriented short-fibre composites [97–100].

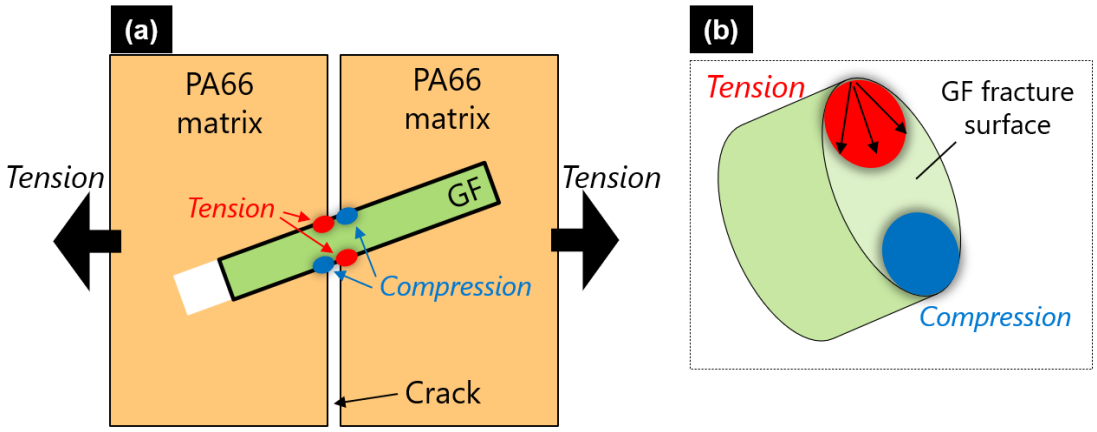


Fig. 5.12. Schematic illustration of stress distributions leading to fibre-failure under bending: (a) in an aligned fibre embedded in PA66 matrix, (b) on a fibre fracture surface.

5.4.4 Novelty and implications

The main contributions of the research reported in this Chapter, including the novelty and the potential impact, are summarised as follows:

1. The results reported in this Chapter has provided the first characterisation of the fracture toughness of IM-SFRPs under the combined effect of fibre orientation, moisture level, and temperature (Fig. 5.7): previous research [18,20,21,32] had focused only on (i) the effect of fibre orientation under 23°C-DAM conditions, or (ii) the effect of temperature or moisture level on the toughness at one fibre orientation state only.

2. This is the first characterisation of the full R-curve (including a propagation fracture toughness value) of IM-SFRPs, thus progressing over previous research which has focused only on initiation [18–21,24,30–32] or average [19,25–29] fracture toughnesses. Fig. 5.6 demonstrates the importance of characterising the propagation fracture toughness in IM-SFRPs, which was at least 80% higher than the initiation fracture toughness (for 0°-coupons). This can significantly influence the industrial design of damage-tolerant and energy-absorbing components (e.g. as commonly used in automotive components).

3. The comparison between the two fracture toughness data reduction methods (FE-supported compliance calibration and DIC-based J-integral calculation, Fig. 5.6) showed that both methods (applied here to IM-SFRPs for the first time) deliver the same propagation fracture toughnesses, although only the J-integral method can measure the initiation toughness. This result enables users to select the most suitable method for their needs. The J-integral method requires full-field DIC measurements and tracking of the crack tip, but provides full R-curves. On the other hand, the compliance calibration method only requires global load-displacement curves, but only provides a reliable value of the propagation toughness.

4. Whilst previous research on the fracture toughness of IM-SFRPs has focused only on the experimental characterisation, the FE simulation presented in Section 5.4.1 demonstrates that the fracture toughness characterised by CT tests can be effectively used in FE simulations with cohesive zone modelling. These FE simulations are able to predict not only the peak load but also the subsequent gradual load decrease in load-displacement curves observed experimentally, as well as the work of fracture.

5.5 Conclusions

This chapter has characterised the fracture toughness of injection moulded PA66-GF50 under the combined effect of fibre orientation, moisture level and temperature. The conclusions can be summarised as follows:

1. The fibre orientation had a significant effect on the propagation fracture toughness of IM-SFRPs: the toughness decreased by 12% when the fibre orientation component across the notch direction decreased from $a_{YY} = 0.72$ (corresponding to 0° coupons) to $a_{YY} = 0.26$ (corresponding to 90° coupons) in 23°C-DAM conditions. This fibre orientation effect was

explained by a shift in damage mechanisms observed through fractography, dominated by fibre pull-out and matrix tensile failure at 0°, by plastic matrix shearing at 45°, and by matrix tensile failure at 90°.

2. Environmental effects are significant to the propagation fracture toughness, which increased by 31.6% from a DAM condition to RH50 at room temperature, and by 9.6% from 23°C to 80°C under RH50 conditions, for the 0° coupons. For the 90° coupons, the toughness increased by 12.8% from DAM to RH50 (under 23°C), and by 3.7% from 23°C to 80°C (under RH50). However, there was no effect of environmental conditions on the initiation toughness.

3. The propagation fracture toughness was between 80% and 132% higher than the initiation fracture toughness, which indicated that it is important to measure not only the initiation fracture toughness but also the propagation fracture toughness for SFRPs.

4. Propagation fracture toughness calculated using the FE-supported compliance calibration method were in good agreement with those calculated via the DIC-based J-integral method; the latter can output the initiation toughness and the full R-curve as well, but requires full-field DIC measurements and tracking the crack tip optically.

5. Both the initiation and propagation fracture toughnesses are needed to predict the response of IM-SFRP coupons with severe geometric notches, and have been successfully demonstrated to be suitable inputs for trilinear cohesive laws in FE simulations.

This chapter proposed a methodology to characterise the full R-curves of IM-SFRPs, and provided the first full dataset for the fracture toughness of PA-GF IM-SFRP under the combined effect of fibre orientation, moisture level, and temperature. This methodology and its results can therefore support industry to design safer and more efficient damage-tolerant IM-SFRP components, as will be illustrated in Chapters 6 and 7.

Chapter 6 - Predicting failure in injection-moulded short-fibre subcomponents under varied environmental conditions through fracture mechanics

6.1 Introduction

When designing IM-SFRP components, it is necessary to predict when and where failure will occur using FEA. The state-of-the-art coupled FEA (reviewed in Section 2.6) predicts the initial stiffness and the subsequent non-linear behaviour well, at both coupon and component levels [16,76,77,79,80]. However, existing failure criteria for IM-SFRPs (e.g. the Tsai-Hill criterion [5,16]), which consider failure initiation only and neglect the finite toughness of the material, often under-predict the failure load in components (as described in Section 2.6). Despite some literature [16,76,77,79,80,101] using coupled FEA for IM-SFRPs, the material's progressive failure (i.e. finite fracture toughness) is yet to be considered in such coupled FEA. This leads to overly conservative design, and hence excessively heavy and costly components in industry.

Chapter 3 and Chapter 5 have quantified how the elastic moduli, tensile strength and fracture toughness of IM-SFRPs decrease with increasing machining angle (and, therefore, with a reduction of the fibre orientation component along the loading direction). These measurements have been done at coupon level, which have a relatively uniform skin-core microstructure. However, more complex fibre orientation states and loading conditions need to be considered at the (sub)component level [79,101–103]. There is no literature on combining the characterisation of damage mechanisms with the prediction of sequence of failure events for IM-SFRPs at (sub)component level. (Sub)components are more challenging than coupons because they have more complex and non-uniform microstructure across the whole geometry, and typically combine different damage mechanisms in a complex sequence of failure events.

The T-M equivalence concept introduced in Section 2.2 has been verified in for the elastic modulus and the tensile strength of PA66-GF50 coupons in Chapter 3. These observations agree with the conclusions from previous literature using IM-SFRP coupons [50–52]; however, the concept of T-M equivalence has not been investigated for the fracture toughness or any mechanical behaviour at the subcomponent/component level.

Therefore, this chapter focuses on the experimental testing and FE simulations of PA66-GF50 subcomponents with the following objectives: (i) to develop a new FE methodology to predict failure of IM-SFRPs more accurately by accounting for the material's progressive failure through CZM, (ii) to validate the sequence of failure events predicted by the FE simulations using fractography, and (iii) to validate the T-M equivalence for fracture toughness at coupon level and the mechanical response at subcomponent level. Section 6.2 presents the additional fracture toughness characterisation using CT tests (required to provide the inputs for the coupled FEA). Section 6.3 then explains the experimental methods to manufacture and test IM-SFRP subcomponents, with the novel results detailed in Section 6.4. Section 6.5 describes the methodologies for virtual testing of the IM-SFRP subcomponents, with FE simulation results detailed in Section 6.6. The results are discussed in Section 6.7, and conclusions drawn in Section 6.8.

6.2 Coupon characterisation

In addition to the characterisation of the fracture toughness of PA66-GF50 presented in Chapter 5 (under 23°C-DAM, 23°C-RH50 and 80°C-RH50), further CT tests were performed under 60°C-DAM and 120°C-DAM, using the methodology detailed in Chapter 5 and the compliance calibration data reduction method. These new environmental conditions were selected as they were anticipated to be approximately equivalent to 23°C-RH50 and 80°C-RH50 (respectively), because the shift of the glass transition temperature from DAM to RH50 conditions is ΔT_g =38.9°C (as already shown in Fig. 3.8 for the Young's modulus, tensile strength, and failure strain). This additional characterisation was performed for two reasons: (i) to verify the robustness of the new FE methodology developed in this chapter with five distinct environmental conditions, and (ii) to discuss the T-M equivalence for the fracture toughness of the PA66-GF50 material.

The propagation fracture toughness (calculated through the compliance calibration method) under the five different environmental conditions, as a function of homogenised fibre orientation component along the loading direction, $a_{YY}(\theta)$ (characterised in Section 3.3.2), is shown in Fig. 6.1. The fracture toughness increased with an increase in a_{YY}, moisture content and temperature. The fracture toughness obtained under 23°C-RH50 and 60°C-DAM, and

obtained under 80°C-RH50 and 120°C-DAM were very similar to each other (though there is a small mismatch between 80°C-RH50 and 120°C-DAM).

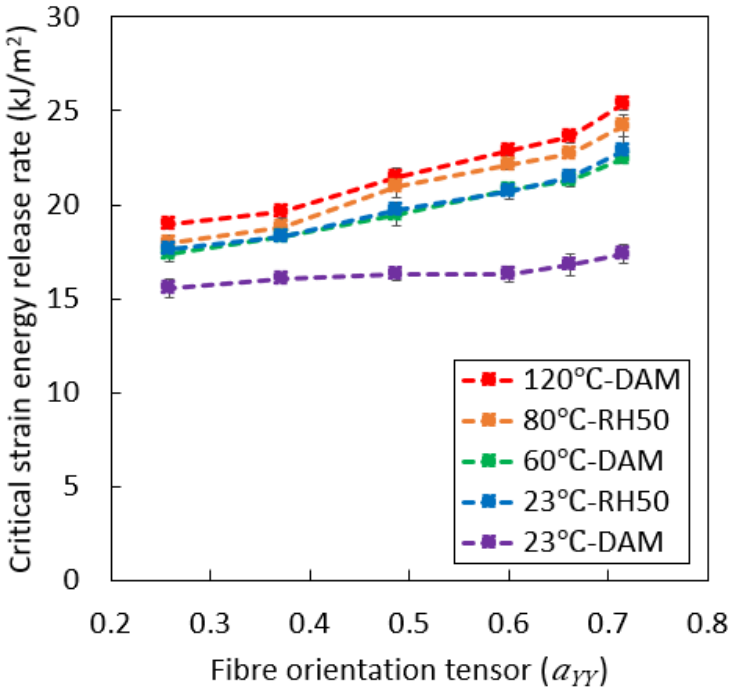


Fig. 6.1. Propagation fracture toughness of PA66-GF50 as a function of fibre orientation tensor, for five different environmental conditions.
All datapoints have error bars representing one standard deviation (some error bars are sufficiently small to be hidden behind the corresponding datapoint).
(*) The results under 23°C-DAM, 23°C-RH50 and 80°C-RH50 conditions have been presented in Chapter 5; the results under 60°C- and 120°C-DAM are new to this chapter.

6.3 Experimental methods for subcomponents

6.3.1 Manufacturing of IM-SFRP subcomponents

PA66-GF50 subcomponents (shown in Fig. 6.2) were manufactured with the same material as that used for the coupons (Chapters 3-5), by injection moulding using a SE130D (SUMITOMO) machine, with the moulding conditions specified in Table 6.1. The geometry of the subcomponents has been selected to be representative of automotive engine mounts manufactured by Asahi Kasei Corporation. Some injection-moulded subcomponents were stored in aluminium-lined bags to maintain them at DAM conditions, whilst others were conditioned based on ISO1110 [83] for testing at RH50.

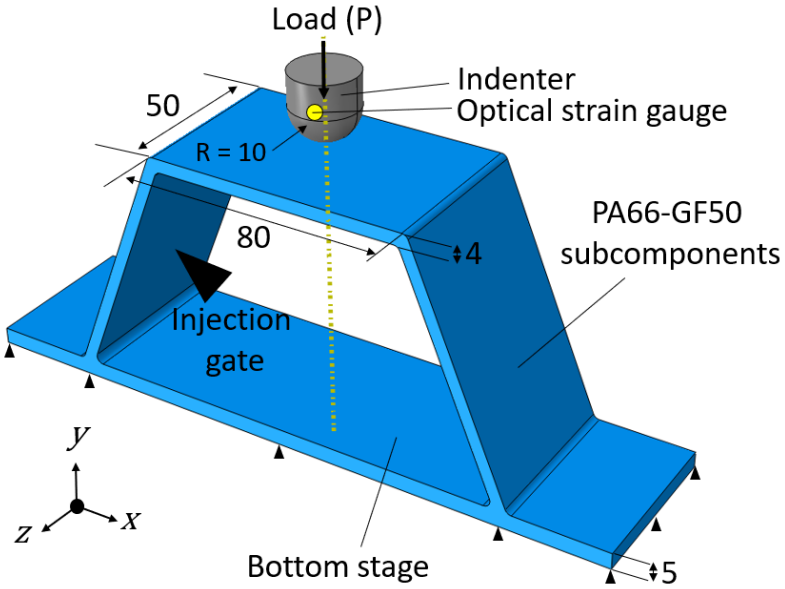


Fig. 6.2. Geometry of the subcomponents, boundary conditions and testing set up (all dimensions in mm).

Table 6.1. Injection moulding parameters for the subcomponents

Cylinder temp. (°C)	Mould temp. (°C)	Injection time (s)	Holding pressure (MPa)	Cooling time (s)
290	90	3.0	70	30

6.3.2 Static indentation test of IM-SFRP subcomponents

The subcomponents were tested by applying a load (P) through continuous quasi-static displacement control of the indenter along the negative y direction, with an optical strain gauge to track the displacement of the indenter, as shown in Fig. 6.2. The bottom stage of the subcomponent was supported by the lower face of the testing machine. The testing specifications are shown in Table 6.2, and the procedures for high temperature testing have been explained in Section 3.2.3.

Table 6.2. Testing specifications for PA66-GF50 subcomponents.

Number of subcomponents	Cross head speed (mm/min)	Environmental conditions
Five per test condition	1.0	23°C-DAM, 23°C-RH50, 60°C-DAM, 80°C-RH50, 120°C-DAM

6.3.3 Fractography

Selected fracture surfaces were separated from the subcomponent using a dry handsaw and mounted on stubs using carbon-black-loaded epoxy adhesive. These samples were sputter-coated with gold for 20 s and examined using a Hitachi S-3700 SEM, with an acceleration voltage of 12 kV.

6.4 Experimental results for subcomponents

6.4.1 Overall response of PA66-GF50 subcomponents under static indentation

Fig. 6.3 shows the load-displacement curves of subcomponents under the five different environmental conditions. The subcomponents exhibited softer behaviour under wetter or hotter conditions. Brittle and unstable failure was seen under 23°C-DAM, whilst under all the other conditions there was more plastic behaviour and stable failure progression following the maximum load. The load-displacement curves obtained under 23°C-RH50 and 60°C-DAM were very similar to each other, as were those obtained under 80°C-RH50 and 120°C-DAM. The standard deviations of the maximum load in these curves are summarised in Table 6.3.

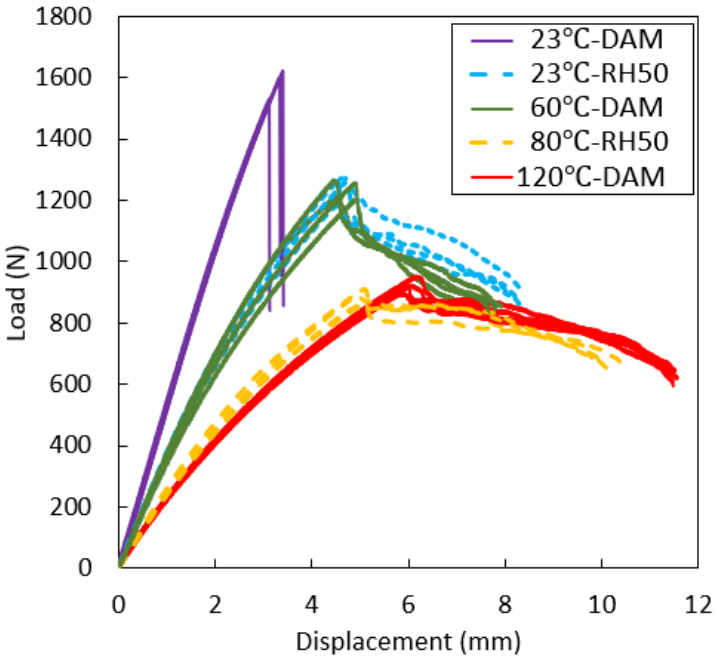


Fig. 6.3. load-displacement curves of PA66GF50 subcomponents at under five different environmental conditions.

Table 6.3. Averaged maximum load and the standard deviation in the load-displacement curves of subcomponents under five different environmental conditions.

	23°C-DAM	23°C-RH50	60°C-DAM	80°C-RH50	120°C-DAM
Average maximum load (N)	1591	1238	1236	888	923
Standard deviation (N)	31	39	24	21	19
Coefficient of variation (%)	1.9	3.2	2.0	2.3	2.1

All subcomponents failed through cracking of the subcomponent beneath the indenter, as shown in the representative photograph in Fig. 6.4 (a); schematic illustrations of the location of the fracture plane after the tests are shown in Fig. 6.4 (b) and (c). The crack initiated at the backface to the loading point (indicated in Fig. 6.4 (a)), and became visible when the maximum load was reached in the test; the crack then propagated in the y-z plane towards the frontface of the loading point and towards the subcomponent front and back edges. These macroscopic crack initiation and propagation directions were consistently observed for all tested subcomponents, regardless of the environmental conditions.

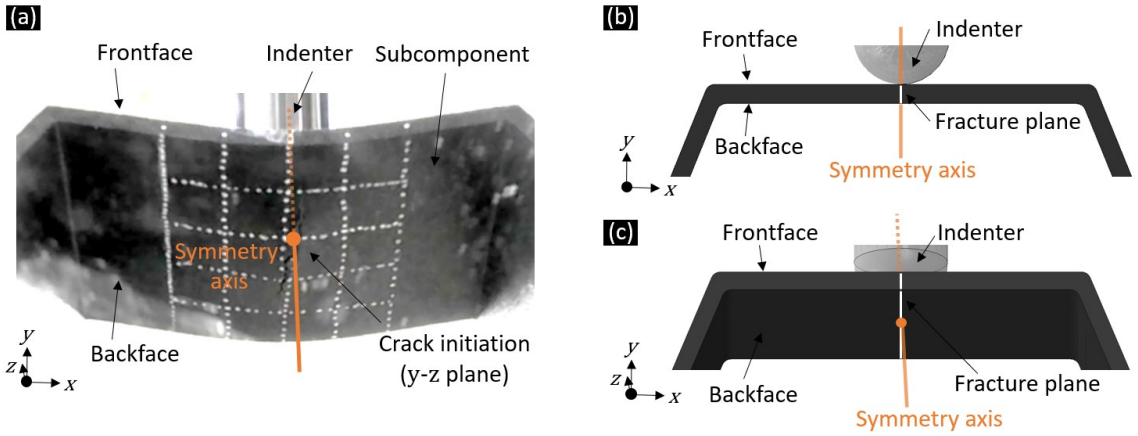


Fig. 6.4. Crack initiation and propagation in PA66-GF50 subcomponent: (a) crack initiation location (photograph taken at the maximum load during the test), (b) schematic illustration of fracture plane $y - z$ from the front, and (c) schematic illustration of fracture plane $y - z$ from the backface.

6.4.2 Fracture surfaces of the subcomponents under different environmental conditions

An optical image and several scanning electron micrographs of the fracture surface (in the $y - z$ plane) of a subcomponent tested under 23°C-DAM are shown in Fig. 6.5. Most fibres were aligned *perpendicular* to the fracture plane (i.e. in the $x -$ direction) in the skin regions, and *parallel to* the fracture plane (i.e. in the $z -$ direction) in the core region. The crack path was

symmetric from the mid-width of the fracture plane (with respect to the $x-y$ plane, i.e. along the $z-$ direction). The damage mechanisms of the subcomponent tested under 23°C-DAM are summarised below:

- At the crack initiation site (bottom skin, along the symmetry axis at the backface, Fig. 6.5 (a)): a typical T-fracture surface was observed, with brittle PA66 matrix fracture and fibre pull-out [53]. The riverlines [53] in the matrix show that the crack had propagated radially from the initiation site, as also inferred from the macroscale photograph in Fig. 6.4 (a). Residual matrix attached to fibre surface was also seen, indicating a good interfacial adhesion between the PA66 matrix and GF. This type of fracture surface was also reported in previous work using PA66-GF coupons [31,104].
- In the core region, along the symmetry axis (Fig. 6.5 (b)): the PA66 matrix presented macro-scale aligned steps, indicative of in-plane shear failure with interfacial debonding, leading to a typical L-fracture surface [53]. From the riverlines in the matrix, it was determined that the crack had propagated upwards (away from the crack initiation site and towards the loading point).
- At the top skin, along the symmetry axis near the frontface (Fig. 6.5 (c)): the fracture surface was obscured by post-failure crushing damage, due to the compressive stress state in this region.
- At the bottom skin, away from the symmetry axis (near the front of the subcomponent, Fig. 6.5 (d)): a typical T-fracture surface was observed. The riverlines in the matrix were consistent with the crack having propagated downwards (i.e. away from the core and towards the backface).
- At the top skin, away from the symmetry axis (near the front of the subcomponent, Fig. 6.5 (e)): a typical T-fracture surface was observed. The riverlines in the matrix suggest that the crack had propagated diagonally upwards (i.e. away from the core and towards the frontface).

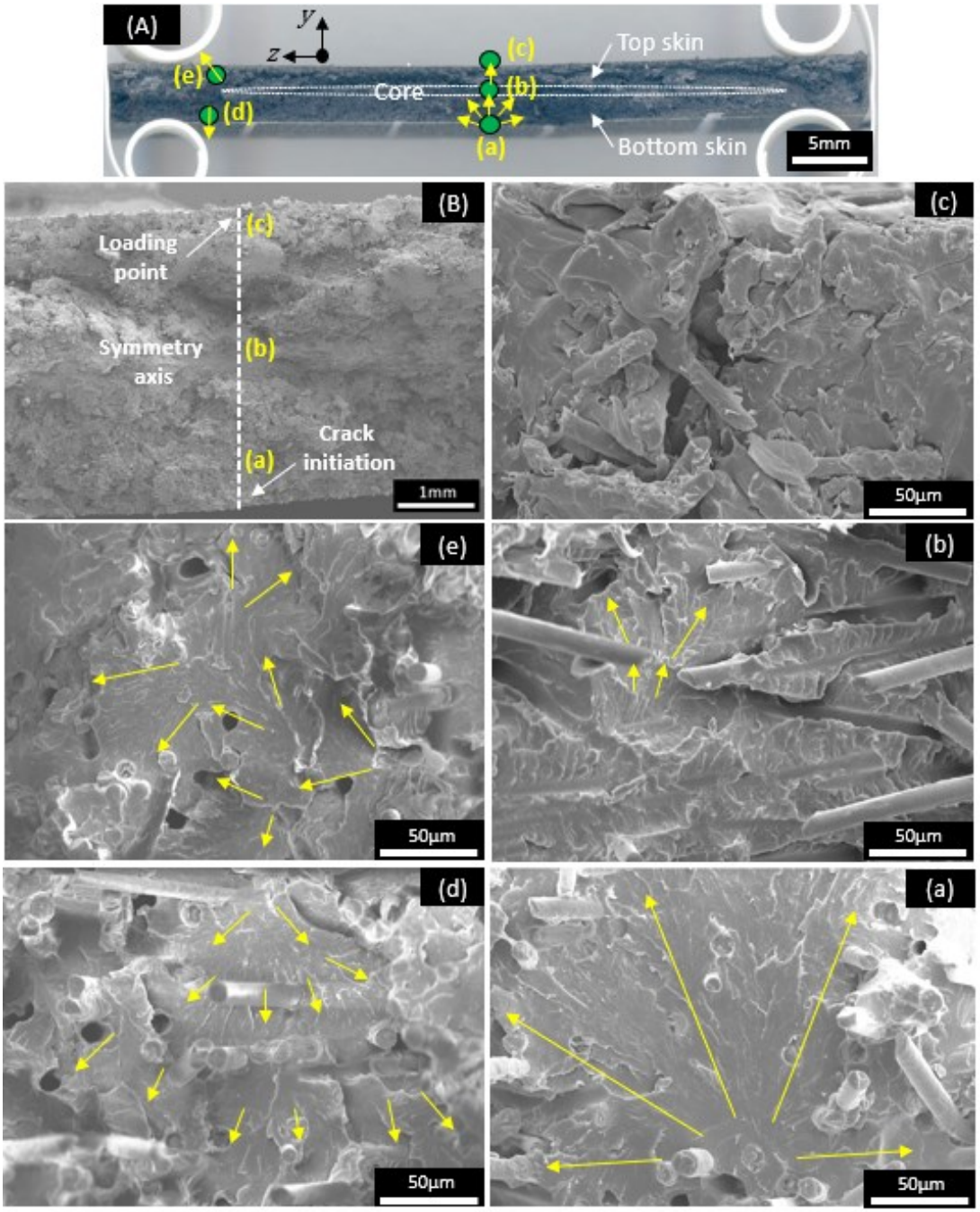


Fig. 6.5. (A) Representative optical image of the fracture surface of a subcomponent tested at 23^{O}C DAM, and (B) representative scanning electron micrographs of fracture surfaces of a subcomponent tested at 23°C-DAM, near the symmetry axis; Subfigures (a)-(e) correspond to the regions identified in Subfigure (A) with green circles. The yellow arrows represent the local direction of crack propagation, identified by the matrix morphologies (riverlines).

Scanning electron micrographs in the crack initiation site (i.e. at the region identified in Fig. 6.5 (a)) and in the core region in the symmetry axis (i.e. at the region identified in Fig. 6.5 (b)) under the different environmental conditions are shown in Fig. 6.6 and Fig. 6.7, respectively.

For all conditions except 23°C-DAM, the fracture surfaces presented a large degree of matrix plastic deformation, which was exacerbated for the 80°C-RH50 and 120°C-DAM conditions.

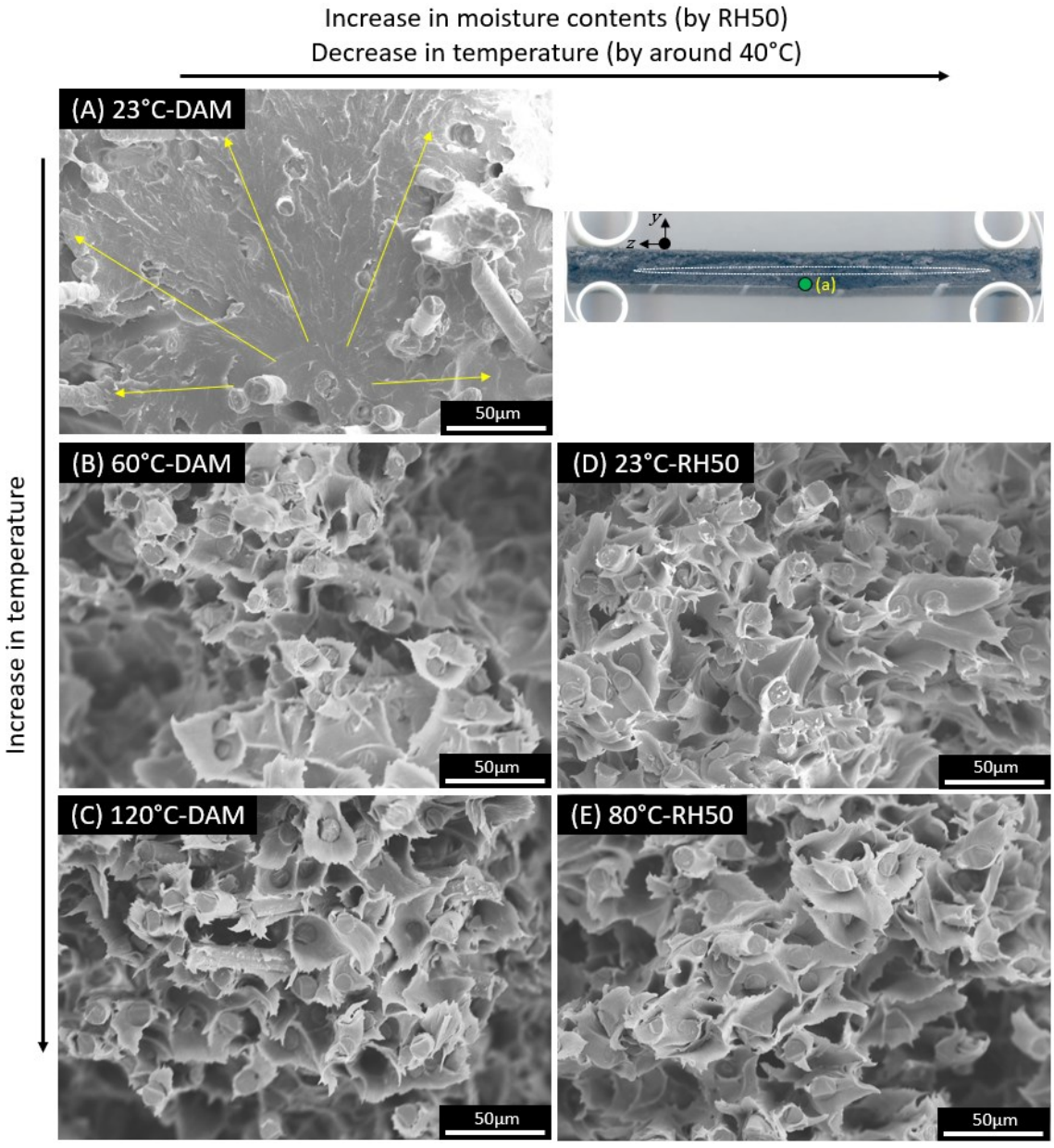


Fig. 6.6. Scanning electron micrographs of fracture surfaces of the subcomponents under different environmental conditions at the crack initiation site in skin region (region in Fig. 6.5 (a)).

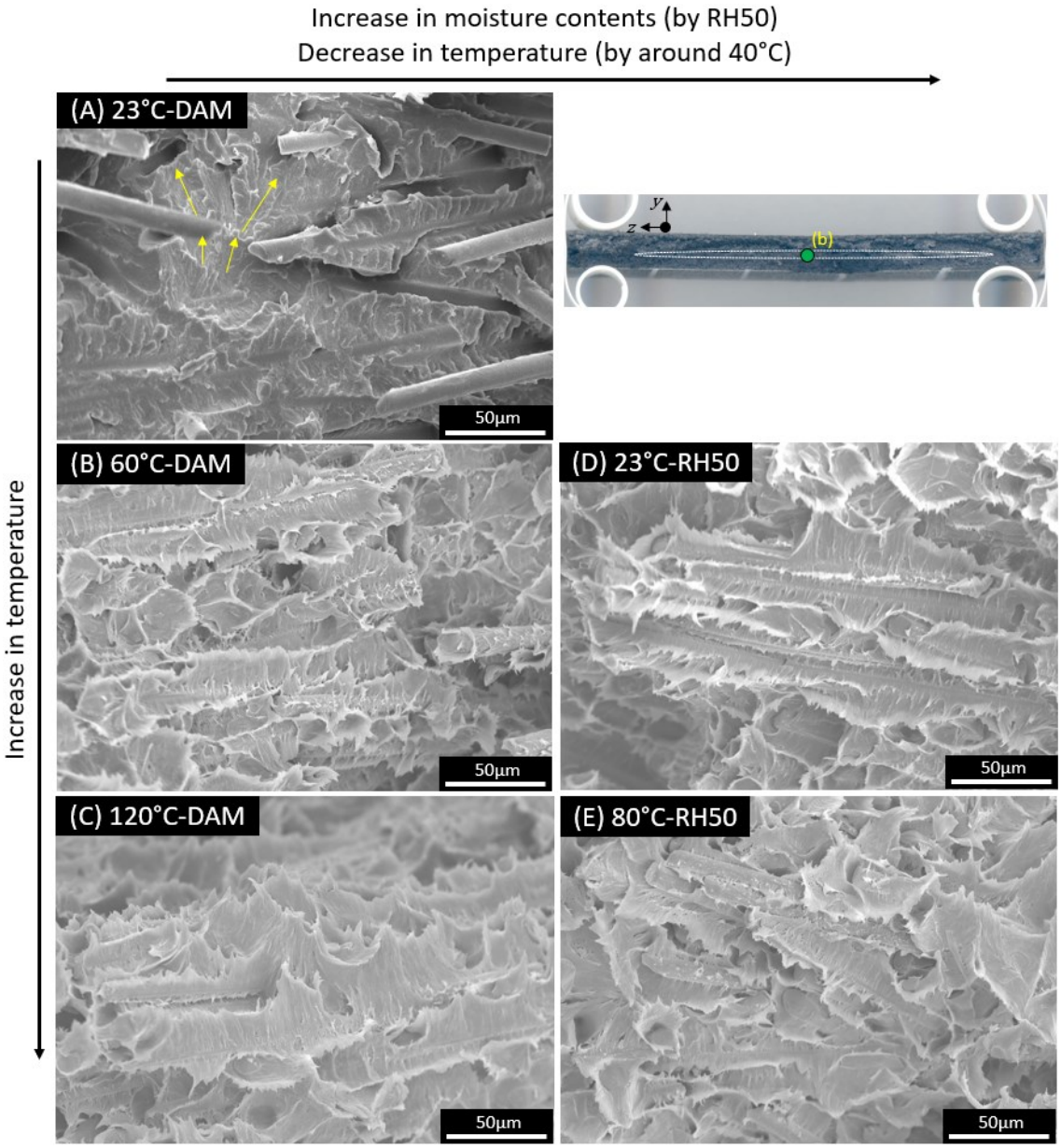


Fig. 6.7. Scanning electron micrographs of fracture surfaces of the subcomponents under different environmental conditions in the core region along the symmetry axis (region in Fig. 6.5 (b)).

6.5 Virtual testing of the subcomponents

6.5.1 Process simulation of the subcomponents

The Moldflow software [69] was used to simulate the injection moulding process and predict the fibre orientation in the subcomponents. The mesh used had 936305 elements, with 40 layers across the thickness. The same settings as used for the coupons in Chapter 4 were selected, with injection-moulding conditions as in the actual manufacturing of the subcomponents (shown in

Table 6.1). The full 3D fields of predicted fibre orientation distributions were passed onto the FE simulations through Digimat-MAP, using the same procedure as that described in Chapters 2. The Moldflow Rotational Diffusion model [72,74,75] was selected based on the results of comparing the fibre orientation models in Chapter 4.

The fibre orientation tensor predicted by the process simulation is shown in Fig. 6.8. The predicted fibre orientation tensor across the fracture plane is shown in Fig. 6.8 (c), where $a_{xx} \approx 0.8$ for the skins, and $a_{xx} \approx 0.2$ for the core.

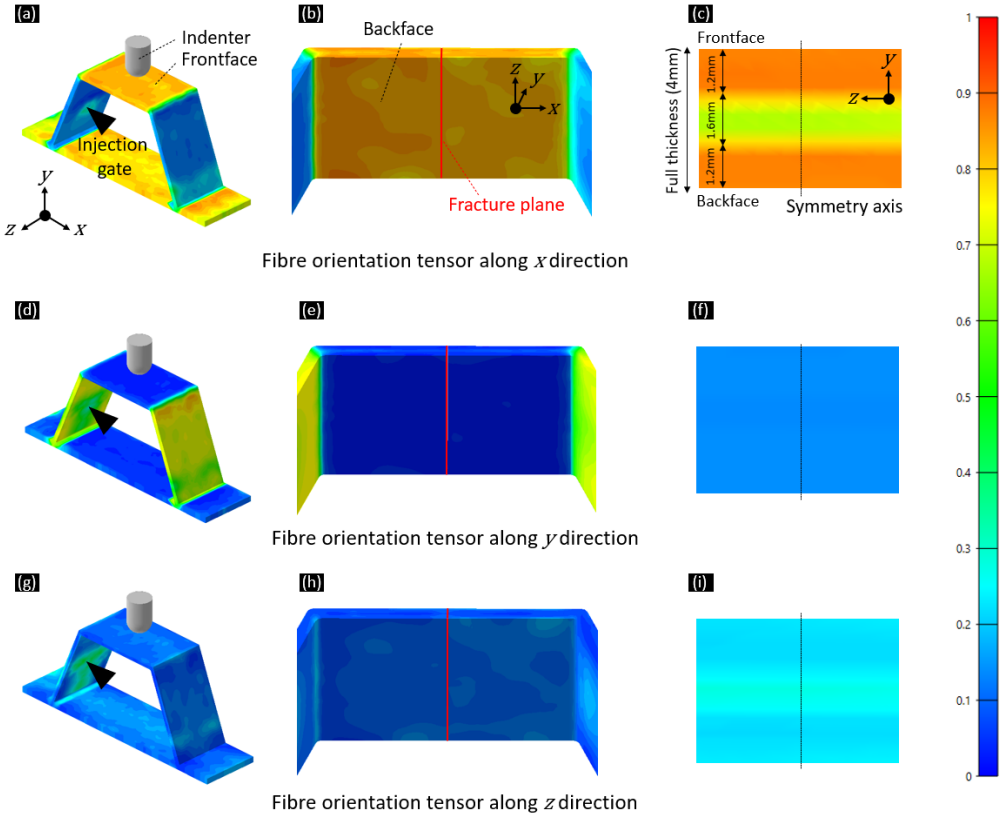


Fig. 6.8. Predicted fibre orientation tensor in the subcomponents: on the overall subcomponent surface, along the x (a), y (d) and z (g) directions; on the backface, along the x (b), y (e) and z (h) directions; local view of the fracture plane (indicated in Subfigure (b)), along the x (c), y (f) and z (i) directions.

6.5.2 Structural simulation of the subcomponents according to the state of the art

This Section reports the simulation of the subcomponents under static indentation, according to the state-of-the-art coupled FEA procedure [5,77], using Abaqus [78] to perform the FEA.

The mesh and the boundary conditions used in the FE model are shown in Fig. 6.9. The FE model has been entirely meshed with solid 8-node hexagonal elements (C3D8R). The indenter

(radius of 10 mm) was modelled using an analytical rigid surface, with a prescribed displacement of 15 mm (allowing only movement along the y direction) and a general contact to the subcomponent (with friction coefficient 0.2). The bottom stage of the subcomponent (indicated in Fig. 6.4 (b)) was removed from the FEA model to reduce the computation time, and the newly generated two bottom faces were fixed with full constraint (preliminary FE simulations showed that the effect of the bottom stage was negligible). Convergence of the FE simulation results with respect to numerical parameters has been confirmed through preliminary simulations, as detailed in Appendix D.

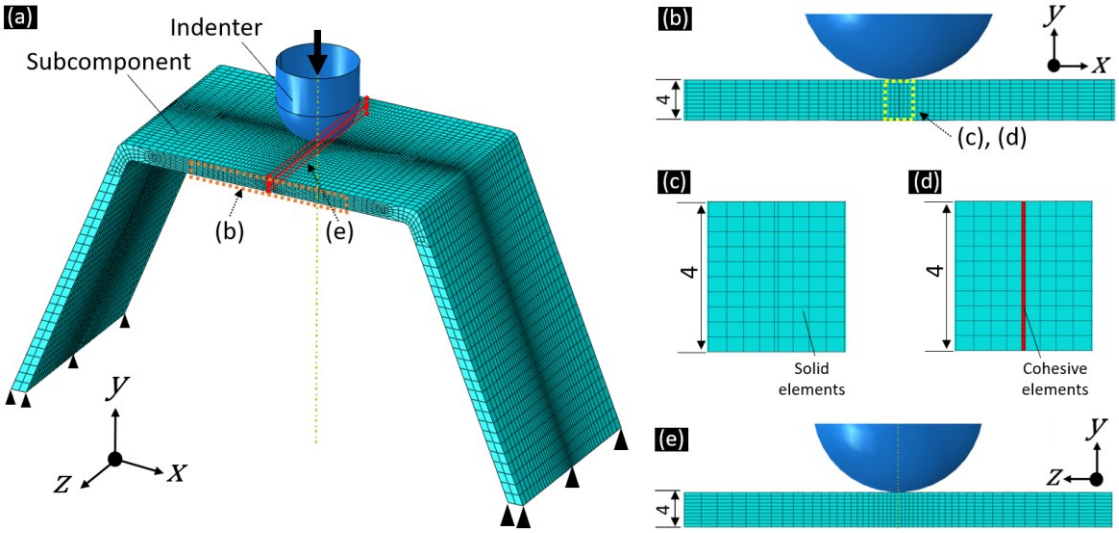


Fig. 6.9. FE model of the subcomponents: (a) Global view of the subcomponent and the indenter, (b) Zoom-in of the mesh at the front edge, (c), Zoom-in of the mesh around the fracture plane at the front edge for coupled FEA only with solid elements, (d) Zoom-in of the mesh around the fracture plane at the front edge for coupled FEA with solid and cohesive elements, and (e) Mesh on the fracture plane (all dimensions in mm).

The fibre orientation tensor fields predicted in Section 6.5.1 were mapped onto the FE model of the subcomponent using Digimat-MAP [5]. The coupled FEA of the subcomponents were then submitted using the procedure described in Chapter 2, with Digimat's elastic-plastic material models and the Tsai-Hill 3D transversely-isotropic failure criterion calibrated in Chapter 4 [5].

6.5.3 FE modelling of the subcomponents using combined methodologies of coupled FEA and cohesive zone modelling

As discussed in the Introduction (Section 6.1), the state-of-the-art simulation methodology for IM-SFRPs used in Section 6.5.2 can detect failure initiation (as predicted by the Tsai-Hill criterion), but cannot account for the propagation of failure, governed by the fracture toughness of the material. Therefore, in this Section, a methodology was proposed to account for the effect of fracture toughness on the failure prediction of the subcomponents, by combining CZM with the state-of-the-art coupled process-structural simulation explained in Section 5.2.

To combine CZM with the coupled FEA of the subcomponents, a layer (0.1 mm thick) of COH3D8 cohesive elements was added at the fracture plane (as shown in Fig. 6.9) observed in the experiments (Fig. 6.4). The CEs initially behave linearly, with a stress versus separation relationship defined by their stiffness, until failure initiates at a critical stress (the values of the stiffness and critical stress will be defined next in this Section). Further separation of the CE's faces leads to stiffness degradation (and to a progressive linear reduction of the CE's ability to transfer stresses), until full separation (and CE deletion) happens when the stiffness is fully degraded. The energy per unit area dissipated by the CEs is the same as the input value of the fracture toughness (also defined next in this Section).

The injection-moulding process creates a skin-core microstructure in the subcomponents, and the mechanical properties are fibre orientation-dependent. Therefore, the layer of cohesive elements was partitioned into regions to consider the local properties in the coupled FEA by mimicking the skin-core microstructure predicted by the process simulation. Each 1.2 mm skin layer was modelled with three elements through the thickness, and the 1.6 mm core layer was modelled with four elements through the thickness. This partitioning is fundamental given that the subcomponent experiences bending in the fracture plane and, therefore, the skins and core experience different strain states; consequently, it is necessary to de-homogenise the averaged values of fracture toughness measured in the CT coupons, as mentioned at the end of Section 6.2.

Since the Digimat software does not support homogenisation of SFRPs with CEs, the input of Young's modulus (with stiffness calculated based on the geometric thickness of the cohesive elements), critical stress and fracture toughness of the cohesive elements had to be determined according to the fibre orientation tensor homogenised within the skin ($a_{xx} = 0.8$) and within

the core ($a_{xx} = 0.2$) regions of the fracture plane, as predicted by the process simulation of the subcomponent (shown in Fig. 6.8). Since these fibre orientation tensor values are slightly outside the bounds experimentally characterised and homogenised with the coupons (i.e. $0.26 - 0.72$, as shown in Fig. 6.1), the experimentally-characterised properties were then extrapolated to these relevant fibre orientations, as summarised in Table 6.4 and Table 6.5, and used as the properties of the cohesive elements in the skins and core regions of the fracture plane. This de-homogenisation step is conceptually similar to the one carried out automatically by Digimat for the Young's modulus and stress-strain response explained in Section 6.5.2, although it deviates on two aspects: (i) the fracture toughness is de-homogenised into skin and core values rather than into individual integration points, and (ii) this uses a linear extrapolation of experimental measurements rather than a Mori-Tanaka/Voigt mean-field model.

In the coupled FEA with CZM, three different analyses were implemented to assess the effect of the input of fracture toughness and the shape of the cohesive law:

- "*FEA (CZM skin-core)*": using a bilinear cohesive law, assigning distinct properties to the skin and core layers (with $a_{xx} = 0.8$ and $a_{xx} = 0.2$, respectively) of the fracture plane, as described previously;
- "*FEA (CZM skin)*": also using a bilinear cohesive law, but assigning only the properties of the skin layers (i.e. corresponding to $a_{xx} = 0.8$) through the entire thickness of fracture plane. This methodology should represent the initial stages of fracture accurately, since the local bending experienced by the subcomponent in the fracture plane triggers failure initiation at the skins, but it will not represent the later stages of fracture accurately since the toughness of the core is largely overestimated in this case;
- "*FEA (CZM trilinear)*": using trilinear cohesive laws, calibrated with the same methodology as used in Chapter 5 (detailed in Appendix C) using the experimental R-curves obtained from the J-integral method, assigning distinct properties to the skins and core layers of the fracture plane. This was applied only to the 23°C-DAM and -RH50 conditions; the shape of cohesive laws used in these FE simulations are summarised in Fig. 6.10.

For all cases, the maximum nominal stress initiation criterion and energy-based mode-independent propagation were selected; these selections would not influence the results, because the cohesive elements were modelling a symmetry plane (where no shear is applied).

Table 6.4. Input properties for bilinear cohesive law used for cohesive elements in skin ($a_{xx} = 0.8$).

	Young's modulus (GPa)	Critical stress (MPa)	Fracture toughness (kJ/m^2)
23°C-DAM	16.0	190	18.0
23°C-RH50	12.0	150	25.0
60°C-DAM	12.0	150	25.0
80°C-RH50	9.0	90	26.5
120°C-DAM	8.0	90	27.5

Table 6.5. Input properties for bilinear cohesive law used for cohesive elements in core ($a_{xx} = 0.2$).

	Young's modulus (GPa)	Critical stress (MPa)	Fracture toughness (kJ/m^2)
23°C-DAM	10.0	110	15.0
23°C-RH50	5.0	80	17.0
60°C-DAM	5.0	80	17.0
80°C-RH50	3.5	55	18.0
120°C-DAM	2.5	55	18.5

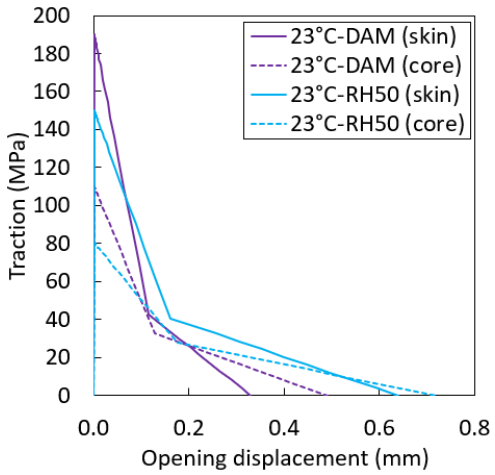


Fig. 6.10. Trilinear cohesive laws used for cohesive elements in skin and core at 23°C-DAM and 23°C-RH50.

6.6 FE Simulation results for the subcomponents

6.6.1 Prediction of maximum failure load of PA66-GF50 subcomponents

Fig. 6.11 compares the load-displacement curves of the subcomponents up to the maximum load, as obtained from experiments and the coupled FEA, both using (i) the state-of-the-art

methodology based on the Tsai-Hill criterion (described in Section 5.2) and (ii) the proposed methodology using cohesive elements to account for the finite toughness of the material (described in Section 5.3). A good agreement was observed in the initial stiffness and progressive softening in all cases; regarding the prediction of the maximum load, the following differences were observed (as summarised in Table 6.6):

- The coupled FEA based on Tsai-Hill failure criterion (*FEA (Tsai-Hill)* in Fig. 6.11, which neglects the material's finite fracture toughness) predicted failure initiation at a load at least 16.2% lower than the maximum load in the experimental results.
- The *FEA (CZM skin)* simulations (which consider the material's finite fracture toughness but not the complex skin-core microstructure in the fracture plane) over-predicted the maximum load measured experimentally by at least 9.3% for all conditions except 23°C-DAM (in which case it over-predicted by 1.8% only).
- The *FEA (CZM skin-core)* simulations (which consider both the material's finite fracture toughness and the complex skin-core microstructure in the fracture plane) showed an excellent agreement of maximum failure load with the experimental data under all environmental conditions (with a maximum error below 2.6%).
- The *FEA (CZM trilinear)* simulation under 23°C-DAM and 23°C-RH50 predicted the maximum failure load slightly earlier than the experimental results (under-prediction by 3.4% and 2.1% in failure loads, respectively, Fig. 6.12), which showcases an excellent agreement. However, the computational time of the *FEA (CZM trilinear)* simulations until the maximum load was between 550 and 600 hours with a Intel(R) Core(TM) i7-9700 CPU at 3.60 GHz and with a 32.0 GB RAM; this is an excessive increase compared to the *FEA (CZM skin-core)* simulations, which took only 24 hours to complete, and whose predicted maximum loads differed from the *FEA (CZM trilinear)* ones only by 4.9% and 2.5%. Therefore, the *FEA (CZM trilinear)* simulations under high temperature were not conducted in this work, as (i) it is unrealistic to use this methodology in practical situations, and (ii) the *FEA (CZM skin-core)* simulations provide a sufficiently close approximation with significantly reduced computational cost.

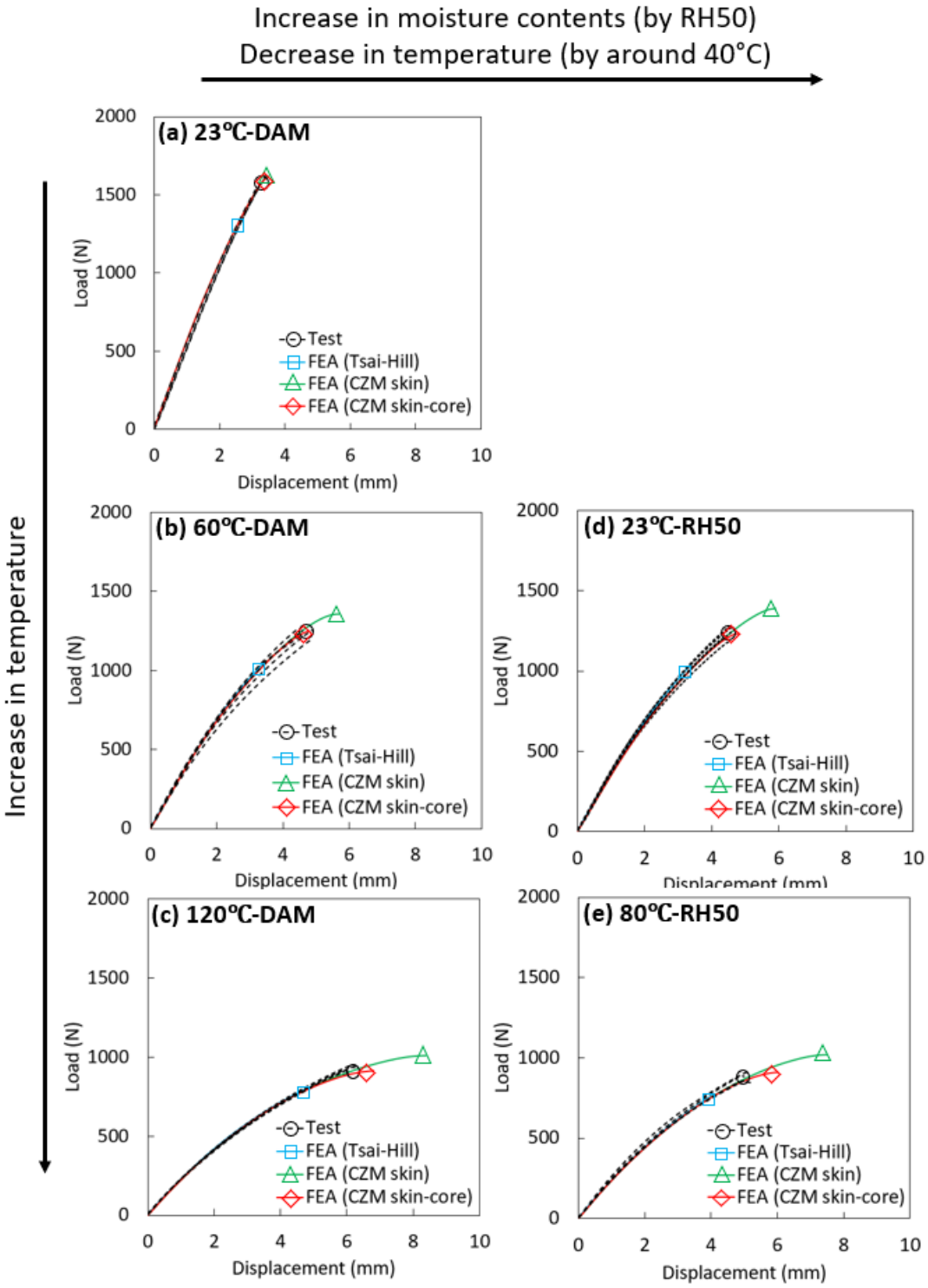


Fig. 6.11. Load-displacement curves of the subcomponents from experimental tests and coupled FEA until maximum load using the state-of-the-art methodology (*FEA (Tsai-Hill)*) or bilinear cohesive laws (*FEA (CZM skin)* or *FEA (CZM skin-core)*).

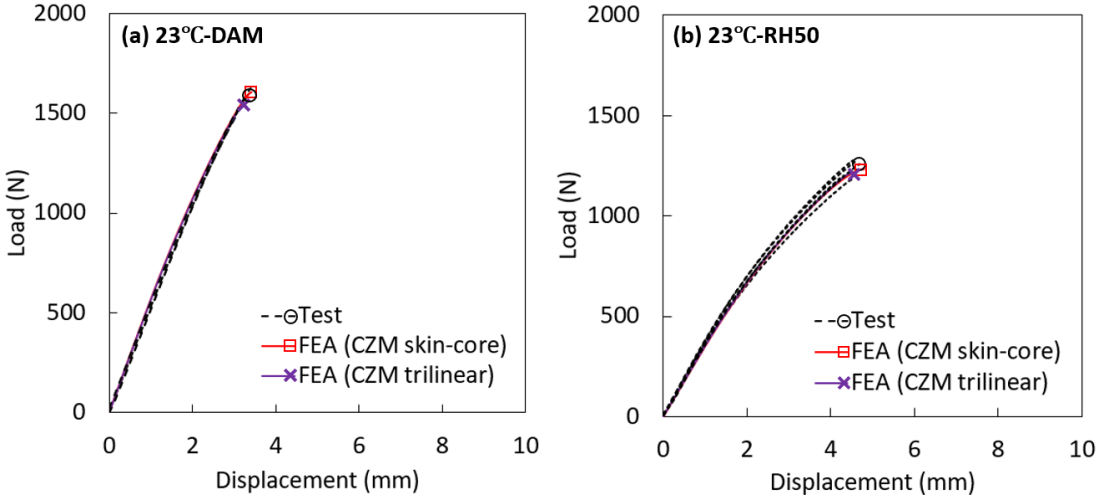


Fig. 6.12. Load-displacement curves of the subcomponents from experimental tests and coupled FEA until the maximum load using bilinear (*FEA (CZM skin-core)*) and trilinear *FEA (CZM trilinear)* cohesive laws.

Table 6.6. Error of the maximum failure load predicted for the subcomponents by the different FEA methodologies for varied environmental conditions, compared to the average from experiments.

	Tsai-Hill (%)	CZM skin (%)	CZM skin-core (%)	CZM trilinear (%)
23°C-DAM	- 23.4	+ 1.8	+ 1.5	- 3.4
23°C-RH50	- 23.6	+ 12.1	- 0.4	- 2.1
60°C-DAM	- 22.5	+ 9.7	- 1.2	---
80°C-RH50	- 17.0	+ 14.8	+ 2.6	---
120°C-DAM	- 16.2	+ 9.3	- 0.9	---

6.6.2 Prediction of the sequence of failure events and post-peak behaviour using cohesive zone modelling

Load-displacement curves of the subcomponents from experiments and the coupled FEA combined with CZM, including the post-peak behaviour, are shown in Fig. 6.13. The *FEA (CZM skin-core)* methodology was able to predict the increase in the stability of the failure process as the temperature and moisture level increase, as observed in the experiments. However, the FEA predictions just after the maximum load were always slightly more stable than the experimental results. This was particularly noticeable under 23°C-DAM conditions (where the FEA predicted a progressive decrease of the load-carrying ability of the subcomponent rather than brittle fracture), while a nearly-perfect match can be observed under 120°C-DAM and 23°C-RH50 conditions.

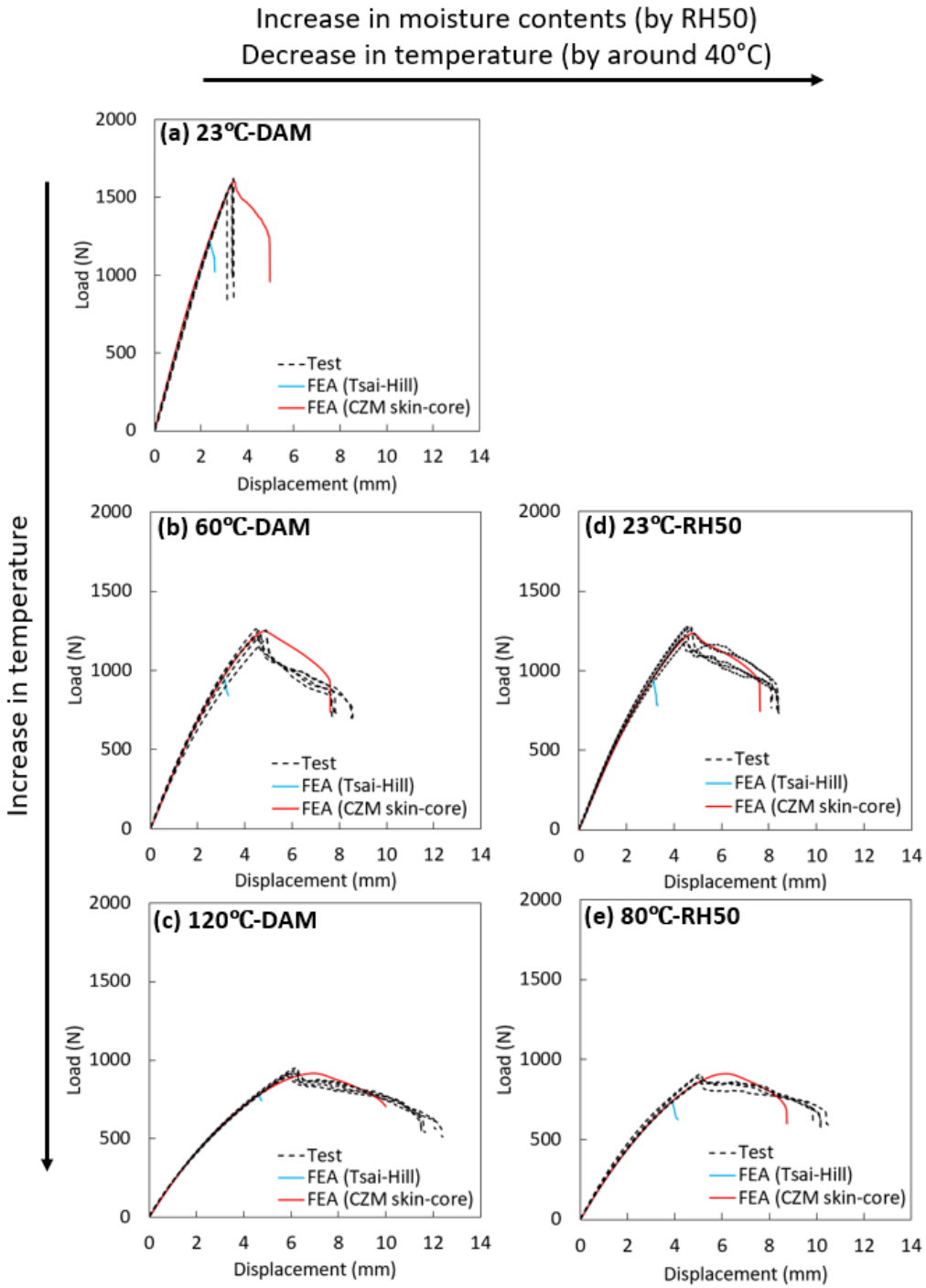


Fig. 6.13. Load-displacement curves of the subcomponents from experiments and coupled FEA including the post-peak behaviour, using different methodologies.

The stiffness degradation of the cohesive elements in the *FEA (CZM skin)* and *FEA (CZM skin-core)* during the analysis at 23°C-DAM is shown in Fig. 6.14. Damage initiated at the symmetry axis from the bottom skin region, and it propagated radially in the model with uniform cohesive properties in the entire fracture surface, i.e. *FEA (CZM skin)*. The model which accounts for the skin-core-dependent cohesive properties, i.e. *FEA (CZM skin-core)*, also showed damage

initiation at the bottom skin region. However, preferential damage propagation in the core region was seen, which disturbed the radial pattern of damage propagation. The same trend was also seen at 23°C-RH50 and 60°C-DAM, as shown in Fig. 6.15 and Fig. 6.16, respectively.

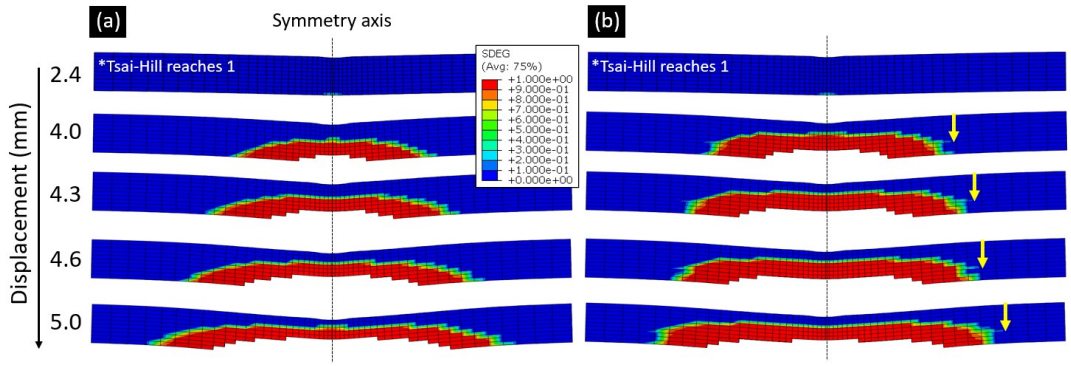


Fig. 6.14. Stiffness degradation and deletion of cohesive elements in the coupled FEA combined with CZM at 23°C-DAM: (a) *FEA (CZM skin)* and (b) *FEA (CZM skin-core)*. The yellow arrows indicate the transition between the bottom skin region and the core region.

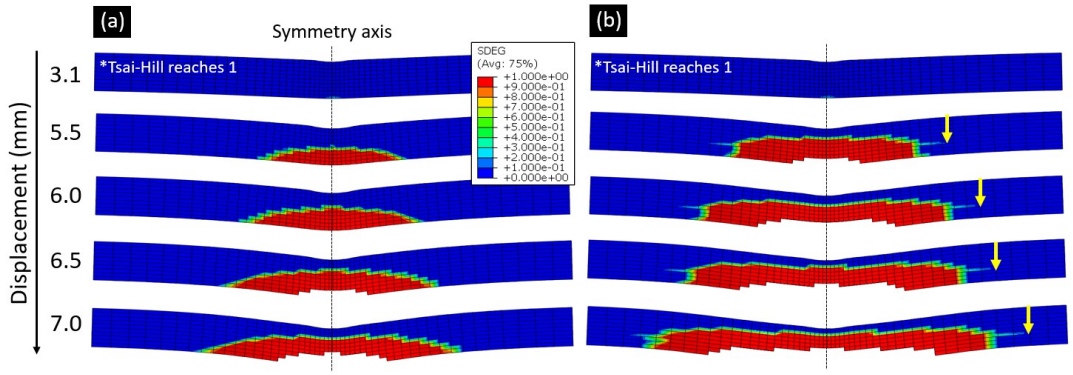


Fig. 6.15. Stiffness degradation and deletion of cohesive elements in the coupled FEA combined with CZM at 23°C-RH50: (a) *FEA (CZM skin)* and (b) *FEA (CZM skin-core)*. The yellow arrows indicate the transition between the bottom skin region and the core region.

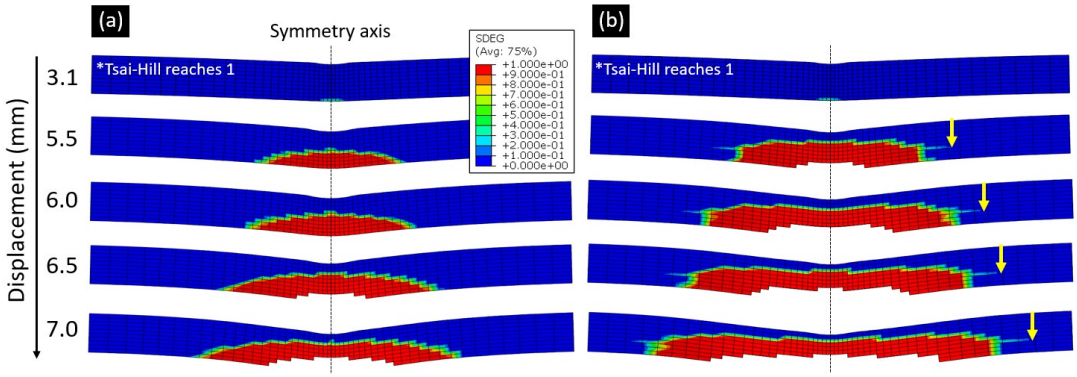


Fig. 6.16. Stiffness degradation and deletion of cohesive elements in the coupled FEA combined with CZM at 60°C-DAM: (a) *FEA (CZM skin)* and (b) *FEA (CZM skin-core)*. The yellow arrows indicate the transition between the bottom skin region and the core region.

6.7. Discussion

6.7.1 Damage mechanisms and sequence of failure events at 23°C-DAM conditions

Based on both the morphology of the riverlines on the PA66 matrix on the fracture surface obtained under 23°C-DAM (shown in Fig. 6.5), and the damage propagation predicted by the coupled FEA combined with CZM (shown in Fig. 6.14), it is possible to propose a sequence of failure events for the subcomponent under static indentation as summarised in Fig. 6.17:

- Stage (A), Crack initiation: the crack initiated at the mid-width of bottom skin region (close to the backface), beneath the indenter (Fig. 6.5 (a)).
- Stage (B), Radial crack propagation: the crack propagated radially from the initiation site until it reached the core region.
- Stage (C), Preferential crack propagation through core region: once the crack reached the skin/core interface, it propagated preferentially through the core region. This hypothesis was based on (i) the preferential damage of the cohesive elements predicted by the FE simulation (shown in Fig. 6.14), and (ii) the downwards propagation direction observed experimentally in the core nearer the front and back edges of the subcomponent (as described in the next Stage (D)). The preferential crack propagation in the core was due to the lower fracture toughness in the core (with a preferential fibre alignment along the fracture plane) compared to that in the skin (with a preferential fibre alignment nominal to fracture plane).
- Stage (D), Downwards crack propagation in the core, nearer the edges of the subcomponent. From the riverlines on the PA66 matrix, it was deduced that the crack had propagated downwards (Fig. 6.5 (d)), which could be caused by the crack reaching the edges of the subcomponent in the core before fracture in the bottom skin, as explained in Stage C.
- Stage (E), Upwards crack propagation through the top-skin region: in the top-skin region, the crack propagated upwards and outwards, leading to the complete failure of the subcomponent (Fig. 6.5 (e)).

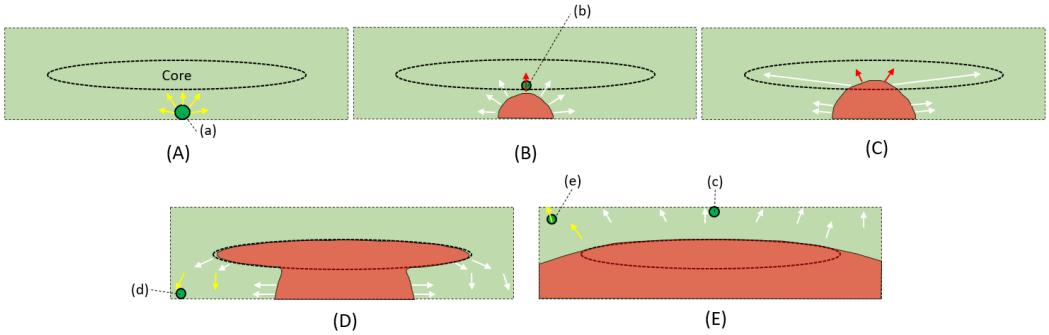


Fig. 6.17. Schematic illustration of the sequence of failure identified from the micrographs and coupled FEA combined with CZM at 23°C DAM (yellow arrows: crack propagation by matrix failure/interfacial debonding (observed experimentally); red arrows: crack propagation by shear failure (observed experimentally); white arrows: estimated crack propagation direction; green circles: SEM observation points; dark-orange areas: damaged region).

6.7.2 Prediction of PA66-GF50 subcomponent failure using FE models

The results from the *FEA (Tsai-Hill)* state-of-the-art methodology in Fig. 6.11 and Table 6.6 clearly demonstrate that the failure models currently implemented in commercially-available software, based solely on failure initiation criteria (e.g. Tsai-Hill), are not sufficient to accurately predict the maximum failure load observed experimentally in subcomponents with complex geometries and loading conditions (under-predicting the failure load by at least 16.2%). In Fig. 6.11, the load-displacement curves from *FEA (CZM skin-core)* showed excellent agreement not only in the initial stiffness and progressive softening, but also in the ultimate failure point with the experimental data, under all environmental conditions (with a maximum error within 2.6%).

For each environmental condition, the displacement at which cohesive failure initiation is predicted by the *FEA (CZM)* methodology was virtually the same as the displacement at which the failure criterion was first met in the *FEA (Tsai-Hill)* models. This suggests that the *FEA (CZM skin-core)* methodology was able to predict the maximum load accurately not because it provides a better failure initiation criterion than the Tsai-Hill models, but because the CZM methodology accounts for the damage propagation process and for the finite fracture toughness of the material, which are not considered in the Tsai-Hill criterion.

Since failure of the subcomponents initiated at the bottom skin, the *FEA (CZM-skin)* methodology was equally able to predict the initial stages of failure as the *FEA (CZM skin-core)* methodology. However, the former presented a larger error in the predicted maximum failure load, especially under wet, hot and hot-wet conditions (over-prediction by at least 9.3%). This

demonstrates that, although fracture initiates at the bottom skin due to bending (which could be easily predicted without an FE simulation), it propagated stably across the skin and within the core before the maximum failure load was reached, for most environmental conditions (which could only be predicted with a full FE simulation including progressive material failure and crack propagation). These results indicate that considering the effect of the complex skin-core microstructure and the local fibre orientation fields at the fracture plane on the input properties for cohesive elements has a large importance on the accuracy of the predicted failure load of IM-SFRP components.

This thesis's implementation of the *FEA (CZM skin-core)* methodology assumes that the relationship between (i) the **local** (i.e. distinguishing the skins and the core) fibre orientation component across the fracture plane and (ii) the **local** mode-I fracture toughness is well described by the **homogenised** CT data shown in Fig. 6.1. This assumption is producing good results for the subcomponent analysed; this might be favoured by the normality between the local principal fibre-orientation directions and the fracture plane, both in the subcomponent, and in the CT coupons at $\theta = 0$ and $90°$ (which have the most impact in defining the skin and core toughnesses used in the simulations). Nevertheless, further investigation is needed on the robustness of homogenising the relationship between fracture toughness and fibre orientation in the CT tests for the angled cases ($20° \leq \theta \leq 60°$).

After the maximum failure load in Fig. 6.13, *FEA (CZM skin-core)* could not predict the unstable load drop observed in the experiments under 23°C-DAM, while it showed good agreement for the stable reduction of the load-carrying ability of the subcomponents tested under the other environmental conditions. This mismatch is likely due to a combination of factors, including the compliance of the experimental testing jig. In addition, under 23°C-DAM, the subcomponent failed catastrophically in a brittle way (which necessarily produces very high strain rates locally at the crack front), while the CT tests (used to measure the fracture toughness of the PA66-GF50 material required as inputs for the FE simulations) showed ductile/stable failure (which produces comparatively lower local strain rates) as shown in Fig. 5.9. Therefore, there might be a small mismatch between the input of fracture toughness in the FE model and the one in the real subcomponents under 23°C-DAM conditions, due to this mismatch in failure stability. It is also possible that the de-homogenisation process used for the fracture properties (based on the linear extrapolation of values averaged across the thickness of CT coupons, as explained in Section 5.3) overestimated the fracture properties of the core, stabilising failure.

Nevertheless, this mismatch seems to not affect the accuracy of maximum load predictions, even for the environmental conditions leading to the most brittle material response.

6.7.3 Effect of temperature and moisture on the damage mechanisms and fracture morphology

In the skin regions, the scanning electron micrographs of the fracture surfaces obtained under 23°C-DAM conditions presented a brittle PA66 matrix behaviour (with riverlines on the matrix fracture surface and with fibre pull-out), which is consistent with the brittle failure observed (Fig. 6.3 and Fig. 6.5) globally in these subcomponents after the maximum load. The fracture surfaces obtained under all other conditions mainly showed tensile fibre failure with large matrix deformation, without riverlines on the matrix fracture surfaces, which is consistent with the stable failure observed in those subcomponents after the maximum load. In the core region, matrix in-plane shear failure with interfacial debonding was observed, under all environmental conditions.

For the same stable failure mode (i.e. observed under 60°C- and 120°C-DAM, and 23°C- and 80°C-RH50 conditions), increasing the temperature and/or adding moisture promoted further plastic deformation of the matrix. This larger matrix deformation under hotter or wetter conditions is because the PA66 matrix presented a softer and more ductile behaviour than under colder or drier conditions [20,21,39], which stabilised the failure process. This shows that previous work at the coupon level - which concluded that hotter or wetter conditions lead to a softer, weaker and more ductile response, with a decrease of Young's modulus and strength [14–16,20,21,39–42], can be directly translated into subcomponents.

As the PA66 matrix showed large plastic deformations under hotter and/or wetter conditions, no crack path could be identified from fractographic results (Fig. 6.6 and Fig. 6.7), except for the subcomponents tested at 23°C-DAM. Nevertheless, the directions of damage progression predicted by the *FEA (CMZ skin-core)* methodology at both 23°C-RH50 and 23°C-DAM (Fig. 6.14 and Fig. 6.15) were very similar, suggesting a consistent preferential damage propagation in the core region. Therefore, the sequence of failure events under the other environmental conditions are also expected to be similar to that at 23°C-DAM conditions, i.e. with preferential crack propagation in the core.

6.7.4 Temperature-moisture equivalence

The load-displacement curves of subcomponents tested under "23°C-RH50 and 60°C-DAM (Pair-A)", and "80°C-RH50 and 120°C-DAM (Pair-B)" showed very similar behaviour within each pair (Fig. 6.3); the same trend was also found for at the coupon-level results of fracture toughness (measured using CT tests, Fig. 6.1 (c)), and for the Young's modulus and the tensile strength measured using dog-bone coupons (Fig. 6.1 (a) and (b)). Both Pair-A and Pair-B have a difference in testing temperature similar to the shift of the glass transition temperature from DAM to RH50 conditions (ΔT_g =38.9°C in Fig. 3.8). Therefore, these results provide further support to the temperature-moisture equivalence, i.e. that there is an equivalence between increasing the moisture level and increasing the testing temperature by the corresponding shift in DMA curves in this PA66-GF50 materials – not only regarding coupon-level Young's modulus and strength as previously suggested [50–52], but also on the fracture toughness and subcomponent response.

While the similarity of the results in Pair-A (23°C-RH50 and 60°C-DAM) is very good, Pair-B (80°C-RH50 and 120°C-DAM) has a small mismatch (slightly stiffer and more brittle behaviour observed under 80°C-RH50 conditions than under 120°C-DAM) in the results of Young's modulus, fracture toughness (Fig. 6.1) and load-displacement curves of subcomponents (Fig. 6.3). A likely explanation is that water evaporated from the surface of the PA66-GF50 coupons and subcomponents during the tests under 80°C-RH50 conditions, making it slightly drier than intended.

Given that it is very likely that water evaporation affected the response measured experimentally for the coupons and subcomponents tested under 80C-RH50 conditions, and that the temperature-moisture equivalence was demonstrably very accurate for Pair-A, the results produced by the tests performed under 120C-DAM might be more representative of true behaviour under real 80°C-RH50 conditions. In any case, the difference in mechanical properties within Pair-B is very small; therefore, the uncertainty associated with water evaporation (or other mechanism leading to the deviation from the temperature-moisture equivalent) is likely to fall within the levels acceptable for industry.

Altogether, these results imply that considering the temperature-moisture equivalence [50–52] might have the potential to reduce the number of experiments needed for material characterisation and component qualification in industry, not only for standard coupons (as

reviewed in Chapter 2 [50–52]), but also for fracture toughness coupons and for (sub)components. This is especially useful for reducing the amount of wet-conditioned testing, which would lead to a potential saving of many weeks for moisture conditioning of samples, and it could also increase the reliability of the properties measured for applications under hot-wet conditions.

6.7.5 Novelty and implications

The main contributions of the research reported in this Chapter, including the novelty and the potential impact, are summarised as follows:

1. This work has provided the first attempt to undertake coupled process/structural simulations of IM-SFRPs accounting for progressive material failure (using CZM). This represents a step change in the ability of coupled simulations to predict failure of (sub)components [76,80]. All inputs of the CEs were calibrated using experimentally-measured properties (stiffness and strength as characterised in Chapter 3, and fracture toughness as characterised in Chapter 5 and Section 6.2), and considering fibre orientation effects on IM-SFRPs, so the results of the FE simulations of the subcomponents are fully predictive. This methodology showed a significant improvement (within a 2.6% error) over the state-of-the-art methodology (underestimating by 16-24%) for failure load prediction, as presented in Fig. 6.11 and Table 6.6. It has also been demonstrated that this methodology is robust by successfully applying it consistently to five different environmental conditions.

2. The subcomponents used in this work (Fig. 6.2, representing automotive engine mounts) are a step change in the complexity of geometries analysed through coupled process/structural simulations of IM-SFRPs [16,63,77], which showcases the need to account for progressive material failure in real-life structures (rather than simple coupons). Although the microstructure of the subcomponent's fracture plane was relatively simple (i.e. with a mostly symmetric skin-core microstructure), its interaction with the indentation-type loading generated a complex sequence of failure events (as discussed in Section 6.7.1), significantly different from that observed at the coupon level (in which failure occurred uniformly across the thickness). This difference between

subcomponents and coupons has a significant impact on the accuracy of the state-of-the-art simulation methodology. Whilst the failure initiation (i.e. Tsai-Hill's) criterion could accurately predict the coupon test results (as shown in Section 4.4), it introduced errors of at least 16% in the simulation of the subcomponents (as shown in Fig. 6.11). Considering progressive material failure, as in this proposed improved methodology, is vital to correctly predict the response of (sub)components.

3. This work used a combination of fractography and FE simulations to identify and justify the sequence of failure events at the subcomponent level and how it is affected by the complex skin-core microstructure characteristic of IM-SFRPs, which have not been reported previously. Fractographic results suggested an unexpected reversed crack propagation (Fig. 6.5 (d) and Fig. 6.17), and the coupled FEA using CZM (Fig. 6.14 (b), Fig. 6.15 (b) and Fig. 6.16 (b)) suggested that this was caused by preferential damage propagation in the core region due to its lower toughness (compared to that of the skins). Combining fractography with FE simulations can therefore provide guidance on what levels of fibre-orientation homogenisation are suitable for IM-SFRP subcomponents/components, which have more complex geometries and more heterogeneous microstructures than IM-SFRP coupons.

4. Regarding the T-M equivalence: whilst previous research focused only on the modulus and stress-strain behaviour at the coupon level [50–52], the concept of temperature-moisture equivalence has now been confirmed for the material's fracture toughness (using CT tests, Fig. 6.1) and also for the subcomponent level, until final failure (Fig. 6.3), as detailed in Section 6.7.4. This conclusion has the potential to significantly reduce the amount of work for material characterisation and component testing in industry.

6.8 Conclusions

This chapter has proposed and validated a methodology to account for the finite fracture toughness in the failure prediction of IM-SFRP subcomponents. The conclusions of this chapter can be summarised as follows:

1. Coupled FEA using CZM calibrated with the experimentally measured fracture toughness of PA66-GF50 (*FEA (CZM skin-core)*) showed the capability to predict the experimental maximum load of subcomponents under all environmental conditions within a 2.6% error. This represents a significant improvement over the state-of-the-art methodology currently available in commercial software for IM-SFRPs (described in Section 2.6), which considers failure initiation criteria only (and not propagation), and which underestimates the failure load by 16-24%.

2. This improvement in the accuracy of failure predictions is due to the ability of the proposed methodology to account simultaneously for (i) the finite fracture toughness of the material, and (ii) the dependence of the fracture toughness on the complex skin-core fibre orientation distribution created across the thickness of the subcomponents. Without considering the skin-core microstructure (as done in *FEA CZM skin*), the errors in the predicted failure load could reach 14%.

3. This coupled FEA using CZM was able to predict the post-peak load response of the subcomponents under wet and/or hot conditions. However, under 23°C-DAM conditions, the FEA predicted a stable failure process, while a brittle sudden failure was observed experimentally. This difference is likely due to a change of failure mode (brittle/unstable in the subcomponents, ductile/stable in the CT tests) and experimental artifacts.

4. The skin-core microstructure of IM-SFRPs significantly influenced the sequence of failure events and the local crack propagation directions in PA66-GF50 subcomponents. For the geometry analysed in this work, fractographic analysis suggests that crack propagated preferentially along the weaker and more brittle core, leading to an unexpected reversed crack direction near the edges of the subcomponents. This preferential damage propagation within the core was captured in the FEA with CZM accounting for the distinct local properties in the skin and core regions of the fracture surface.

5. Considering the temperature-moisture equivalence shows the potential to reduce the amount of experimental work required for material characterisation, not only for modulus and full stress-strain behaviour from dog-bone tensile tests (as observed in Chapter 3 and reported previously in the literature [50–52]), but also for the material's fracture toughness from CT tests. In addition, whilst previous research [50–52] has focused only

on the coupon level, the concept of temperature-moisture equivalence was confirmed for the subcomponent level until final failure as well.

6. A large difference in the morphologies on the fracture surfaces of subcomponents due to the effect of moisture level and testing temperature was observed: fibre failure with ductile matrix behaviour was observed in hotter/wetter conditions, while brittle matrix failure was observed under 23°C-DAM conditions. The sequence of failure events could not be deduced from the fracture surfaces obtained under wet/hot/hot-wet conditions due to large plastic deformation of the PA66 matrix, but it could be captured using FEA, and it was consistent for all environmental conditions.

7. Combining FEA and fractography techniques provides a more comprehensive picture of the sequence of failure events in subcomponents than using each technique individually. For the subcomponent analysed in this work, combining these two techniques was fundamental to reach the 2nd and 4th conclusions mentioned above.

The new FE simulation methodology proposed in this Chapter is promising to design safer and more efficient damage-tolerant IM-SFRP components. This FE simulation methodology is validated using a real automotive component used in the automotive industry in Chapter 7.

Chapter 7 - Predicting failure in injection-moulded short-fibre components through fracture mechanics

7.1 Introduction

As reported in Chapter 2, the state-of-the-art coupled FEA for IM-SFRPs (reviewed in Section 2.6) shows good agreement with experimental results regarding the initial stiffness and the subsequent non-linear behaviour, at both coupon and subcomponent levels [16,76,77,79,80]. However, to predict failure of subcomponents accurately, the material's progressive failure and its finite fracture toughness need to be accounted for, as concluded in Chapter 6.

Nevertheless, the progressive failure and finite fracture toughness of IM-SFRPs is yet to be considered in any coupled FEA for components [76,79,80]. This leads to overly conservative design, and hence excessively heavy and costly components in industry. Therefore, at the component level, it is vital to validate the new FE simulation methodology proposed in Chapter 6 (considering the material's progressive failure).

Moreover, Chapter 6 has shown that an in-depth understanding of the sequence of events and damage mechanisms can be obtained by combining fractography with coupled FE simulations considering progressive failure, at the subcomponent level. In components, a more complex sequence of failure events needs to be considered, due to more complex fibre orientation states and loading conditions (compared with those in coupons and subcomponents) [79,101–103]. However, there is no literature characterising the damage mechanisms and the sequence of failure events for IM-SFRPs at the component level.

Therefore, Chapter 7 focuses on the experimental characterisation and failure prediction of an IM-SFRP component with the following objectives:(i) using fractography, to characterise failure and how it is affected by the manufacturing process and variability, and (ii) to validate the new FE methodology to predict progressive failure of IM-SFRPs (as proposed Chapter 6), at the component level. This chapter is organised as follows: Sections 7.2, 7.3 and 7.4 detail the experimental testing, process simulations, and the coupled FE simulations for IM-SFRP

components, respectively. All the relevant results are discussed in Section 7.5, and the main conclusions are drawn in Section 7.6.

7.2 Experiments

7.2.1 Procedures

7.2.1.1 Manufacturing of PA66-GF50 components

PA66-GF50 components were manufactured with the same material as characterised in Chapters 3 and 5, and as used for the subcomponents in Chapter 6. The components were injection moulded using a SE130D (SUMITOMO) machine, with the moulding conditions specified in Table 7.1.

The geometry of the components is defined in Fig. 7.1; this geometry has been selected by the industrial partner Asahi Kasei Corporation from real automotive engine mounts used in the automotive industry. Engine mount suspends the engine through a metal shaft, to support static and dynamic loads, and to isolate noise and vibration [105]; therefore, it is a semi-structural component. The engine mounts manufactured with PA66-GF50 provide weight savings of up to 50% over traditional steel or aluminium mounts [106].

The location of the injection point (defined by the mould) and the resulting weldline (as predicted by the process simulation reported in Section 7.3) are shown in Fig. 7.2. Note that the injection point is shifted by 2 mm towards the negative z- direction (backface) from the mid-width of the component. Therefore, whilst the overall component has a symmetric geometry about the x-y plane, the manufacturing conditions and, consequently, its microstructure are asymmetric. The mould partition coincides with the mid-width x-y plane, which generates a draft angle of approximately 0.3° (this is not represented in the schematic in Fig. 7.1, but is visible in the real component shown in Fig. 7.2 (b)). After manufacturing, the injection-moulded components were stored in aluminium-lined bags to maintain them at DAM conditions.

Table 7.1. Injection moulding parameters for the components.

Cylinder temp. (°C)	Mould temp. (°C)	Injection time (s)	Holding pressure (MPa)	Cooling time (s)
290	90	3.0	70	30

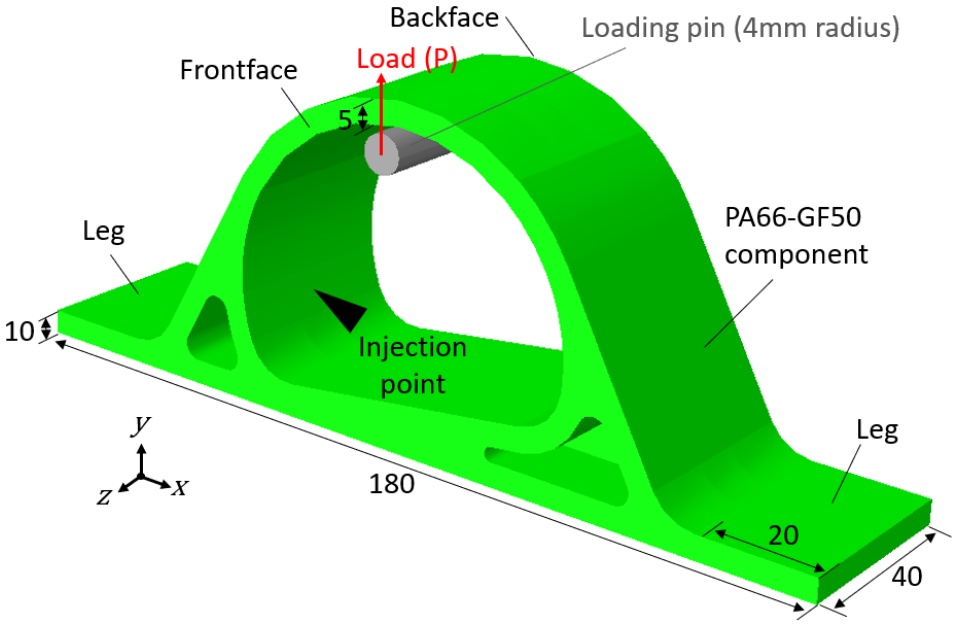


Fig. 7.1. Overall 3D view of the geometry of the component (all dimensions in mm).

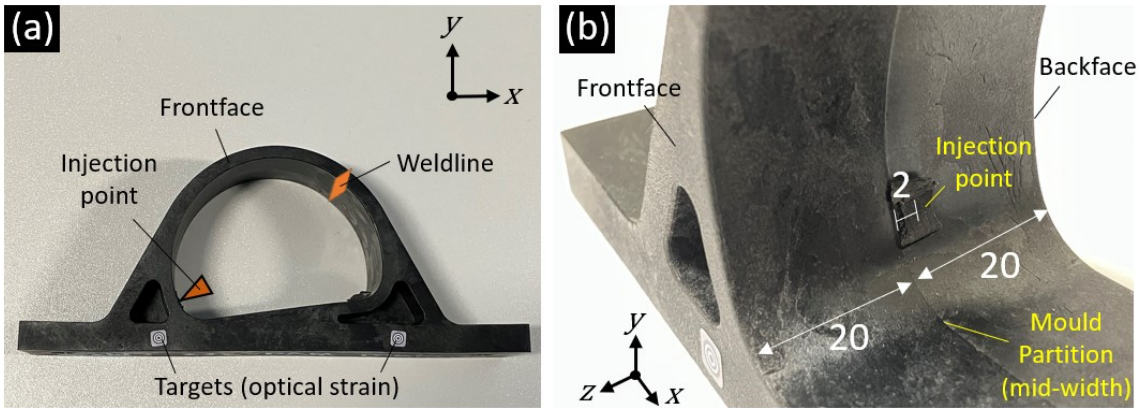


Fig. 7.2. Location of the injection point, weldline, and mould partition in the component: (a) global view, and (b) zoom-in of the injection point (all dimension in mm).

7.2.1.2 Mechanical tests of PA66-GF50 components under quasi-static conditions

PA66-GF50 components were tested under quasi-static conditions under 23°C-DAM, using the set-up shown in Fig. 7.3 and the testing specifications in Table 7.2. The legs of the components were clamped (using steel fixtures) directly to the baseplate of the testing machine using a torque wrench (with a torque of approximately 10 Nm). The position of the component along its length (i.e. x-) direction was established by the following steps: (i) the component was hung by the loading pin (steel, with 4 mm radius) placed inside the engine mount's opening, (ii) the placement of the component was adjusted to make its bottom surface parallel to the

baseplate of the testing machine, and (iii) the loading pin was moved down until the component and the machine's baseplate were in light contact.

A load (P) was then applied through continuous quasi-static displacement control of the loading pin along the positive y- (upwards) direction. The loading pin was lubricated to allow for its rotation during the tests. This loading setup represents a simplified worst-case scenario of the real application of the engine mount component, which holds the engine in place and absorbs its vibrations.

The displacement of the loading pin was measured with an optical strain gauge, by tracking a target on the pin (shown in Fig. 7.3 (a)); displacements were also tracked at two additional targets near the bottom of the component (shown in Fig. 7.2 (a) and Fig. 7.3 (a)). The full-field displacement/strain on the surface of the components was also characterised using 3D-DIC; this focused on two distinct regions (where failure had been predicted and observed): on the top surface of the component (above the loading pin), and on the weldline (as shown in Fig. 7.3 (c)).

In the tests, the orientation of the components with respect to their front- and back-faces was controlled. Five components were tested with the frontface forwards (as shown in Fig. 7.3 (b)), and four components were tested with the backface forwards (i.e. by rotating them 180° around the y-axis), to investigate the possibility of asymmetries in the testing set-up (more details will be discussed in Section 7.2.2.1).

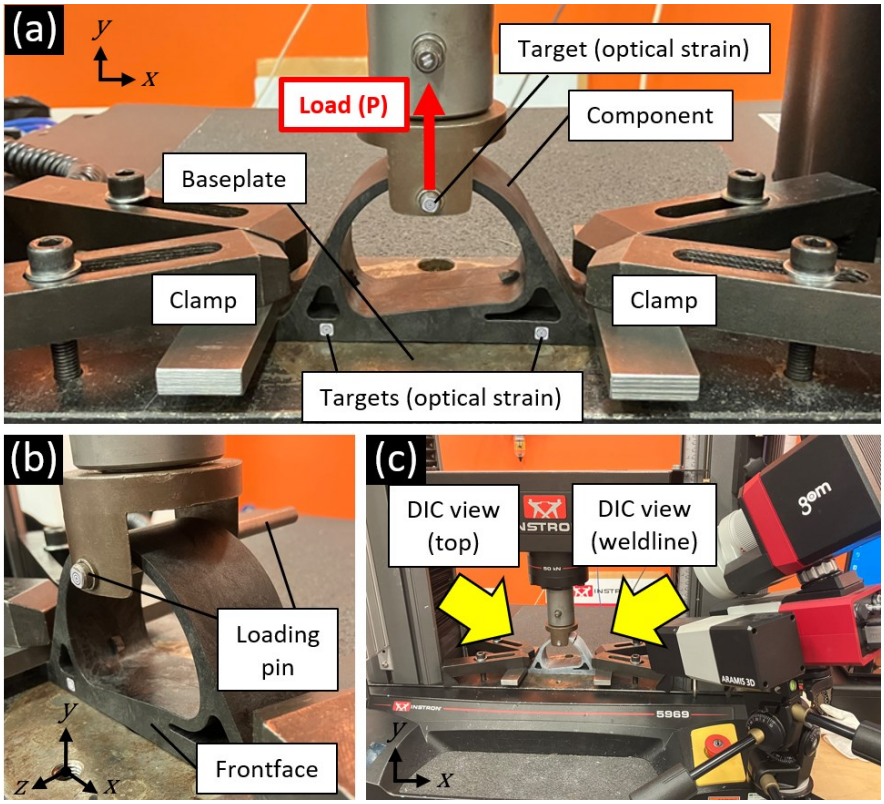


Fig. 7.3. Testing set-up for the components:
(a) frontface view, (b) angled view, and (c) set-up for DIC measurements.

Table 7.2. Testing specification for PA66-GF50 components

Number of components tested	Cross head speed (mm/min)	Environmental conditions
9	1.0	23°C-DAM

7.2.1.3 Fractography

Selected fracture surfaces were separated from the component using a dry handsaw and mounted on stubs using carbon-black-loaded epoxy adhesive. These samples were sputter-coated with gold for 20 s, and examined using a Hitachi S-3700 SEM, with an acceleration voltage of 12 kV.

7.2.2 Results

7.2.2.1 Failure modes of PA66-GF50 components

Fig. 7.4 shows the load-displacement curves of the components under 23°C-DAM conditions. Although all nine components tested were nominally identical (i.e. were manufactured with the

same material, using the same mould, and under the same conditions), they failed at two different locations, as shown in Fig. 7.5. Five components failed at the top of the component, along the y-z plane, above the point of contact with the loading pin ("*Top-failure*", Subfig. (a)); four components failed at the weldline ("*Weld-failure*", Subfig. (b)). Each of these failures happened when the applied load reached the maximum value in each test. In the components with *Top-failure*, no macroscopic evidence of plasticity or damage was seen elsewhere in the component (except for the fracture plane, Fig. 7.5 (c) and (d)). In the components with *Weld-failure*, a witness mark was observed on the contact area between the component and the pin (Fig. 7.5 (e)), especially at the mid-width of the component (i.e. at the mould partition). The load-displacement curves and failure modes of the components were not affected by their front/back orientation (which was controlled as described in Section 7.2.1.2).

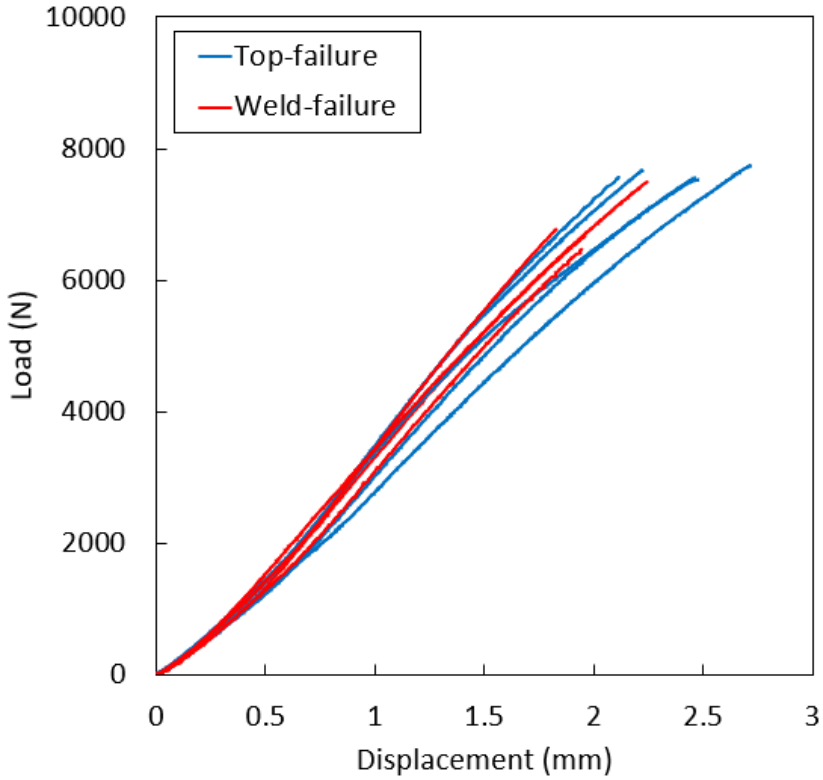


Fig. 7.4. Load-displacement curves of PA66-GF50 components.
(all specimens showed unstable failure after the maximum load).

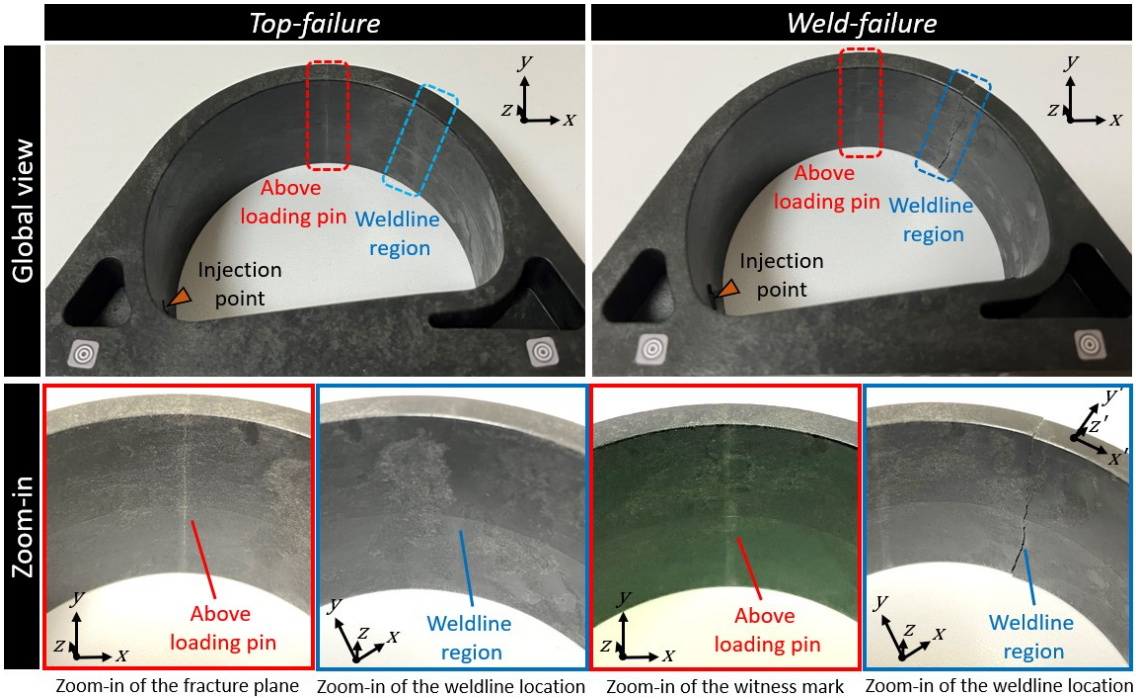


Fig. 7.5. Observation of the two fracture locations in PA66-GF50 components (after failure): *Top-failure* component (left) and *Weld-failure* component (right).

The average and standard deviation of the maximum load are summarised in Table 7.3. A lower average maximum load (by 753 N) with larger standard deviation (by 299 N) was seen in components with *Weld-failure*.

Table 7.3. Averaged maximum load and their standard deviation of the components tested.

	Top-failure (5 components)	*Weld-failure* (4 components)
Average maximum load (N)	7609	6856
Standard deviation (N)	82	381
Coefficient of variation (%)	1.1	5.6

Fig. 7.6 and Fig. 7.7 show the strain contours obtained from the DIC measurements, just before the components failed with *Top-failure* and *Weld-failure*, respectively. Higher values of local strains were observed at the top (above the loading pin) of the component with *Top-failure* (Fig. 7.6); however, at this location, no additional strain concentrations were captured near the front- or back-edges of the component, possibly due to limitations in the viewing window (this will be further discussed in Section 7.5.2). In addition, there was a mild increase in the von Mises equivalent strain in the region of the weldline.

For the components with *Weld-failure* (Fig. 7.7), strain concentrations were seen at the outer surface of the weldline in Fig. 7.7 (b), especially near the front- and back-edges of the component.

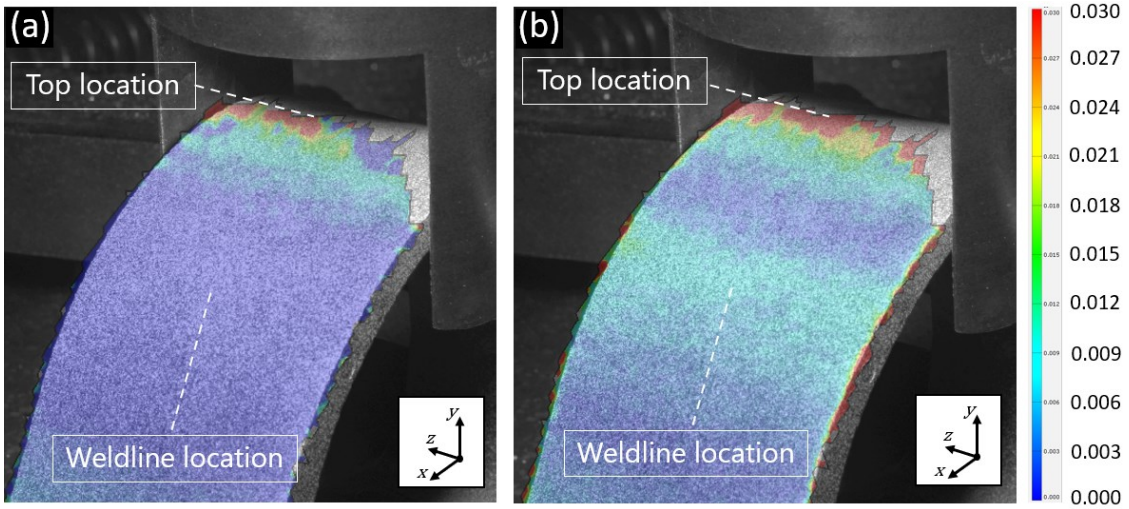


Fig. 7.6. Contour of strains obtained from DIC measurements just before a component failed at the top (*Top-failure*): (a) strain along the x-direction, and (b) equivalent strain.

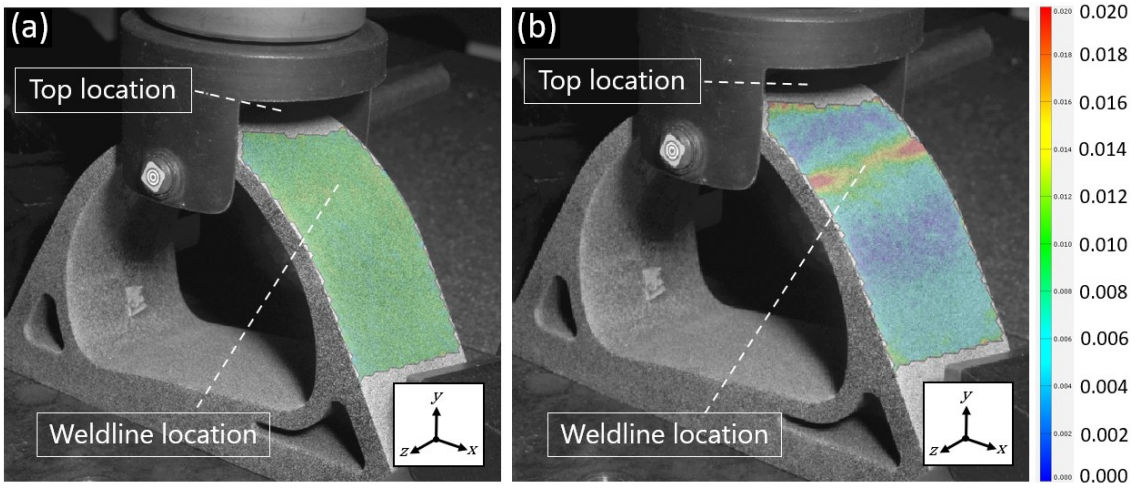


Fig. 7.7. Contour of strains obtained from DIC measurement just before a component failed at the weldline (*Weld-failure*): (a) strain along the x-direction, and (b) equivalent strain.

7.2.2.2 Initial response and non-linearity correction

For all components tested, the load-displacement curves (Fig. 7.4) showed an initial non-linear response, with a degree of scattering beyond a displacement of approximately 0.3 mm. Subsequently there was an apparent strain-hardening response up to a load of approximately 4 kN, after which there was an inflection of the load-displacement curves. Therefore, the apparent

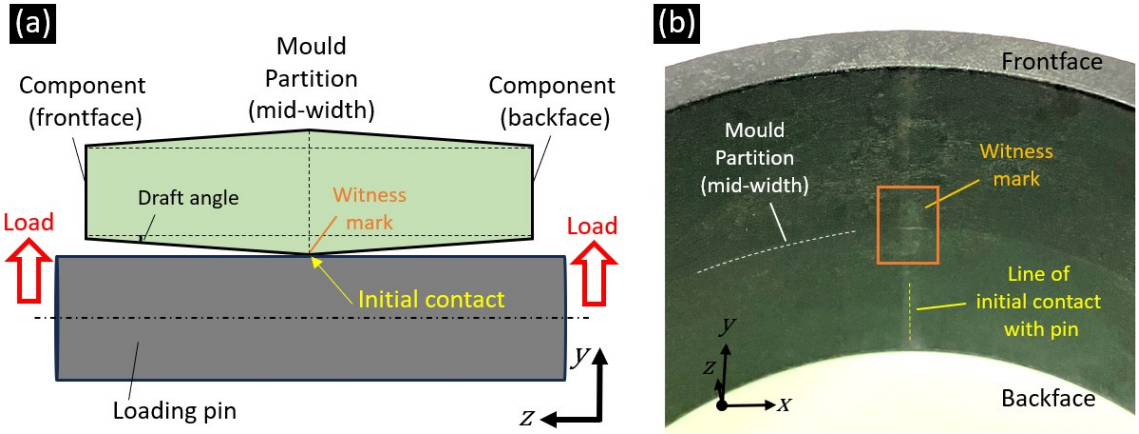
tangent stiffness of the load-displacement curves was calculated at two different zones: (i) at the beginning of the loading curves (displacements between 0.1-0.2 mm), and (ii) after the inflection points (displacements between 0.8-0.9 mm); these are summarised in Table 7.4. The average stiffness obtained at the displacement between 0.8-0.9 mm was approximately 50% higher than that corresponding to 0.1-0.2 mm.

Table 7.4. Averaged stiffness calculated from the load-displacement curves of the components at displacements between 0.1-0.2 mm and 0.8-0.9 mm.

	Top-failure		*Weld-failure*	
	0.1-0.2 mm	0.8-0.9 mm	0.1-0.2 mm	0.8-0.9 mm
Average stiffness (N/mm)	2623	3897	2589	4068
Standard deviation (N/mm)	148	468	122	298
Coefficient of variation (%)	5.6	12.0	4.7	7.3

The following possible causes for this initial non-linear response and apparent strain-hardening were hypothesised and investigated:

1. Lateral displacement and/or rotation of the loading pin: further analysis tracking the displacements of additional optical extensometer targets on the pin showed that the lateral displacement of the loading pin was smaller than 0.1 mm, and pin rotations were below 0.4°. FE simulations [107] suggest that these deviations are more than an order of magnitude smaller than those required to noticeably affect the load-displacement curve. Therefore, this hypothesis was discarded.
2. Movement of the component's legs (sliding along the x - direction): further analysis tracking the displacement of two additional optical extensometer targets at the bottom of the component showed lateral displacements smaller than 0.02 mm. Moreover, there was no clear evidence of a correlation between the lateral displacement of the component and the onset of strain-hardening in the load-displacement curves. Therefore, this hypothesis was discarded as well [107].
3. Localised deformation of the component along the contact region with the loading pin (i.e. along the mid-width plane, parallel to the y-z plane). This localised deformation is actually visible as a witness mark in Fig. 7.5 (e). This witness mark was most evident at the mid-width plane (parallel to the x-y plane), which suggests that localised deformation was magnified by the mid-width edge (on the mould partition) created by the draft angle, as illustrated in Fig. 7.8).



(a) Schematic of the geometry of the component at the top along the mid-length ($y - z$) plane, highlighting that the loading pin initially contacts the component locally at the mid-width/partition plane. The change in the thickness of the component in this schematic is not to scale (the draft angle from the mid-width to the edge is approximately 0.3°).

(b) Zoom-in of a component with *Weld-failure* after testing, highlighting the witness mark at the mould partition, at the top of the specimen

Fig. 7.8. Formation of a witness mark due to contact between the loading pin and the component.

Therefore, it can be concluded that the strain-hardening behaviour in the load-displacement curves (Fig. 7.4) was most likely due to localised deformations occurring just above the loading pin, concentrated at the mid-plane due to the small variation of the thickness in the component generated by the draft angle. However, it is unrealistic to consider this variation of the thickness of the component at the top in the FE simulations (to be described in Section 7.4.2), while maintaining a structured mesh (as required for the representation of *Top-failure* using cohesive elements). Therefore, to ensure a fair comparison between the tests and the FE simulations, the experimental load-displacement curves were corrected to remove the effect of this localised deformation, by the following two steps: (i) substituting the measured curve up to 0.8 mm (the initial hardening point) by regression lines (with the apparent stiffness measured in the 0.8-0.9 mm displacement interval), and (ii) shifting the starting point of each modified curve to zero displacements. The resulting corrected load-displacement curves are presented in Fig. 7.9.

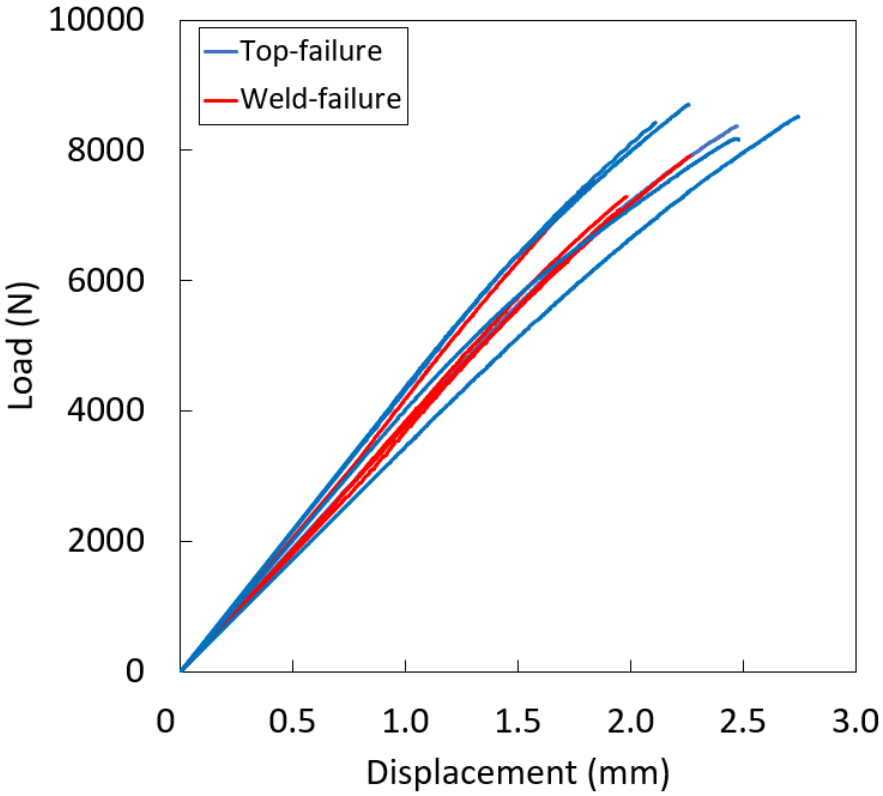


Fig. 7.9. Load-displacement curves of PA66-GF50 components after correcting for the initial non-linearity (below 0.8 mm).

7.2.2.3 Fractography

Several scanning electron micrographs of the fracture surface (parallel to the $y-z$ plane) of a component with *Top-failure* are shown in Fig. 7.10. Ductile fracture surfaces with a small degree of matrix plastic deformation were found at the top of the frontface as shown in Fig. 7.10 (a), while brittle fracture surfaces were observed elsewhere. Riverlines in the matrix [53] show that the crack had propagated downwards (negative y-direction) and towards the backface (negative z-direction). These features were confirmed to be representative of *Top-failure* components, as they were consistent with the fracture surface of another component, and are corroborated by simulations (as discussed in Section 7.5.3). The location of ductile fracture surfaces was also independent of the front/back orientation of the component during the tests.

Several scanning electron micrographs of the fracture surface (parallel to the $y'-z'$ plane, defined in Fig. 7.5 (f)) of a component with *Weld-failure* are shown in Fig. 7.11. Brittle fracture was observed on most of the surface (e.g. Subfigures (a) – (f)); riverlines in the matrix show that

the crack had propagated upwards (positive y'-direction). Ductile fracture with a small degree of matrix plastic deformation was found on some regions at the bottom mid-width of the fracture surface (e.g. Subfigures (g) and (h)). These regions with ductile fracture were also observed in another component (Fig. 7.11 (B)), at a slightly different location; defects were observed in some regions where the fracture surfaces presented ductile features.

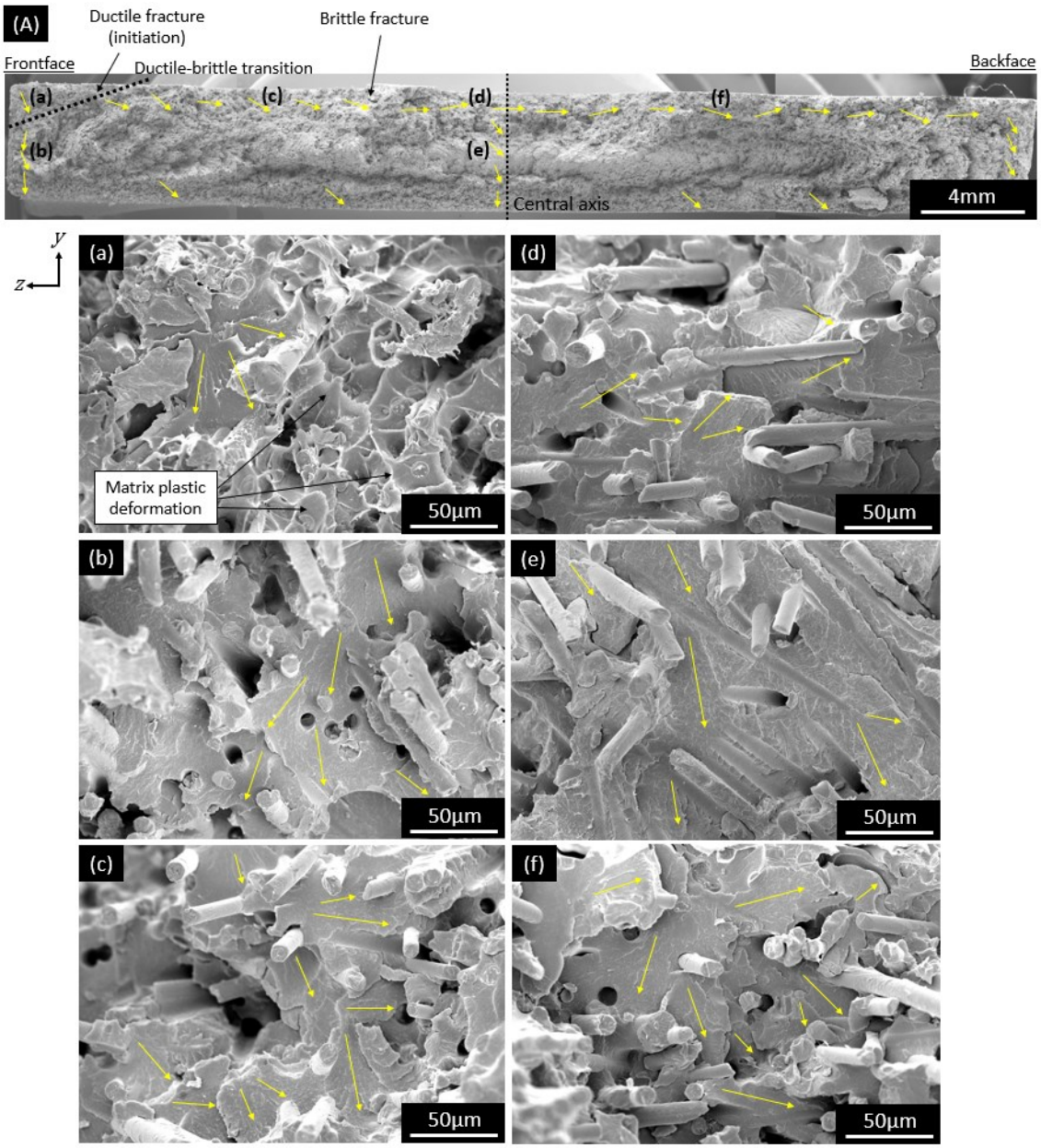


Fig. 7.10. Representative scanning electron micrographs of the fracture surface of a component with *Top-failure*: (A) global view; Subfigures (a)-(f) correspond to the regions identified in Subfigure (A). The yellow arrows represent the local direction of crack propagation, identified by matrix fracture morphologies (riverlines).

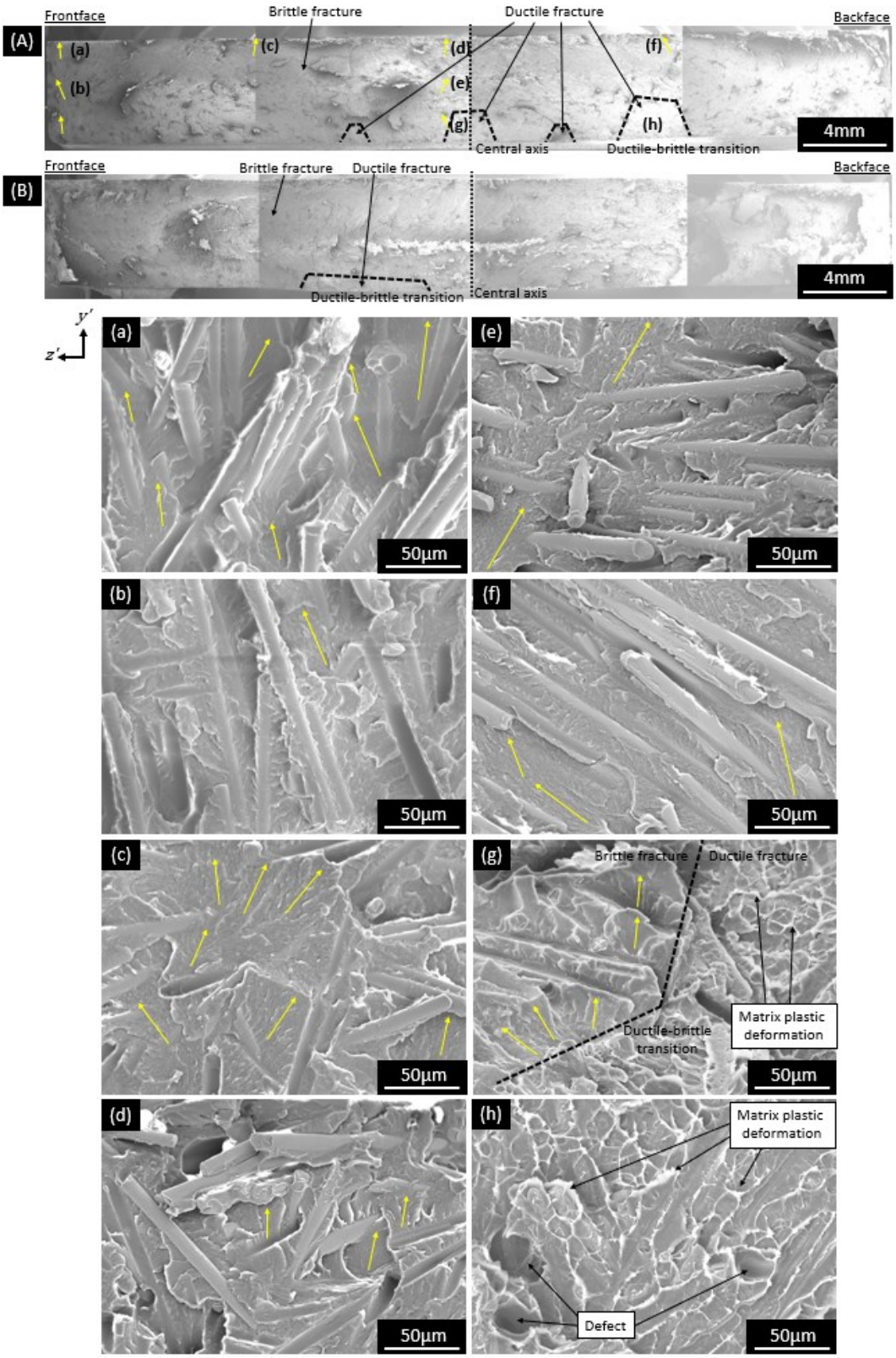


Fig. 7.11. Representative scanning electron micrographs of the fracture surfaces of components with *Weld-failure*. (A) and (B): global views from the two different components; Subfigures (a)-(h) correspond to the regions identified in Subfigure (A). The yellow arrows represent the local direction of crack propagation, identified by matrix fracture morphologies (riverlines).

7.3 Process simulations of PA66-GF50 components

7.3.1 Procedures

The Moldflow software [69] was used to simulate the injection moulding process and predict the fibre orientation fields in the components, using the MRD fibre orientation model (as in Chapter 6). The 3D mesh used had 2,587,198 elements, with 40 layers across all thickness directions. The same settings as used for the subcomponents in Chapter 6 were selected, with injection-moulding conditions as in the actual manufacturing of the components (shown in Table 7.1).

7.3.2 Results

Fig. 7.12 (a) shows the predicted fibre orientation tensor along the x-direction on the overall component surface. This contour clearly shows the location of the weldline, which agrees with the fracture plane of the *Weld-failure* components observed experimentally in Fig. 7.5. Local views of the fracture plane (observed experimentally) in *Top-failure* and *Weld-failure* are shown in Fig. 7.12 (b) and (c). Fig. 7.12 (b) shows that the *Top-failure* fracture plane has a complex fibre orientation distribution, which is not fully captured by the typical and simpler skin-core-skin microstructure of IM-SFRPs (as was seen, for instance, in the subcomponent in Chapter 6). In addition, the fibre orientation tensor at the top of the component (i.e. across the *Top-failure* plane) was slightly lower near the frontface (i.e. the face furthest away from injection point) than that near the backface. Fig. 7.12 (c) shows that the fibre orientation field on the *Weld-failure* plane is more homogeneous than that on the *Top-failure* plane.

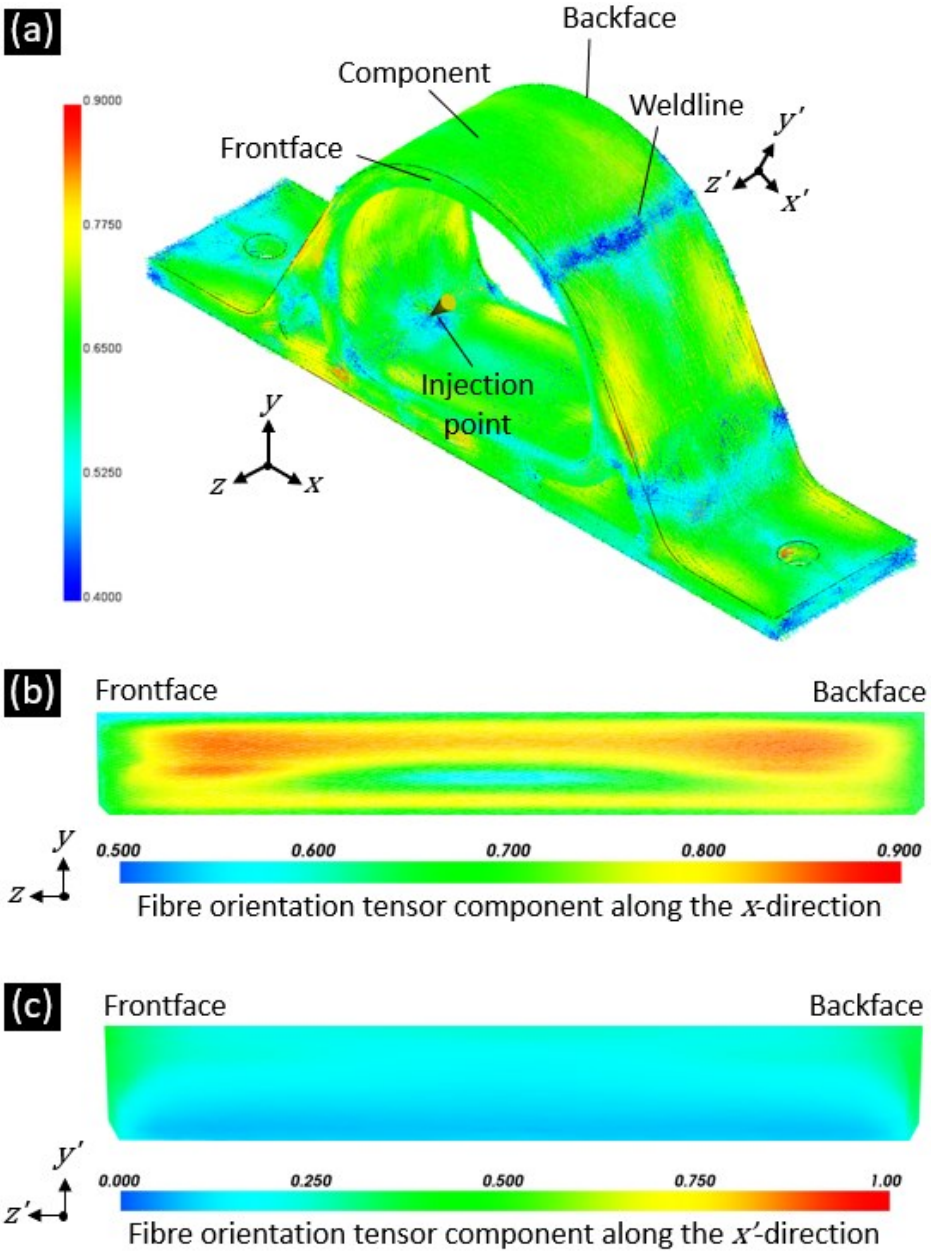


Fig. 7.12. Predicted fibre orientation tensor in the component:
(a) on the overall component surface, along the x-direction, (b) local view across the *Top-failure* fracture plane, and (c) local view across the *Weld-failure* fracture plane.

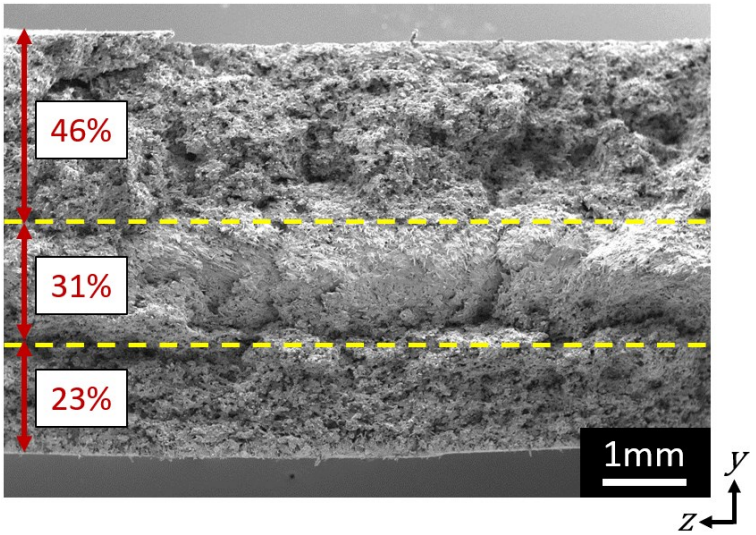


Fig. 7.13. Scanning electron micrographs of fracture surfaces at the mid-width of a component with *Top-failure* (same location as Fig. 7.10 (e)). The yellow dotted lines indicate the interface between apparent skin and core layers, with their proportions across the thickness indicated.

Fig. 7.14 proposes two simplified partitioning patterns of the *Top-failure* fracture plane, which will be used in the subsequent Sections to capture this fibre orientation distribution in the coupled FEA. The corresponding average fibre orientation tensors in these partitions are summarised in Table 7.5.

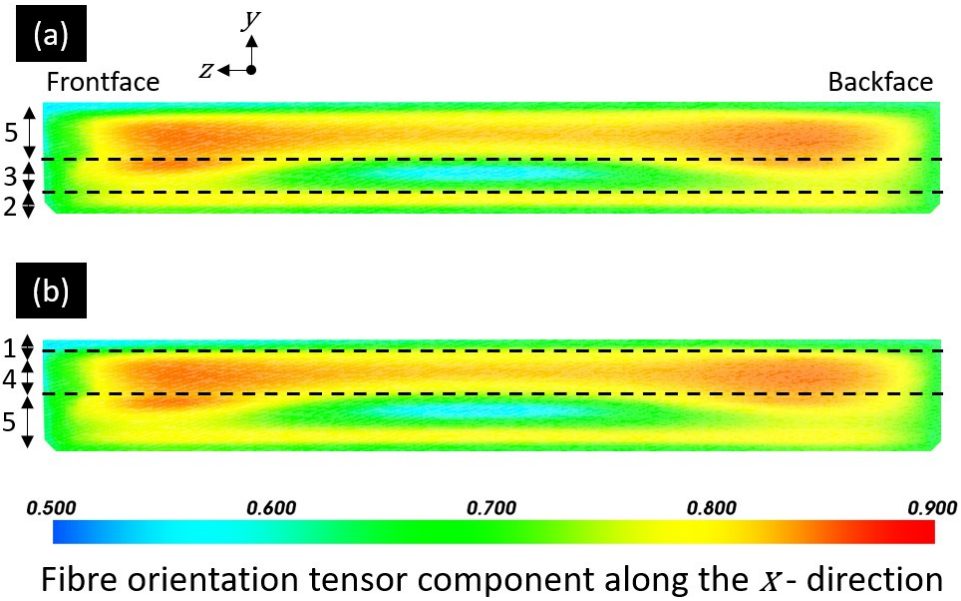


Fig. 7.14. Partitioning patterns for the fibre orientation states in the *Top-failure* fracture plane to be used in the coupled FE simulations:
(a) *FEA (CZM 5:3:2)*, and (b) *FEA (CZM 1:4:5)*. The dimensions on the left represent the relative thickness of the partitions (the total component thickness is 5 mm).

Table 7.5. Average fibre orientation tensors at the fracture plane in *Top-failure* components, for the two different partitioning patterns shown in Fig. 7.14.

Partition patterns	Ratio of partitioned region	Averaged fibre orientation tensor (a_{xx})
(a) *FEA (CZM 5:3:2)*	5:3:2	0.80 / 0.50 / 0.80
(b) *FEA (CZM 1:4:5)*	1:4:5	0.70 / 0.80 / 0.70

7.4 Coupled FE simulations of PA66-GF50 components

This Section reports on the simulation of the components tested in Section 7.2, using the same strategy according to either (i) the state-of-the-art coupled FE methodology [5,77] described in Section 2.6 (which considers failure initiation only), and (ii) the new methodology proposed in Chapter 6 (which accounts for progressive failure through CZM). Both methodologies couple injection-moulding simulations to FE simulations of the experimental tests to account for the predicted local fibre orientation tensor (Fig. 7.12), as previously used for the subcomponents in Section 6.5. The elastic-plastic material model calibrated in Chapter 4, with the Tsai-Hill 3D transversely-isotropic failure criterion integrated in Digimat software [5], was also used for these FE simulations.

7.4.1 Methodology

7.4.1.1 Component modelling

The 3D geometry of the component was fully modelled, partitioned and meshed as shown in Fig. 7.15; the only significant simplification made was neglecting the 0.3° draft angle, as explained in Section 7.2.2.2, as this would make it even more challenging to generate a structured 3D mesh. The component was meshed with 8-node hexahedral reduced integration elements (C3D8R), using 10 layers of elements across the thickness, and a total of 72,490 elements. Preliminary analyses [107] have shown that this produced converged results.

7.4.1.2 Boundary conditions

The loading pin was modelled using solid 8-node hexagonal elements (C3D8R) to account for its deformation during the testing. To achieve this, each (front and back) end-surface of the pin was constrained to its centre, where a prescribed displacement of 3 mm was applied (allowing only movement along the y-direction). The component was placed between three fixed

analytical surfaces (as shown in Fig. 7.15 (b)), representing the clamping fixtures above the legs and the base surface of the testing machine bellow. The interaction between the component and the loading pin or the analytical surfaces was modelled with general contact (with a friction coefficient of 0.2, which was provided by the industrial partner, Asahi Kasei Corporation).

Based on preliminary simulations [107], it was concluded that the geometry and these boundary conditions needed to be fully modelled; this is because further simplifications (e.g. representing the pin with a rigid surface, or fully fixing the legs of the component) led to significantly different predictions of apparent initial stiffness.

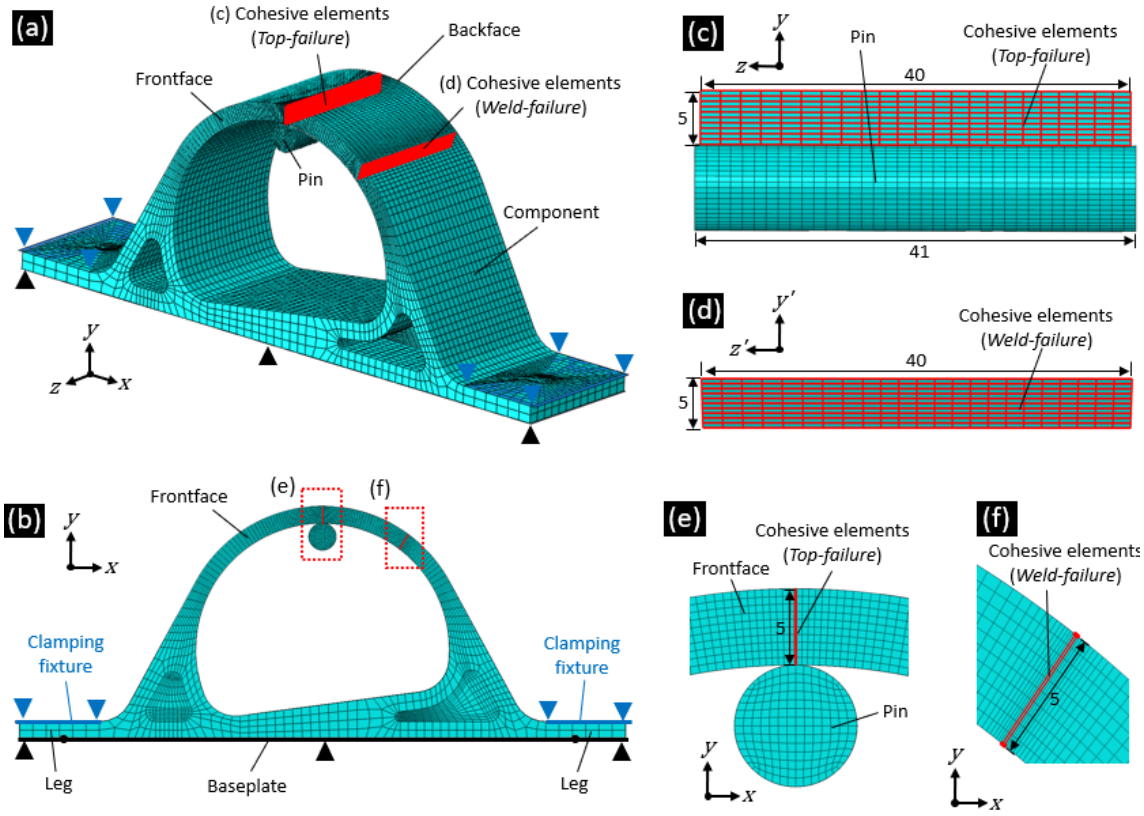


Fig. 7.15. FE model of the components:
(a) Global view of the component, with fracture planes shown in red, (b) view from the frontface, with fracture planes shown in red and analytical surfaces shown in blue or black; meshes on the fracture plane for (c) *Top-failure* and (d) *Weld-failure*; zoom-in of the mesh at the edge of frontface around the cohesive elements for (e) *Top-failure,* and (f) Weld-failures (all dimensions in mm).

7.4.1.3 Coupled FEA of PA66-GF50 components with CZM

For the new coupled FEA methodology combined with CZM (proposed and applied to subcomponents in Section 6.5.3), one layer of cohesive elements was placed along one of the two expected fracture planes. These coincided with the actual fracture locations observed experimentally: (i) at the top of the component, above the loading pin, to simulate *Top-failure,* or (ii) along the weldline, in the location predicted by the process simulation, to simulate *Weld-failure*. A preliminary convergence study [107] was conducted to determine the suitable size and thickness of cohesive elements; based on this convergence study, cohesive elements with 0.1 mm thickness (same thickness as that used for the subcomponents in Chapter 6) were assigned at these expected fracture planes, as shown in Fig. 7.15. The material properties used for the cohesive elements (i.e. stiffness, critical stress and fracture toughness, neglecting mode-I vs. mode-II dependence) were determined using the same methodology as described for the subcomponents in Section 6.5.3, according to the predicted fibre orientation tensor fields at the fracture planes (Fig. 7.14 and Table 7.5), as summarised in Table 7.6.

For the simulations of *Weld-failure*, two different inputs will be used in the coupled FEA with CZM: (i) properties from neat PA66 matrix, and (ii) estimated properties of a PA66GF50 material with a perfectly-transverse fibre orientation state (i.e. extrapolated to $a_{YY} = 0$ from the dogbone and CT coupons' test results in Fig. 3.6 and Fig. 5.7).

Table 7.6. Input properties for cohesive elements in *Top-failure* simulations with different partition patterns.

Partition patterns and relevant a_{xx}	Young's modulus (GPa)	Critical stress (MPa)	Fracture toughness (kJ/m^2)
FEA (CZM 5:3:2) (a_{xx} = 0.80/0.50/0.80)	16.0 / 10.0 / 16.0	190 / 120 / 190	18.0 / 15.5 / 18.0
FEA (CZM 1:4:5) (a_{xx} = 0.70/0.80/0.70)	15.0 / 16.0 / 15.0	165 / 190 / 165	17.0 / 18.0 / 17.0

Table 7.7. Input properties for cohesive elements in *Weld-failure*.

	Young's modulus (GPa)	Critical stress (MPa)	Fracture toughness (kJ/m^2)
(i) *FEA (CZM PA66)* [30]	3.0$^{(*)}$	95$^{(*)}$	5.3
(ii) *FEA (CZM* $a_{x'x'} = 0$*)*	15.0	110	15.0

$^{(*)}$The Young's modulus and critical stress of neat PA66 were provided by Asahi Kasei.

7.4.2 Results

7.4.2.1 Failure prediction in coupled FEA

Fig. 7.16 compares the load-displacement curves of the components up to the maximum load, as obtained from experiments and the coupled FEA. This considers either (i) the proposed methodology using cohesive elements to account for the finite toughness of the material (detailed in Section 7.4.1), or (ii) the state-of-the-art methodology based on the Tsai-Hill initiation criterion (as reviewed in Section 2.4 and detailed in Section 6.5.2). A good agreement was observed in the initial stiffness (after removing the spurious initial non-linearity, likely caused by localised plasticity at the witness mark, as described in Section 7.2.2.2) and progressive softening in all cases. Regarding the prediction of the maximum load, the following differences between methodologies were observed (as summarised in Table 7.8):

- Considering *Top-failure* (and the different *FEA (CZM)* partitioning patterns defined in Fig. 7.14 and Table 7.5):
    - the coupled FEA based solely on the Tsai-Hill failure criterion (*FEA (TH)*) predicted failure initiation at a load 14.2% lower than the maximum load in the experimental results;
    - *FEA (CZM 1:4:5)*, accounting for progressive failure, showed an excellent agreement of maximum failure load with the experimental data (with an error of 0.6%), while the alternative fracture-surface partition (*FEA (CZM 5:3:2)*) overestimated the experimental maximum load by 9.1%.
- Considering *Weld-failure*:
    - the coupled FEA based solely on the Tsai-Hill failure criterion (*FEA (TH)*) predicted failure initiation at a load 56.2% higher than the maximum load in the experimental results;
    - the *FEA (CZM PA66)* showed an excellent agreement of maximum failure load with the experimental data (with an error of 2.3%), while the alternative (using transverse properties, *FEA (CZM* $a_{x'x'} = 0$*)*) overestimated the maximum load by 36.8%.

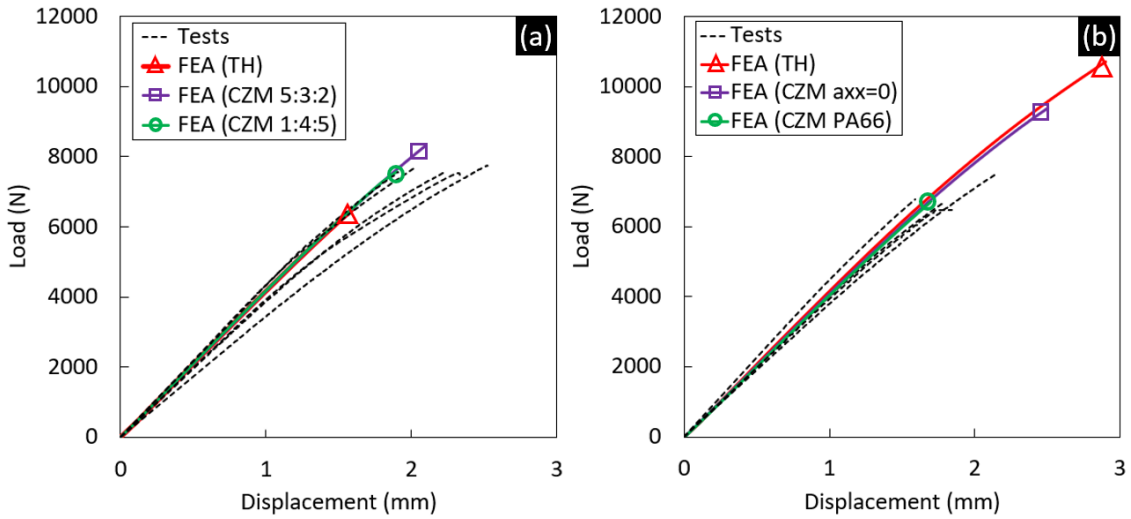


Fig. 7.16. Load-displacement curves of the components from experimental tests and coupled FEA with CZM until the maximum load: (a) *Top-failure*, and (b) *Weld-failure*.

Table 7.8. Error of the maximum failure load predicted for the components by the different FEA methodologies, compared to the average from experiments.

	Top-failure (%)	Weld-failure (%)
FEA (TH), initiation	-14.2	+ 56.2
FEA (CZM 5:3:2)	+ 9.1	---
FEA (CZM 1:4:5)	- 0.6	---
FEA (CZM PA66)	---	-2.3
FEA (CZM $a_{x'x'} = 0$)	---	+ 36.8

7.4.2.2 Sequence of failure events predicted by coupled FEA

Fig. 7.17 shows the stiffness degradation of the cohesive elements assigned at the fracture plane in the coupled FEA combined with CZM. Considering *Top-failure* (Fig. 7.17 (a)), damage initiated at the top and frontface corner, then propagated downwards (along the negative y-direction) and towards the backface (along the negative z-direction). Considering *Weld-failure* (Fig. 7.17 (b)), damage initiated at the bottom of the fracture plane, slightly away from the frontface/backface edges, then propagated upwards (along the positive y-direction). The predicted damage initiation locations and directions of damage propagation match those observed in the experiments (shown in Fig. 7.10 and Fig. 7.11), as will be discussed in Section 7.5.3.

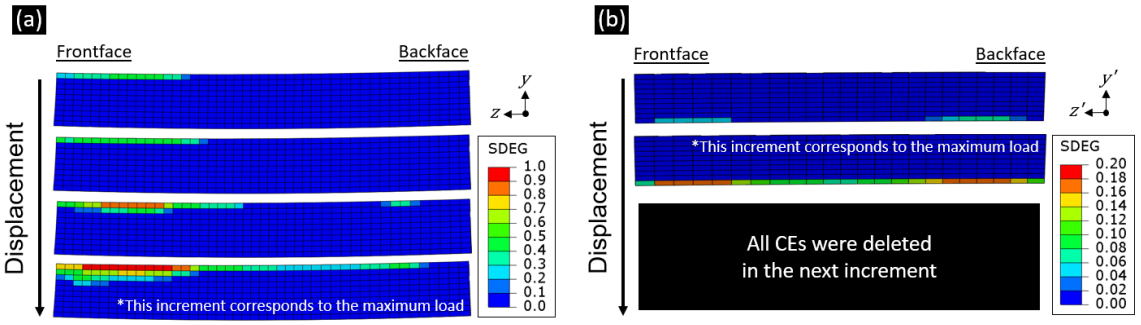


Fig. 7.17. Stiffness degradation of the cohesive elements in the coupled FEA combined with CZM at 23°C-DAM: (a) *Top-failure* (*FEA (CZM 5:3:2)*) and (b) *Weld-failure* (*FEA (CZM PA66)*).

7.5 Discussion

7.5.1 Prediction of PA66-GF50 component failure using coupled FEA combined with CZM

The load-displacement curves in Fig. 7.16 show that all coupled FEA methodologies have an excellent agreement with experiments regarding the initial stiffness and progressive non-linear response. However, they also clearly demonstrate that using failure initiation criteria only (i.e. *FEA (TH)*) is not sufficient to accurately predict the maximum load observed experimentally in components with complex geometries. For the *Top-failure* case, this led to underpredicting the maximum load by 14.2%. This underprediction of the maximum load based solely on failure initiation in the component agrees with that observed for the subcomponents in Chapter 6.

As discussed at the subcomponent level in Section 6.7.2 (Fig. 6.11), the newly proposed methodology using coupled FEA with CZM (Fig. 7.16) presents a much better prediction of the maximum load measured experimentally than using the Tsai-Hill criterion alone, at the component level as well (as summarised in Table 7.8). This is true regardless of the partitioning pattern selected for the *Top-failure* fracture plane. Nevertheless, *FEA (CZM 5:3:2)* overestimated the maximum load by 9.1%, while *FEA (CZM 1:4:5)* showed an excellent agreement, with an error of only 0.6%. This difference is likely due to a more realistic representation of the local fibre orientation fields around the area of failure initiation (i.e. top half of the fracture plane) captured by *FEA (CZM 1:4:5)* (which considers two partitions in the top half of the fracture plane) than by *FEA (CZM 5:3:2)* (which completely homogenised the local fibre orientations in the top half of the fracture plane). This demonstrates that accurate FE simulations must capture a rather fine representation of the fibre orientation fields at fracture initiation sites.

Considering now the case of *Weld-failure* (Fig. 7.16 (b)), *FEA (CZM PA66)* showed an excellent agreement between the predicted maximum load and the experimental data (with an error of 2.3%), while *FEA (CZM* $a_{x'x'} = 0$*)* overestimated the maximum load by 36.8%. This suggests that failure at a weldline is not governed by the local fibre orientation, but rather by other effects that might not be currently captured by process simulations. For instance, it is possible that defects (i.e. voids) could have been formed at the weldline during injection-moulding [45,46], as observed in Fig. 7.11 (h). These defects could initiate failure and lead to unstable crack propagation in the PA66 matrix. This hypothesis is corroborated by the larger variability of the maximum load for the components with *Weld-failure* than those with *Top-failure* (Table 7.3), which suggests that *Weld-failure* might be triggered by the presence of defects. In addition, it is also possible that the local fibre volume fraction at the weldline is lower than overall [46]; this would reduce the mechanical properties of the material at the weldline, making them closer to those of the neat PA66 matrix. Previous literature investigating the tensile strength of PA66-based IM-SFRP coupons at weldlines [108] concluded that their properties were close to the matrix strength, which also supports this hypothesis. For *Weld-failure*, the prediction of initiation according to the Tsai-Hill criterion (which is does not consider any defects or reductions in fibre volume fraction) overestimated the experimental failure load by 56.2% (Fig. 7.16 (b)).

Overall, the results of the coupled FEA of real components further highlight the deficiencies of the methodology based on failure initiation criteria only, and clearly demonstrate that it is vital to account for the finite toughness of the material. This is here demonstrated for the first time at the component level. These results also highlight that the component's more complex geometry and microstructure create further simulation challenges, regarding e.g. the need to capture the details of the fibre orientation distribution on the fracture plane (Fig. 7.14 and Fig. 7.16 (a)), the influence of asymmetries in the injection-moulding process on the failure initiation site (Fig. 7.17 (a)), the coexistence of multiple possible fracture planes (*Top-* and *Weld-failure*), and the definition of properties of weldlines (as discussed in the previous paragraph).

7.5.2 Damage mechanisms and sequence of failure events in components

Based on both the morphology of the riverlines on the PA66 matrix on the fracture surface (shown in Fig. 7.10 and Fig. 7.11), and the damage propagation predicted by the coupled FEA combined with CZM (shown in Fig. 7.17), it is possible to propose a sequence of failure events for the component with *Top-failure*. This sequence of failure events (which was consistent

regardless of the front/back orientation of the components during testing) is illustrated in Fig. 7.18 and Fig. 7.19, and is summarised below:

- Stage (A), Crack initiation: the crack initiated at the top of the frontface (i.e. the face furthest away from the injection point, regardless of whether it was facing the front or the back of the test setup), where the component underwent ductile fracture (Fig. 7.10 (a)). This location of crack initiation was consistent across components, and could be predicted by the coupled FEA with CZM (Fig. 7.17 (a)). This initiation site is justified as follows: while the geometry of the component and loading are symmetric, the microstructure in the component is asymmetric, due to the position of the injection point (Fig. 7.2 (b)). The fibre orientation tensor across the fracture plane near the frontface (i.e. the face furthest away from injection point) was slightly lower than that near the backface (as discussed in Fig. 7.12 in Section 7.3.2), which caused this consistently asymmetric damage mechanism.
- Stage (B), Crack propagation downwards and towards the backface, with a clear transition from ductile fracture to brittle fracture. This transition can be explained due to the increase in the local strain rate after crack initiation. This direction of crack propagation could be also predicted well by the coupled FEA with CZM (Fig. 7.17 (a)).

For the components with *Weld-failure*, the combined analysis of fractography and FE simulations suggests the following sequence of events:

- Stage (I), Crack initiation: the crack initiated near the mid-width of the bottom skin, where the component failed with ductile fracture (Fig. 7.11 (g) and (h)). Because the precise initiation site varied amongst components (e.g. Fig. 7.11 (A) and (B)), this initiation is likely caused by the presence of defects (specifically voids [45–47], which were observed in the SEM images (Fig. 7.11 (h)). The overall location of crack initiation could be predicted by the coupled FEA with CZM (Fig. 7.17 (b)), although the variability of the exact initiation site between different components could not be predicted, which further supports that it was governed by stochastic defects.
- Stage (II), Upwards crack propagation in the bottom skin: the crack propagated upwards, with a transition from ductile to brittle fracture. This transition can be explained due to the increase in the local strain rate after the first crack initiation. The upwards direction

of crack propagation during *Weld-failure* could be also predicted well by the coupled FEA with CZM (Fig. 7.17 (b)).

- Stage (III), Upwards crack propagation until final failure: the crack propagated further upwards with brittle fracture, crossing the entire thickness of the component.

In the component testing, five components failed with *Top-failure*, while four components failed with *Weld-failure*. A possible explanation is that there might be a scattering in the quality of weldline (e.g. void content and their severity) among those nine components. This hypothesis is corroborated by the larger variability of the maximum load for the components with *Weld-failure* (5.6%) than those with *Top-failure* (1.1%) (Table 7.3).

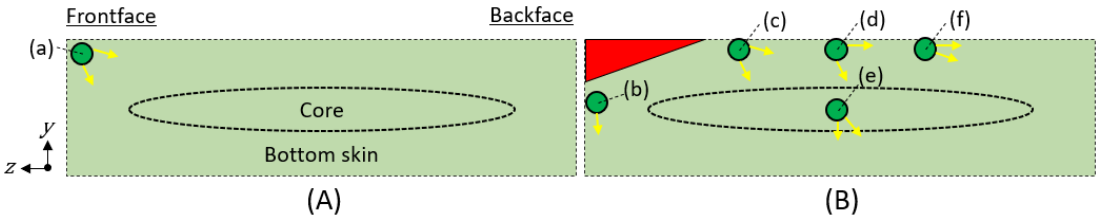


Fig. 7.18. Schematic illustration of the sequence of failure events, identified from the micrographs and coupled FEA combined with CZM for *Top-failure*.
Green circles: SEM observation points; yellow arrows: crack propagation by matrix failure/interfacial debonding (observed experimentally); red areas: damaged region with ductile fracture observed in SEM images.

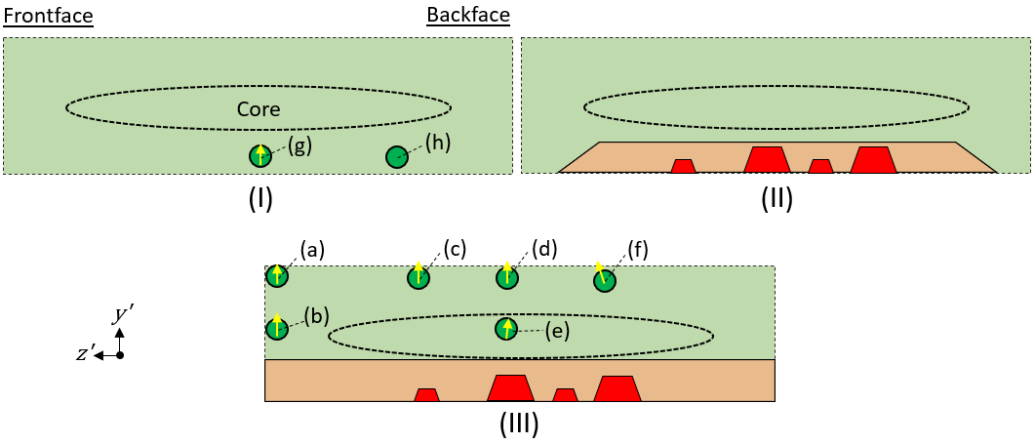


Fig. 7.19. Schematic illustration of the sequence of failure events, identified from the micrographs and coupled FEA combined with CZM for *Weld-failure*.
Green circles: SEM observation points; yellow arrows: crack propagation by matrix failure/interfacial debonding (observed experimentally); red areas: damaged region with ductile fracture observed in SEM images; light-orange areas: damaged region with brittle fracture.

7.6 Conclusions

This chapter has coupled experimental testing, fractography and FEA to characterised failure mechanisms in IM-SFRP components, and validated the new FE methodology to predict progressive failure of IM-SFRPs (as proposed Chapter 6) at the component level. The conclusions of this chapter can be summarised as follows:

i. The proposed coupled FEA using CZM (*FEA (CZM 1:4:5)*) showed the capability to accurately predict the maximum load of real components used in the automotive industry (with an error of only 0.6% in this case, compared to experiments). This represents a significant improvement over the state-of-the-art methodology (*FEA (TH)*) currently available in commercial FEA software for IM-SFRPs, which considers failure initiation only, and which underestimates the failure load significantly (by 14.2% for this component).

ii. In components, the fibre orientation fields do not mimic the typical skin-core-skin microstructure of IM-SFRP coupons. Therefore, the pattern used to partition the material properties of the cohesive elements on expected fracture surfaces has a significant influence on the accuracy of predicted maximum load. For the particular component analysed in this chapter and considering *Top-failure*, *FEA (CZM 1:4:5)*, which considered a more detailed description of local fibre orientation fields near the crack initiation site, predicted the maximum load with an error of only 0.6%; on the contrary, *FEA (CZM 5:3:2)*, which homogenised the local fibre orientation in the neighbourhood of the initiation site, overestimated the maximum load by 9.1%.

iii. The locations of failure initiation in the components with '*Top-failure*' (analysed using fractography) revealed that, even for symmetric geometries, small asymmetries in the manufacturing process (e.g. in the position of the injection point) can affect the local fibre orientation distributions and trigger an asymmetric failure process. Coupled FEA using CZM successfully predicted these asymmetries in the location of failure initiation and propagation.

iv. Failure of components along a weldline cannot be accurately predicted by failure initiation criteria based on the local fibre orientation distribution only; for the particular component analysed here, this would lead to an overestimation of the failure load by more than 50% (*FEA (TH)*). Coupled FEA using CZM can predict the failure load in weldlines (within 2.3% error for this particular component) if using the cohesive

properties of neat resin *FEA (CZM PA66)*, rather than the estimated properties of a transversely-aligned composite (*FEA (CZM* $a_{x'x'} = 0$*)*, which induced an error of 36.8%).

v. A large difference in the fracture morphologies was observed between components with *Top-failure* and with *Weld-failure*. Both of them presented ductile matrix fracture only at the failure initiation sites, and shifted to brittle matrix fracture in the other regions. However, flatter fracture surfaces without significant fibre pull-out were observed in components with *Weld-failure*, probably due to the transverse alignment of fibres, lower fibre volume fraction, and presence of defects in the weldline.

Chapter 8 - Discussion

8.1 On the accuracy of failure prediction from coupons to components

The state-of-the-art coupled FEA (detailed in Section 2.6) from coupons to components were conducted using either (i) conventional initiation failure criterion (i.e. Tsai-Hill's criterion) which is available in commercial software, or (ii) newly developed coupled FEA methodology combined with CZM calibrated using experimentally-measured fracture toughnesses (proposed in Section 6.5.3). The following findings are drawn from this study, regarding the prediction of failure:

- Considering dogbone coupons with a simple unnotched geometry (Chapter 4), the Tsai-Hill initiation criterion is sufficient to predict the maximum load, within a 6% error compared to experimental results. This is because the dogbone coupons experience uniform strains across their entire cross-section, and the most brittle regions of the cross-section (i.e. the skins) are also the main load carrier. Therefore, the remote stress for failure initiation coincides with that for final fracture. The failure in dogbone coupons is fully controlled by failure initiation, and any consideration of progressive failure would not influence the predicted response;
- Considering the CT coupons with severe geometric notches (Chapter 5), it was found that trilinear cohesive laws calibrated using both the initiation and propagation fracture toughnesses are needed, even at coupon level. Coupled FEA with these trilinear cohesive laws successfully predicted not only the peak load but also the subsequent gradual load decrease in load-displacement curves observed experimentally, as well as the work of fracture;
- Considering the subcomponents (Chapter 6) and components (Chapter 7), having more complex geometries and loading conditions, it was found that the Tsai-Hill initiation criterion underestimates the failure load by 14% to 24% (depending on environmental conditions, and except those with weldline failure). By considering the fracture toughness in the coupled FEA using bilinear cohesive laws, the capability to predict the experimental maximum load improved dramatically, to within a 2.6% error for all environmental conditions;

- Considering the effect of the shape of cohesive laws on the accuracy of failure prediction, trilinear cohesive laws presented the best accuracy for CT coupons having severe geometric notches (Chapter 5). However, in the subcomponents (Chapter 6), the difference in the predicted maximum load from coupled FEA using CZM between the bilinear and trilinear laws was negligible (always within 5%). Moreover, the coupled FEA with trilinear laws took about 25 times longer than that with bilinear laws to complete the analysis until the maximum load. This difference in likely due to the level of stress concentration; it is realistic to use bilinear laws for real components without severe geometric notches.

8.2 On the sequence of failure events in IM-SFRP (sub)components

A combination of fractography and FE simulations was used to identify and justify the sequence of failure events in the subcomponent (Chapter 6) and component (Chapter 7). Those sequence of failure events were affected by the complex skin-core microstructures, leading to either an unexpected crack initiation location or unexpected direction of crack propagation. These observations obtained from the combination of fractography and FEA can be summarised as follows:

- The subcomponents experienced preferential damage propagation in the core region, due to its lower toughness (compared to that of the skins);
- The components, although symmetric in their geometry (with respect to the mid-plane across the front- and back-faces), had crack initiation consistently from one edge (on the frontface) only, due to the asymmetry of their microstructures (created due to an asymmetric location of the injection point).

The coupled FEA using CZM proposed in this study (detailed in Chapter 6) successfully captured these unexpected crack initiation locations or propagation directions. Combining FEA and fractographic techniques provides a more comprehensive picture of the sequence of failure events in (sub)components than using each technique individually.

8.3 On the T-M equivalence

The concept of T-M equivalence was applied to the dogbone coupons (Chapter 3), the CT coupons (Chapter 5) and the subcomponents (Chapter 6). Two different pairs of temperature-moisture, 23°C-RH50 and 60°C-DAM ("Pair-A"), and 80°C-RH50 and 120°C-DAM ("Pair-B") were used in this study.

The T-M equivalence has been verified for the elastic modulus and the tensile strength of PA66-GF50 coupons, which agrees with the conclusions from previous literature (reviewed in Section 2.2) using IM-SFRP coupons. Moreover, this work has confirmed that this concept is applicable to the material's fracture toughness at coupon level, and also to the mechanical response at the subcomponent level, until final failure. This is especially useful for industry to reduce the amount of time spent moisture-conditioning samples, which usually takes a few weeks or more according to standards [83]. Moreover, these findings could also increase the reliability of the properties measured under hot-wet conditions, which includes the spurious effect of water evaporation during the testing, and might actually correspond to slightly drier conditions than those predefined.

8.4 Novelty of this research

The main novelty from the experimental work and the FE simulations developed in this research are summarised as follows:

- Chapter 5 has provided the first characterisation of the fracture toughness of IM-SFRPs under the combined effect of fibre orientation, moisture level, and temperature. Moreover, this is the first characterisation of the full R-curve (including a propagation fracture toughness) of IM-SFRPs. These results demonstrated the importance of considering these microstructural and environmental factors when characterising the energy absorption of IM-SFRPs, and that there is a significant difference between the initiation and propagation fracture toughness;
- This work is the first attempt to use the two fracture toughness data reduction methods (FE-supported compliance calibration and DIC-based J-integral calculation) for IM-SFRPs (Chapter 5). Both methods delivered the same propagation fracture toughnesses, although only the J-integral method can measure the initiation toughness;

- Previous research (reviewed in Section 2.2) on the fracture toughness of IM-SFRPs has focused only on the experimental characterisation. This study (Chapter 5) demonstrated that the fracture toughness can be effectively used in FE simulations with cohesive zone modelling to predict not only the peak load but also the subsequent gradual load decrease observed experimentally;
- The effect of the shape of the cohesive law (bilinear or trilinear) on failure prediction was investigated for the first time for IM-SFRPs (Chapters 5 and 6). Trilinear law calibrated using both initiation and propagation fracture toughness was needed for CT coupons with severe geometric notches, while there were only within 5% difference found for the subcomponents having more complex geometry and loading conditions;
- This study has provided the first attempt to undertake coupled FEA (accounting for the manufacturing and in-service phases of IM-SFRP components) combined with CZM (Chapters 6 and 7). This methodology showed a significant improvement over the state-of-the-art methodology for failure load prediction. This FE simulation methodology is robust, as shown by its successful application consistently to five different environmental conditions and two different geometries (including a real automotive component, in Chapter 7);
- Regarding the T-M equivalence, whilst previous research (reviewed in Section 2.2) focused only on the modulus and stress-strain behaviour at the coupon level, this study has confirmed that the concept of temperature-moisture equivalence is applicable to the material's fracture toughness (Chapter 5) and also to the subcomponent level until final failure (Chapter 6).

8.5 Potential impact of this research

The findings from the experimental work and the FE simulations developed in this research have the following potential impacts for academia and industry:

- The protocols developed for the design and testing of CT specimens presented in Chapter 5 can be used by other researchers and engineers to quantify the initiation and propagation fracture toughnesses of IM-SFRPs, as well as their full R-curve and cohesive law. Moreover, the propagation fracture toughness showed consistent results between the data reduction methods used (FE-supported compliance calibration and DIC-based J-integral calculation); this indicates that future users can select one of these data

reduction methods, depending on the equipment and expertise available, and also on the properties they are aiming to characterise;

- The comparisons between the accuracy of bilinear and trilinear cohesive laws in Chapters 5 and 6 provide guidance to researchers and engineers on the trade-offs between computation cost and accuracy, and how this depends on specimen geometry. In the subcomponents (Chapter 6), the bilinear law calibrated using only propagation fracture toughness presented excellent accuracy of failure prediction, with significantly better computational efficiency compared to the trilinear law.
- This study has considered the effect of fracture toughness on specimens across the scales, with three levels of complexity: from coupons (Chapter 5) to subcomponents (Chapter 6) and up to real components used in the automotive industry (Chapter 7). The conclusions summarised in Section 8.1 show that it is required to introduce the material's progressive failure and finite fracture toughness in the design of IM-SFRP components; this finding was consistent across the scales, and it has been verified in components with a representative complexity in geometry, microstructure, and loading conditions. Therefore, the newly proposed FE simulation methodology in this study (detailed in Chapters 6 and 7) provides more confidence in the design of safer and more efficient damage-tolerant components in industry;
- The combination of fractography and FE simulations has shown the potential to identify and justify the sequence of failure events in IM-SFRP components – which is critical to improve design and manufacturing processes. This methodology is helpful to investigate failure of components, especially when unexpected failures occur at the development stage in industry.
- This study has confirmed that the concept of T-M equivalence is applicable to the characterisation of IM-SFRPs across the scales, including the material's fracture toughness measured in coupons and the overall mechanical response of components. This conclusion has the potential to significantly reduce the amount of work for material characterisation and component testing in industry, especially for wet-conditioned testing. This could lead to a potential saving of many weeks for moisture conditioning of samples, and it could also increase the reliability of the properties measured for applications under hot-wet conditions (as discussed in Section 8.3).

Chapter 9 – Conclusions

The state-of-the-art FE simulation methodology for IM-SFRPs, which is based on failure initiation criteria only, cannot predict their ultimate load-bearing capability and post-failure behaviour accurately. This leads to overly conservative design, and hence excessively heavy and costly components in industry. Therefore, this study proposed a new methodology to predict failure of PA66-based IM-SFRPs from coupon level to component level, considering the material's progressive failure using experimentally-measured fracture toughness.

A novel characterisation of the initiation and propagation fracture toughness of a PA66-GF50 material was conducted. Compact tension testing, using newly-designed coupons, demonstrated a significant effect of fibre orientation, service temperature and moisture contents on the propagation fracture toughness of the PA66-GF50 material. Full R-curves were calculated using either an FE-based compliance calibration method, or the J-integral method based on full-field measurements from 3D-DIC. These results showed that both methods delivered the same propagation fracture toughnesses, although only the J-integral method can measure the initiation toughness.

A new FE methodology to predict failure of PA66-GF50 (sub)components was proposed. This methodology combines the coupled FEA with CZM calibrated with the experimentally-measured fracture toughness obtained. The coupled FEA with CZM presented good agreement of failure points with the subcomponent tests (within 3% error), under all different environmental conditions used. This demonstrated an excellent improvement of the accuracy of failure prediction compared to the conventional methodology using failure initiation criterion (i.e. the Tsai-Hill's criterion), which underestimated the failure load by about 20%.

The damage mechanisms of the PA66-GF50 (sub)components were deduced using fractography. The obtained mechanisms were discussed with the FE simulation results to provide a more comprehensive picture of the sequence of failure events, which has not been reported previously for IM-SFRPs at (sub)component level. The damage initiation and propagation patterns predicted by the FE simulations could successfully capture the sequence of failure events deduced from the experiments, including an unexpected reversed crack propagation.

The concept of Temperature-Moisture equivalence was applied to the coupons and subcomponents used in this study. While previous research has focused only on the modulus and stress-strain behaviour of dogbone coupons, this study verified the validity of Temperature-Moisture equivalent on (i) the material's fracture toughness measured from CT tests, and (ii) the load-displacement behaviour of subcomponents until final failure. These results showed the potential to reduce the amount of experimental work required for material characterisation

In summary, the output from this research will provide more confidence in the design of safer and more efficient damage-tolerant IM-SFRP components, with direct application in the automotive industry and beyond.

Chapter 10 - Future work

Based on the results and findings of the research reported in this thesis, a number of aspects warrant further study. Three possible ideas for the future work are proposed in this Chapter.

10.1 Strain rate effects on the mechanical properties and the damage mechanisms of IM-SFRPs

In this thesis, all the material characterisations (Chapters 3-5), (sub)component tests (Chapters 6 and 7) and FE modelling (Chapters 6 and 7) were conducted under quasi-static conditions; these results will contribute to design lighter and more costly-effective component by predicting accurately the maximum-bearing load of components used in real industrial applications. However, the requirement for the design of these components is not limited to quasi-static conditions; it also requires considering the behaviour under high-rate conditions.

Moreover, the damage mechanisms of the PA66GF50 material studied were influenced by changes of local strain rate, even though the remote loading was quasi-static. This was verified across the scales, and provides evidence that strain rate is a key factor to the properties and the response of IM-SFRPs. At the coupon level (Chapters 3 and 5), the fracture surface of dogbone coupons – which was created under high local strain rates due to unstable failure – showed more brittle features than that of CT specimens – which was created stably under lower local strain rates. For both subcomponent and component levels (Chapter 6-7), the fracture surfaces showed a clear transition between stable crack-initiation and unstable crack-propagation regions. Moreover, Chapter 6 suggested that, for the subcomponents tested under 23°C-DAM conditions, the transition from stable to unstable failure could not be predicted by the coupled FEA (even with CZM) because strain-rate sensitive properties was not considered. Therefore, an in-depth understanding and characterisation of strain rate effects on the mechanical properties of IM-SFRPs will provide more insights into investigating failure of those components, and has the potential to increase the accuracy of FE simulations (especially regarding the peak and post-peak regimes).

To include the strain rate effect in the FE methodology proposed in this thesis (as described in Section 6.5.3), the material models (both the elastic-plastic model natively available in

Digimat and the properties of cohesive elements) need to be updated to strain-rate-dependent models [5]. This requires calibrating these models with dogbone and CT coupons' testing data under several strain rates.

Although there is some literature characterising the strain rate effects on the tensile properties of IM-SFRPs at the coupon level [23,32,42,109–112], no literature has characterised the propagation fracture toughness (or full R-curves) under high-rate conditions. Therefore, to investigate those details, further experimental characterisations would need to be carried out, including:

- Tensile CT tests under varied testing speeds (or local strain rates at the crack tip).
- Characterisation of the local strain rate during the crack propagation in the coupons, subcomponents and components.

The two main challenges to conduct these experimental characterisations are (i) the generation of controlled strain rates locally at the failure region (rather than remotely), and (ii) the measurement of local strain fields at the failure region, using 3D-DIC equipped with high-speed cameras. These challenges have been (at least partially) addressed for continuous-fibre composites [113–116], so there is scope to adapt similar strategies for IM-SFRPs.

10.2 Development of a toughness model for coupled FEA using CZM

The proposed coupled FEA methodology considering the material's progressive damage (as detailed in Section 6.5.3) provided accurate prediction of the maximum load of IM-SFRP subcomponents and components (within 3% error), as shown in Fig. 6.11 and Fig. 7.16. Therefore, these simulations will contribute to design lighter and costly effective IM-SFRP components in industry. However, Fig. 7.16 also demonstrated that these FE simulations must capture realistic fibre orientation fields at fracture initiation and propagation sites (as discussed in Section 7.5.1). Moreover, there are still room to improve the methodology to make it more user-friendly for daily work in industry. Considering this background, possible future work can be proposed as follows:

- Creating a local fracture toughness material model, depending on the local fibre orientation distribution. The current methodology manually interpolates or

extrapolates the homogenised fracture toughness vs. the homogenised fibre orientation normal component experimentally measured in CT specimens, in order to obtain the CE inputs for individual partitions, as a function of the respective averaged fibre orientation normal component. However, this methodology could be made more accurate by creating a model that predicts the local fracture toughness of pseudo-grains based on the full local fibre orientation tensor (rather than a single component) and a few material-dependent parameters to be calibrated from experimental measurements, considering the actual skin-core microstructure of the CT coupons, as currently done for the elastic and plastic properties (as detailed in Chapter 4).

- Automatic mapping of local properties for the CE layer: in this study, the properties for CEs have been considered as homogenised in three discrete partitions of the cohesive layer (i.e. skin-core-skin in the coupons and subcomponents (Chapters 5-6), and two different partition patterns tested for the component in Chapter 7); the size and location of those partitions are decided by the user, based on process simulation results. This can be improved by developing a methodology which maps the properties for CEs automatically at each integration point of each CE; it would consider finer details of fibre orientation effects in the simulations, and reduce the amount of work required in daily applications in industry;
- For completeness, the fracture toughness model should consider not only pure mode-I loading conditions (as in this study), but also pure mode-II and mixed-mode conditions.

10.3 Characterisation of the weldline in the components

IM-SFRP components were tested and their failure mechanisms were characterised in Chapter 7. For those components failed at the weldline (*Weld-failure*), the observations suggest that their failure is likely due to the presence of defects (i.e. voids, as inferred in Fig. 7.11 (h)).

In general, weldlines are one of the concerning factors in the design of components, as weldlines can be much weaker than the other locations of the components [43–49]. Therefore, it is helpful for the automotive industry to have a methodology for accurate prediction of weldline failures, with a clear and comprehensive understanding of the damage mechanisms generated at weldlines in components. In Chapter 7, failure at weldlines could be predicted using

the newly proposed FEA methodology; however, this required using fracture properties of the neat PA66 matrix, rather than those extrapolated for a transverse PA66GF50 aligned composite.

This means that, even if process simulations are used to identify the fibre orientation fields throughout a component, an accurate prediction of a mostly-transverse fibre orientation distribution at weldlines is not sufficient to allow for good predictions of failure loads during structural simulations. Instead, it is required that process simulations are able to identify the presence a location of weldline, and that coupled FEA are able to assign a different (from the bulk IM-SFRP) material to weldlines, possibly with properties knocked-down depending on the exact flow conditions (and, consequently, defects) under which the weldline was locally created.

To investigate more details, further experimental characterisation needs to be carried out, including:

- Observing polished cross-sectional surfaces of components at their weldlines (as predicted by process simulations), before any mechanical testing. This simple methodology might provide some insight on the types and severity of defects (e.g. voids) present at weldlines, which will be helpful to identify causes of the failure initiation at weldlines and how to simulate them;
- Conducting X-ray computed tomography to analyse and quantify the presence of defects (e.g. voids) at weldlines quantitatively (similar methodologies have been widely used for the characterisation of the microstructure of IM-SFRPs [46] and other materials [117–120]), before conducting mechanical testing. This could provide a clearer relationship between the types and severity of defects at weldlines, and the subsequent properties of IM-SFRPs are weldlines.

A possible challenge for the characterisation of defects and void content in components using X-ray computed tomography is limitations in the resolution vs. size of the sample scanned. To characterise voids as the ones identified on the fracture surface of '*Weld-failure*' components (with a diameter below 40 µm), the sample size for X-ray computed tomography [46,117–120] is much smaller than the component used in this study (width: 40 mm, thickness: 5 mm). Observation of the polished cross-section is easier for the characterisation of large samples (i.e. components), but it is destructive (so observed specimens cannot be mechanically tested afterwards). Therefore, it might be helpful to combine these two characterisations to overcome the individual limitations of each method.

Bibliography

[1] Grand View Research, Lightweight materials market size report analysis by product (aluminium, polymers & composites), by application (automotive, aviation, energy), by region, and segment forecasts, 2017-2024, John Wiley and Sons Inc.

[2] L. Jiang, Y. Zhou, F. Jin, Design of short fiber-reinforced thermoplastic composites: A review, Polym Compos 43 (2022) 4835–4847.

[3] V. Mathes, The composites industry: plenty of opportunities in heterogeneous market, Reinf Plast 62 (2018) 44–51.

[4] Custom Market Insight Consulting, Global injection molded automotive parts market 2024–2033 (2023).

[5] Hexagon, Digimat 2022.2 user's documentation.

[6] A. Bernasconi, F. Cosmi, D. Dreossi, Local anisotropy analysis of injection moulded fibre reinforced polymer composites, Compos Sci Technol 68 (2008) 2574–2581.

[7] S.G. Advani, C.L. Tucker, The use of tensors to describe and predict fiber orientation in short fiber composites, J Rheol 31 (1987) 751–784.

[8] N. Goldberg, F. Ospald, M. Schneider, A fiber orientation-adapted integration scheme for computing the hyperelastic Tucker average for short fiber reinforced composites, Comput Mech 60 (2017) 595–611.

[9] P.J. Hine, N. Davidson, R.A. Duckett, I.M. Ward, Measuring the fibre orientation and modelling the elastic properties of injection-moulded long-glass-fibre-reinforced nylon, Compos Sci Technol 53 (1995) 125–131.

[10] R.S. Bay, C.L. Tucker, Stereological measurement and error estimates for three-dimensional fiber orientation, Polym Eng Sci 32 (1992) 240–253.

[11] J.S. Cintra, C.L. Tucker, Orthotropic closure approximations for flow-induced fiber orientation, J Rheol 39 (1995) 1095–1122.

[12] D.H. Chung, T.H. Kwon, Improved model of orthotropic closure approximation for flow induced fiber orientation, Polym Compos 22 (2001) 636–649.

[13] D. Dray, P. Gilormini, G. Régnier, Comparison of several closure approximations for evaluating the thermoelastic properties of an injection molded short-fiber composite, Compos Sci Technol 67 (2007) 1601–1610.

[14] M. De Monte, E. Moosbrugger, M. Quaresimin, Influence of temperature and thickness on the off-axis behaviour of short glass fibre reinforced polyamide 6.6 - Quasi-static loading, Compos Part A Appl Sci Manuf 41 (2010) 859–871.

[15] S. Mortazavian, A. Fatemi, Effects of fiber orientation and anisotropy on tensile strength and elastic modulus of short fiber reinforced polymer composites, Compos B Eng 72 (2015) 116–129.

[16] E. Kurkin, M. Spirina, O.U. Espinosa Barcenas, E. Kurkina, Calibration of the PA6 short-fiber reinforced material model for 10% to 30% carbon mass fraction mechanical characteristic prediction, Polymers 14 (2022).

[17] D. Micota, A. Isaincu, L. Marşavina, Experimental testing of two short-fiber reinforced composites: PPA-GF33 and PPS-GF40, Mater Desig Proc Commun 3 (2021).

[18] S. Fara, A. Pavan, Fibre orientation effects on the fracture of short fibre polymer composites: on the existence of a critical fibre orientation on varying internal material variables, J Mater Sci 39 (2004) 3619–3628.

[19] S. Hashemi, J. Mugan, Fracture mechanics of short glass fibre-reinforced nylon composite, J Mater Sci 28 (1993) 3983–3990.

[20] F.T. Ibáñez-Gutiérrez, S. Cicero, I.A. Carrascal, On the influence of moisture content on the fracture behaviour of notched short glass fibre reinforced polyamide 6, Compos B Eng 159 (2019) 62–71.

[21] D. Ferreño, I. Carrascal, E. Ruiz, J.A. Casado, Characterisation by means of a finite element model of the influence of moisture content on the mechanical and fracture properties of the polyamide 6 reinforced with short glass fibre, Polym Test 30 (2011) 420–428.

[22] A. Hassan, R. Yahya, A.H. Yahaya, A.R.M. Tahir, P.R. Hornsby, Tensile, impact and fiber length properties of injection-molded short and long glass fiber-reinforced polyamide 6,6 composites, J Reinf Plast Compos 23 (2004) 969–986.

[23] A. Hassan, A.A. Hassan, M.I. Mohd Rafiq, Impact properties of injection molded glass fiber/polyamide-6 composites: Effect of testing parameters, J Reinf Plast Compos 30 (2011) 889–898.

[24] B. Mouhmid, A. Imad, N. Benseddiq, D. Lecompte, An experimental analysis of fracture mechanisms of short glass fibre reinforced polyamide 6,6 (SGFR-PA66), Compos Sci Technol 69 (2009) 2521–2526.

[25] S.Y. Fu, B. Lauke, E. Ma Èder, X. Hu, C.Y. Yue, Fracture resistance of short-glass-fiber-reinforced and short-carbon-fiber-reinforced polypropylene under Charpy impact load and its dependence on processing, J Mater Proc Technol 89–90 (1999) 501–507.

[26] T.-P. Dao, H. Giang Le, S.-C. Huang, Investigation of formulation of the energy release rate in the fracture mechanics of short fiber composite, J Eng Technol and Educ 9 (2012) 451–459.

[27] J. Karger-Kocsis, Instrumented impact fracture and related failure behavior in short-and long-glass-fiber-reinforced polypropylene, Compos Sci Technol 48 (1993) 273–283.

[28] A. Rios De Anda, L.A. Fillot, D.R. Long, P. Sotta, Influence of the amorphous phase molecular mobility on impact and tensile properties of polyamide 6,6, J Appl Polym Sci 133 (2016).

[29] F. Ramsteiner, R. Theysohn, The influence of fibre diameter on the tensile behaviour of short-glass-fibre reinforced polymers, Compos Sci Technol 2 (1985) 231–240.

[30] M. Akay, D.F. O'regan, R.S. Bailey, Fracture toughness and impact behaviour of glass-fibre-reinforced polyamide 6,6 injection mouldings, Compos Sci Technol 55 (1995) 109–118.

[31] J. Karger-Kocsis, K. Friedrich, Fracture behavior of injection-molded short and long glass fiber-polyamide 6.6 composites, Compos Sci Technol 32 (1988) 293–325.

[32] Z.A. Mohd Ishak, U.S. Ishiak, Microstructure-related fracture behaviour of injection moulded short fibre reinforced polyarylamide in dry and wet states, J Mater Sci 33 (1998) 3377–3389.

[33] N. Takeda, D.Y. Song, K. Nakata, Effects of temperature and water content on impact properties of injection-molded glass nylon-6 composites, Advanced Composite Materials 5 (1996) 201–212.

[34] S.T. Pinho, P. Robinson, L. Iannucci, Fracture toughness of the tensile and compressive fibre failure modes in laminated composites, Compos Sci Technol 66 (2006) 2069–2079.

[35] S. Pimenta, S.T. Pinho, P. Robinson, K.H. Wong, S.J. Pickering, Mechanical analysis and toughening mechanisms of a multiphase recycled CFRP, Compos Sci Technol 70 (2010) 1713–1725.

[36] R.W. Truss, P.J. Hine, R.A. Duckett, Interlaminar and intralaminar fracture toughness of uniaxial continuous and discontinuous carbon fibre/epoxy composites, Compos Part A Appl Sci Manuf 28 (1997) 627–636.

[37] T.H. Becker, M. Mostafavi, R.B. Tait, T.J. Marrow, An approach to calculate the J-integral by digital image correlation displacement field measurement, Fatigue Fract Eng Mater Struct 35 (2012) 971–984.

[38] F.Z. Li, C.F. Shih, A. Needleman, A comparison of methods for calculating energy release rates, Eng Fract Mech 21 (1985) 405–421.

[39] J. Chaichanawong, C. Thongchuea, S. Areerat, Effect of moisture on the mechanical properties of glass fiber reinforced polyamide composites, Adv Powd Technol 27 (2016) 898–902.

[40] M.F. Arif, F. Meraghni, Y. Chemisky, N. Despringre, G. Robert, In situ damage mechanisms investigation of PA66/GF30 composite: Effect of relative humidity, Compos B Eng 58 (2014) 487–495.

[41] Z. Wang, Y. Zhou, P.K. Mallick, Effects of temperature and strain rate on the tensile behavior of short fiber reinforced polyamide-6, Polym Compos 23 (2002) 858–871.

[42] B. Mouhmid, A. Imad, N. Benseddiq, S. Benmedakhène, A. Maazouz, A study of the mechanical behaviour of a glass fibre reinforced polyamide 6,6: Experimental investigation, Polym Test 25 (2006) 544–552.

[43] M.C. Quintana, P. Frontini, Weld line strength factors in a reinforced injection molded part: Relationship with predicted fiber orientation, J Reinf Plast Compos 39 (2020) 219–230.

[44] G. Jadhav, V. Gaval, S. Solanke, M. Divekar, N. Darade, A. Satpute, G.P. Goutham, Weld-lines and its strength evaluation in injection molded parts: A review, Polym Eng Sci (2023).

[45] M.B. Baradi, C. Cruz, T. Riedel, G. Régnier, Mechanical and microstructural characterization of flowing weld lines in injection-molded short fiber-reinforced PBT, Polym Test 74 (2019) 152–162.

[46] M.B. Baradi, C. Cruz, T. Riedel, G. Régnier, Frontal weld lines in injection-molded short fiber-reinforced PBT: Extensive microstructure characterization for mechanical performance evaluation, Polym Compos 40 (2019) 4547–4558.

[47] L.S. Turng, H. Kharbas, Effect of process conditions on the weld-line strength and microstructure of microcellular injection molded parts, Polym Eng Sci 43 (2003) 157–168.

[48] Y.C. Kagitci, N. Tarakcioglu, The effect of weld line on tensile strength in a polymer composite part, Int J Adv Manuf Technol 85 (2016) 1125–1135.

[49] C.H. Wu, W.J. Liang, Effects of geometry and injection-molding parameters on weld-line strength, Polym Eng Sci 45 (2005) 1021–1030.

[50] L. V. Pastukhov, M.J.W. Kanters, T.A.P. Engels, L.E. Govaert, Influence of fiber orientation, temperature and relative humidity on the long-term performance of short glass fiber reinforced polyamide 6, J Appl Polym Sci 138 (2021).

[51] V. Miri, O. Persyn, J.M. Lefebvre, R. Seguela, Effect of water absorption on the plastic deformation behavior of nylon 6, Eur Polym J 45 (2009) 757–762.

[52] A. Launay, Y. Marco, M.H. Maitournam, I. Raoult, Modelling the influence of temperature and relative humidity on the time-dependent mechanical behaviour of a short glass fibre reinforced polyamide, Mech Mater 56 (2013) 1–10.

[53] E. Greenhalgh, Failure analysis and fractography of polymer composites, Woodhead Publishing in Materials (2009).

[54] C.L. Tucker, E. Liang, Stiffness predictions for unidirectional short-fiber composites: Review and evaluation, Compos Sci Technol 59 (1999) 655–671.

[55] E. Ghossein, M. Lévesque, Homogenization models for predicting local field statistics in ellipsoidal particles reinforced composites: Comparisons and validations, Int J Solids Struct 58 (2015) 91–105.

[56] B. Raju, S.R. Hiremath, D. Roy Mahapatra, A review of micromechanics based models for effective elastic properties of reinforced polymer matrix composites, Compos Struct 204 (2018) 607–619.

[57] H.M. Sertse, J. Goodsell, A.J. Ritchey, R.B. Pipes, W. Yu, Challenge problems for the benchmarking of micromechanics analysis: Level I initial results, J Compos Mater 52 (2018) 61–80.

[58] G. Robert, O. Moulinjeune, MMI TECHNYL Design focus on fatigue simulation, Digimat Users' Conference 2018 (2018).

[59] Ludovic Chauvet, Design to cost and manufacturing of automotive structural parts, Digimat Users' Conference 2017 (2017).

[60] A. Kech, V. Le Baube, J.-M. Kaiser, R. Bosch Gmbh, An anisotropic linear thermo-visco-elastic material model and the application on residual stress calculations, Digimat Users' Conference 2018 (2018).

[61] C. Kuhn, Körner Enrico, Advances in long fiber polymers-application and prediction, Digimat Users' Conference 2018 (2018).

[62] Luca M, Assessment of state of the art prediction methodology for mechanical properties of CF-SMC structures, Digimat Users' Conference 2017 (2017).

[63] S. Kammoun, I. Doghri, L. Adam, G. Robert, L. Delannay, First pseudo-grain failure model for inelastic composites with misaligned short fibers, Compos Part A Appl Sci Manuf 42 (2011) 1892–1902.

[64] T. Mori, K. Tanaka, Average stress in matrix and average elastic energy of materials with misfitting inclusions, Acta Metall 21 (1973) 571–574.

[65] Eshelby JD, The determination of the elastic field of an ellipsoidal inclusion, and related problems, The Royal Society 2441 (1957) 376–396.

[66] R. Talreja, C.V. Singh, Damage and failure of composite materials, Cambridge University Press (2012).

[67] G.P. Tandon, G.J. Weng, The effect of aspect ratio of inclusions on the elastic properties of unidirectionally aligned composites, Polym Compos 5 (1984) 327–333.

[68] Y. Benveniste, A new approach to the application of Mori-Tanaka's theory in composite materials, Mech Mater 6 (1987) 147–157.

[69] Autodesk, Moldflow - plastic injection and compression mould simulation for design and manufacturing.

[70] Jeffery G. B., The motion of ellipsoidal particles immersed in a viscous fluid, Royal Soc 102 (1922) 161–179.

[71] F. Folgar, C.L. Tucker, Orientation behavior of fibers in concentrated suspensions, J Reinf Plast Compos 3 (1984) 98–119.

[72] H.C. Tseng, R.Y. Chang, C.H. Hsu, Comparison of recent fiber orientation models in injection molding simulation of fiber-reinforced composites, J Thermoplast Compos Mater 33 (2020) 35–52.

[73] J. Wang, J.F. O'Gara, C.L. Tucker, An objective model for slow orientation kinetics in concentrated fiber suspensions: Theory and rheological evidence, J Rheol 52 (2008) 1179–1200.

[74] A. Bakharev, H. Yu, S. Ray, R. Speight, J. Wang, Using new anisotropic rotational diffusion model to improve prediction of short fibers in thermoplastic injection molding, ANTEC (2018).

[75] A.J. Favaloro, C.L. Tucker, Analysis of anisotropic rotary diffusion models for fiber orientation, Compos Part A Appl Sci Manuf 126 (2019).

[76] M. Landervik, J. Jergeus, Digimat material model for short fiber reinforced plastics at Volvo Car Corporation, 10th European LS-DYNA Conference (2015).

[77] A. Isaincu, M. Dan, V. Ungureanu, L. Marsavina, Numerical investigation on the influence of fiber orientation mapping procedure to the mechanical response of short-fiber reinforced composites using Moldflow, Digimat and Ansys software, in: Mater Today Proc (2020) 4304–4309.

[78] Dassault Systemes, Abaqus Analysis User's Guide Version 6.14.

[79] W. Chai, X. Liu, Y. Shan, X. Wan, E. Jiang, Research on simulation of the bending fatigue test of automotive wheel made of long glass fiber reinforced thermoplastic considering anisotropic property, Adv Eng Software 116 (2018) 1–8.

[80] B. Du, Z. Li, H. Bai, Q. Li, C. Zheng, J. Liu, F. Qiu, Z. Fan, H. Hu, L. Chen, Mechanical property of long glass fiber reinforced polypropylene composite: from material to car seat frame and bumper beam, Polymers 14 (2022).

[81] M. Sulmoni, A. Wedgewood, Z. Zhang, Influence of different Digimat models on the failure prediction accuracy, Digimat Users' Meeting 2016 (2016).

[82] R. Gutkin, M.L. Laffan, S.T. Pinho, P. Robinson, P.T. Curtis, Modelling the R-curve effect and its specimen-dependence, Int J Solids Struct 48 (2011) 1767–1777.

[83] ISO 1110 Plastics - Polyamides - accelerated conditioning of test specimens (1998).

[84] A. Hassan, N.M. Salleh, R. Yahya, M.R.K. Sheikh, Fiber length, thermal, mechanical, and dynamic mechanical properties of injection-molded glass-fiber/polyamide 6,6: Plasticization effect, J Reinf Plast Compos 30 (2011) 488–498.

[85] D. Frihi, A. Layachi, S. Gherib, G. Stoclet, K. Masenelli-Varlot, H. Satha, R. Seguela, Crystallization of glass-fiber-reinforced polyamide 66 composites: Influence of glass-fiber content and cooling rate, Compos Sci Technol 130 (2016) 70–77.

[86] J. Pan, W.J.D. Shaw, Effects of processing parameters on material properties of mechanically processed polyamide, J Appl Polym Sci 56 (1995) 557–566.

[87] A. Benaarbia, A. Chrysochoos, G. Robert, Thermomechanical behavior of PA6.6 composites subjected to low cycle fatigue, Compos B Eng 76 (2015) 52–64.

[88] J.L. Thomason, J.Z. Ali, J. Anderson, The thermo-mechanical performance of glass-fibre reinforced polyamide 66 during glycol-water hydrolysis conditioning, Compos Part A Appl Sci Manuf 41 (2010) 820–826.

[89] G. Catalanotti, P.P. Camanho, J. Xavier, C.G. Dávila, A.T. Marques, Measurement of resistance curves in the longitudinal failure of composites using digital image correlation, Compos Sci Technol 70 (2010) 1986–1993.

[90] S.-Y. Fu, Lauke Bernd, The fibre pull-out energy of misaligned short fibre composites, J Mater Sci 32 (1997) 1985–1993.

[91] Klaus Friedrich, Application of fracture mechanics to composite materials, Compos Mater Series 6 (1989) 3–671.

[92] V. Venoor, J.H. Park, D.O. Kazmer, M.J. Sobkowicz, Understanding the effect of water in polyamides: a review, Polym Review 61 (2021) 598–645.

[93] M. Broudin, P.Y. Le Gac, V. Le Saux, C. Champy, G. Robert, P. Charrier, Y. Marco, Water diffusivity in PA66: Experimental characterization and modeling based on free volume theory, Eur Polym J 67 (2015) 326–334.

[94] R. Puffr, J. Šebenda, On the structure and properties of polyamides. XXVII. The mechanism of water sorption in polyamides, J Polym Sci C: Polym Symp 16 (1967) 79–93.

[95] C.P.S. Kuda-Malwathumullage, G.W. Small, Determination of moisture content of polyamide 66 directly from combination region near-infrared spectra, J Appl Polym Sci 131 (2014).

[96] I. Carrascal, J.A. Casado, J.A. Polanco, F. Gutiérrez-Solana, Absorption and diffusion of humidity in fiberglass-reinforced polyamide, Polym Compos 26 (2005) 580–586.

[97] V.C. Li, Y. Wang, S. Backer, Effect of inclining angle, bundling and surface treatment on synthetic fibre pull-out from a cement matrix, Compos 21 (1990) 132–140.

[98] R.C. Wetherhold, L.K. Jain, The toughness of brittle matrix composites reinforced with discontinuous fibers, Mater Sci Eng, A 151 (1992) 169–177.

[99] S. Fu, B. Zhou, C. Lung, On the pull-out of fibres with a branched structure and the inference of strength and fracture toughness of composites, Compos Sci Technol 47 (1993) 245–250.

[100] L.K. Jain, R.C. Wetherhold, Effect of fiber orientation on the fracture toughness of brittle matrix composites, Acta Metall, Mater 40 (1992) 1135–1143.

[101] K Sethuraman, K Palanisamy, Material characterization of injection molded thermo plastic materials for finite element analysis - practical challenges, ICSSS-2013 (2013).

[102] J. Kim, A. Slyamov, E. Lauridsen, M. Birkbak, T. Ramos, F. Marone, J.W. Andreasen, M. Stampanoni, M. Kagias, Macroscopic mapping of microscale fibers in freeform injection molded fiber-reinforced composites using X-ray scattering tensor tomography, Compos B Eng 233 (2022).

[103] G. Dogossy, T. Morauszki, F. Ronkay, Experimental investigation and applicability of multi-stage simulations in the case of a thick-walled injection-moulded composite, Appl Sci 12 (2022).

[104] Z.A.M. Ishak, J.P. Berry, Hygrothermal aging studies of short carbon fiber reinforced nylon 6.6, J Appl Polym Sci 51 (1994) 2145–2155.

[105] Trelleborg Vibracoustic, Automotive vibration control technology fundamentals, materials, construction, simulation and applications, Vogel Business Media (2015).

[106] Rebounding automotive industry welcome news for FRP (2011) (www.reinforcedplastics.com).

[107] Wisely, Yeung, MSc thesis: Simulation of injection-moulded composite structures for automotive applications (2023).

[108] A. Meddad, B. Fisa, Weldline strength in glass fiber reinforced polyamide 66, Polym Eng Sci 35 (1995) 893–901.

[109] Y. Zhou, P.K. Mallick, A non-linear damage model for the tensile behavior of an injection molded short E-glass fiber reinforced polyamide-6,6, Mater Sci Eng A 393 (2005) 303–309.

[110] M. Schoßig, C. Bierögel, W. Grellmann, T. Mecklenburg, Mechanical behavior of glass-fiber reinforced thermoplastic materials under high strain rates, Polym Test 27 (2008) 893–900.

[111] S. Hashemi, Temperature, strain rate and weldline effects on strength and micromechanical parameters of short glass fibre reinforced polybutylene terephthalate (PBT), Polym Test 30 (2011) 801–810.

[112] S. Mortazavian, A. Fatemi, Tensile behavior and modeling of short fiber-reinforced polymer composites including temperature and strain rate effects, J Thermoplast Compos Mater 30 (2017) 1414–1437.

[113] H. Liu, J. Liu, Y. Ding, J. Zheng, X. Kong, J. Zhou, L. Harper, B.R.K. Blackman, A.J. Kinloch, J.P. Dear, The behaviour of thermoplastic and thermoset carbon fibre composites subjected to low-velocity and high-velocity impact, J Mater Sci 55 (2020) 15741–15768.

[114] L. Ma, F. Liu, D. Liu, Y. Liu, Review of strain rate effects of fiber-reinforced polymer composites, Polymers 13 (2021).

[115] H. Liu, J. Liu, C. Kaboglu, H. Chai, X. Kong, B.R.K. Blackman, A.J. Kinloch, J.P. Dear, Experimental and numerical studies on the behaviour of fibre-reinforced composites subjected to soft impact loading, Structural Integrity (2019) 992–1001.

[116] A.J. Comer, K.B. Katnam, W.F. Stanley, T.M. Young, Characterising the behaviour of composite single lap bonded joints using digital image correlation, Int J Adhes Adhes 40 (2013) 215–223.

[117] Y. Wan, I. Straumit, J. Takahashi, S. V. Lomov, Micro-CT analysis of internal geometry of chopped carbon fiber tapes reinforced thermoplastics, Compos Part A Appl Sci Manuf 91 (2016) 211–221.

[118] G. Samaras, D. Bikos, P. Cann, M. Masen, Y. Hardalupas, J. Vieira, C. Hartmann, M. Charalambides, A multiscale finite element analysis model for predicting the effect of micro-aeration on the fragmentation of chocolate during the first bite, Eur J Mech, A/Solids 104 (2024).

[119] G. Cai, T. Shirai, Y. Wan, K. Uzawa, J. Takahashi, Application of X-ray computed tomography to measuring fiber orientation distribution of chopped carbon fiber tape reinforced thermoplastics, Appl Compos Mater 28 (2021) 573–586.

[120] I.K. Mohammed, M.N. Charalambides, J.G. Williams, J. Rasburn, Modelling the microstructural evolution and fracture of a brittle confectionery wafer in compression, Innov Food Sci and Emerg Technol 24 (2014) 48–60.

Appendix A

FE-supported compliance calibration of CT coupons

A.1. FE model for compliance calibration (VTM-CC)

All FE simulations were conducted using Abaqus Standard [78]. The geometry of the CT coupon (with a nominal thickness $t_0 = 2$ mm) and the boundary conditions are shown in Fig. A.1. A prescribed load of $P_0 = 1$ N along the $+Y$ direction was applied to a reference point (RP-1, with zero displacements in X and Z, and zero rotations in X and Y) connected with a 'link' Multi-Point Constraint (MPC) [78] to the boundary of the upper hole of the CT coupon (with the "link" constraint allowing only in-plane rotations and movement along the $+Y$ direction of the upper-hole boundary). The boundary of the lower hole was also constrained with a "link" MPC to another reference point (RP-2, with zero displacements in X, Y and Z, and zero rotations in X and Y), thus allowing only in-plane rotations of the lower-hole boundary.

The FE Virtual Test Model (VTM) used for Compliance Calibration (VTM-CC) has been entirely meshed with solid 8-node hexagonal elements (C3D8 [78]), using 10 elements through the thickness and a target in-plane element size of 0.5 mm. A 'seam' [78] was used to represent the initial notch and the crack extension in the CT coupons; for each testing condition (i.e. each distinct combination of machining angle, moisture level and temperature), a set of 8 models was created, with different 'seam' lengths to generate crack lengths (Δa) between 8 and 22 mm. Each set of models assumed homogeneous and orthotropic material properties, obtained from Digimat's elastic model [5] calibrated in Chapter 4, thus accounting for the effect of machining angle, moisture level, and temperature. The properties of the fibre and the matrix used for the homogenization are shown in Table 4.2.

The outputs of the VTM-CC models used for the compliance calibration method (described in Appendix A.2) were (i) the compliance of the CT coupon as a function of crack length, $C_{\mathrm{FE}}(\Delta a) = d_{\mathrm{FE}}(\Delta a)/P_0$, and (ii) the nominal J-integral as a function of crack length, $J_0(\Delta a)$ (calculated directly during the simulation).

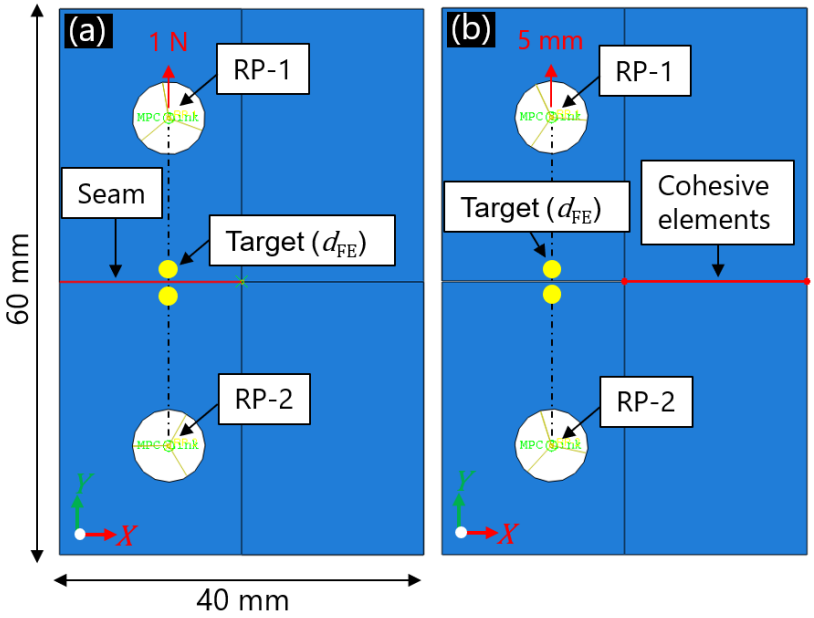


Fig. A.1. Image of VTM (a) used for Compliance Calibration (VTM-CC, described in Appendix A.1, where the relative Y- displacement between the yellow targets is used as d_{FE} to calculate the compliance) and (b) with Cohesive Elements (VTM-CE, described in Appendix B.2).

A.2. Data reduction of CT tests using FE-supported compliance calibration

The FE-supported compliance calibration method [34,35] was used to transform the experimentally-measured load-displacement curves of CT coupons – $P(d_{\mathrm{DIC}})$ – into R-curves – $G(\Delta a)$ – using the FE model VTM-CC mentioned in Appendix A.1. The procedure for calculating the strain energy release rate G with this method is the following:

1. Calculating the experimental compliance C_{DIC} as a function of the displacement from the DIC (d_{DIC}) between the targets in Fig. 5.1 as $C_{\mathrm{DIC}}(d_{\mathrm{DIC}}) = d_{\mathrm{DIC}}/P(d_{\mathrm{DIC}})$.
2. Computing the equivalent crack growth for every point in the experimental load-displacement curve – i.e. $\Delta a_{\mathrm{eq}}(d_{\mathrm{DIC}})$ – by interpolating the experimental compliance C_{DIC} with respect to the compliance predicted by the VTM-CC model C_{FE}, i.e. selecting Δa_{eq} so that $C_{\mathrm{DIC}}(d_{\mathrm{DIC}}) = C_{\mathrm{FE}}(\Delta a_{\mathrm{eq}}) \cdot t_0/t$, where t is the thickness of the actual coupon and t_0 is the thickness of the coupon in the FE model.
3. Calculating energy release rate G as

$$G = J_0(\Delta a_{\mathrm{eq}}) \cdot \left(\frac{P/P_0}{t/t_0}\right)^2$$

where P_0 is the load applied to the FE model, and $J_0(\Delta a_{\mathrm{eq}})$ is the J-integral for that P_0 and t_0, for the equivalent crack growth Δa_{eq}.

Appendix B

Design of CT coupons

B.1. Design criteria

This appendix describes the FE simulations used to design the geometry of the CT coupons used in this study, which was selected to fulfil the required criteria mentioned in Section 5.2.1:

i. feasibility to machine their geometry from the existing plates (shown in Fig. 3.1);
ii. no undesired failure modes (including buckling) predicted by the FE simulation of the CT test;
iii. plastic zones predicted by FE simulations mostly confined to the crack tip and uniformly distributed along the through-the-thickness direction of the coupons;
iv. post-processing the load-displacement curve predicted by the FE simulation (using cohesive zone modelling) through the compliance calibration recovers the input fracture toughness (used in the cohesive elements).

B.2. Virtual CT tests with simulation of crack propagation using Cohesive Elements (VTM-CE)

To address Criteria (ii) and (iv), the FE models described in Appendix A were modified so as to enable the simulation of the CT tests – including crack initiation and propagation, simulated with CZM – under each testing condition. This required (a) adding a layer (0.1 mm thick) of COH3D8 cohesive elements at the fracture plane ahead of the initial notch, (b) at the initial notch, removing the 'seam' and separating the nodes representing the two notch faces, and (c) replacing the prescribed load of 1 N at the upper-hole reference point (RP-1) with a prescribed displacement of 5 mm. The cohesive law used was assumed bilinear; its maximum traction was set as the tensile strength of the dog-bone tensile test at the corresponding machining angle, moisture level and temperature (shown in Fig. 3.5), and the fracture toughness was estimated from the available literature.

The VTM-CE simulations were used to verify that there were no indications of undesired failure modes (including buckling) during the virtual CT tests. Moreover, the results of the VTM-CE simulations were post-processed using the FE-supported compliance calibration method (described in Appendix A), which was confirmed to recover the fracture toughness used as input; this suggested that overall dimensions of the CT coupons were sufficiently larger than the length of the damage process zone associated with crack propagation.

B.3. Estimation of plastic zones using coupled simulations with plasticity models (VTM-CP)

To address criterion (iii), the FE models described in Appendix A were modified to enable the simulation of plastic zones and their distribution along the through-the-thickness direction of the coupons under each testing condition. This required considering the effect of plasticity in the material model, and also of fibre orientation variations across the coupon's thickness on the mechanical properties. Therefore, coupled FEA using Digimat's elastic-plastic material model [77] calibrated in Chapter 4 was used for this simulation. The fibre orientation tensor (shown in Fig. 4.1) was then mapped onto an Abaqus FEA model of the CT coupon similar to the one used for compliance calibration (VTM-CC, in Fig. A.1 (a)). Finally, this coupled FEA of CT coupon (hereby designated VTM-CP) was submitted using the methodology described in Chapter 2. Apart from considering fibre orientation variations and plasticity, rather than assuming homogeneous and linear-elastic properties, these models were identical to the VTM-CC ones.

Fig. B.1 and Fig. B.2 show the contour of plastic strain energy density in the entire coupon and in the area used for the J-integral calculation (shown in Fig. 5.2) from the VTM-CP FE simulations at a 0-degree machining angle and under 23°C-DAM and 80°C-RH50 conditions, at the d_{DIC} displacement corresponding to crack initiation in the experimental coupons (which is very close to the displacement corresponding to the maximum load observed in the experimental test). The energy contours show that the plastic region is fully contained within the J-integral region under 23°C-DAM, and that even under 80°C-RH50 most of the energy was dissipated at the crack tip, inside the J-integral region. Moreover, under both environmental conditions simulated, those contours are approximately unchanged along the through-the-thickness direction, which confirms the validity of using DIC data obtained only on the coupon's surface to calculate the J-integral.

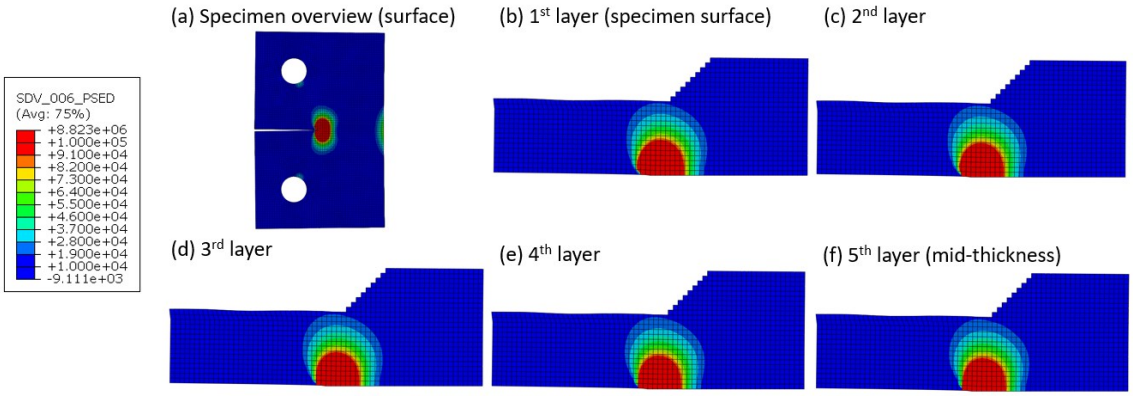


Fig. B.1. Contours of plastic strain energy density (units: J/m^3) from the VTM-CP FE simulations (with 10 layers of elements in the through-the-thickness) at a 0-degree machining angle, under 23°C-DAM: (a) overview of coupon surface, (b)-(f) J-integral area for each element layer in the through-the-thickness direction.

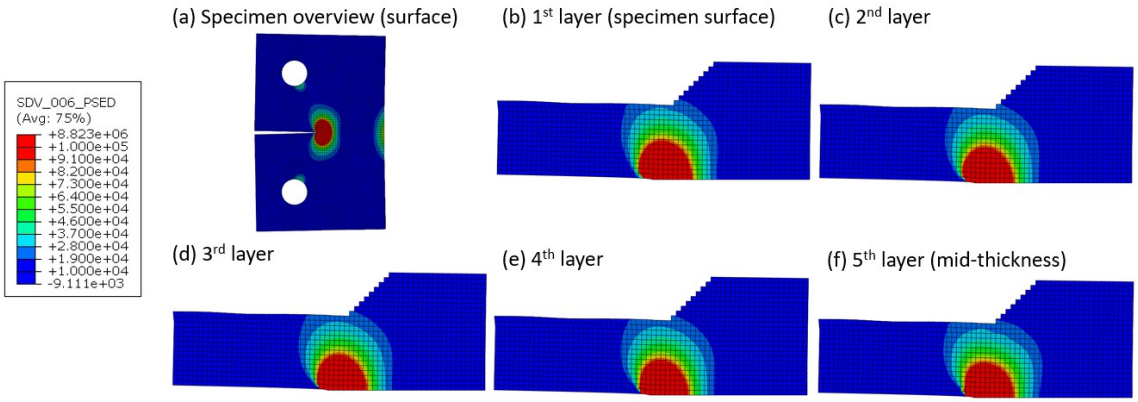


Fig. B.2. Contours of plastic strain energy density (units: J/m^3) from the VTM-CP FE simulations (with 10 layers of elements in the through-the-thickness at 0-degree machining angle under 80°C-RH50: (a) overview of coupon surface, (b)-(f) J-integral area for each element layer in the through-the-thickness direction.

Appendix C

Simulation of crack initiation and propagation in CT coupons using cohesive laws calibrated with the experimental results

To verify the representativeness of the fracture toughness measurements shown in Section 5.3.1, FE simulations of the CT tests were conducted using the experimentally-measured fracture toughness values as the inputs for CZM. The FE model of VTM-CE (shown in Fig. A.1 (b)) mentioned in Appendix B was used with three different cohesive laws: a bilinear cohesive law using either (i) the initiation fracture toughness or (ii) the propagation fracture toughness, and (iii) a trilinear law calibrated with the experimental R-curves from the J-integral method (values summarised in Table C.1). The orthotropic elastic properties (Young's modulus, shear modulus and Poisson's ratio) obtained from the calibrated Digimat's elastic material model were used for the bulk of the coupon, modelled with solid elements (as done for the VTM-CE simulations).

Table C.1. Initiation and propagation fracture toughness of PA66-GF50 used in the FE simulations.

	Initiation toughness (kJ/m^2)	Propagation toughness (kJ/m^2)
23°C-DAM 0°	10.0	18.0
23°C-DAM 90°	6.9	15.6
23°C-RH50 0°	11.3	22.6
80°C-RH50 0°	11.2	26.0

The trilinear cohesive laws were calibrated based on the method explained by Gutkin et al. [82] using experimental data. The dog-bone coupon's tensile test results (shown in Fig. 3.5) were used for the elastic stiffness and cohesive strength (as also done for the bilinear cohesive laws). The maximum crack opening displacement was measured from DIC of the CT tests, at the moment when the R-curves reached a plateau region (indicated in Fig. 5.5), at the location shown in Fig. C.1. The calibrated trilinear cohesive laws are shown in Fig. C.2.

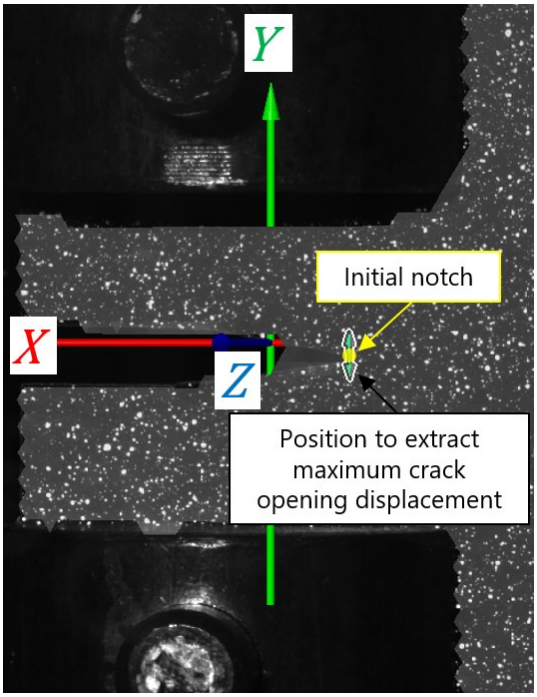


Fig. C.1. Position to extract the maximum crack opening displacement from DIC results, to calibrate the trilinear cohesive laws used in the FE simulations of the CT coupons.

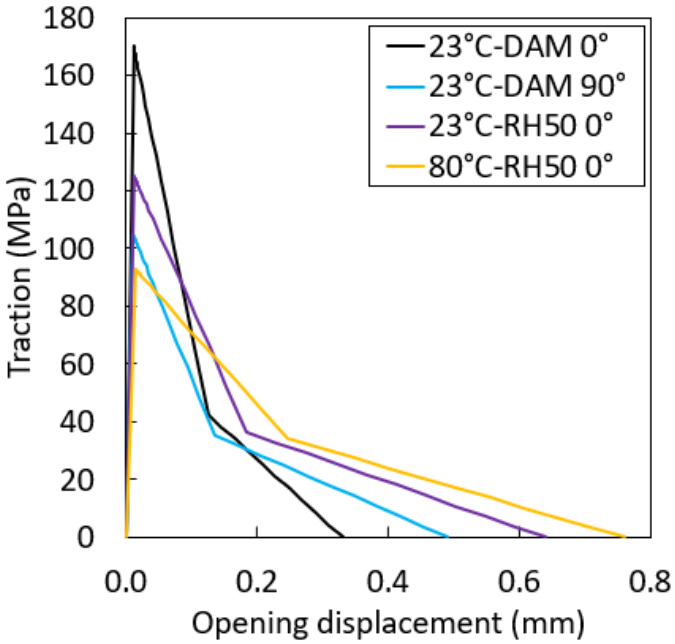


Fig. C.2. Calibrated trilinear cohesive law used in the FE simulations of the CT coupons.

Appendix D

Convergence study in the virtual testing of the subcomponents

Convergence studies of the parameters used in the coupled FEA of the subcomponents combined with CZM in Chapter 6 were conducted. The *FEA (CZM skin)* model (described in Section 6.5.3) was used to study the effect of the 'stabilization parameter', 'number of CE layers in the through-the-thickness (along the y) direction' and 'thickness of CEs (along the x direction)'. The parameters used in this study are summarised in Table D.1, and the results are shown in Fig. D.1. The predicted load-displacement curves and the maximum load were converged within the parameters used; therefore the parameters as shown with black in Fig. D.1 (stabilization: 0.01, number of CE layers: 10, CE thickness: 0.1 mm) were selected for the coupled FEA of the subcomponents entirely in Chapter 6.

Table D.1. Parameters used in the convergence studies for the FE simulations of subcomponents.

Stabilization (-)	number of CE layers (-)	CE thickness (mm)
0.005, 0.01, 0.05, 0.1	4, 8, 10, 12	0.05, 0.1, 0.2, 0.4

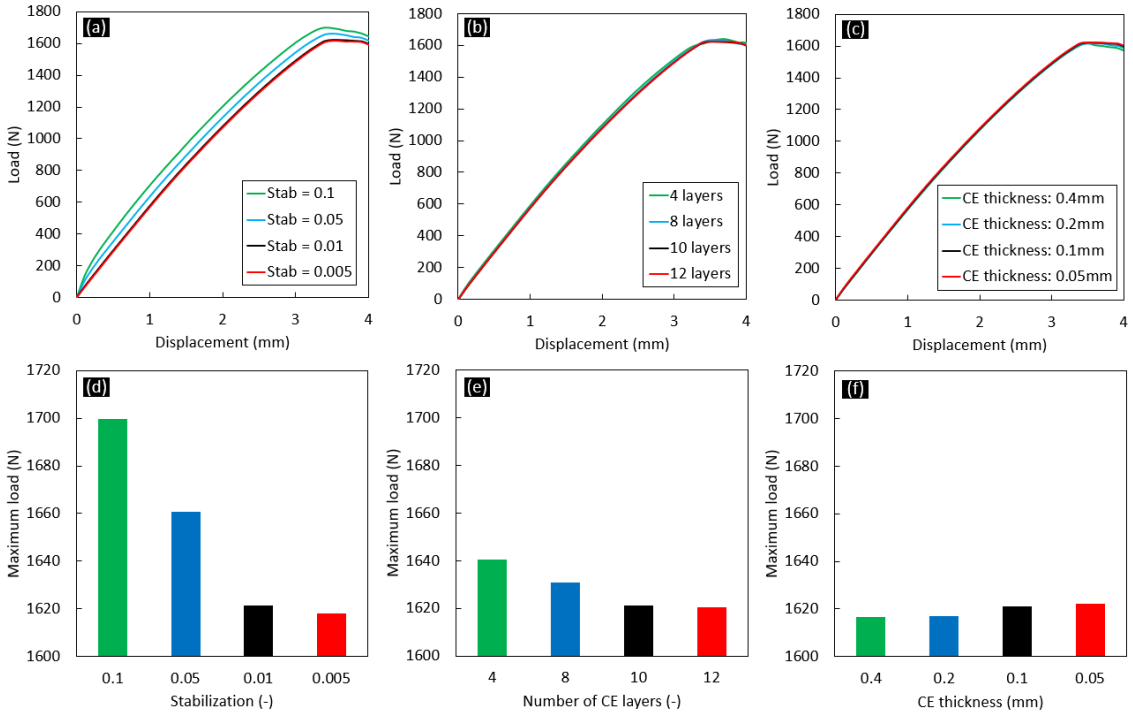


Fig. D.1. Load-displacement curves of the subcomponents from *FEA (CZM skin)* model using different numerical parameters: (a) stabilization, (b) number of CE layers and (c) CE thickness; the maximum load from these predicted curves is shown for different values of (d) stabilization, (e) number of CE layers and (f) CE thickness.